Origine des fractionnements isotopiques de l'azote et des gaz rares dans les météorites et les atmosphères planétaires

Maïa Kuga

Thèse de doctorat présentée en vue d'obtenir le titre de
Docteur de l'Université de Lorraine (Spécialité : *Géosciences*)

par **Maïa Kuga**

Origine des fractionnements isotopiques de l'azote et des gaz rares dans les météorites et les atmosphères planétaires

Origin of isotopic fractionations of nitrogen and noble gases in meteorites and planetary atmospheres

Soutenance publique prévue le 27 juin 2014

Membres du jury :

Président du jury	M. Pete Burnard
Rapporteurs	Mme Sylvie Derenne
	M. Conel Alexander
Examinateurs	Mme Lydie Bonal
	Mme Nathalie Carrasco
Directeur de thèse	M. Bernard Marty
Co-directeur de thèse	M. Guy Libourel
Invité	M. Yves Marrocchi

CRPG-CNRS, 15 rue Notre Dame des Pauvres, 54500 Vandoeuvre-lès-Nancy

L'impossible, nous ne l'atteignons pas, mais il nous sert de lanterne.

René Char

A ma grand-mère Jelena

Remerciements

Une fois n'est pas coutume... Voici venu le moment tant attendu (mais si difficile !) des remerciements.... Remerciements pour toutes celles et tous ceux qui ont contribué de près ou de loin à ce que ces presque quatre années de thèse se passent pour le mieux, scientifiquement, et humainement.

Un thésard est si peu sans son directeur de thèse... aussi je tiens particulièrement à remercier Bernard Marty, pour m'avoir offert la possibilité d'effectuer cette thèse en cosmochimie, au moment où je m'égarais vers d'autres horizons. Merci de m'avoir fait confiance pendant ces presque quatre années, de m'avoir laissé une complète liberté dans mes choix d'expérimentations, d'analyses et de collaborations. Je remercie également Guy Libourel, qui m'a guidée de loin, mais dont la bonne humeur m'a souvent remonté le moral et redonné de la motivation.

Je tiens à remercier tout aussi particulièrement Yves Marrocchi, bien que non officiellement directeur de thèse, car c'est avec tout autant d'énergie et d'enthousiasme qu'il s'est investi dans ce travail et je lui en suis très reconnaissante. Merci pour ta motivation, les discussions sans fin la tête dans les étoiles, pour le soutien moral, pour ton amitié, pour Pierre Desproges, pour le comté et les grognements !

Je remercie chaleureusement Sylvie Derenne et Conel Alexander d'avoir accepté d'être rapporteurs et de m'avoir fait part de leur enthousiasme pour ce travail. Si les météorites et la phase Q étaient des objets obscurs pour Nathalie Carrasco, Titan et les plasmas l'étaient tout autant pour moi, et je la remercie infiniment pour sa curiosité et son enthousiasme pour ce travail de thèse ; pour sa joie et sa motivation qu'elle communique dès la première rencontre ; pour m'avoir (presque) intégrée à l'équipe du LATMOS ; et aussi pour avoir accepté de faire partie du jury. Un très grand merci à Lydie Bonal pour avoir accepté d'évaluer ce travail de thèse, mais aussi pour les nombreuses discussions enrichissantes que nous avons pu avoir, pour la démystification des spectres Raman du carbone, pour ses encouragements. Enfin je remercie Pete Burnard d'avoir accepté de présider le jury, d'avoir eu de l'intérêt pour ce travail, mais aussi pour m'avoir appris à me servir d'un spectro gaz rares, pour son aide lors des longues sessions d'analyses et pour ne pas m'en avoir trop voulu d'avoir mis de l'air dans le vieil Helix lors de mon deuxième jour au laboratoire... Sorry !

Je remercie également Guy Cernogora, pour son aide immense, sa connaissance sur les plasmas, sa pédagogie, sa gentillesse. Sans lui, nous croirions sûrement encore que le Nébulotron est une vague lampe UV... et les fractionnements isotopiques de l'azote et des gaz rares dans les plasmas seraient toujours un mystère... Merci de nous avoir aidés à l'élucider en partie !

Merci à l'équipe « expérimentation » du sous-sol du CRPG, Delphine, François, et Tix, pour leur bonne humeur, le chauffage l'hiver grâce aux fours et pour la découverte de Radio

Magnum ! Un grand merci à Tix, pour m'avoir initiée à l'expérimentation et pour m'avoir aidée à faire marcher le Nébulotron du début jusqu'à la fin.

Un immense merci à toute l'équipe gaz rares avec qui j'ai eu un très grand plaisir à travailler pendant ces quatre ans, parfois jusqu'à des heures tardives ou bien des dimanches matins pluvieux autour d'un café et d'un spectro, et pour le ménage et les bières du vendredi après midi... Sarah, Evelyn, Ju, Guillaume, Léo, Arnaud, Nico Puch, Pete, Bouchaib, PH, Raphaël, Antonio (ci incontriamo in Sicilia!!). Un merci tout spécial à Magali, avec qui j'ai pu partager des moments gaz raresques intenses, pour les fous rires et pour le soutien! Et bien sûr, Monsieur Zim (je garde le meilleur pour la fin ! - ne rougis pas trop quand même !! -), merci à toi de m'avoir transmis (comme à tous ceux avant et après moi !) tes connaissances presque infinies sur les gaz rares et les spectros statiques, merci de ne jamais désespérer quand les spectros ne marchent pas, merci pour les rigolades et pour ton accent lorrain !

Ce travail est aussi le fruit de collaborations au CRPG et ailleurs : Merci à Thomas Rigaudier et Christian France-Lanord de m'avoir accueillie au labo des stables du CRPG, d'avoir levé quelques mystères sur les lignes en verre des isotopes stables et leur analyse et d'avoir accepté de passer des échantillons de gaz « mortel » sans trop de crainte !! Au LATMOS, je tiens à remercier Nathalie Carrasco et Guy Cernorgora, encore une fois, Edith Hadamcik pour sa gentillesse et les collaborations à venir, mais aussi Thomas Gautier pour son accueil et les vacances au Québec, Benjamin Fleury et Ludovic Vettier pour l'aide technique au Latmos et au Synchrotron ! A l'IPAG, un immense merci à Eric Quirico, pour m'avoir accueillie dans son laboratoire, d'avoir pris du temps pour répondre au nombre incalculable de mes questions sur la matière organique, le Raman et l'infra-rouge et d'avoir relu une partie de mon manuscrit, merci à Frod d'avoir éclairé ma lanterne sur l'interprétation des spectres infra-rouge mais aussi pour la soirée inoubliable à la LPSC 2013, on a quand même bien rigolé, Pierre Beck et Lydie Bonal pour les discussions à Grenoble ou ailleurs. Au Muséum, un grand merci à Laurent Rémusat pour les discussions inspirantes sur la matière organique des météorites et à Sylvain Bernard, d'avoir pris de son temps au synchrotron pour passer mes échantillons au STXM, merci à toi pour la rédaction du papier aussi ! A l'IPGP, merci à l'équipe des isotopes stables, Pierre Cartigny, Vincent Busigny et Magali Ader pour m'avoir permis de faire quelques manips dans leur labo, pour les discussions fort agréables et inspirantes que nous avons pu avoir. A l'ENS Lyon, je tiens à remercier Gilles Montagnac pour le Raman UV. A Géoressources, merci à Marie-Camille Caumon pour le Raman et à Odile Barrès pour l'infra-rouge. A l'école des Mines de Nancy, je remercie particulièrement Thomas Gries pour avoir répondu à toutes mes questions sur le fonctionnement des plasmas microondes.

Le CRPG est un lieu où il fait bon vivre pendant sa thèse, merci à tout ceux qui participent à cette bonne ambiance : la team des déjeuners à la cafet du CRPG, Camille et Martin (merci pour le soutien, les fous rires, les grognements, les références de ma thèse, l'accent alsacien, vous n'aurez pas la Lorraine dans l'Alsace ! merci pour tout quoi !), Emilie (à quand la prochaine boum ?), Yves (on attend toujours cette fameuse soirée ragga ! Mais j'aime quand même bien ce que vous faites), Laurette (et Julien ! les fous rires me

manquent !), Florian (et Jo !), Lydéric, Julien C., Marianne, Pioupiou (bon on se la refait quand ta soirée de départ ?), Eric H., Magali et tous ceux que j'ai oubliés. Une mention spéciale à l'équipe de voile du CRPG, même si on n'a pas gagné la course (c'est normal, on n'avait plus de spi), on était quand même les meilleurs. Merci à Pierre pour la fabrication des pièces pour le Nébulotron ou les gaz rares, toujours au poil et pour la veille ! Un immense merci à Cati, Aurélie et Isabelle pour la gestion des missions, parfois abracadabrantes. Et bien sûr le service général avec Bruno, Nordine et Yannick.

En dehors du labo, j'ai eu beaucoup de soutien aussi, en particulier de la part des copains de Nancy, mes colocs préférés Audrey, Fab et Mike, que de bons souvenirs dans cette maison ! Audrey, merciiiiiiiiiiiiiiiiiiiiiiiiii ! T'es la plus belle ! Et aussi Fabien Fabulous, le Brau, la Shteuf, Crilou, Coco, Dam's, Bruno, Guillaume, Bérangère, Sonic, les Folimandingue, Anne, Nastasia et tous ceux que j'ai oubliés. Merci pour ces bonnes soirées, pour la musique, la danse, le théâtre, les discussions sur tout et rien. Vous n'imaginez pas à quel point vous avez pu me ressourcer. Un merci tout spécial au Rem's, qui m'a introduite dans ce monde lorrain, inconnu à moi il y a encore 5 ans... Pendant ces quatre ans, j'ai aussi passé beaucoup de temps dans les salles de danse... Indispensable pour oublier la science quelques heures durant... Un immense merci à Sylvie et à la Compagnie Averses, j'ai pris un énorme plaisir à danser avec vous, j'espère qu'on continuera à faire des roulades dans l'herbe et des chandelles les yeux rivés vers les nuages ! Btissame, merci pour ta présence pendant ces 5 ans à Nancy, tu auras presque réussi à me faire aimer la Lorraine, presque..., Coline pour ta joie de vivre, Denis, j'attends la prochaine danse, t'es quand même mon cavalier attitré !, Yann, merci pour ta motivation, pour le tango, pour ton goût sans fin de la vie et des belles choses. Maylis, Benoît, Anne-So et Elodie, la team ENS, merci pour ces beaux weekends randonnée de l'extrême, dans la neige jusqu'au genou, dans le brouillard vosgien ou encore sur les pentes automnales glissantes du Dévoluy... La prochaine destination ?

Enfin, je n'aurais pas pu en arriver là sans l'aide et les encouragements de mes parents et de mes sœurs... Et sans doute non plus sans le soutien qui m'a été apporté pendant quatre ans par Guillaume, merci à toi pour ta présence, ton intégrité, ta tendresse pendant cette période pas évidente qu'est la thèse.

Table of contents

Chapter 3

Chapter 4

Chapter 5

Résumé

La formation et l'évolution du système solaire repose sur des processus physiques et chimiques complexes, dont la description à différentes échelles est permise aujourd'hui par les observations astronomiques, les modélisations numériques, les simulations expérimentales et l'étude des cosmomatériaux. Ces différentes approches ont abouti à un modèle global de la formation du système solaire tel que nous le connaissons aujourd'hui, dont les étapes principales sont : (1) la naissance du Soleil, l'étoile centrale ; (2) la formation d'un disque protoplanétaire composé de gaz et de poussières et (3) l'accrétion des premiers corps solides, les planétésimaux, jusqu'aux planètes. Le disque protoplanétaire, composé initialement de gaz et de poussières, est un système dynamique en évolution constante, au cours de ses quelques millions d'années de vie depuis la formation de l'étoile centrale jusqu'à la dissipation tardive du gaz primordiale et la mise en place des planètes actuelles. Les modélisations numériques et les observations de disques en rotation autour d'étoiles jeunes indiquent une stratification radiale et verticale du disque, à la fois en température, densité, irradiation, et donc en processus physico-chimique. A l'extérieur ou à la surface du disque, l'ionisation de la matière (gaz ou poussières) par différentes sources de radiations semble gouverner les réactions chimiques et la croissance des glaces et autres grains solides par des processus de photochimie et/ou de réactions ions-molécules. Dans la région interne, où se forment ensuite les planètes telluriques, les processus de condensation, principalement lié au gradient de température dans cette région, semblent gouverner la formation des premiers solides. Ces grains, puis les planétésimaux issus de leur accrétion ont vraisemblablement été transportés efficacement à travers le disque, résultant en un mélange de différentes populations de solides et de planétésimaux, de composition chimique contrastée, formés proche de l'étoile ou à l'extérieur du disque. De nombreuses inconnues demeurent dans ce schéma global, notamment les processus chimiques et physiques à l'œuvre dans le disque protoplanétaire et contrôlant l'accrétion des premiers corps planétaires. Lors de l'évolution du disque protoplanétaire, le rapport poussières/gaz va progressivement augmenter, signant la disparition massive du gaz, initialement le composant principale de la nébuleuse protosolaire primordiale (rapport poussières/gaz ~ 0.01 ; proche de celui du milieu interstellaire local). Une partie du gaz primordial est conservée dans les objets du système solaire actuel, dans les atmosphères des planètes de gaz géantes mais aussi dans les corps solide du système solaire interne (atmosphères planétaires et intérieur des planètes et des corps solides).

La compréhension de l'origine des éléments extrêmement volatils (composés riches en hydrogène, carbone, azote (H, C, N) et gaz rares) dans le système solaire interne ainsi que de

leurs abondances et compositions isotopiques est primordiale pour étudier la formation des environnements planétaires et en particulier celui de la Terre et de son atmosphère ; mais reste une question ouverte encore aujourd'hui. Par ailleurs, la notion d'héritage chimique et isotopique du gaz primordial et/ou son évolution dans certaines régions du disque protoplanétaire avant d'être intégré dans les corps solides sont des problématiques très débattues, dont les mécanismes physiques et chimiques sont encore peu compris. Ces questions ont été explorées au cours de cette thèse, qui s'est attaché en particulier à l'étude de l'origine des compositions isotopiques de l'azote et des gaz rares dans les météorites primitives et les atmosphères planétaires, par une approche expérimentale.

Les échantillons de météorites et de comètes dont nous disposons dans nos collections sont considérés comme les meilleurs échantillons représentatifs de la composition des petits corps solides du système solaire. L'étude des météorites est particulièrement déterminante pour la compréhension des processus responsables de la formation des premiers solides du système solaire et de l'accrétion et de la croissance des planétésimaux à l'origine des planètes, dont la Terre. Cependant, l'établissement d'un lien entre les processus physiques et chimiques ayant lieu dans le disque protoplanétaire et les planètes et les astéroïdes actuels, à travers l'étude des météorites, n'est pas aisé. En effet, parmi les météorites dont nous disposons dans nos collections, les chondrites, météorites non-différenciées, sont considérées comme primitives ; mais ont subi malgré tout des modifications depuis leur formation, par chauffage et/ou altération aqueuse. Les chondrites de type 3, i.e. ayant subi le moins de modifications par métamorphisme thermique ou altération aqueuse depuis leur formation, sont considérées comme ayant le mieux conservé leurs caractéristiques chimiques et texturales primordiales. Certaines chondrites, notamment les chondrites carbonées, peuvent contenir jusqu'à plusieurs poids pourcents de matière carbonée, composée d'éléments chimiques pouvant être extrêmement volatils en fonction de leur spéciation chimique : carbone, azote, hydrogène, oxygène, soufre (C, N, H, O, S). Après l'hydrogène et l'hélium (He), le carbone, l'azote et l'oxygène sont les produits primaires de la nucléosynthèse stellaire. Les composés CHON, donc de nature organique, sont ainsi les principaux composés volatils que l'on trouve dans les environnements astrophysiques. Les composés organiques de nature extraterrestre ont été identifiés dans les météorites dans les années 1970, et sont majoritairement présents dans les météorites sous forme de macromolécule de type kérogène (Matière Organique Insoluble, MOI), dont l'origine, interstellaire ou solaire, et le(s) mécanisme(s) de formation de cette macromolécule organique, sont activement débattue encore aujourd'hui.

L'une des particularités de cette MOI des météorites est de présenter des variations du rapport isotopique de l'azote ($^{15}N/^{14}N$) de plusieurs facteurs, à l'échelle submicrométrique, sans commune mesure avec les variations isotopiques observées dans les échantillons terrestres. Ces variations isotopiques observées à l'échelle de la MOI des météorites s'inscrivent dans une gamme de variation isotopique du rapport $^{15}N/^{14}N$ encore plus grande à l'échelle de tout le système solaire. La composition isotopique de l'azote du Soleil, considérée comme représentative de la composition isotopique du gaz primordial de la nébuleuse protosolaire, est pauvre en ^{15}N ($(^{15}N/^{14}N)_{Soleil} = 2.27\pm0.03\times10\text{-}3$). A l'exception de Jupiter et de quelques minéraux réfractaires présents dans les météorites, tous les objets et composés

contenant de l'azote dans le système solaire sont enrichis en ^{15}N par rapport à la nébuleuse protosolaire. L'origine de ces variations de la composition isotopique de l'azote dans les matériaux du système solaire est encore mal comprise mais semble être la conséquence de fractionnements isotopiques spécifiques à l'azote. Plusieurs mécanismes responsables d'enrichissements conséquents en ^{15}N par rapport à un réservoir de départ ont été proposés, faisant intervenir soit l'ionisation de composés riches en azote (réactions ion-molécules à basse température), soit la photodissociation de l'azote moléculaire N_2 (self-shielding / prédissociation accidentelle de N_2) dans la nébuleuse protosolaire ou le disque protoplanétaire, par des agents d'ionisation, principalement des photons UV provenant du soleil jeune. En revanche, ces modèles ont très peu été testés expérimentalement, et jamais dans le but de former de la matière organique complexe comme celle observée dans les météorites avec des fractionnements isotopiques de l'azote associés.

Une seconde particularité de la MOI des météorites, en plus d'être le siège d'anomalies isotopiques en azote, est d'être intimement liée au principal réservoir de gaz rares piégés dans les météorites. Ces gaz rares (He, Ne, Ar, Kr et Xe), éléments extrêmement volatils par définition, contenus dans les météorites primitives, présentent des compositions isotopiques et élémentaires différentes de celle du soleil, considérée comme représentative de la composition du gaz de la nébuleuse protosolaire. L'inventaire des gaz rares lourds (Ar, Kr et Xe) dans les météorites est dominé par le composant appelé « Q » (pour Quintessence), composant supposé comme représentatif du principal réservoir des gaz rares dans le système solaire (en dehors du Soleil) lors de la formation des premiers solides. En effet, les gaz rares Q sont mesurés dans la très grande majorité des météorites. Ces gaz rares piégés sont très concentrés, comparé à une roche terrestre, et présentent une composition élémentaire et isotopique fractionnée par rapport à la composition solaire, montrant un enrichissement systématique en élément/isotope lourd par rapport à la référence solaire, et ce, quelle que soit la météorite analysée. En revanche, la phase porteuse des ces gaz rares Q, la « Phase Q », est encore mal caractérisée. On la suppose de nature carbonée car les gaz rares Q semblent étroitement liés à la MOI des météorites. Si la nature de la phase porteuse des gaz rares Q reste imprécise, il a été montré expérimentalement, à plusieurs reprises, que l'apparition d'un fractionnement élémentaire et isotopique des gaz rares lourds, en particulier pour le Xe, semble liée à l'ionisation des gaz rares. En revanche, le mécanisme physique responsable du piégeage des gaz rares dans la matière carbonée ainsi que du fractionnement élémentaire et isotopique n'est pas contraint.

Dans le cadre de ce travail de thèse, nous nous sommes également intéressé à l'atmosphère de Titan, le plus gros satellite de Saturne. Titan possède en effet une atmosphère dense, composée à plus de 95% d'azote moléculaire (N_2), le reste étant majoritairement du méthane (CH_4). La haute atmosphère de Titan est soumise à l'irradiation des photons du soleil, provoquant la photodissociation de N_2 et CH_4, à l'origine une cascade de réactions photochimiques aboutissant à la production d'aérosols organiques en quantité, donnant cette teinte orange caractéristique de la surface de cette planète. La mission Cassini/Huygens a permis d'apporter de nombreuses informations quantitatives sur les espèces volatiles présentes dans l'atmosphère de Titan mais aussi d'identifier la présence

d'azote dans les particules solides atmosphériques. Le rapport isotopique de l'azote a été mesuré à plusieurs altitudes dans l'atmosphère de Titan, dans l'azote moléculaire N_2 et dans HCN, principale molécule azotée produite par les réactions photochimiques et la dissociation de N_2. Ces mesures indiquent un enrichissement en ^{15}N dans HCN par rapport à N_2 de plus de 300 ‰, suggérant l'effet du phénomène de self-shielding lors de la photodissociation de N_2 dans la haute atmosphère de Titan par les photons UV du Soleil, comme cela avait déjà été évoqué pour la nébuleuse protosolaire. En revanche, la composition isotopique de l'azote dans les aérosols organiques, pourtant un réservoir conséquent d'azote dans l'atmosphère de Titan, est inconnue, de même que la conservation d'anomalies isotopiques dans un schéma réactionnel depuis la dissociation de N_2 jusqu'à la formation d'un grain organique solide. Des expériences de laboratoire ont démontré leur capacité à produire des aérosols organiques à partir de mélanges gazeux représentatifs de l'atmosphère de Titan, en revanche, l'aspect isotopie de l'azote n'avait jamais été exploré.

L'origine des gaz rares Q, de la MOI qui les contient et des anomalies isotopiques de l'azote dans le système solaire fait partie des questions les plus tenaces et les plus importantes en cosmochimie. Les résoudre apporterait un éclairage certain sur les processus physico-chimique ayant lieu dans le système solaire jeune mais aussi sur l'origine des éléments volatils des planètes et sur l'évolution de leurs atmosphères. L'objectif de cette thèse est de contraindre les conditions dans lesquelles la matière organique réfractaire peut se former, associée à des fractionnements isotopique et élémentaire de l'azote et des gaz rares qui y sont incorporés.

Pour répondre à ces questions, des expériences plasmas ont été réalisées dans deux atmosphères de gaz, $CO+N_2$ et CH_4+N_2, avec l'ajout de gaz rares, pour représenter les compositions chimiques de la nébuleuse protosolaire et de l'atmosphère de Titan, respectivement (*Chapitre 2*). Deux expériences de plasma froid ont été utilisées pour produire des solides carbonés : (i) le Nébulotron, dédié à la simulation des processus ayant eu lieu dans le jeune système solaire (plasma microondes, CRPG, Nancy) et (ii) le réacteur PAMPRE, utilisé pour investiguer les processus chimiques ayant lieu dans la haute atmosphère de Titan (plasma radiofréquence, LATMOS, Guyancourt). Dans ces plasmas froids, ce sont les électrons qui, de part leur fonction de distribution en énergie, apportent l'énergie requise pour l'ionisation et/ou la dissociation de CO, CH_4, N_2 et des gaz rares. Ces premières réactions d'ionisation et de dissociation des composés gazeux initient un réseau de réactions chimiques qui aboutissent à la croissance de grains solides riches en carbone, dans lesquels l'azote peut être incorporé en tant qu'hétéroatome et dans lesquels les gaz rares peuvent également être piégés efficacement.

Les solides carbonés produits dans le Nébulotron par la dissociation de CO seul ou de $CO+N_2$ ont été caractérisés ex-situ par plusieurs techniques analytiques (*Chapitre 3*). Ces particules solides ont une texture carbonée de type turbostratique, avec des hétérogénéités apparentes à l'échelle micrométrique. Les composés solides produits sont riches en oxygène, azote mais aussi en hydrogène, montrant la présence d'une source de contamination en hydrogène (mais probablement aussi en azote et en oxygène) dans le réacteur plasma du

Nébulotron. Ces composés organiques sont polyaromatiques et présentes de nombreuses fonctions, cycliques ou non, riches en oxygène et azote. Les résultats de la caractérisation de ces composés organiques synthétisés dans le Nébulotron indiquent des propriétés communes avec la MOI des météorites, comme les rapports élémentaires H/C, OC/ et N/C ; la structure polyaromatique, le degré de désordre de la structure carbonée et quelques fonctions organiques riches en oxygène et azote. La plupart de ces propriétés physico-chimiques sont rarement regroupées dans les précédents analogues de laboratoires pour la MOI ou les composés organiques extraterrestres. Ces résultats suggèrent que la formation de composés organiques complexes dans un environnement de plasma pourrait être pertinent pour la formation de la MOI des météorites (ou de précurseurs à la MOI).

Le fractionnement isotopique de l'azote lors de la formation de composés organiques riches en azote dans des plasmas froids a été exploré (*Chapitre 4*). La composition isotopique (exprimée en $\delta^{15}N$ (‰ de déviation par rapport à la composition isotopique de l'air terrestre)) et la spéciation de l'azote incorporé dans les particules organiques solides produits dans le Nébulotron (CO-N_2) et dans PAMPRE (CH_4-N_2) ont été analysées. Les aérosols du Nébulotron et de PAMPRE montrent un appauvrissement comparable en ^{15}N, de -15‰ à -25‰ par rapport au gaz N_2 de départ, et ce quelque soit la spéciation de l'azote dans la structure moléculaire du composé organique, différente pour les deux types d'aérosols synthétiques. Cet appauvrissement en ^{15}N est important comparé aux variations isotopiques de l'azote que l'on peut mesurer dans les échantillons terrestres naturels. Ce fractionnement isotopique a été interprété comme résultant d'un fractionnement isotopique cinétique (dépendant de la masse), ayant pu avoir lieu lors des différentes étapes de synthèse des particules solides depuis la dissociation de l'azote moléculaire N_2 par les électrons dans le plasma. Ces résultats ont plusieurs implications :

- Les expériences de synthèse organique par plasma ne reproduisent pas les enrichissements exceptionnels en ^{15}N mesurés dans certains cosmomatériels, probablement parce que le mécanisme de dissociation de N_2 dans un plasma (impact électronique et collisions entre particules lourdes) ne se produit pas par self-shielding ou par prédissociation accidentelle (bien que cette dernière puisse avoir lieu dans les plasma, elle aurait lieu trop rarement pour affecter la compositions isotopique finale du solide formé).
- Dans le cas de l'atmosphère de Titan, une fraction d'aérosols organiques produits dans la haute atmosphère est initiée par la dissociation de N_2 et CH_4 par impact électronique, en particulier sur la face « nuit » du satellite. Les fractionnements isotopiques cinétiques pour l'azote pourraient donc jouer un rôle non négligeable dans le bilan de masse isotopique de l'azote dans l'atmosphère de Titan.
- Enfin, l'atmosphère de la Terre à l'Archéen a pu contenir à plusieurs reprises des quantités importantes d'aérosols organiques, formés par des réactions photochimiques à partir de la dissociation de N_2, CO_2 $\pm CH_4 \pm H_2$, etc... qui composaient l'atmosphère de la Terre à cette époque. Les compositions isotopiques négatives de l'azote qui ont été mesurées dans des sédiments organiques d'âge Archéen pourraient en partie être le résultat de synthèse

organique abiotique, associé à un fractionnement isotopique cinétique lors de la formation d'aérosols riche en azote dans l'atmosphère de la Terre primitive.

Les fractionnements élémentaire et isotopique, ainsi que l'efficacité de piégeage des gaz rares lourds (Ar, Kr et Xe) piégés dans les particules solides organiques produites dans le Nébulotron ont été quantifiés (*Chapitre 5*). Les profils élémentaires et isotopiques mesurés dans les solides synthétiques du Nébulotron sont semblables à ceux obtenus dans les précédentes expériences de piégeage de gaz rares dans des matériaux solides et au profil des gaz rares Q des météorites. Ces profils élémentaires et isotopiques fractionnés par rapport au gaz de départ suggèrent fortement le rôle essentiel des gaz rares ionisés. Les fractionnements élémentaire et isotopique résultent probablement de deux mécanismes différents : (i) des taux d'ionisation différents des différents gaz rares dû à des énergies d'ionisation contrastées et (ii) la diffusion ambipolaire des gaz rares ionisés à la surface des particules solides, respectivement. La diffusion ambipolaire est suggérée pour la première fois pour rendre compte du fractionnement isotopique dépendant de la masse du krypton et du xénon, observé à la fois dans les échantillons synthétiques du Nébulotron et dans la Phase Q des météorites. Ces résultats expérimentaux suggèrent que l'implantation d'ions de faible énergie cinétique peut être un mécanisme efficace pour piéger des gaz rares dans des composés riches en carbone. En revanche, toutes les propriétés des gaz rares Q des météorites n'ont pas été reproduites dans les expériences du Nébulotron, en particulier le comportement très réfractaire de la Phase Q et l'efficacité de piégeage des gaz rares (bien plus importante dans la MOI), qui demeurent des questions ouvertes.

Ces travaux de thèse pris dans leur ensemble ont plusieurs implications concernant les conditions de formation de la MOI des météorites primitives et de l'acquisition des gaz rares piégés et de la composition isotopique de l'azote :

- les résultats expérimentaux obtenus au cours de cette thèse suggèrent que les mécanismes de fractionnement isotopique de l'azote et des gaz rares dans un plasma, mais aussi dans le cas des cosmomatériaux, sont différents. En effet, les principales propriétés des gaz rares Q des météorites sont reproduites dans les expériences, ce qui n'est pas le cas des forts enrichissements en ^{15}N de la MOI chondritique. Ce comportement différent indique que l'ionisation des gaz rares ne dépend pas de la source d'ionisation (électrons/photons UV) alors que la dissociation de l'azote moléculaire N_2 ne semble produire des forts fractionnements isotopiques seulement si la source d'irradiation est constituée de photons UV. D'autres processus que la dissociation de N_2 par impact électronique seulement sont requis pour rendre compte des enrichissements et des anomalies en ^{15}N par rapport à la composition isotopique de la nébuleuse protosolaire mesurées dans la MOI des météorites et dans les autres corps planétaires ou cosmomatériaux. La dissociation de N_2 par les photons UV du soleil jeune et/ou les réactions ion-molécules dans la nébuleuse solaire ou le disque protoplanétaire restent les meilleurs mécanismes proposés à ce jour.

- Les expériences réalisées au cours de cette thèse reproduisent relativement bien les principales caractéristiques des gaz rares Q mais aussi de la MOI des météorites. Les profils élémentaire et isotopique fractionnés des gaz rares ne peuvent être reproduits que dans un environnement ionisé. Ainsi, puisque la Phase Q, porteuse des gaz rares fractionnés, et la MOI semblent intimement liés dans les météorites, cela suggère que les précurseurs de la MOI se sont formés dans une région de la nébuleuse solaire ou du disque partiellement ionisée et illuminée par des radiations suffisamment énergétiques pour ioniser tous les gaz rares (i.e., > 25 eV pour l'hélium). L'énergie d'ionisation des gaz rares est plus grande que les énergies de dissociation des composés gazeux principaux de la nébuleuse solaire : H_2, CO, N_2. Ce dernier a donc pu être (photo)dissocié et/ou soumis à du self-shielding, selon la densité de la colonne de gaz et de la nature du champ d'irradiation. Les expériences présentes montrent par ailleurs que des matériaux organiques complexes peuvent être formés à partir de la dissociation des gaz CO et N_2. Ainsi, la synthèse de précurseurs de la MOI des météorites, sous forme de composés organiques complexes, dans de tels environnements partiellement ionisés, a pu être compatible avec un fractionnement isotopique des gaz rares mais aussi de l'azote.

Abstract

The formation and the evolution of the solar system rely on complex physical and chemical processes, which description at different scales is accounted by astronomical observations, numerical modeling, experimental simulations and studies of primitive cosmomaterials. Meteorites are the best samples available representative the constitutive materials of the small bodies of the solar system, and their study can help to understand some of the processes responsible for the formation of the first solids in the solar system and for the accretion and growth of planetesimals and planets.

Organic compounds of extraterrestrial origin were identified in meteorites in the 70's. The origin of this organic matter, which is kerogen-like, is still actively debated and nor the location neither the mechanisms of its formation are constrained. Interestingly, large amounts of noble gases, which display elemental and isotopic fractionation patterns different from those of the protosolar gas, were measured in these organic compounds. In addition, this organic macromolecule is also the host of large D and ^{15}N enrichments relative to the composition of the protosolar gas. The physical/chemical processes responsible for the fractionations observed for these volatile elements, e.g. noble gases, nitrogen and hydrogen, are not constrained. Studying the behavior of volatile elements under a variety of conditions representative of the protosolar nebula would help to circumscribe the environment of formation of the meteoritic organic compounds as well as the origin of planetary atmospheres.

This thesis work, which is presented in this manuscript, deals with an experimental study on the processes responsible for the isotopic fractionation of noble gases and nitrogen, associated to the synthesis of organic solids analogues. For that purpose, a plasma setup was used, in which organic solid particles are produced by the dissociation of gases representative of the solar nebula, in addition to noble gases, under varying conditions. The synthetic organic solids were characterized by a variety of analytical techniques to determine their molecular and structural features. Nitrogen isotopes were measured in these organic compounds to identify the isotopic fractionation process occurring in a plasma environment. Finally, the content, the elemental and isotopic fractionations of the noble gases trapped into the synthetic organics were analyzed, and some physical processes were proposed to account for the experimental results and for the observations in primitive meteorites. This work helps to give new constraints on the astrophysical environment of the formation of the organics present in primitive meteorites.

This manuscript is composed by five chapters.

A general introduction is given is Chapter 1. The main events of the formation and evolution of the solar system formation are highlighted. Some of the physical and chemical processes occurring in the solar nebula and relevant for this study are described. Some key elements on the composition of primitive meteorites and of comets are given. Finally, a state of the art of the nitrogen isotopes variations in the solar system, and of the characteristics of the noble gases trapped in primitive meteorites is outlined.

Chapter 2 is dedicated to the description of the physical and chemical processes occurring in plasmas. The experimental setups that were used in this thesis, e.g. the PAMPRE setup (LATMOS, Guyancourt) and the Nebulotron setup (CRPG, Nancy), as well as the experimental conditions, are detailed.

The physicochemical characterization of the solid organic particles produced in the Nebulotron setup is given in Chapter 3. The analytical techniques that were used are briefly described. In the light of the results, a comparison between the molecular and structural features of the Nebulotron samples and those of the organic compounds in meteorites is outlined.

Chapter 4 is dedicated to the results on the nitrogen isotopic fractionation occurring in the two experimental setups. This study is presented in the form that was published in EPSL.

The study on the content elemental and isotopic fractionation of the noble gases trapped in the organic solids formed in the Nebulotron setup is presented in Chapter 5. The analytical methods for the measurement of noble gases are described. The Xe, Kr and Ar concentrations, as well as the elemental and isotopic fractionation patterns, measured in the experimental samples are given and discussed in the light of the characteristics of the noble gases trapped in primitive meteorites. The physical processes responsible for these features that were inferred from this study are described.

Finally, the new constraints provided by this work are summarized in the last section of the manuscript. Some perspectives of future work that I think relevant are outlined as well.

Chapter 1

Introduction

Table of contents

1.1 Context

The origin of extremely volatile elements (e.g., H, C, N compounds, and noble gases) in the inner solar system is not well understood, limiting by our poor understanding of the mechanisms responsible for the formation of planetary environments. Solar volatiles, those found in primitive meteorites and those in planetary atmospheres and interiors, have contrasting abundances and isotopic compositions. This thesis aims to understand the relationships between these components, which is still unclear today. In particular, trapping volatile elements into organic solid compounds have been investigated. As the planets presumably grew by accreting objects similar to meteorite parent bodies, and, as the latter ultimately formed from the solar nebula gas, the dynamical, physical and chemical processes that occurred in the early solar system since its formation are a key to understand these relationships. The main steps of the formation and evolution of the solar nebula are described in the first part of this Introduction. The second part summarizes the isotopic variations of nitrogen and the noble gases observed among solar system objects and reservoirs. These two types of elements are interesting for several reasons: nitrogen isotopes present among the largest variations ever observed for any element, and noble gas isotopic compositions show surprising heterogeneities given their presumed chemical inertness.

1.2 Formation and evolution of the solar nebula

The idea that the solar system was born out of the contraction and evolution of a molecular cloud leading to the formation of a protoplanetary disk originates back to Kant and Laplace in the 18th century (Woolfson, 1993). Since then, three major phases were identified: (i) the birth of the central star, (ii) the formation of the protoplanetary disk and (iii) the accretion of planetesimals, of embryos and eventually planets.

1.2.1 The birth of the Sun

Stars, like the Sun, were probably born in clusters from localized regions of giant molecular clouds (Fig. 1.1).

These interstellar clouds, according to astronomical observations, are composed primarily of H_2, He and 1% of other species like heavier volatile species such as CO, silicate, hydrocarbon and ice dust grains (Asplund et al., 2009). Average densities are on the order of 10^3-10^4 particles/cm^3 and the temperatures are typically 10-50 K (Montmerle et al., 2006). Gravitational forces are responsible for the increase in the density, and eventually initiate the contraction and the rapid collapse of the dense core, over timescales of ~ 1 Myr (10^6 years) (Boss and Ciesla, 2014, Montmerle et al., 2006). During this prestellar phase, a first optically thick core is formed (Boss and Ciesla, 2014, Feigelson and Montmerle, 1999).

The thermal pressure of H_2 supports this central core, while the remainder of the cloud continues to fall onto the core. When the density and the temperature are high enough, the H_2 molecules break apart, causing a second collapse that results in the birth of the protostar.

Subsequently, the fusion of deuterium begins. At this stage, bipolar outflows along the rotation axis of the protostar/circumstellar disk system are observed, probably expelling much of the excess angular momentum of the infalling material, and clearing away the molecular cloud material. This is the *T-Tauri* or *pre-main sequence stage of a nascent star*, still fed by gravitational contraction. When the temperature is high enough, the proto-star starts to burn hydrogen. This ends the protostellar phase and the star begins its main sequence phase.

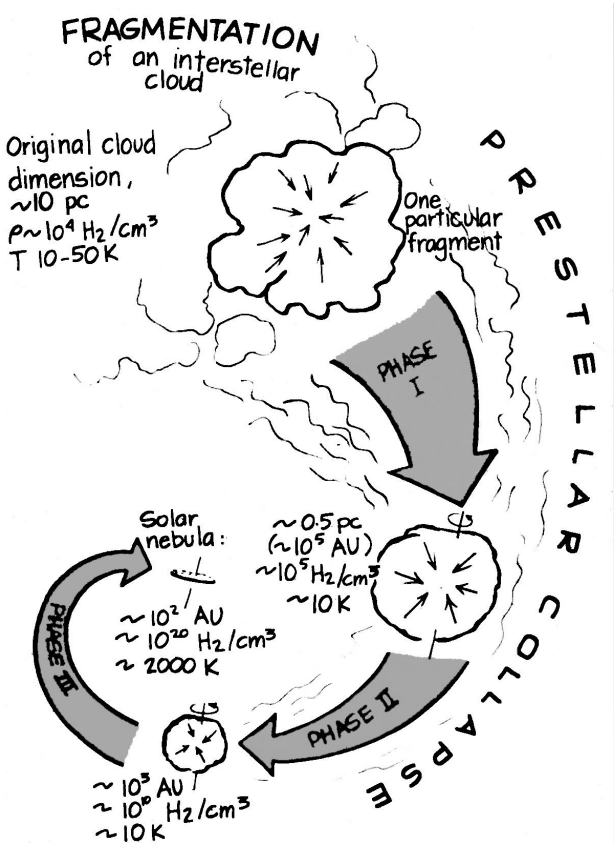

Figure 1.1. Schematic illustration of the solar nebula's birth, by J. Wood.

1.2.2 The protoplanetary disk

1.2.2.1 Formation

The infalling gases and dust from the initial cloud continuously accrete first directly onto the protostar, and eventually, only a flattened circumstellar disk remains: this is the *protostellar disk*. After ~ 10^5 years, most of the matter in the disk has fallen onto the T-Tauri star because of "turbulent viscosity" (magnetorotational instabilities for instance). As a result, the temperatures in the disk generally decrease, although intense accretion episodes

are observed, suggesting that young disks are gravitationally unstable (Hartmann et al., 1993). **After 5 My or so, the accretion onto the star ceases and the *prestellar disk*, almost empty, evolves toward a *protoplanetary disk*, in which increasingly larger solids are able to grow**.

1.2.2.2 Physical properties

Since the mid-90's, protoplanetary disks (PPD) have been routinely observed around T-Tauri stars through their infrared and (sub) millimeter thermal emission. These disks are, for the most part, relatively cool (T ~ 10-1000 K), and are rich in dust. Most observed disks have inferred masses that represent ~ 1% that of the central star (Armitage, 2011, Williams and Cieza, 2011). PPD are observed to be geometrically thin (height << radius, with thickness H being proportional to $R^{1/2}$ (R being the radius): Dullemond et al., 2002, Williams and Cieza, 2011), with R ranging between a few tens to a few hundreds of AU. Disks are characterized by strong radial and vertical temperature and density gradients (Henning and Semenov, 2013, Fig. 1.2)

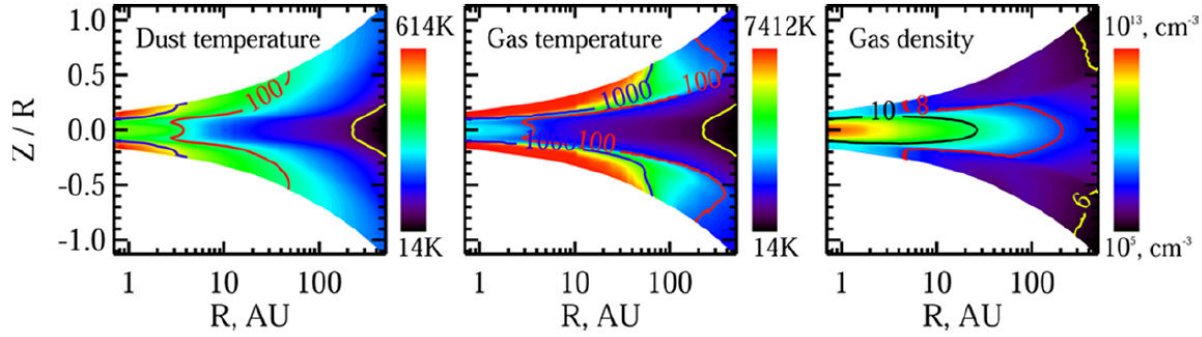

Figure 1.2. Calculated radial and vertical profiles of the dust temperature (left), the gas temperature (middle) and the gas density (right). The high values are marked by red color whereas the low values are marked by dark blue/black colors (from Henning and Semenov, 2013).

Several models have been developed to account for the angular momentum transport, among them turbulent 'α-models' (D'Alessio et al., 1998), in which charged particles orbiting around a central star will be subject to Lorentz forces under the influence of a magnetic field. These forces will destabilize radially the distribution of the angular momentum of orbiting particles, resulting in turbulence. This process, called magnetorotational instability (MRI), occurs when the angular momentum of an orbiting fluid tends to decrease with increasing distance from the rotation axis, and MRI is very effective, even for weak magnetic fields, at transporting angular momentum. Thus, ionization is a key process that results in the regulation of the motion of a protostar disk.

In the inner part of the disk, temperatures are high enough for thermal ionization to occur, whereas non thermal sources such as X-rays and UV radiations emitted by the central star, radioactive decay and cosmic rays from the stellar environment, initiate ionization of the gas at larger radial distances (Armitage, 2011). Disks in which angular momentum

transport occurs via the MRI are expected to develop a radially "layered" structure, where active MRI zones are located in ionized regions. A dead zone can develop at the mid-plane, where ionization rates (ionization degree $<10^{-10}$) are too low to initiate MRI (Armitage, 2011, Henning and Semenov, 2013, Fig. 1.3). Grain growth and grain settling are strongly coupled with ionization; so that disk chemistry and disk physical structure are intimately linked.

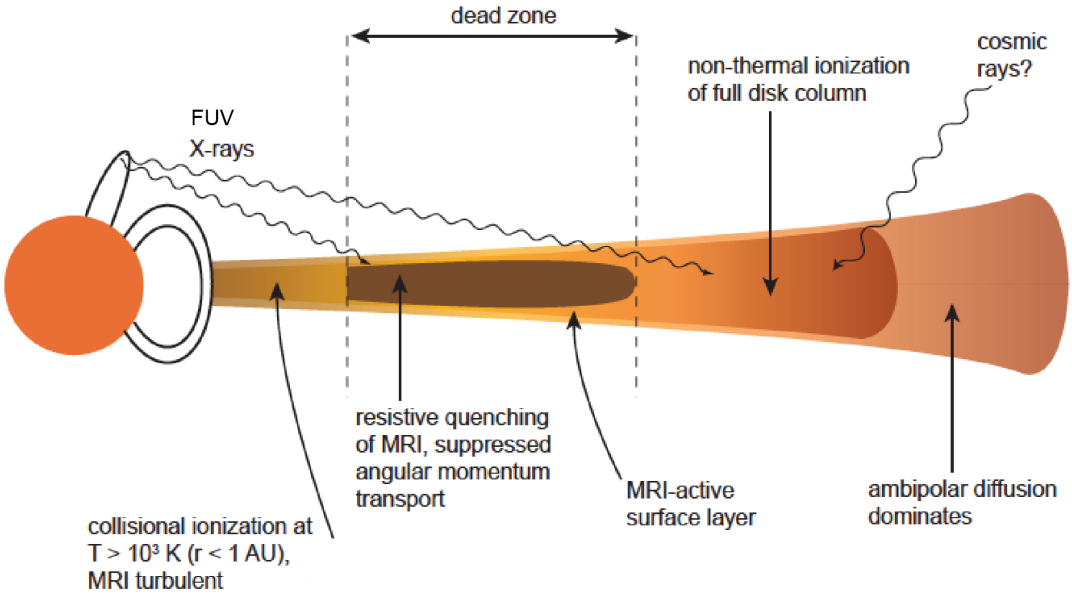

Figure 1.3. Schematic structure of a layered PPD due to angular momentum transport via MRI (adapted from Armitage, 2011).

1.2.2.3 Composition

PPDs are made of dust and gas. Solid particles represent only 1% of the initial mass of the disk (dust/gas ratio close to the one of the local interstellar medium of the solar system, Birnstiel et al., 2010), but dominate the disk opacity. In the interstellar medium, dust is mainly composed of sub-micron sized amorphous silicates, associated with graphite grains and polycyclic aromatic hydrocarbons (PAHs, large molecules rather than grains: Henning, 2010, Tielens, 2008). In PPDs, two kinds of dust grains are present: (i) grains inherited from the circumstellar envelope that survived vaporization in the solar nebula, and (ii) grains formed by condensation in the solar nebula due to temperature gradient in the disk. Close to the central star, only refractory elements can be in solid form, whereas further away in the PPD, more volatile species can exist in the gas phase or are locked up in solids, following the classical condensation sequence (Ebel, 2006, Grossman, 1972). Gas accounts for 99% of the total mass of the ISM, and the same is true, at least initially, for PPDs (Birnstiel et al., 2010). Its detection is, however, made difficult by the limited spectroscopic resolution of most

observation instruments. The presence of H_2, along with trace gases, such as, CO, HCO^+, H_2CO, NH_2^+, CS, CN, HCN and HNC have inferred from observations in the mid-infrared and (sub)-millimeter wavelength regime (Dutrey et al., 2014).

1.2.2.4 Chemistry

Chemical reactions in disks are mostly regulated by their temperature and density structures, together with stellar and interstellar radiation fields, as well as by cosmic rays. As shown in Figs. 1.2 and 1.3, PPDs are characterized by vertical and radial temperature and density gradients, and by a variety of radiation fields at various disk locations. These locally different disk properties imply a potentially rich and diverse disk chemistry. Fig. 1.4. shows a schematic picture of a T Tauri disk:

(1) Within 1 AU, inner disks are characterized by their high temperatures (from 100K up to 5000K) and high densities up to 10^{12} cm^{-3}. The gas phase is expected to be composed of H_2, CO and N_2 molecules together with H_2O, OH, simple hydrocarbon, PAH and N-bearing molecules (Caselli and Ceccarelli, 2012, Grossman, 1972). At these high temperatures, chemistry approaches a quasiequilibrium. **Refractory grains (e.g. calcium-aluminum rich inclusions, magnesium-rich silicates, etc. …) are formed by condensation from the gas** as a function of temperature, which decreases with the radial distance from the star (Grossman, 1972). Further away from the central star, the decreasing temperatures ultimately enable the freeze-out of volatile molecules, below their condensation temperatures. The condensation of water vapor occurs at about 150K, marking the so-called "**water snow line**", which was located at 2-5 AU, at the midplane, in the early solar nebula. The snowline would have tended to migrate inward as the disk evolved and accretion slowed. The CO snow line was located at larger radial distances of about 20 AU, where the temperature drops below 20K.

(2) In the disk surface layers, stellar and interstellar radiation fields (UV and X-rays) ionize and dissociate molecules, resulting in the formation of chemical compounds through **ion-molecule reactions**. In this photon-dominated region, **photochemistry** is particularly important, but it is in competition with photoevaporation and photodissociation, which are the main mechanisms by which newly formed compounds are lost at the disk surface. This region is also where **UV self-shielding** starts to take place in some models (Clayton, 2002, Henning and Semenov, 2013).

(3) Below the disk surface, the warm molecular zone is partly shielded from the radiations and molecules can survive, although **photochemistry** still plays an important role. UV self-shielding is expected to be an important mechanism controlling the photodissociation of molecular isotopologues such as CO or N_2 in the region. Beyond the snowline, H_2O is still frozen onto the dust grains and **gas-grain reactions** may occur.

(4) and (5) In the deep interior of PPDs, where temperatures drop below 20K, molecular freeze-out becomes important and ultimately dominant at the midplane. These regions are completely shielded from radiations (apart from cosmic rays). Here, **ice and grain surface processes** are dominant.

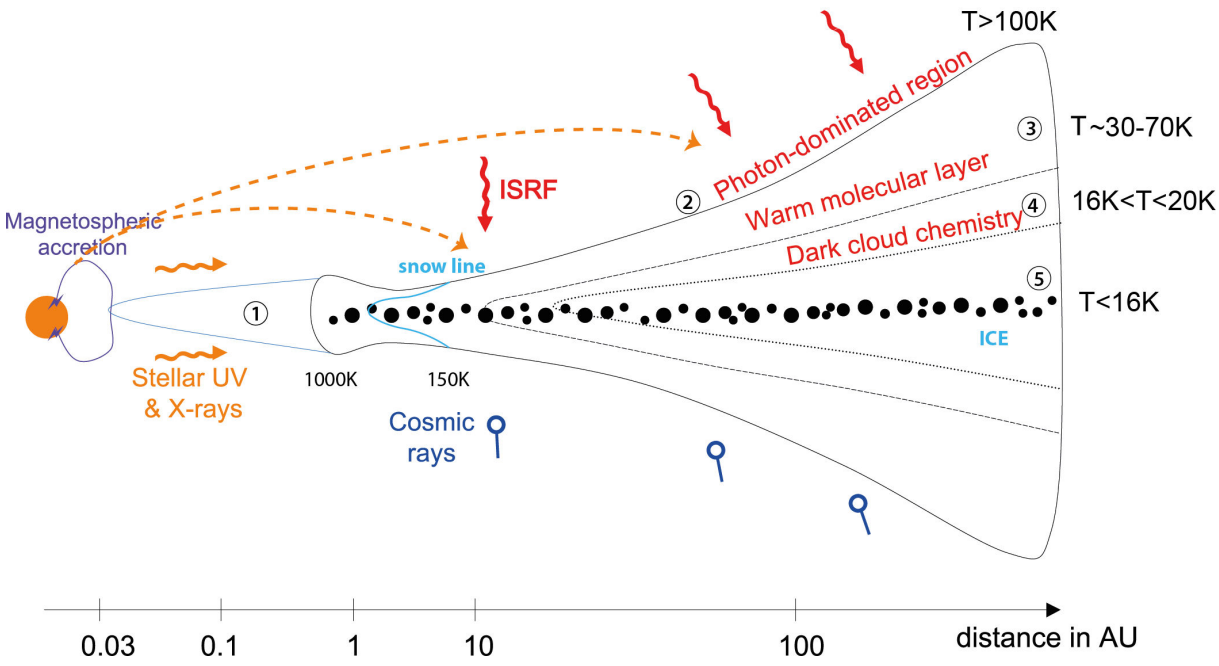

Figure 1.4. Cartoon of the chemical structure of a protoplanetary disk around a Sun-like star (adapted from Caselli and Ceccarelli, 2012 and Henning and Semenov, 2013). The various regions are labeled 1-5 (see text). The black dots represent the coagulated dust onto the disk mid-plane. ISRF = Interstellar Radiation Field.

1.2.3 Planetesimal an planet formation

Terrestrial planet formation occurred through three distinct modes of growth that were ordered in time in the protoplanetary disk (PPD) (e.g. Morbidelli et al., 2012 and Fig. 1.5).

1.2.3.1 From dust to planetesimals...

Grains agglomerate due to collisions, helped by electrostatic and magnetic forces, forming compact aggregates up to millimeter to centimeter sizes (Morbidelli et al., 2012). As soon as they reach such sizes, they sediment rapidly to the midplane of the disk and become decoupled from the gas on timescales of 10^3 years or so (Hayashi et al., 1985). While laboratory experiments have been successful at making dust grains sticking together, building larger objects is problematic because of the "meter-size barrier": once they rich this size, the solid bodies start to migrate rapidly relative to the as, so that collision velocities rise and become destructive rather than constructive. Several hypotheses have been proposed in the last 15 years to overcome this barrier: a very fast accretion of planetesimals (Morbidelli et al., 2009), "stickiness" provided by ice or carbonaceous coatings on dust grains (Weidenschilling, 2000), and local gravitational instabilities (Cuzzi et al., 2008, Johansen et al., 2007, Johansen and Youdin, 2007). In particular, this last "*clumping*" scenario is consistent with the sizes of solid bodies in the asteroid and Kuiper belts, and implies that the planetesimal formation occurred sporadically, which is consistent with the chronological

constraints on meteorite formation (Amelin et al., 2002, Bouvier and Wadhwa, 2010, Burkhardt et al., 2008, Qin et al., 2008, Villeneuve et al., 2009).

1.2.3.2 ... to planetary embryos...

The accretion of embryos (1000-5000 km) is dominated by gravitational attraction between planetesimals, through *runaway* and *oligarchic growth* processes (Greenberg et al., 1978, Ida and Makino, 1993, Kokubo and Ida, 1998, 2000). The runaway/oligarchic growth processes forms planetary embryos of Lunar to Martian size around 1 AU on very short timescales of 10^5-10^6 years (Kokubo and Ida, 1998). During such short interval of time, the decays of short-lived ^{26}Al ($T_{1/2}$ = 700,000 years) and ^{60}Fe ($T_{1/2}$ = 1.5 Myr) (Mishra and Chaussidon, 2014, Mishra et al., 2010, Mostefaoui et al., 2005, Tachibana and Huss, 2003, Villeneuve et al., 2009) were able to provide sufficient energy to melt partially these bodies or totally, depending on their sizes and respective building durations. For instance, Mars, which is thought to be a planetary embryo, was possibly built up in a few Myrs (Dauphas and Pourmand, 2011). The formation of the giant planet cores seems intimately related to the runaway/oligarchic growth of embryos by their rapid and mutual accretion up to 10 Earth masses, beyond the snowline, although the process is not well understood yet (Morbidelli et al., 2008, Raymond et al., 2013). Giant planets growth must have been completed in the presence of the nebular gas-disk and thus predated the formation of the terrestrial planets (Morbidelli et al., 2012).

1.2.3.3 ... to terrestrial planets

When the disk gas was lost after a few 10^6 years, either by accretion onto the Sun, or, by photoevaporative loss (Alexander, 2008, Haisch et al., 2001), the embryos become rapidly unstable and their orbit began to interact (Raymond et al., 2009; Chambers and Wetherill, 1998). In the terrestrial region in a PPD, embryos accrete each other in low velocity collisions, known as "*chaotic growth*" or "*late-stage accretion*" processes (Raymond et al., 2006). In the Solar System Jupiter likely perturbed the embryos' and planetesimals' eccentricities in the inner part of the accretion disk, resulting in the elimination of the embryos originally present in the asteroid belt and in the formation of a small number of terrestrial planets in the 0.5 – 2 AU region on a timescale of 30-100 My (Chambers and Wetherill, 1998). This scenario is consistent with several of the key observations and notably accounts for the mass deficit of the asteroid and Kuiper belts, the number of terrestrial planets formed and, possibly, the formation of the Moon (Canup, 2012, Stewart and Leinhardt, 2012) and the timescale of Earth's accretion as provided by radiochronometers (Kleine et al., 2009; Avice and Marty, 2014).

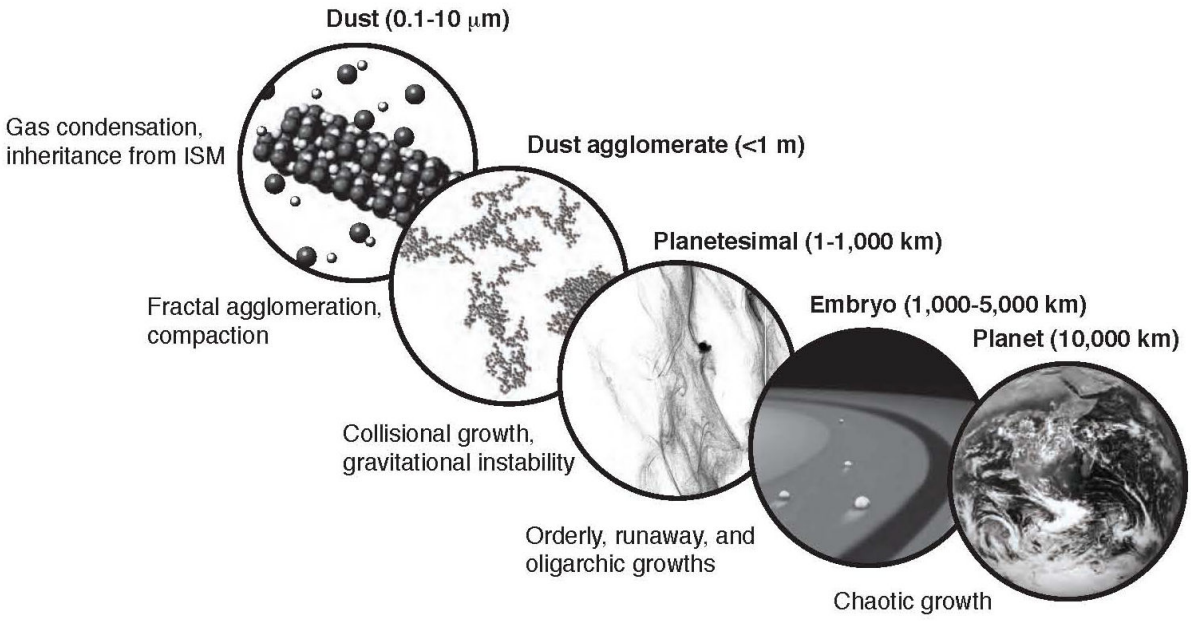

Figure 1.5. Schematic evolution of planetary formation events (adapted from Dauphas and Chaussidon, 2011).

1.2.4 Transport and scattering in the disk

1.2.4.1 Vertical and radial mixing of dust grains

Some radial and vertical mixing must have occurred early in the protoplanetary disk. Vertical mixing is inferred from the observation of PAH compounds in the photon-dominated zone of the disk. Since these compounds are formed in the warm molecular layer and since they are efficiently destroyed by extreme UV and X-ray photons, their presence in the upper atmosphere of the disk hints at some replenishing mechanism, possibly vertical transport (Caselli and Ceccarelli, 2012). The presence of presolar grains in the matrices of chondrites, as well as D-rich organics, that possibly formed in the outer disk, also points out efficient radial and vertical transport in the PPD, before/during the accretion of the chondrite parent bodies (Huss and Lewis, 1995, Remusat et al., 2010). Turbulence, via gravitational and magnetorotational instabilities, may have triggered such mixing in the disk.

1.2.4.2 Planetesimal scattering

Early in the history of the PPD (before gas dissipation and after planetesimal formation), Jupiter and Saturn would have migrated inward in the disk, driven by gas drag and then outward by the coupling of their eccentricities ("Grand Tack" model, Walsh et al., 2011). Such a swing would have caused planetesimal scattering beyond the giant planets orbits, and a repopulation of the inner asteroid belt with bodies from both the inner and the

outer part of the disk (Fig. 1.6). Such a scenario provides a close match of the present-day architecture of the inner solar system.

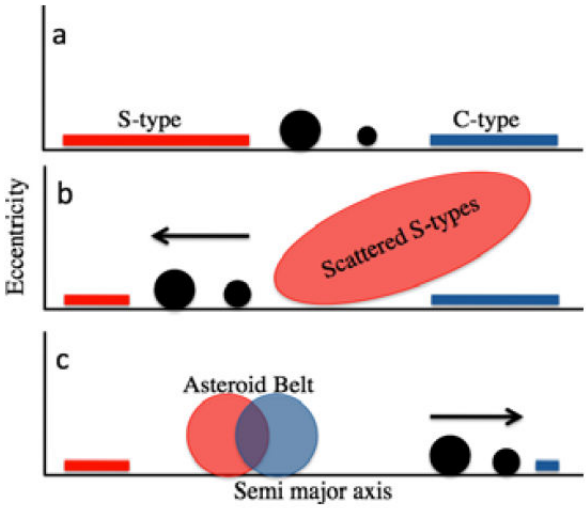

Figure 1.6. Schematic view of the Grand Tack, where the large black circles are Jupiter and Saturn. The S-type planetesimals (red) are representative of the volatile-poor/dry asteroids formed in the inner part of the disk. The parent population of the C-type asteroids (blue) is formed beyond the giant planets orbit. (a) initial conditions: of the disk, Jupiter forms, Saturn is growing; (b) inward (arrow) migration of Jupiter and Saturn, resulting in the scattering of most S-type asteroids beyond the giant planets; and (c) final configuration with an asteroid belt repopulated with bodies from both the inner and the outer parts of the disk (from Walsh et al., 2012).

Later on in the history of the PPD, and once the Moon was already formed, resonance between giant planets eccentricities might have triggered a second scattering event, causing the "Late Heavy Bombardment" of the terrestrial planets, which occurred 4.1-3.8 Gyr ago ("Nice model", Gomes et al., 2005, Morbidelli et al., 2012).

The protoplanetary disk is an evolving and dynamic system. The disk thermal and density structure, radiation field, and grain properties undergo dramatic transformations during the few Myr of its lifetime. Ionization occurs in different regions of the disk, governing grain growth via photochemistry and ion-molecule reactions. In return, ionized atoms and molecules control most of the physical and dynamic processes. Radial and vertical transport of solids was likely efficient and resulted in the mixing of different planetesimals populations throughout the disk.

The models presented above provide some dynamical constraints on the general processes that resulted in the present-day architecture of the solar system, and are globally consistent with the timing of solar system formation. However, several issues are not resolved yet. Observational constraints help to deduce properties of the planetesimal disk. In particular, the composition of solar system bodies, including primitive materials in meteorites, comets and planets provide a detailed window into their formation history.

1.2.5 Asteroid and comets: leftover planetesimals

Most of meteorites and cosmic dust that fall to the Earth come from asteroids and comets, which are thought to be leftover planetesimals.

1.2.5.1 Chondrites come from asteroids

The measurement of pre-atmospheric orbits of meteorites as well as shared optical and near-infrared spectral features with asteroid bodies (Chapman and Salisbury, 1973, Gaffey et al., 1993), point to parent bodies of meteorites originating in the main asteroid belt.

Based on their bulk compositions and textures, there are two major categories of meteorites: chondrites and non-chondritic meteorites. The latter have experienced melting and subsequent differentiation, and are subdivided into achondrites, stony irons and iron meteorites. Among meteorites, chondrites provide the best clues on the origin of the solar system, as they display the most primitive features. Chondrites are divided into three main classes: carbonaceous (CI, CM, CO, CV, CR, CH, CB and CK, related to C-type asteroids), ordinary (H, L and LL, related to S-type asteroids, the most abundant in the asteroid belt) and enstatite (EH and EL, related to E-type asteroids) (Fig. 1.7).

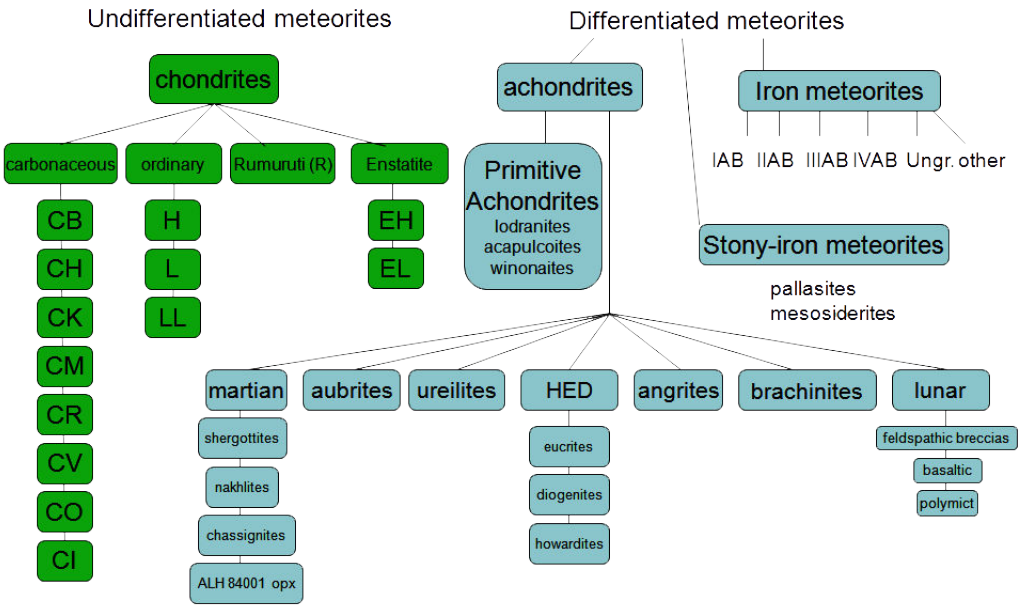

Figure 1.7. Classification of meteorites (credits: NASA).

Chondrites are complex aggregates of components present in variable proportions depending on the chondrite group: chondrules (20-80%), refractory inclusions (hereafter CAI, 0.01-10%), metal (0.1-50%), and matrix material (1-80%). CAIs are high temperature assemblages, almost entirely composed of crystalline silicates and oxides rich in Ca and Al. These objects are thought to be the products of rather localized heating close to the Sun. They are the oldest recognized objects in the solar system, with absolute Pb-Pb ages of 4.5685 Ga (Connelly et al., 2012). CAI ages are usually considered by cosmochemists as the

time zero for solar system formation. Chondrules are sub-millimeter- to centimeter-sized solidified silicates melt droplets, mainly composed of olivine, pyroxene, Fe-Ni metal and commonly contain sulfides, oxides and a glassy mesostasis. Their igneous textures indicate that they were at some point fully or partly melted. Our current understanding is that chondrules formed over a time period of 0 - 4 Myr after CAIs (Villeneuve et al., 2009, Connelly et al., 2012). Matrix materials are heterogeneous and mainly consist of sub-micron sized grains of olivine, pyroxene, Fe-Ni metal and sulfides set in an amorphous material composed of Si, Al, Fe, Ni and S. Phyllosilicates, carbonates and organic matter can also be observed in chondritic matrices. Organic matter is also found in all chondrites (with exception of CKs and Rs, where metamorphism and oxidation have probably destroyed it). Carbon appears as nanoglobules and diffuse carbon-rich material in between matrix grains. In many cases, the matrix contains a significant amount of presolar grains. Chondrules, CAI, metal and matrix materials formed under diverse conditions and timescales in the solar system, and offer insights into high temperature primary processes that took place early in the accretion disk. The presence in chondritic matrix of organic compounds, presumably formed in the outer solar system or in the parent molecular cloud, together with presolar grains, provides evidence that dust has been physically admixed after the formation of CAIs and chondrules. This suggests that chondrites accreted materials formed in diverse regions of the disk, hence can be regarded as clastic sedimentary rocks.

Chemically, the most primitive meteorites are the CI chondrites as, except for the most volatile elements and Li, their elemental abundances are close to those in the solar photosphere (Fig. 1.8). Compared to CIs, all other chondrite types are depleted in volatile elements. The chemical fractionation between chondrites are best understood in terms of equilibrium condensation, which assumes that minerals condensed from, or equilibrated with, a homogeneous solar nebula gas at different temperatures (Grossman, 1972).

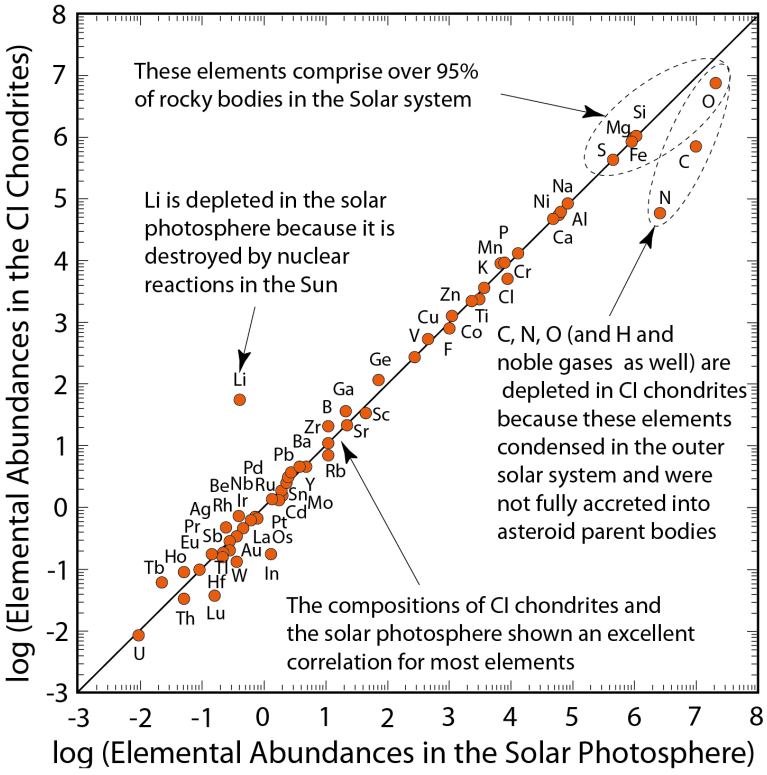

Figure 1.8. Elemental abundances in CI chondrites compared to the abundances in the solar photosphere (the abundance of Si is set at 10^6 Si). H and noble gases are not shown (adapted from Lauretta, 2011).

All chondrites were modified to some degree by geological processes within their parent asteroids. The three main processes were: aqueous and hydrothermal alteration, thermal metamorphism and impacts, resulting in changes in their primary texture, mineralogy, and chemical and isotopic compositions (Krot et al., 2006). These secondary features are the basis of the petrologic classification of chondrites (Van Schmus and Wood, 1967) with petrologic types 1 - 6 providing a guide to the extent and nature of asteroidal processing.

Despite their complexity, chondrites represent our best witnesses of the formation and evolution of the solar system.

1.2.5.2 Cometary materials and the asteroid-comet continuum

Comets are active bodies that develop an extended coma (tail) when they approach the Sun close enough to sublimate water and other volatiles from their surface. Cometary nuclei today reside in two distinct reservoirs, the Oort Cloud (>10,000 AU) and the Kuiper Belt (between 30 and 100 AU). They are thought to have formed beyond the water snowline in the accretion disk. The comet nucleus represents the bulk of the comet's mass and is made of equal amounts of ices and dust (Greenberg, 1998). Spectroscopic observations of cometary tails have shown that the ice compositions are dominated by H_2O and CO with traces of CO_2, HCN and NH_3, with strong variability from one comet to another one (Irvine et al., 2000, Mumma and Charnley, 2011). The dust is primarily composed of sub-micron-sized porous silicate aggregates (Gounelle, 2011, Mumma and Charnley, 2011). All molecules detected in comets resemble those observed in star-forming regions, although the relative abundances are not the same. This reinforces the hypothesis of a low-temperature formation for comets, independently supported by the isotopic composition of hydrogen in their water ices and organic molecules (Bockelée-Morvan et al., 2008, Bockelée-Morvan et al., 1998). Cometary nuclei are therefore thought to contain the least modified material from the formation of the first solids in the outer solar nebula. However, the results from the Stardust Mission to the comet Wild 2 have somewhat questioned this assumption, by showing the presence of CAIs and chondrules that are similar in composition, mineralogy and oxygen isotopic composition to those found in carbonaceous chondrites (Brownlee et al., 2006, McKeegan et al., 2006, Zolensky et al., 2006). The latter observations support the hypothesis of an asteroid-comet continuum and reinforce the idea of dust transport and scattering of planetesimals throughout the accretion disk (Gomes et al., 2005, Gounelle, 2011, Morbidelli et al., 2012, Briani et al., 2011, Ciesla, 2007).

The link between the physical and chemical processes occurring in protoplanetary disk, the remnant planetesimals and the present-day planets, via the study of meteorites, is not simple. Meteorites are objects that have undergone reprocessing since their formation, likely resulting in the lost of some of their primordial features. On the other hand, pristine components are essential to improve our understanding of the dynamics and chemistry in accretion disks, with the underlying questions: To which degree are the primordial features conserved? What is the extent of chemical/isotopic resetting materials in meteorites?

Volatile elements are a powerful tool to address these questions because, as their sublimation temperature is low, their abundances can help to trace the physical and chemical processes experienced by their host phases. However, volatile elements are prone to isotopic fractionation and exchange. Therefore, the isotopic compositions of volatile elements are potential tracers of the evolution of reservoirs in the solar nebula, as well as of their inheritance. This study has focused on the volatile content of primitive meteorites, as they represent the bridge between the primordial solar nebula and the terrestrial planets.

1.3 Volatile elements in solar system bodies

After H and He, the primary products of stellar nucleosynthesis are C, N and O. Thus, CHON are the main volatile building blocks that can be found in astrophysical environments (although O is only partially volatile since much of it is in refractory oxides and silicates in chondrites and planets). In most primitive carbonaceous chondrites, C and N are mostly hosted by the macromolecular organic compound (hereafter IOM for Insoluble Organic Matter), which in turn is the main reservoir of volatile elements in these objects.

1.3.1 Organic matter in carbonaceous chondrites

Carbonaceous chondrites contain up to about 4wt% carbon, mostly in the form of organic matter, with minor fractions hosted by carbonates, elemental carbon phases (graphite and nanodiamonds) and refractory carbides. The organic matter occurs dispersed and as sub-micron sized globules throughout the matrix (De Gregorio et al., 2013). Its in-situ analysis is therefore difficult and its extraction from the bulk chondritic material is the usual way to study organic matter in chondrites. About 70 to 99% of the chondritic organic matter fraction consists of an insoluble macromolecular material (e.g., IOM) whereas a small fraction is in the soluble form (Pizzarello et al., 2006). Carbon, H and O are the main constituents of IOM, while N and S are minor heteroatoms. Chondritic IOM is the main reservoir of D and N isotopic anomalies and of noble gases, and is described in the following parts.

1.3.1.1 The Insoluble Organic Matter

IOM is isolated from the bulk rock by solvent and acid treatments (Gardinier et al., 2000). In most cases, the acid residue is not pure organic matter and still contains non-dissolved oxides, sulfides and nanodiamonds (Lewis et al., 1975).

IOM has been studied through a variety of analytical techniques, both destructive and non-destructive: elemental analysis (Alexander et al., 2007), py-GCMS (Huang et al., 2007, Remusat et al., 2005, Sephton, 2013), infrared, NMR and XANES spectroscopies (Cody and Alexander, 2005, De Gregorio et al., 2013, Gardinier et al., 2000, Le Guillou et al., 2014, Orthous-Daunay et al., 2013), Raman spectroscopy (Bonal et al., 2007, Bonal et al., 2006, Busemann et al., 2007, Quirico et al., 2014, Quirico et al., 2003), electron paramagnetic resonance (EPR, Binet et al., 2004) and Transmission Electron Microscopy (TEM, Derenne et al., 2005, Le Guillou et al., 2012).

Elemental analysis of IOMs from unheated chondrites reveals typical formula of ~ $C_{100}H_{65}N_3O_{20}S_3$ (Alexander et al., 2007). Most of carbon atoms (50-80%) are in aromatic

structures whereas the rest are in aliphatic bonds (Cody and Alexander, 2005). Aromatic units are small, with aliphatic between aromatic moieties of 2-9 carbon atoms. This results in a carbon skeleton with a high degree of cross-linking, definitely different from terrestrial organic compounds such as kerogen. A structural model of the IOM of Murchison gathering most of the results from the last 20 years has been proposed by Derenne and Robert, 2010, and is shown in Fig. 1.9.

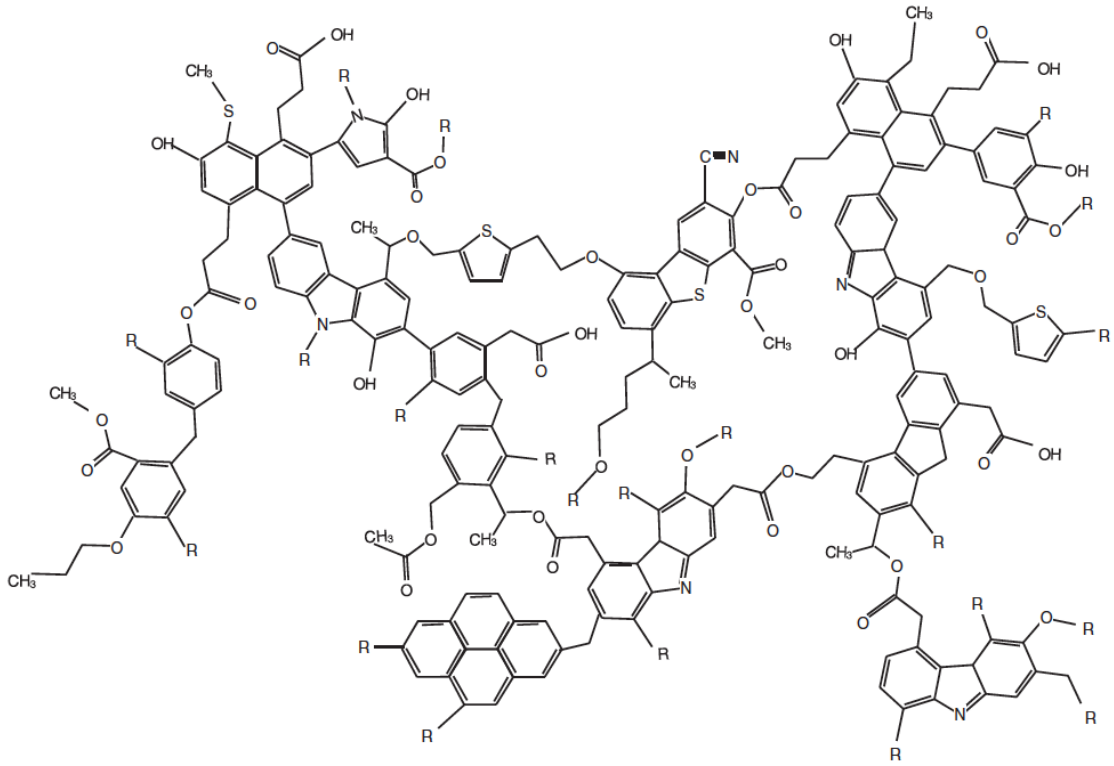

Figure 1.9. Model of the molecular structure of the IOM of Murchison (from Derenne and Robert, 2010).

As outlined above, in situ characterizations are rare (De Gregorio et al., 2013, Le Guillou et al., 2014), due to analytical limitations. Therefore, interactions between organics and silicate in the matrix of chondrite are poorly known.

1.3.1.2 C, H and N isotopic compositions

Bulk C, H and N isotopic analysis on 75 IOMs from different chondrites revealed that most of them are enriched in D relative to the Earth and to the solar compositions. Bulk ^{15}N-enrichments are more modest. The magnitude of the enrichment varies from one type of chondrite to the other. In particular, IOMs from CR chondrites show high D and ^{15}N enrichments. δ^{13}C variations are small compared to those of D/H and δ^{15}N, and are in the range of terrestrial rocks for most of them (Alexander et al., 2007, Fig. 1.10).

NanoSims analysis of IOMs from various types of chondrites has revealed isotopic heterogeneities at the submicron-scale. Extreme D and ^{15}N-enrichments are concentrated in

localized submicron zones, the so-called "hotspots" (Bonal et al., 2010, Briani et al., 2009, Busemann et al., 2006, Remusat and et al., 2009). These hotspots display among the largest D and ^{15}N enrichments ever measured in the solar system bodies and reservoirs.

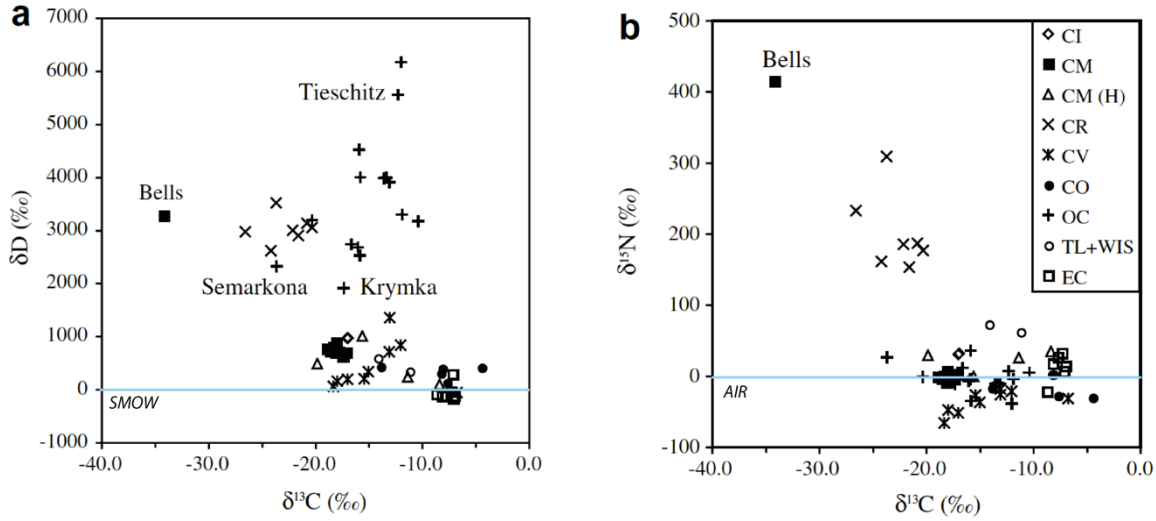

Figure 1.10. C, H and N isotopic compositions of bulk IOMs from various types of chondrites (adapted from Alexander et al., 2007). The blue lines show the mean H isotopic composition of the terrestrial oceans (SMOW) and the N composition of terrestrial air. Variations of terrestrial H and N isotopic ratios are small compared to those measured in IOMs.

1.3.1.3 Origin(s)

No consensus exists on the formation mechanism(s) of IOM. Several models have been proposed in the last 30 years, at hot/warm or low temperatures, either in the ISM or in the solar nebula. Fischer-Tropsch type reactions at high temperatures (>500 K) are expected to produce organic macromolecules but do not account for the isotopic characteristics of chondritic IOM (Nuth, 2008). The unique isotopic composition of IOM likely points out very specific formation mechanism(s). Indeed, based on the significant D and ^{15}N enrichments, it has been suggested that IOM is largely of interstellar origin (Robert and Epstein, 1982) or at least formed from interstellar precursors. Indeed, D and ^{15}N enrichments are observed in the ISM and are thought to result from low temperature ion-molecule reactions (Aléon, 2010, Millar et al., 1989, Terzieva and Herbst, 2000). An interstellar origin was also inferred from the polyaromatic structure of IOM, as many PAHs are present in the ISM (Pendleton and Allamandola, 2002).

An interstellar origin is, however, debated. Spectral features of interstellar organic compounds are clearly different from those of IOM and laboratory experiments simulating organic synthesis by irradiation of ices in conditions representative of the ISM never produced the polyaromatic structure observed in IOM (Dartois et al., 2004), although the NMR spectra of such synthetic products seems to be close of those of some chondritic IOMs

(Cody and Alexander, 2005). Furthermore, it has been shown that in the Orgueil meteorite, the deuterium could have been added to the IOM after its formation, more likely in the accretion disk rather than in the ISM (Gourier et al., 2008, Remusat et al., 2006). The carrier(s) of the noble gases, which is intimately liked to the IOM (see next section), seem to be derived from the solar gas and therefore, point out a local origin as well. The polyaromatic structure of IOM appears to require energetic processes, either during strong irradiation in the upper atmosphere of the disk (UV photons only do not seem to be sufficient, e.g., Dartois et al., 2004), or pyrolysis of a precursor closer to the Sun. If large D and ^{15}N enrichments are produced only at low temperatures - and this is debated - IOM precursors must have been redistributed in the disk in order to acquire their isotopic composition.

The hypothesis of one single step formation of IOM in the ISM followed by direct incorporation in the solar system is therefore ruled out, and requires more complex scenarios that need further investigations.

1.3.1.4 Processing on the parent body

The main concern regarding IOM is whether its current chemical structure observed even in the most primitive meteorites has preserved primordial signatures that can be used to constrain the environment of formation or whether parent body processes have blurred the primordial features.

The IOM structural composition varies from one chondrite to another one. This chemical variability is often interpreted as a result of post-accretional parent body processes, causing the loss of H, N and O as well as aliphatic chains from a common precursor (Alexander et al., 2007). On the other hand, recent FTIR and Raman studies on IOMs in least processed chondrites of type 1, 2 and 3 suggest that different precursors of IOMs were present before accretional processes and that some of their features have been preserved (Orthous-Daunay et al., 2013, Quirico et al., 2009, Quirico et al., 2014). These authors further suggest that IOM modification by fluid circulation on the parent body was limited but thermal processing (either of short or long duration) on the parent body likely induced modifications of the chemistry and the carbon structure of the IOM precursors, confirming previous studies by Bonal et al., 2007, Bonal et al., 2006, Busemann et al., 2007.

A robust averaged molecular model is now available for chondritic IOM. Structural, chemical and isotopic heterogeneities are observed between the different groups of chondrites, and also at the submicron scale. The place and timing of the formation of IOM is debated. Isotopic anomalies presumably point to an interstellar origin, but, alternatively, they may have been acquired in the solar nebula. No consensus exists on the mechanism(s) of formation of the precursor(s) of this polyaromatic molecule. Further processing in the solar nebula and on the parent body may have modified its primordial features, but the extent of these modifications is not known.

Hints on the origin of IOM might be found in the study of nitrogen and noble gases associated with IOM, which has been the object of this thesis:

(i) If IOM displays large nitrogen (and deuterium) isotopic heterogeneities, those observed throughout the solar system are even larger. These huge variations might reflect specific fractionation mechanisms and/or different isotopic reservoirs but their origin(s) is poorly constrained.

(ii) Chondritic trapped noble gases are intimately related to IOM and they display elemental and isotopic patterns that are different from those of the solar composition. The acquisition mechanism of these trapped noble gases is not well-known, and may help to constrain the place and timing of the formation of their host, e.g. IOM.

1.3.2 Nitrogen isotopic variations in the solar system

1.3.2.1 Different isotopic components

The nitrogen isotopes have been measured in a variety of N-bearing molecules in the solar system objects, and are characterized by large variations (Fig. 1.11). Some of the ^{15}N-enrichments are secondary (atmospheric processing for the atmospheres of Mars, of Titan, and possibly of the Earth), but the primitive objects (asteroids and comets) likely indicate primary signatures.

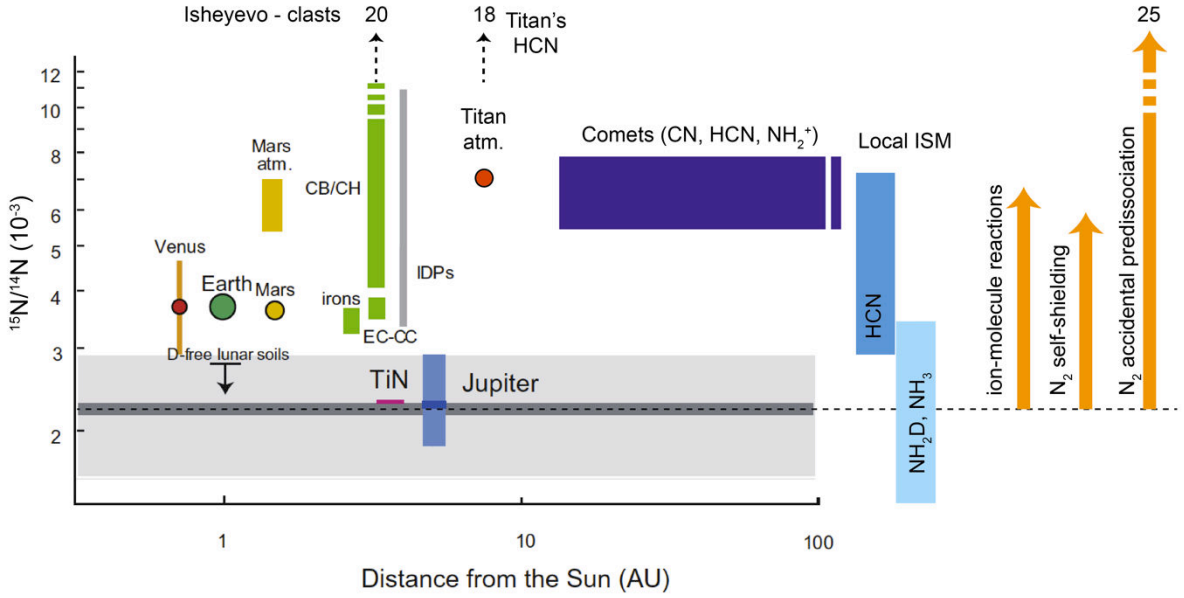

Figure 1.11. Nitrogen isotope variations in solar system reservoirs as a function of the distance from the Sun. The dark gray line ("Solar") is the $^{15}N/^{14}N$ ratio determined in the Genesis targets (Marty et al., 2011, Marty et al., 2010), and the light gray area represents its 2σ uncertainty. The magnitude of nitrogen isotopic fractionation resulting from ion-molecule reactions, N_2 self-shielding and N_2 accidental predissociation are shown for comparison. The figure is adapted from Marty et al., 2010. Data come from Marty et al., 2010 and references therein, Rousselot et al., 2014, Niemann et al., 2010, Vinatier et al., 2007, Hily-Blant et al., 2013, and references therein. Fractionation models: Terzieva and Herbst, 2000, Lyons et al., 2009, Chakraborty et al., 2013.

Three distinct groups are identified in the solar system:

(i) The Sun: the solar nitrogen isotopic composition has been recently documented thanks to the analysis of the solar wind sampled by Genesis (Marty et al., 2011, Marty et al., 2010), with a $^{15}N/^{14}N$ ratio of $2.27\pm0.03\times10^{-3}$ or $\delta^{15}N$ = -383±8 ‰ ($\delta^{15}N$ = (($^{15}N/^{14}N$)sample/($^{15}N/^{14}N$)air -1)×1000). This ^{15}N-poor isotopic composition is thought to be representative of what was the most important N reservoir, the protosolar nebula (PSN). Similarly ^{15}N-depleted values have been measured in Jupiter's atmosphere (Owen et al., 2001) and in TiN in chondritic CAI (Meibom et al., 2007). Any object in the solar system, with the exception of Jupiter and CAIs, is enriched in ^{15}N compared to the protosolar nebula.

(ii) Inner solar system bodies (Earth, Mars and bulk chondrites): they have $^{15}N/^{14}N$ ratios around the terrestrial value of 3.676×10^{-3}, with limited variations (~±20%, with some exceptions: Bells or CB/CH chondrites for instance) on a solar system scale (Alexander et al., 2007, Alexander et al., 2012). Compared to the PSN, inner solar system bodies are enriched by about 60% in ^{15}N.

(iii) Comets: Cometary nitrogen isotopic ratios have been measured in HCN and CN molecules, revealing fairly constant $^{15}N/^{14}N$ ratio ($5.9\times10^{-3}<^{15}N/^{14}N<7.7\times10^{-3}$, Jehin et al., 2009). Recent measurements on cometary NH_2^+ have been performed, with an average $^{15}N/^{14}N$ ratio of 7.9×10^{-3} (Rousselot et al., 2014). This suggests that cometary ices have a unique $^{15}N/^{14}N$ ratio. Therefore, cometary nitrogen analyzed so far (HCN and NH_2^+) appears enriched by about 200% in ^{15}N relative to the PSN. However, HCN and NH_3 may not be the main N reservoirs in comets, but possibly N_2 and N-bearing refractory organics, but their nitrogen isotopic composition is not known yet. Further major results will probably come out soon form the instruments on board Rosetta.

Strong ^{15}N-enrichments with $\delta^{15}N$ up to 3,000 ‰ (and up to 5,000‰ in the CB/CH-like meteorite Isheyevo, Bonal et al., 2010, Briani et al., 2009) have been found in the IOM hotspots (see the above section)

Hily-Blant et al., 2013) have proposed that there existed two distinct nitrogen reservoirs in the cold ISM, with NH_2 and NH_3 molecules having $^{15}N/^{14}N$ ratios (~ 1.9×10^{-3}) close to or lower than the protosolar value, and HCN being enriched (~ 5×10^{-3}). In the solar system, the situation appears different, as PSN N_2 is ^{15}N-poor, whereas HCN and NH_2 (and presumably NH_3) are ^{15}N rich.

1.3.2.2 Fractionation processes

Solar nucleosynthesis appears unable to account for the ^{15}N enrichments of most solar system reservoirs: the CNO cycle is low (<6%) in the core of the Sun, the Sun is a well stratified star with no evidence for transfer of nucleosynthesized nuclei from the core to the outer convective zone. There is a possibility of nucleosynthesis during solar flare events in the Sun's upper atmosphere, but the C isotope compositions of solar system reservoirs do not show the large variations that N does, demonstrating that, if such events contributed to N

and C isotope production, they must have been quantitatively unimportant (Geiss and Bochsler, 1982).

Thus, variations in the nitrogen isotopic compositions of the solar system materials are likely to have been caused by isotope fractionation processes that were specific to this element. Different fractionation mechanisms have been proposed (Fig. 1.11):

(i) ion-molecule reactions. These reactions, occurring in the gas phase and at low temperature (<40K) are thought to be responsible for the large D enrichments observed in simple gas phase molecules in the ISM (Millar et al., 1989). Because IOM displays large D excesses, which are often (but not always) correlated with large ^{15}N enrichments, ion-molecule reactions in a cold and dense environment have been proposed as a possible fractionation mechanism. However, classical ion-molecule reaction models fail to produce the large ^{15}N enrichments observed in IOM hotspots (Terzieva and Herbst, 2000). Under specific conditions *only* (prestellar cores), such chemical models can yield larger nitrogen isotopic fractionation, with $^{15}N/^{14}N$ ratios up to 2.0×10^{-2}, that are not necessarily correlated with D excesses (Rodgers and Charnley, 2008a, Rodgers and Charnley, 2008b, Wirström et al., 2012).

(ii) N_2 self-shielding: self-shielding of the $^{14}N_2$ isotopologue upon photoabsorption in the UV range has been proposed, in line with the possibility of CO self-shielding to account for mass-independent oxygen isotope variations in the solar system (Clayton, 2002). This process was explored for Titan's atmosphere (Liang et al., 2007), where HCN is enriched by 3,000‰ in ^{15}N relative to the main atmospheric N-bearing species N_2 (Niemann et al., 2010, Vinatier et al., 2007). In this model, self-shielding occurs at the top of Titan's atmosphere during dissociation of N_2 to form HCN, and results agree fairly well with the observations. A full model to quantitatively explore the possibility of nitrogen isotope self-shielding in the solar nebula is presently lacking; preliminary attempts suggest the possibility of significant ^{15}N enrichments by several hundreds of permil in the dissociated products (Lyons et al., 2009), which still fails to account for the most extreme enrichments of ^{15}N in IOM hotspots (in CB/CH meteorites for instance). N_2 self-shielding might have occurred in the UV illuminated regions of the solar nebula (Fig. 1.5), and the ^{15}N-carrier(s) resulting from N_2 photodissociation (HCN, NH_3?) would have to have been locked into solids rapidly to prevent any isotopic re-equilibration with the ambient gas.

(iii) Accidental predissociation of N_2: This quantum mechanical process has been inferred from theory first (Lefebvre-Brion and Field, 2004, Lorquet and Lorquet, 1974, Muskatel et al., 2011, van de Runstraat et al., 1974), then tested by laboratory experiments (Chakraborty et al., 2012, Chakraborty et al., 2013). Accidental predissociation originates in the resonant coupling between two electronic states in the N_2 molecule. The resulting predissociated states have a wide range of lifetimes that depends strongly on the isotopes. Large isotopic fractionations are expected to occur at certain wavelengths only. Chakraborty et al., 2013 have studied the photodissociation of N_2 and H_2 by synchrotron radiation below 100 nm, to form NH_3 gas that was condensed during the experiment and analyzed for its

nitrogen isotopic composition. The largest ^{15}N-enrichments ever measured for usual fractionation processes have been reported in the photoproduced NH_3 (up to 10,000‰). Such a result may have interesting implications for the cometary NH_3, which is also expected to have been the most abundant N-species in the outer solar nebula. As for N_2 self-shielding, such a process depends on the irradiation field and the dissociation product must be condensed in order to conserve the ^{15}N-enrichment.

Further investigations, both modeling and experimental studies, are required in order to decipher which of these models are the most representative of what has occurred in the solar nebula.

Nitrogen isotopic composition span large variations in the solar system objects, all of them are highly enriched in ^{15}N relative to the protosolar reservoir. Different fractionation mechanisms have been proposed, but the required magnitude of the isotopic fractionation is barely reached to account for the most ^{15}N-rich objects (comets, IOM hotspots) and the initial conditions of these models may be too specific. Experimental studies are definitely needed.

1.3.3 Noble gases in chondrites

The noble gases (He, Ne, Ar, Kr and Xe) are rare in solids. Their abundances and isotopic compositions are impacted by physical processes, such as phase changes, nuclear reactions and physical isotopic fractionations. These elements are not rare in the solar system, helium for instance being the second most abundant element. However, they are trapped in solids in very low abundances and therefore the effects of physical processes affecting their compositions can be readily identified. Thus, trapped noble gases in chondrites might have conserved the memory of primordial processes. Furthermore, their study may help to constrain the origin of meteoritic organics, as IOM hosts most of the noble gases present in chondrites. Noble gases cannot be measured in comets by spectroscopic methods, and until the results from the Rosetta mission come out, chondrites (with IDPs and UCCAMs) are the only extraterrestrial materials available for determining the noble gas distribution and reservoirs in the early phases of the solar system formation.

1.3.3.1 The solar reference

As for nitrogen isotopes, the elemental and isotopic composition of the Sun is the reference for noble gases in cosmochemical materials. Solar noble gas abundances can be inferred from spectroscopic observations and models of the solar atmosphere (Asplund et al., 2009, Lodders, 2003). Solar wind abundances may be used too, but they have to be corrected for elemental and isotopic fractionations (Heber et al., 2009, Heber et al., 2012). Solar isotopic compositions are derived from lunar soils, in which solar wind is implanted (Pepin et al., 1995). The recent noble gas measurements in Genesis targets have yielded isotopic ratios

that were indistinguishable from the lunar data (Crowther and Gilmour, 2013, Heber et al., 2012, Meshik et al., 2014).

1.3.3.2 Different components

Most of the noble gas components in extraterrestrial materials were identified by bulk analysis of chondrites. Based on their elemental and isotopic patterns, two main types of noble gas components are present in chondrites:

(i) Some components have an in-situ origin, either produced by radioactive decay (^{4}He, ^{40}Ar and ^{129}Xe for instance), fissiogenic reactions (^{131}Xe, ^{132}Xe, ^{134}Xe and ^{136}Xe from the fission of ^{238}U and ^{244}Pu for instance) or by cosmic ray spallation reactions (^{3}He, ^{21}Ne or ^{38}Ar for instance). Cosmogenic ^{3}He and ^{21}Ne are widely used to calculate the exposure ages of meteorites as for small bodies in space.

(ii) Trapped components, on the other hand, represent the largest fraction of the noble gases present in meteorites. Noble gases in gas-rich meteorites have a "solar" pattern, with high abundances of the lightest gases He and Ne relative to the heavy ones, their origin being implanted solar wind (Suess et al., 1964). The most abundant trapped noble gases in chondrites display a "planetary" pattern, with strong elemental fractionation showing enrichments in heavy elements relative to the light ones when compared to the solar pattern (Mazor et al., 1970). Planetary noble gases consist of a number of individual components characterized by unique isotopic (and sometimes elemental) compositions, which are carried by specific host phases, the latter not being always well characterized. Noble gases carried by presolar grains (nanodiamonds, SiC, graphite) display 'anomalous' isotopic compositions that are explained by stellar nucleosynthetic processes (Huss et al., 2003). The noble gas inventory of the heavy noble gases (Ar, Kr and Xe) in the primitive meteorites is dominated by the "Q" component (Q stands for *Quintessence*, Lewis et al., 1975, also called P1 gases by some authors). For instance, in the CI chondrite Orgueil, about 95% of all ^{132}Xe belongs to this Q component (Huss et al., 1996).

1.3.3.3 Primordial noble gases and the Phase Q

The Q-gases are thought to be representative of the most important noble gas reservoir in the solar system outside of the Sun, because they are ubiquitous in chondrites as well as in some differentiated meteorites (Göbel et al., 1978, Huss et al., 1996). Q-gases are "approximately normal", i.e., they are not too different in isotopic composition from solar gases. Therefore, it is assumed that Q-gases are primordial gases of "local" origin and are derived from solar gases, although it has been proposed that they might precede the solar nebula and originate in the parent molecular cloud. However, Q noble gases notably differ from Solar wind ones in being isotopically mass-dependent fractionated relative to the solar wind composition. Whether or not the solar wind composition reflects the protosolar one is an open question that will be discussed in Chapter 5.

The definition of Q-gases is operational (Lewis et al., 1975): it corresponds to the difference between the measured gas concentrations in oxidized and non-oxidized HF/HCl acid residues extracted from chondrites. The loss upon oxidation (by red fuming HNO_3 or pyridine, Lewis et al., 1975, Marrocchi et al., 2005) of most of the noble gases initially concentrated in the acid residue is associated with a small loss of mass, hence "quintessence". The Q-gases host phase was named Phase-Q (Lewis et al., 1975). This phase is not well characterized because its amount is much lower than that of IOM. It is thought to be carbonaceous and part of, or is intimately linked with, IOM (Ott et al., 1981). On the other hand, the elemental and isotopic characteristics of the Q-gases are now accurately known thanks to several extensive studies (Busemann et al., 2000, Huss et al., 1996). Q-gases display five main features: (1) a very high noble gas concentration, up to 5×10^{-9} mol/g in HF/HCl acid-residues for ^{132}Xe (the concentrations are reported to the acid residue mass as one does not know which fraction of the residue of Phase Q represents), (2) an elemental fractionation of noble gases relative to the solar wind, light noble gases being depleted relative to the heavy ones by several orders of magnitude (Fig. 1.12.a), (3) a mass-dependent isotopic fractionation relative to solar wind favoring the heavy isotopes compared to the light ones, with isotopic fractionation factors of ~ 0.9%/amu for Xe isotopes (Fig. 1.12.b), (4) a high temperature release (>1000°C) that depends on the metamorphic grade of the host meteorite, and (5) a common release temperature for all noble gases.

Many attempts to characterize Phase Q have been made, but none of them have completely succeeded. Recent laboratory experiments have suggested that the Xe isotopic pattern of Phase Q is the result of 'anomalous adsorption' (Hohenberg et al., 2002, Marrocchi et al., 2011). Anomalous adsorption of heavy noble gases involves chemical bonds with the host material, but this model still has to be demonstrated. Interestingly, recent experimental results have shown that **only Xe ions are prone to isotopic fractionation (up to 1.3%/amu) and efficient trapping into solids, whereas neutral Xe is barely trapped and not isotopically fractionated** (Marrocchi et al., 2011). Moreover, it has been suggested several times that the elemental pattern of Q-gases (the so-called "planetary" pattern) could be related to the **ionization energies of the different noble gases** (Göbel et al., 1978, Ott, 2002, Rai et al., 2003). However, the physical processes have never been clearly demonstrated.

Improving our knowledge of the origin of these specific features of Q-gases will help us to better constrain the place and the timing of formation of its host, and the nature of its relationship with IOM.

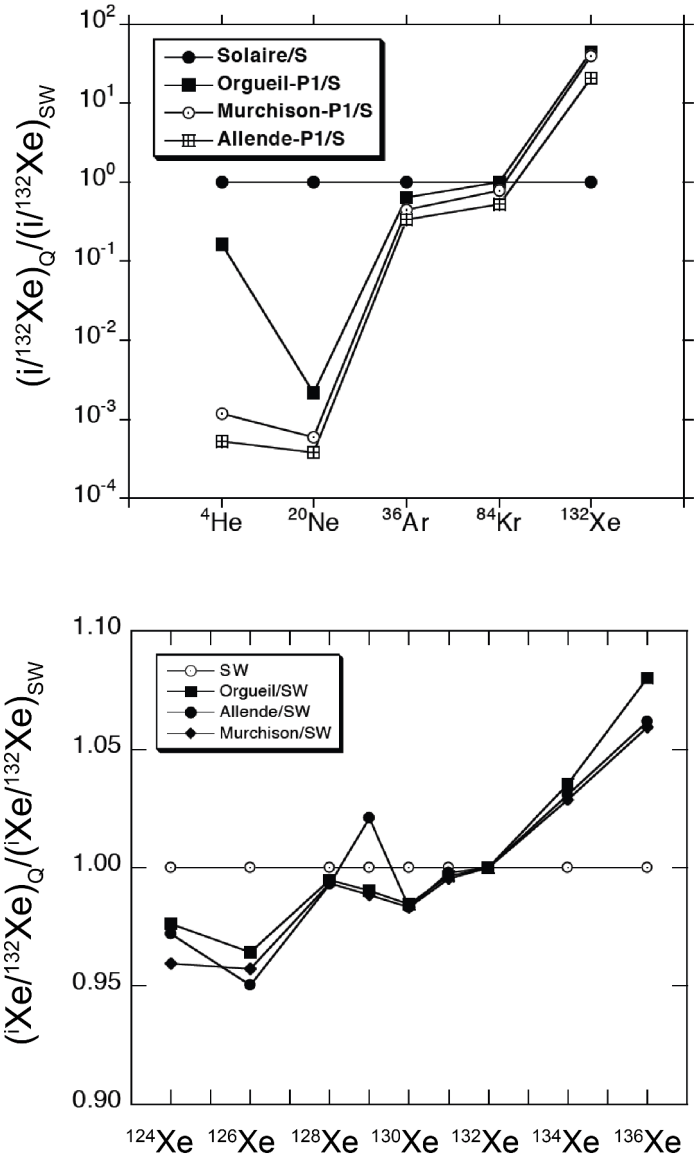

Figure 1.12. Elemental (a) and isotopic compositions (b) of Q-gases relative to the solar composition (data are from Busemann et al., 2000 and Pepin et al., 1995, respectively, figure adapted from Marrocchi, 2005).

1.3.4 The connection with Earth's volatile content

The bulk Earth volatile content has been estimated by adding the atmospheric and mantle inventories (Fig. 1.13, Marty, 2012). Overall, a CI-CM chondrite-like abundance pattern for volatile elements emerges, consistent with a genetic link with chondrites from H and N isotopes (see previous section). However, there are two noticeable exceptions to the chondritic abundance pattern: nitrogen and xenon are both depleted by ~ one order of

magnitude relative to the other volatile elements. The "missing" nitrogen could have been sequestrated in the deep Earth (Marty, 2012 and references therein).

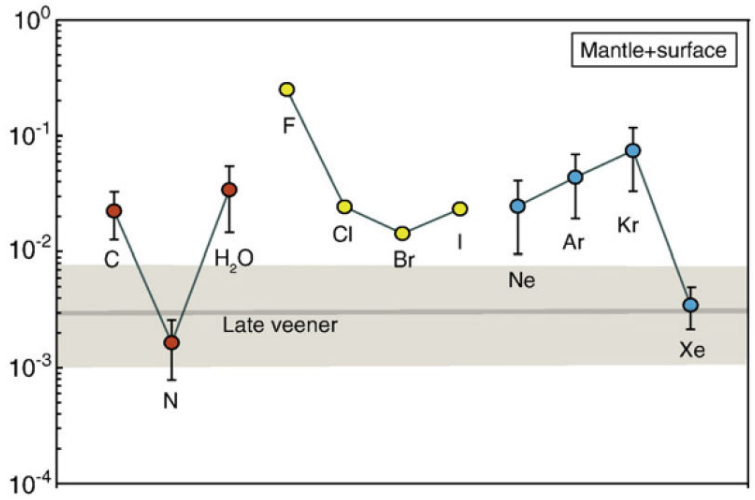

Figure 1.13. Terrestrial composition of volatile elements in Earth for the mantle and atmospheric reservoirs (from Marty, 2012). Abundances are normalized to the mass of the Earth and to the abundances in chondrites.

In addition to being depleted by one order of magnitude in Earth, relative to the CI-CM chondrite composition, atmospheric xenon is enriched in the heavy isotopes by 3-4%/amu, relative to chondritic or solar compositions. In contrast, Kr isotopes are essentially unfractionated. This discrepancy is known as the "xenon paradox". This issue has led to sophisticated models of atmospheric evolution coupled with mantle geodynamics (Pepin, 1991, Tolstikhin and Marty, 1998) and cometary contributions (Dauphas, 2003), but these models fail to explain the Martian volatiles abundances which display the same paradox as the Earth. Sequestrating Xe into mantle reservoirs has been proposed to explain the missing Xe in Earth's atmosphere (Sanloup et al., 2011, Shcheka and Keppler, 2012). However, these models do not account for the isotopic fractionation of atmospheric xenon. Recent noble gas measurements in 3.5 Ga-old Archean sediments suggest strongly that the isotopic composition of atmospheric Xe has evolved from a chondritic composition to the present-day atmospheric composition (Pujol et al., 2011). Based on the experimental results of Marrocchi et al., 2011, it has been proposed that the depletion and isotopic fractionation of atmospheric Xe is due to a preferential atmospheric escape of photo-ionized Xe (Marty, 2012). Although this hypothesis is attractive, several problems remain, notably, a suitable mechanism for losing preferentially Xe relative to other noble gases from the atmosphere through time (Hébrard and Marty, 2014).

Different noble gas components are present in chondrites. Among them, the Q-gases are concentrated in chondritic IOM and are presumably primordial, showing an elemental and isotopic fractionation relative to the solar wind, taken as the reference for the protosolar gas. The origin of these Q-gases and of their host, Phase Q, is not well understood and might originate in the ionization of noble gases. However, the physical processes are not constrained.

1.4 Questions

The organics compounds (e.g., IOM) in chondrites host most of the nitrogen and the noble gases trapped in these objects, suggesting a genetic link between these three components. However, an unified model to account for the formation of IOM, for nitrogen isotopic anomalies and for trapping noble gases with a Q-like composition is lacking. Noble gas ionization may be a key for the isotopic pattern of Xe in Phase Q as well as for the efficiency of trapping into forming solids; and the photodissociation of N_2 might be responsible for large ^{15}N-enrichments. Besides, photochemistry and ion-molecule reactions in the irradiated zones of the solar nebula may have been operational for the formation of complex organic compounds, that could eventually trap noble gases and acquire specific H and N isotopic compositions, simultaneously or at later times. Hence, it seems that **ionization by UV photons or other radiation sources in the solar nebula might have played an essential role in governing the volatile element distribution and their isotopic compositions**.

The questions addressed in this thesis are the following (Fig. 1.14):

(1) Can IOM precursors be produced by the dissociation and further reactions of the main solar gases, e.g., H_2, CO and N_2 in an ionized environment?

(2) Are ^{15}N-erichments observed in organics formed by the (photo)dissociation of N_2?

(3) What is the physical process responsible for the elemental and isotopic patterns of Q-gases, and how is it related to the formation of Phase Q and of IOM?

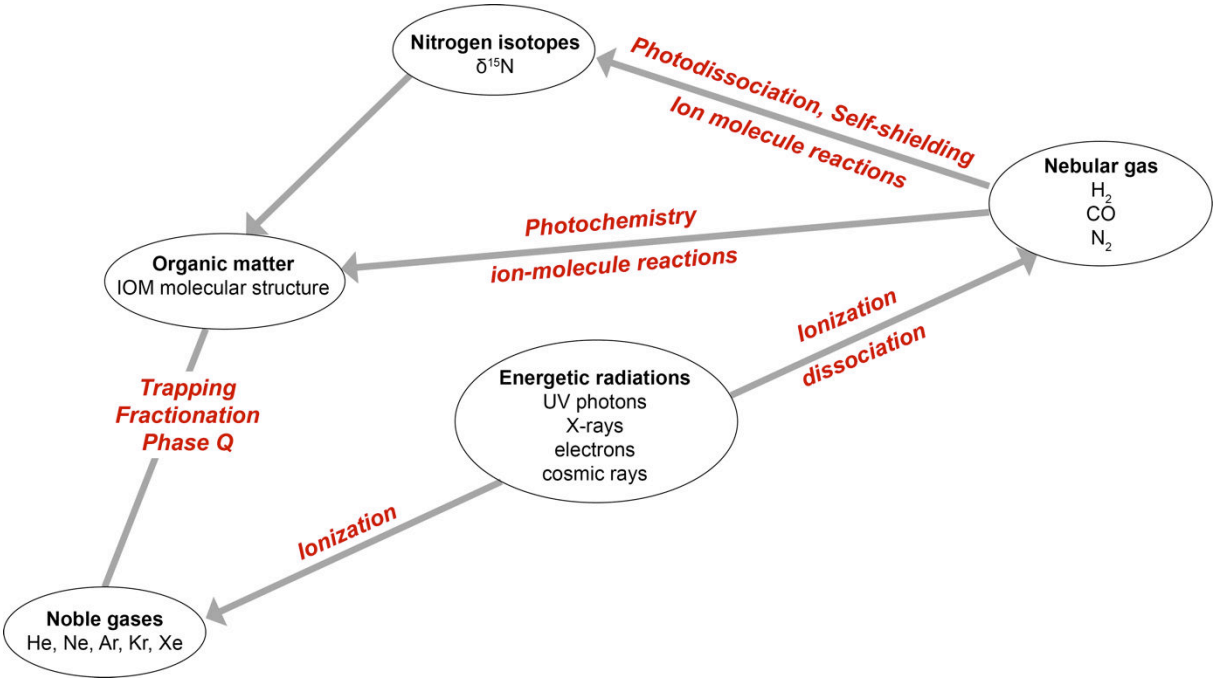

Figure 1.14. Sketch on the relationships between ionization sources, organosynthesis, noble gas trapping and fractionations and nitrogen isotopic fractionation in the solar nebula.

To address these questions, we have designed an experiment in which gas mixtures are ionized to form solid compounds under controlled conditions. We have specifically studied the cases of nitrogen and noble gases in gas phase reminiscent of the PSN composition consisting of CO, N_2 and noble gases (plus traces of H, H_2O). We have adopted electrons for ionizing the gas as the photons that ionize noble gases and dissociate N_2 and CO molecules have wavelengths below 100 nm. Working with UV photons at these wavelengths would have required a window-less setup, which was not available for this work. The main physical processes occurring in a plasma and the two experimental setups used in this thesis are described in Chapter 2.

The characterization of the carbon-rich solids that were obtained from the dissociation of CO and N_2 in the experiments is detailed in Chapter 3.

The results of the study on the isotopic composition of nitrogen resulting from the dissociation of N_2 in the plasma are given in Chapter 4. These results have been published in EPSL (Kuga et al., 2014).

Chapter 5 is dedicated to the results from the noble gas study performed on the synthetic organic solids produced in the plasma setup. The physical processes responsible from the elemental and isotopic fractionations of heavy noble gases, as well as the possible implications for the origin of Q-gases are outlined.

Chapter 2

Experimental production of solid organics

Table of contents

In meteorites, volatile elements (H, C, N, noble gases…) are mainly present in organic compounds. Organics are also the host phases of large isotopic excursions of these elements. In order to investigate the origin of organics in meteorites and the cause(s) of such isotopic excursions, laboratory experiments, combined with the in-situ or ex-situ analysis of natural objects, can provide essential information on the history of formation and evolution of these objects. As discussed in the introductory chapter, several experimental methods can be used to reproduce the organic matter characteristics or the exotic isotopic compositions of primitive meteorites. However, these studies generally address separately the synthesis of the organics and the origins of isotopic fractionations.

One objective of this thesis was to reconcile these two issues by designing an experiment that is prone to isotopic fractionation (ionized environment/photochemistry, Chakraborty et al., 2013, Lyons et al., 2009, Marrocchi et al., 2011) combined with organic synthesis, in conditions that are relevant to environments in the solar nebula or of planetary atmospheres. Special attention was paid to Titan's atmosphere, which is a solid organic factory and presents large isotopic excursions for nitrogen (Liang et al., 2007, Niemann et al., 2010, Vinatier et al., 2007). The solar nebula, mainly composed of H_2, CO and N_2 (Grossman, 1972) and Titan's atmosphere, mainly composed of N_2 and CH_4 (Strobel et al., 2010), are both (i) N_2-rich and carbon-rich, (ii) places of intense organic synthesis, and (iii) environments where exotic isotopic signatures are observed.

In the present work, I used an experimental plasma, which is able to provide an ionizing environment likely supporting isotopic fractionation and which is an adequate source of energy for organic synthesis from gaseous mixtures. I used two experimental setups during my thesis: (i) the PAMPRE experiment (LATMOS, Guyancourt, France), designed to investigate Titan's ionosphere processes, and (ii) the Nebulotron experiment (CRPG, Nancy, France), which was designed to simulate solar nebula processes. In this chapter, I will present an overview of the physics of plasmas, and discuss its use to simulate nebular and planetary photochemical processes. In a second part, the PAMPRE and the Nebulotron experimental setups will be described.

2.1 Plasma basics

In physics and chemistry, a plasma is typically defined as a partially or fully ionized gas. It is usually considered as the fourth state of matter, along with the solid, liquid and gaseous ones, and it corresponds to its most disordered state. It is also the most common one, as 99% of the visible Universe consists of plasma. The interstellar medium, the stars, the stellar winds, the planets' ionospheres and lightning are in a plasma state. Natural and laboratory plasmas (generated in gas discharges) occur over a wide range of sizes, pressures, electron temperatures and densities (Fig. 2.1).

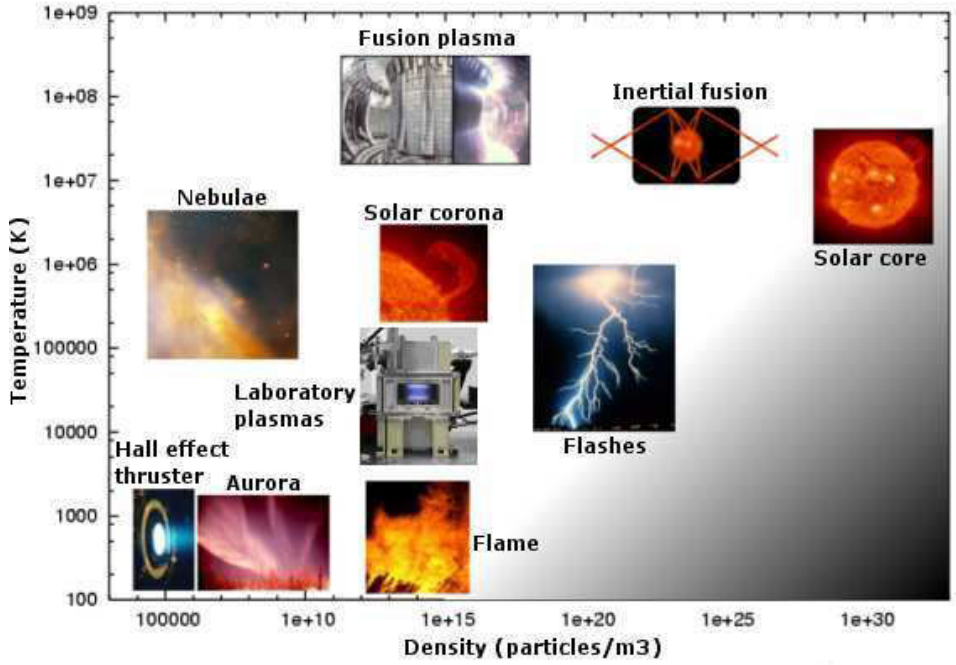

Figure 2.1. Space, natural and laboratory plasma electron temperature and densities.

2.1.1 Fundamental plasma parameters

Plasma is described as an electrically neutral medium of positive and negative charges. Plasmas are closely related to a gas phase but differ in a number of ways, notably because the electrical conductivity of a plasma is very high due to the presence of charged particles. Even if particles are not bonded to one another, they are not free because of interacting electric and magnetic fields governing their collective behavior with many degrees of freedom.

2.1.1.1 Degree of ionization

Ionization is necessary for plasma to exist. The ionization degree α is defined as follows:

$$\alpha = \frac{n_e}{n_e + n_n} \approx \frac{n_e}{n_n} \ll 1,$$

with n_e being the electron density, and n_n being the neutral particle density.

In ~ 1 mbar gas discharges, electronic densities (and ionic, as imposed by the quasi-neutrality of plasmas) are in the range 10^8 – 10^{14} particles.cm^{-3}. These densities are generally low compared to the neutral density, which is ~ 10^{16} particles.cm^{-3} at room temperature and 1 mbar. Under these conditions, the ionization degree α is in the range of 10^{-8} – 10^{-2}.

2.1.1.2 Temperatures

Plasma temperatures are commonly measured in Kelvin (K) or electron-volt (eV; 1 eV = 1.602 10^{-19} J; eV/k_B = 11604 K) and are, informally, a measure of the thermal kinetic energy per particle.

According to the kinetic theory of gases, all species in a plasma in thermal equilibrium should display a Maxwellian kinetic distribution function as well as the same temperature. However, electrons are much lighter than atoms or molecules, and electrons-heavy particles collisions are inefficient compared to electron-electron or heavy particle-heavy particle collisions. As a consequence, substantial temperature differences often develop between the electrons and the neutral and ion particles. The electron temperature T_e and the ion and neutral temperature T_i and T_n are typically different by 1 to 2 orders of magnitude (Fig. 2.2. for an Ar plasma). Plasmas satisfying this $T_e >> T_i \sim T_n$ condition are out of thermodynamic equilibrium and are called non-thermal or **cold plasmas.** These are the plasmas used in this thesis.

The ionization degree introduced above is intimately related to the electron temperature, the density of neutrals and the ionization energies of particles. Such a relationship is described by the Saha-Langmuir equation (Fridman, 2008).

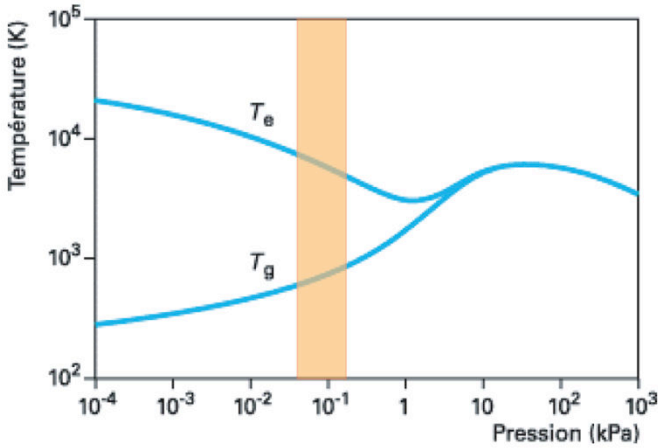

Figure 2.2. Electron temperature T_e and neutral temperature T_g as a function of pressure in an Ar plasma. The orange area represents the pressure conditions used during this thesis and give approximated T_e and T_g values of 10^4 and 800 K, respectively.

The high electron temperature (typically ~ 10^4 K in low-pressure plasmas, e.g. Fig. 2.2) yields chemical reactions for gas temperatures that are lower than the ones required for the initiation of such reactions; this is the main motivation for the use of plasmas in laboratories.

2.1.1.3 Plasma modeling

A mathematical description is required in order to quantify the plasma parameters that govern the reactions occurring in these ionized environments. The state of a plasma is completely described if particle locations and velocities, as well as the distribution of the electromagnetic field, are known. In practice, such degree of precision is difficult to reach and is often not necessary. There are three main approaches to model a plasma:

- Fluid modeling: in such models, the plasma is treated as a single continuous fluid, governed by a combination of Maxwell's equations and the Navier-Stokes equations. Fluid models are accurate when collisions are sufficiently frequent to have a velocity distribution close to a Maxwell-Boltzmann distribution. However, local velocity heterogeneities, often encountered in plasmas, cannot be described in this way.
- Kinetic modeling: in this case, the particle velocity distribution at each point in the plasma is described and does not assume a Maxwell-Boltzmann distribution. Those models are overall much more accurate to describe plasma processes but are also much more time consuming.
- Hybrid Kinetic/Fluid modeling: these models are a combination of fluid and kinetic models and treat some components of the system as a fluid and others kinetically.

2.1.2 Dusty plasmas

As for plasma, dust is present in many environments, especially in space. Plasma and dust have thus many opportunities to interact and give birth to what we call "dusty plasmas" (interstellar medium, ionospheres, comet tails, etc.…). In the laboratory, dust is very often encountered in plasmas and was first considered as contamination in clean setups dedicated to thin film production processes. It was found that dust came either from the electrode pulverization or from the initial gas mixtures (Selwyn et al., 1990). Indeed, reactive gases such as silane (SiH_4) or hydrocarbons are able to produce solid particles with nanometer to millimeter sizes through numerous polymerization reactions. As detailed below, plasma reactivity allows dissociation and polymerization reactions to form dust. The plasma setups used during this thesis are dusty plasmas.

Depending on the geometry of the reactor, dust is produced either in volume (Szopa et al., 2006) or as a thin film deposited on a surface (Fridman, 2008). Dust particles are often negatively charged due to the high electron mobility and thus change the plasma's characteristics. Dusty plasmas are even more complicated to model than simple plasmas.

The mechanisms of dust formation in plasma are not completely understood, but are thought to start with a nucleation or polymerization phase, followed by accumulation and aggregation phases to finally end up with a surface deposition phase in the case of a thin-film deposition (Cavarroc, 2007).

2.1.3 Plasma reactivity

A plasma can be described macroscopically by the fluid dynamics equations: mass, momentum and energy conservation. When the pressure is low, typically ~ 1 mbar, reactions with two species, A and B, are favored:

A+ B -> C + D. (1)

A plasma is composed of many atomic, molecular, neutral or ionized species, in their fundamental state or excited to vibrational or rotational electronic states. Production and loss of species occur via **reactive collisions**. Reactions are characterized by a **reaction rate**

(R, $cm^{-3}.s^{-1}$), determined by the product of the **reaction coefficient** (k, in $cm^3.s^{-1}$, calculated from the **reaction cross section** (σ, in cm^2) and the relative velocity of particles V) and of the **densities** (in cm^{-3}) of the species A and B, based on the kinetic energy of these particles:

$$R = k\,[A]\,[B] \qquad \text{with } k = \langle \sigma\, V \rangle \qquad (2)$$

Generally, the reaction coefficients are calculated for electronic reactions or are measured experimentally for heavy particle collisions.

The chemical-kinetics of plasmas is described by coupled continuity equations. In a stationary regime, one can calculate the balance for each species in a plasma and further build a kinetic model resolving numerically the coupled equations to finally calculate macroscopic physical quantities. This is a difficult exercise, notably because the different reaction rates are not well known, and because the number of present species can be extremely large. Such modeling requires kinetic theory, spectroscopic measurements of excited and ionized species, and measurements in the plasma of electric and plasma parameters. An example of such a kinetic model of the PAMPRE plasma (in pure N_2) used during this thesis can be found in Alves et al., 2012.

2.1.3.1 Electronic and molecular processes

Elementary processes can be divided into two classes: elastic and inelastic collisions. **Elastic collisions** are those in which the internal energies of the colliding particles do not change. The total kinetic energy is thus conserved. All other collisions, like those resulting in ionization or excitation, are inelastic. Most **inelastic collisions** result in an energy transfer from the kinetic energy of colliding particles into internal energy. These inelastic collisions can occur if the kinetic energy of electrons is larger than the **energy threshold of the reaction**, E_s. Among inelastic collisions, we distinguish:

(i) Ionization processes: during ionization, the incident electron must have a kinetic energy with the minimum value of the first ionization potential of the target atom/molecule. The secondary electron is ejected with a certain kinetic energy, depending on the kinetic energy of the incident electron.

- **Direct ionization by electron impact**: neutral and previously non-excited atoms or molecules are ionized by an electron which energy is high enough to provide the ionization act in one collision:

$$A + e^- \rightarrow A^+ + e^- + e^- \qquad (3)$$
$$AB + e^- \rightarrow AB^+ + e^- + e^- \qquad (4)$$

- **Stepwise ionization by electron impact**: previously excited neutral species are ionized.
- **Ionization by collision between heavy particles**: it takes place during ion-molecule or ion-atom collisions, as well as during collisions of excited species.

- **Dissociative ionization**: when the electron energy is relatively high and substantially exceeds the ionization potential, dissociative ionization can take place:

$$AB + e^- \rightarrow A^+ + B + e^- + e^- \qquad (5)$$

(ii) Recombination processes: Recombination processes, contrary to ionization, are highly exothermic.

- **Radiative electron-ion recombination**: a photon is emitted in a radiative cascade and brings back the ionized species into its fundamental state,

$$A^+ + e^- \rightarrow A^* \rightarrow A + h\nu \qquad (6)$$

- **Three-body electron-ion recombination**: excess energy is transformed into the kinetic energy of a free electron,

$$A^+ + e^- + e^- \rightarrow A^* + e^- \qquad (7)$$

- **Dissociative electron-ion recombination**: these processes are common for molecular gases,

$$AB^+ + e^- \rightarrow (AB)^* \rightarrow A + B^* \qquad (8)$$

(iii) Excitation of atomic and molecular species: electronic collisions can lead to excited atoms or molecules. Rotational ($E_s \sim 0.01$ eV), vibrational ($E_s \sim 0.1$ eV) and electronic ($E_s > 10$ eV) states can be affected. Vibrational excitation is one of the most important processes in non-thermal plasmas. It is responsible for the major fraction of energy exchange between electrons and molecules. Rotational excitation, due to its low quantum energy, is rare with respect to vibrational excitation. Electronic excitation by electron-impact requires much higher energies, and generally ends in the dissociation of the molecule.

(iv) Molecular dissociation: electron-impact is able to dissociate molecules by both vibrational and electronic excitation.

- **Dissociation by direct electron-impact**: dissociation through electronic excitation can proceed through different intermediate steps of intramolecular transitions (Fig. 2.3) - either by direct excitation from the ground state to a repulsive state (A) or to an attractive state (B), to an attractive state of excited dissociation products (C), via a predissociation mechanism (D) or to a repulsive state of excited dissociation fragments (E). In all cases, the dissociation takes place at energies above the dissociation potential.

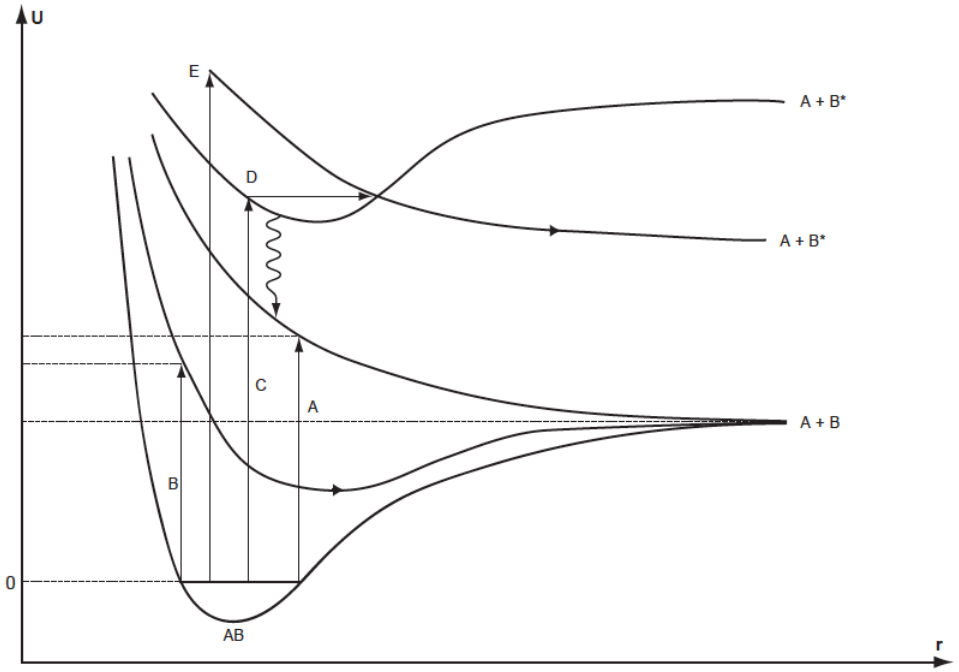

Figure 2.3. Different mechanisms of molecular dissociation through electronic excitation (from Fridman, 2008).

- **Dissociation by vibrational energy transfer** (vibrational-vibrational (V-V) relaxation): the dissociation is induced by the successive excitation energy transfer between vibrational states (Fig. 2.4). In this case, the excitation of the first vibrational states is required, with energy well below the dissociation energy threshold. It is a very efficient process for dissociating molecules in cold plasmas (Alves et al., 2012).

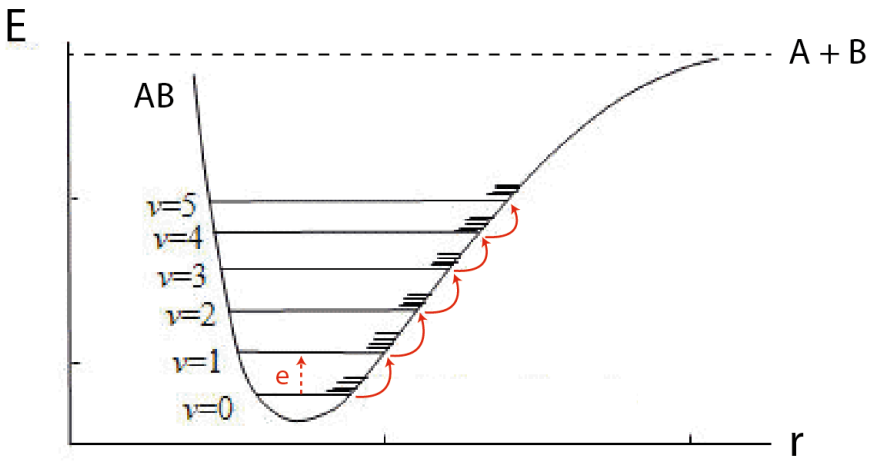

Figure 2.4. Dissociation by resonant V-V energy transfer.

2.1.3.2 Electron-impact cross sections

The most fundamental characteristic of all elementary processes in plasmas is their cross sections, which are essential components in the calculation of the reaction rate coefficients. Examples of experimental electron-impact excitation and ionization cross sections are given in Fig. 2.5. Inelastic cross sections are zero below the reaction threshold, they increase up to a maximum value and, then they decrease for high electron energies, likely due to shorter electron-atom/molecule interaction duration.

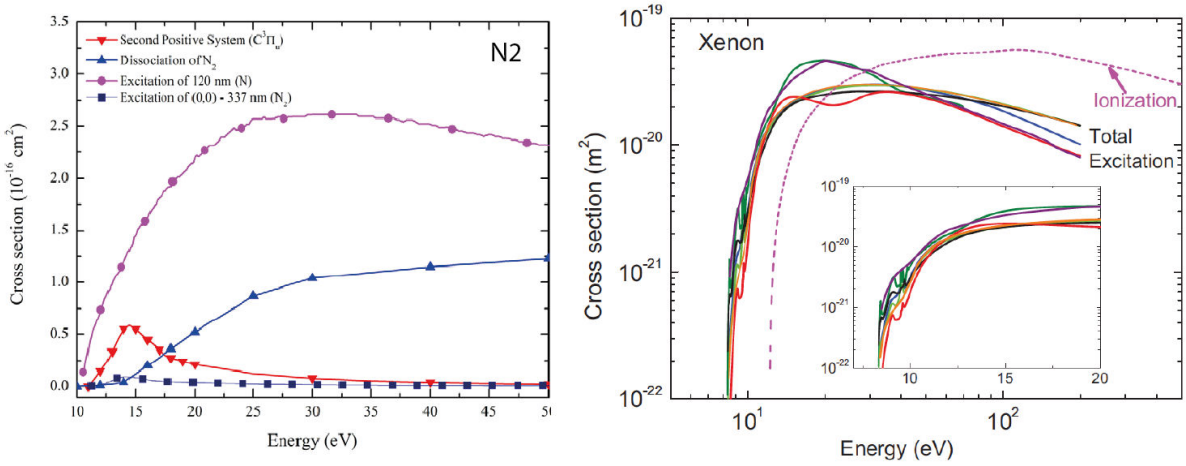

Figure 2.5: Electron-impact excitation and ionization cross section for N_2 and xenon as a function of electron energy. *Left*: electron-impact cross section for the excitation of different N_2 excited states and the dissociation of N_2 (from Fierro et al., 2012). *Right*: total excitation and ionization cross section of xenon (from Bordage et al., 2013).

2.1.3.3 Electron Energy Distribution Function

The first particles that get energy from the electric field of the discharge are the electrons because of their low mass and high mobility. Electrons then transmit the energy to all other plasma components, providing energy for ionization, excitation, dissociation and other plasma-chemical processes. The rates of these processes depend on how many electrons have enough energy ($E_e > E_s$) for the reaction to occur. The **electron energy distribution function** (**EEDF**, f(ε)) is the probability density for an electron to have energy ε. Knowing this function is therefore essential to calculate the reaction rates. The EEDF is determined by electronic collisions; themselves determined by the EEDF. Kinetic models are thus required to calculate the EEDF in a plasma.

The EEDF mainly depends on the electric field, the gas composition and the pressure in the plasma. As a result, it is often very different from the quasi-equilibrium statistical Maxwellian-Boltzmann distribution, especially for the high energy electrons. Examples of EEDF are given in Fig. 2.6. EEDF can be very different from a plasma to another one, and these examples only aim at illustrating the shape of EEDF, and cannot be applied for the plasmas used during this thesis (for which no modeling has been done).

Nonetheless, we can keep in mind some orders of magnitude: the **average electron temperature** T_e in the plasmas used in this thesis is ~ 1 – 3 eV and the **electron density** is in the range 10^8 – 10^{11} cm^{-3}. The EEDF presents a **tail of high energy electrons**, allowing the reactions of ionization, excitation and dissociation (see previous section).

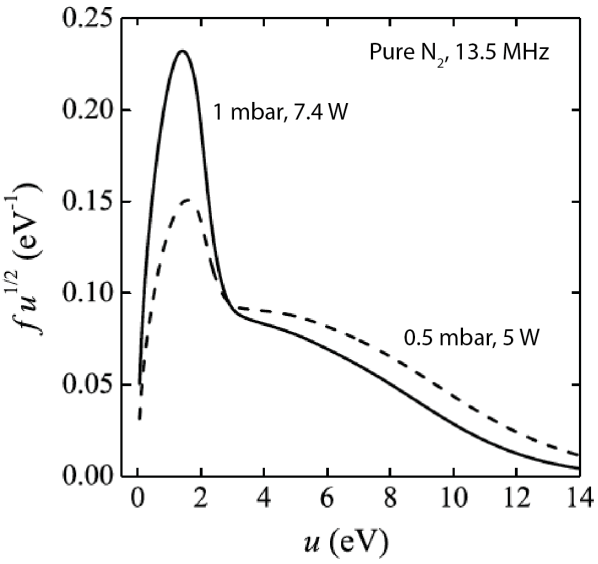

Figure 2.6. Example of EEDF in a N_2 plasma (PAMPRE, from Alves et al., 2012).

2.1.4 Simulating nebular and atmospheric organic chemistry with plasmas

As outlined in the first chapter, one of the aims of this thesis was to produce solid organic materials from gaseous mixtures with compositions that are relatively close to those of the solar nebula gas and to the composition of Titan's atmosphere.

2.1.4.1 Composition of the solar nebula and Titan's atmosphere

- Solar Nebula

The Sun roughly represents 99.8% of the total mass of the present solar system. The general assumption is that the Sun's bulk composition closely resembles the average composition of the material from which the solar system formed. Spectroscopic measurements of the solar photosphere combined with hydrodynamic models of its atmosphere were used to determine most elemental abundances (Asplund et al., 2009, Table 2.1).

	abundance (wt %)		at. ratio
H	71.54	H/C	3717
He	27.03	He/C	316
O	0.6	O/C	1.82
C	0.25		
N	$7.3\ 10^{-2}$	N/C	0.25
Ne	$1.3\ 10^{-3}$	Ne/C	0.32
Ar	$7.8\ 10^{-5}$	Ar/C	$9.3\ 10^{-3}$
Kr	$1.2\ 10^{-7}$	Kr/C	$6.6\ 10^{-6}$
Xe	$1.8\ 10^{-8}$	Xe/C	$6.5\ 10^{-7}$

Table 2.1. Protosolar abundances (wt %) of elements relevant for this study and atomic ratio relative to carbon (data from Asplund et al., 2009).

In the terrestrial planet formation region of the solar nebula, the most abundant gaseous species were plausibly **H_2** (and H_2O) for hydrogen, **N_2** for nitrogen and **CO** for carbon (Grossman, 1972, Zubko et al., 2004).

- Titan's atmosphere

Titan has a dense atmosphere, mainly composed of **N_2** and **CH_4** and contains an organic haze produced by the dissociation and further reactions of N_2 and CH_4 gases in the upper atmosphere. The main gases composing Titan's atmosphere are N_2 and CH_4, with traces of H_2 (Table 2.2).

gas	fraction (%)
N_2	94.7 - 98.3
CH_4	1.6 - 5.1
H2	0.1 - 0.2
CO	0.005
^{40}Ar	0.0007 - 0.0043

trace components: C_2H_6, C_2H_2, C_3H_8, C_2H_4, ^{36}Ar, HCN, CH_3CN, CO_2, CH_3C_2H, C_4H_2, H_3CN, C_6H_6 and H_2O

Table 2.2. Composition of Titan's atmosphere (data from Niemann et al., 2005, Niemann et al., 2010, Strobel et al., 2010).

2.1.4.2 Energies required to initiate chemistry in N_2-CO/CH_4 gas mixtures

This thesis started with the use of CO-N_2 gas mixtures relevant for the solar nebula composition. Both CO and N_2 need to be dissociated, so that their reactive fragments can initiate chemistry in order to produce more complex organic molecules from this gas mixture.

Ionization and dissociation energies of atoms and molecules relevant to this study are reported in the Table 2.3.

atoms	**ionization (eV)**	molecules	**ionization (eV)**	**dissociation (eV)**
He	24.58	**N_2**	15.58	9.76
Ne	21.56	**CO**	14	11.11
Ar	15.76	**CH_4**	12.6	4.4
Kr	14	**H_2O**	12.6	9.5
Xe	12.4	**H_2**	15.42	4.48
H	13.6	**O_2**	12.21	5.08
N	14.54	**CO_2**	13.85	16.6

Table 2.3. Ionization potentials and dissociation energies for atoms and molecules of interest regarding this thesis.

With the exception of H_2 and CH_4, all other atoms/molecules, and notably N_2 and CO, require **energies larger than 9 eV to be ionized or dissociated**.

2.1.4.3 Plasma vs. UV irradiation

In natural environments, especially in planetary atmospheres or in protoplanetary disks surrounding T-Tauri stars, the dissociation of molecules mostly occurs by photodissociation, i.e., is induced by photons (Fogel et al., 2011, Hébrard and Marty, 2014, Herbst, 2014, Levine, 1985, Walsh et al., 2012). Regarding the molecules we are interested in (N_2, CO, noble gases), these photons are in the UV range (< 120 nm). Cosmic particles and X-Rays may also be responsible for the initiation of a complex organic chemistry in such environments (Henning and Semenov, 2013). The role played by the electrons on the chemical reactivity in such environments is not well known. Though, in Titan's atmosphere, electrons seem to have a non-negligible impact in the initiation of the photochemistry from N_2 and CH_4 dissociations and may account for about 10% of the total dissociation rates of these molecules (Lavvas et al., 2011).

Why do we use a plasma, with electron-dominated reactions, to simulate photochemistry? They are several reasons for that and are the following:

(i) Plasma energy deposition is much more efficient than UV photon energy deposition, either with a UV lamp or synchrotron radiation. As a result, dust production is enhanced in a plasma setup and large amounts of materials can be formed in a short (laboratory) period of time.

(ii) UV radiations below 100 nm, which the relevant wavelengths for our study, are absorbed by all materials, and notably silica or MgF_2. Then, working with UV photons requires a window-less setup, which is rather difficult to build and was not available for this work.

(iii) UV radiations below 100 nm are efficiently produced by laser and synchrotron radiation only; two facilities that are difficult to gain access to.

(iv) The high-energy tail of electrons in plasmas allows the dissociation and ionization of molecules and atoms of interest (Fig. 2.7).

Thus, plasmas were ideal for the purposes of this thesis, i.e. providing an ionizing environment able to dissociate CO, N_2, CH_4 and ionize noble gases, while producing large amounts of solid particles for further nitrogen and noble gas isotopes analysis.

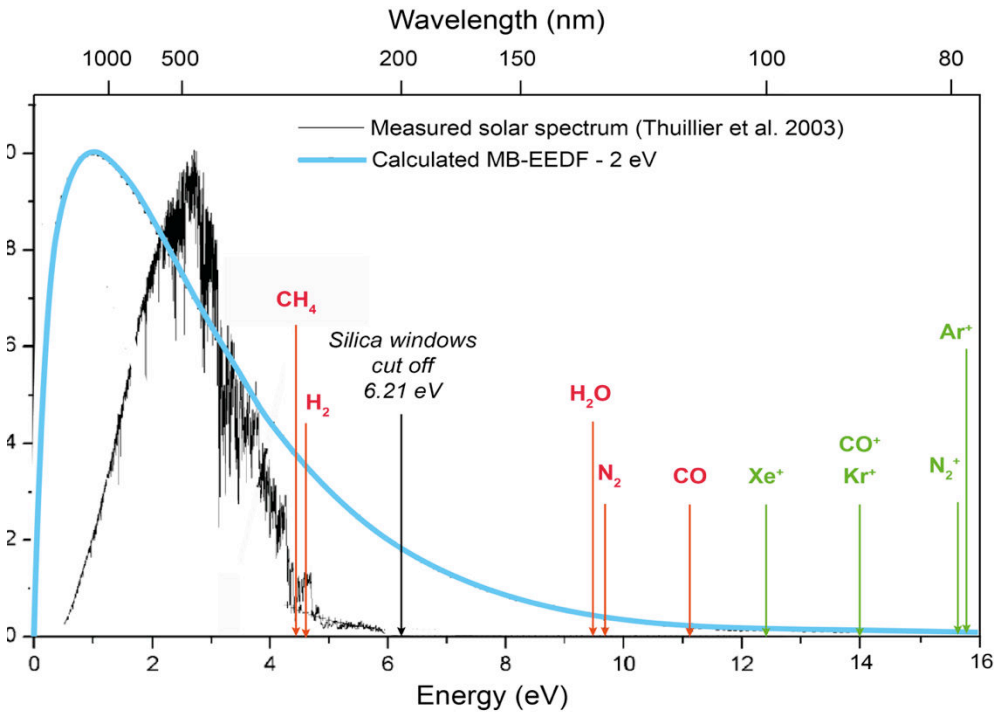

Figure 2.7. Example of a Maxwellian EEDF (blue curve) along with the dissociation (red) and ionization (green) energies of atoms and molecules of interest for this study. For a comparison of shapes and relative intensities as a function of energies, the solar spectrum is given. Adapted from Szopa et al., 2006.

Although it is well adapted to laboratory experiments, the use of plasmas for the study of atmospheric photochemistry is debatable because:

- the dissociation/ionization processes in a plasma are somewhat different from photon-induced reactions because both the reaction cross sections and kinetics are different (Bernard, 2004, Croteau et al., 2011, Liang et al., 2007, Muskatel et al., 2011, Peng, 2013, Zipf and McLaughlin, 1978). As a consequence, electron and photon-induced reactions may not have the same reaction rates and branching ratios. Working in an electron-dominated environment may results in a final set of species that are different and/or in different relative intensities compared to a photon-dominated environment. This was observed in experiments conducted in a plasma and with synchrotron radiation with the same starting gas mixture (N_2-CH_4, Peng et al., 2013). These authors reported that the chemical composition of the gas stationary phase in both experiments was very similar but the relative proportions of species were different.

- the fundamental processes are likely to be different in a plasma and in a UV-dominated system. Indeed, the photodissociation of molecules essentially goes through pre-

dissociation mechanisms (see Fig. 2.4, Lefebvre-Brion and Field, 2004, Lorquet and Lorquet, 1974, Muskatel et al., 2011, van de Runstraat et al., 1974), whereas in plasmas, V-V processes are favored due to both the EEDF shape and the plasma density (see Fig. 2.5, Alves et al., 2012, Fridman, 2008). Such a difference must have consequences on the reaction rates as well as on the isotope fractionation (Liang et al., 2007, Muskatel et al., 2011). This particular point will be discussed in Chapter 4.

2.2 The PAMPRE experiment

2.2.1 Context

A complex organic chemistry, initiated by the dissociation of N_2 and CH_4, takes place in the upper Titan's atmosphere. The presence of aerosols, with size of order 0.1 µm, was suggested initially, when Titan was imaged by the Voyager spacecraft (Tomasko and Smith, 1982). The Huygens probe, onboard Cassini, notably confirmed the high nitrogen content of these aerosols (Israël et al., 2005).

The overall understanding of the chemistry occurring in Titan's atmosphere and of the formation of organic aerosols has also been improved by laboratory experiments. Following the pioneering Urey-Miller experiment (Miller, 1953), tens of different reactors simulating Titan's atmospheric chemistry were built around the world; among them, the PAMPRE setup, that I have occasionally been using during my thesis. The PAMPRE (for *Production d'Aérosols en Microgravité par Plasma REactif*) setup is located in the LATMOS laboratory (Guyancourt, France), and I have used it through a collaboration with Nathalie Carrasco and Guy Cernogora to measure the nitrogen isotopic composition of tholins (see Chapter 4).

2.2.2 Experimental setup and conditions

Since this setup has been extensively described (Alcouffe et al., 2010, Gautier, 2013, Szopa et al., 2006), I will only give a brief picture here.

The PAMPRE experiment consists of a stainless steel reaction chamber, where a radiofrequency discharge (RF, 13.56 MHz) is generated between two electrodes in a metallic cage confining the plasma (Sciamma-O'Brien et al., 2010, Szopa et al., 2006, Fig. 2.8).

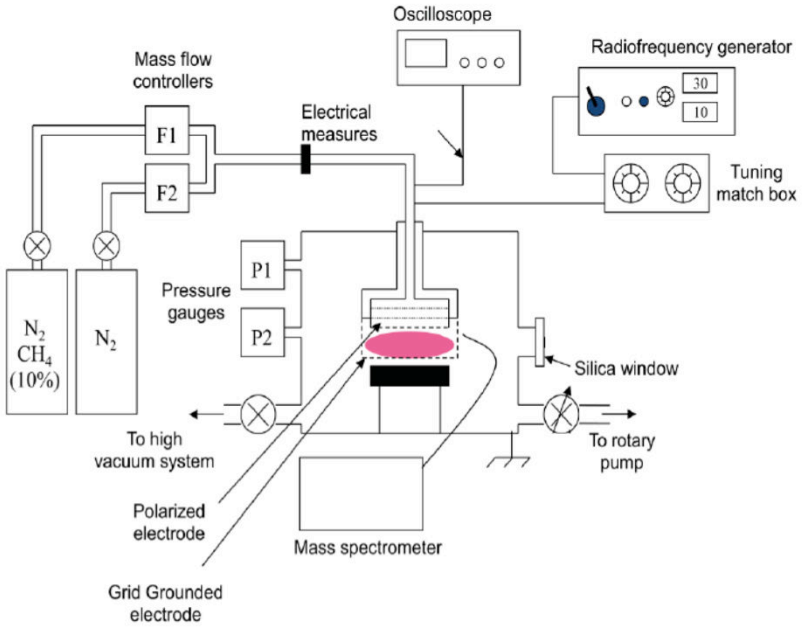

Figure 2.8. PAMPRE experimental setup.

A gas mixture of high purity N_2 and CH_4 is flowed continuously through the plasma discharge. The total mass flow rate used was 55 sccm (standard cubic centimeter per minute) and a valve between the reactor and the primary pump allows the control of the total pressure, which was set to 0.9 mbar. The gas mixture could be adjusted from 0% to 10% of CH_4 in N_2 using two gas tanks (100% N_2 and N_2-CH_4 = 90:10).

Once the plasma is triggered, the electrons initiate chemical reactions and molecular growth that result in the production of hydrocarbons, and N-bearing molecules which eventually end up forming solid particles, called **tholins**. In the PAMPRE setup, these solid particles grow as a suspension in the plasma and when they grow too large they fall to a glass vessel surrounding the metallic cage. After typical runs of 8 h, the spherical solid particles, orange to brown in color, are collected for ex-situ analysis (Fig. 2.9).

A plasma diagnostic and modeling was performed on the PAMPRE setup, especially by Alcouffe et al., 2010 and Alves et al., 2012. These studies provided the main plasma characteristics, notably the neutral gas temperature ($T_n \sim 300 - 340$ K), the average electron temperature ($T_e \sim 1.8$ eV) and its spatial variations inside the reactor, the electron density ($n_e \sim 10^8 - 10^{10}$ cm^{-3}) and the proportion of the different excited and ionized states of N_2. Alves et al., 2012 used pure N_2 plasma only. In their conditions, they calculated an **ionization degree of ~ 10^{-8} - 10^{-6}** and a **dissociation rate up to 4% for N_2**; but these quantities may vary when adding CH_4 to the gas mixture.

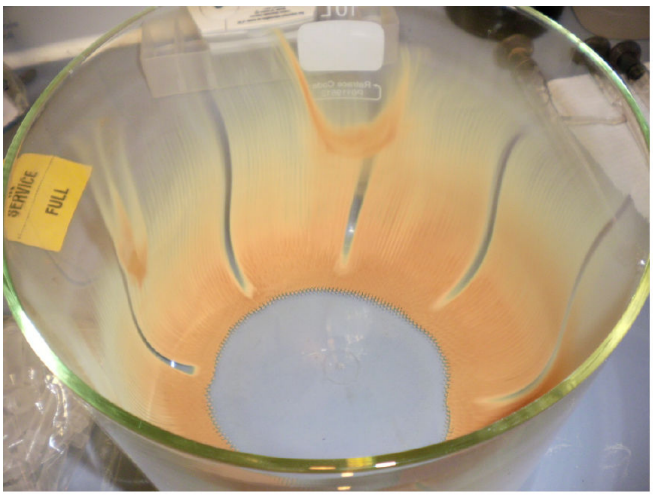

glass vessel used to recover the tholins in the PAMPRE reactor (diameter 20 cm)

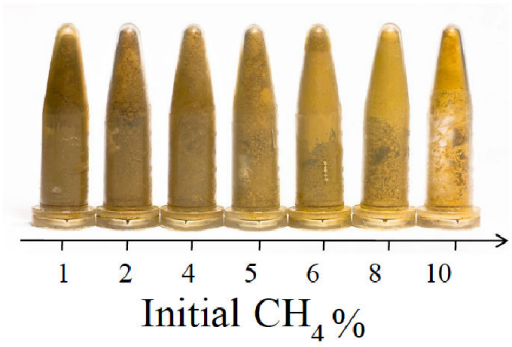

Figure 2.9: Tholins produced in the PAMPRE experiment at different CH_4 % in N_2 (courtesy T. Gautier).

2.2.3 Solid and gas phase characterization

Both the tholins and the volatile species produced in the PAMPRE experiment have been extensively studied, in-situ and ex-situ (Carrasco et al., 2012, Gautier et al., 2011, Gautier et al., 2012, Sciamma-O'Brien et al., 2010, Sciamma-O'Brien et al., 2012). The gas stationary phase is composed of (i) aliphatic and aromatic hydrocarbons, detected up to 6 carbon atoms; and (ii) nitrogen-bearing species, essentially nitriles, along with imines and possibly ammonia. This gas phase composition is qualitatively close to what is observed and modeled in Titan's atmosphere (Carrasco et al., 2012, Gautier et al., 2011). On the solid side, NMR, Raman and mid-IR spectroscopies along with high-resolution mass spectrometry demonstrated that tholins are very complex mixtures of organic molecules, notably hydrocarbons, nitriles, imines and amines (Derenne et al., 2012, Gautier, 2013, Gautier et al., 2012, Pernot et al., 2010, Quirico et al., 2008, Vuitton et al., 2010). Nitrogen is efficiently incorporated into the solids and this suggests a **combined hydrocarbon-N-species polymerization formation process**.

In particular, I have measured the nitrogen isotopic fractionation associated with the tholin formation in the PAMPRE setup. These results are reported in Chapter 4.

2.3 The Nebulotron experiment

The plasma setup that was used the most during this thesis is the Nebulotron, located in Nancy at CRPG.

2.3.1 The Nebulotron: history

The reactor I have been using is the last-but-one of the Nebulotron generation built in the *Muséum National d'Histoire Naturelle* (MNHN, Paris) first, under the guidance of F. Robert and at CRPG afterwards. The name "Nebulotron" comes from "solar nebula", meaning that this experimental setup was designed to simulate nebular processes, essentially high-temperature processes on silicates or refractory elements, except for the generation V that I have been using. The different generations and their applications are summarized in Table 2.4.

generation	years	initiator/user	location	objectives
Nebulotron I	late 90's	F. Robert, S. Coquet	MNHM, Paris	evaporation / condensation of silicates in interstellar medium
Nebulotron II	2000	L. Tissandier, G. Libourel, F. Robert	CRPG, Nancy	evaporation / condensation of silicates in the solar nebula. Applications to chondrules
Nebulotron III - with microwave discharge	2001	L. Tissandier, G. Libourel, F. Robert, Y. Marrocchi	CRPG, Nancy	mass-independant isotopic fractionation of oxygen in silicates, isotopic fractionation of xenon into solid organics. Applications to meteorites
Nebulotron IV	2004	A. Toppani, G. Libourel	CRPG, Nancy	condensation of high-temperature phases. Applications to CAI.
Nebulotron V - with microwave discharge	2002	F. Robert, L. Tissandier, M. Kuga	CRPG, Nancy	UV irradiation of organics, D/H isotopic exchange. Application to interstellar medium and meteorites.
Nebulotron VI	2010	A. Kropft, G. Libourel, L. Tissandier	CRPG, Nancy	condensation of high-temperature phases. Applications to CAI.

Table 2.4. The different Nebulotron generations and their applications.

The Nebulotron V - the one that was used in this thesis - was developed by F. Robert to study isotopic exchange between molecules and ions during UV irradiation of organic compounds (Robert et al., 2011). In this particular case, the microwave plasma was used as a UV lamp, both to generate deuterium ions in D_2 gas and UV photons due to the radiative relaxation of atoms and molecules in the gas phase. Both UV photons and D ions interacted outside the discharge area with organic compounds introduced in the reactor.

During this thesis, we have used the microwave discharge in a different manner. The objective was to produce relatively large amounts of material from the dissociation of gases relevant for the solar nebula. In line with this objective, we have used the microwave cavity not as a UV lamp but as a plasma, taking advantage of the high reactivity of electrons in electric discharges (see discussion above).

2.3.2 The Nebulotron V

2.3.2.1 Geometry of the vacuum line and the reactor

The Nebulotron V consists of a glass vacuum line (total volume ~ 2800 cm^3 – Fig. 2.10), with valves allowing the control of the gas flow pathway. The gases are introduced into the line with mass-flow controllers. The pressure is measured by a Hasting gauge before the reactor and by a Baratron just after the reactor, allowing pressure measurements in the range 10^{-3} – 1000 mbar.

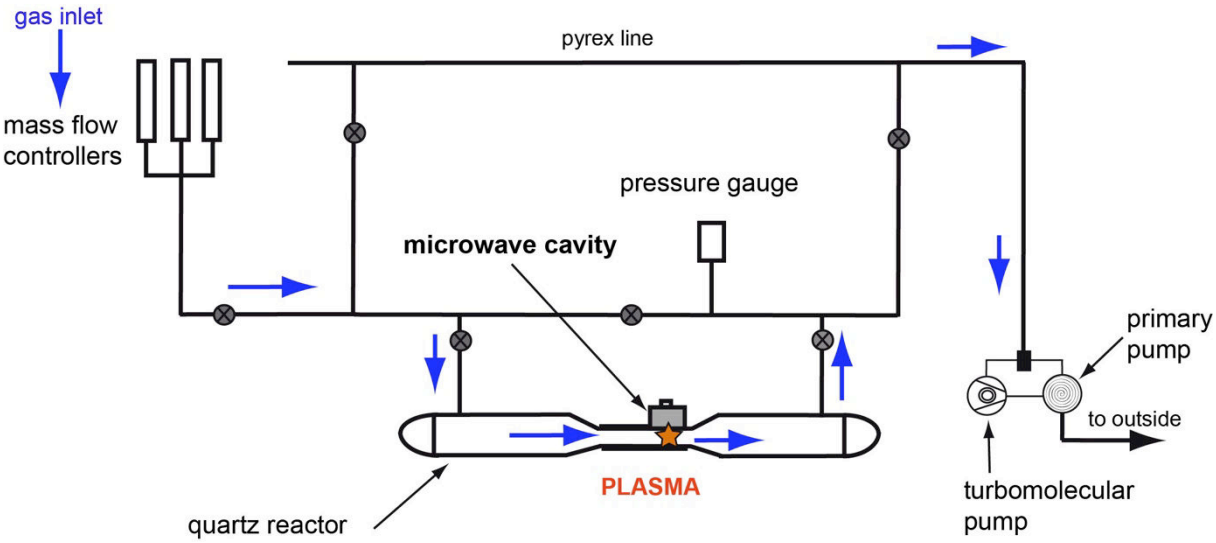

Figure 2.10. Schematics of the Nebulotron glass line.

The line is pumped out by a primary pump equipped with a zeolite filter to avoid oil back streaming to the line. The primary vacuum in the line with the mass-flow controllers isolated is ~ 5.10^{-3} mbar. Because of the low diameter of the valves, the relative dirtiness of the line and the old age of the turbomolecular pump available, the line was only pumped out with the primary pump.

The reactor is a quartz tube, that narrows in the middle, where the microwave cavity is adjusted to produce a plasma (Fig 2.11). The cavity size sets the limit for the diameter of the quartz tube, which is 0.8 cm and 1.2 cm for the internal and external diameters, respectively.

The quartz reactor has been replaced with a smaller one, allowing an easier collection of the synthesized solids (replaced in 2013, Fig. 2.12). We also changed the caps from caps with grease on the first reactor to quartz KF caps on the new one. A part of the line was also improved, notably grease valves were replaced by Teflon ones. All these changes resulted in a better primary vacuum.

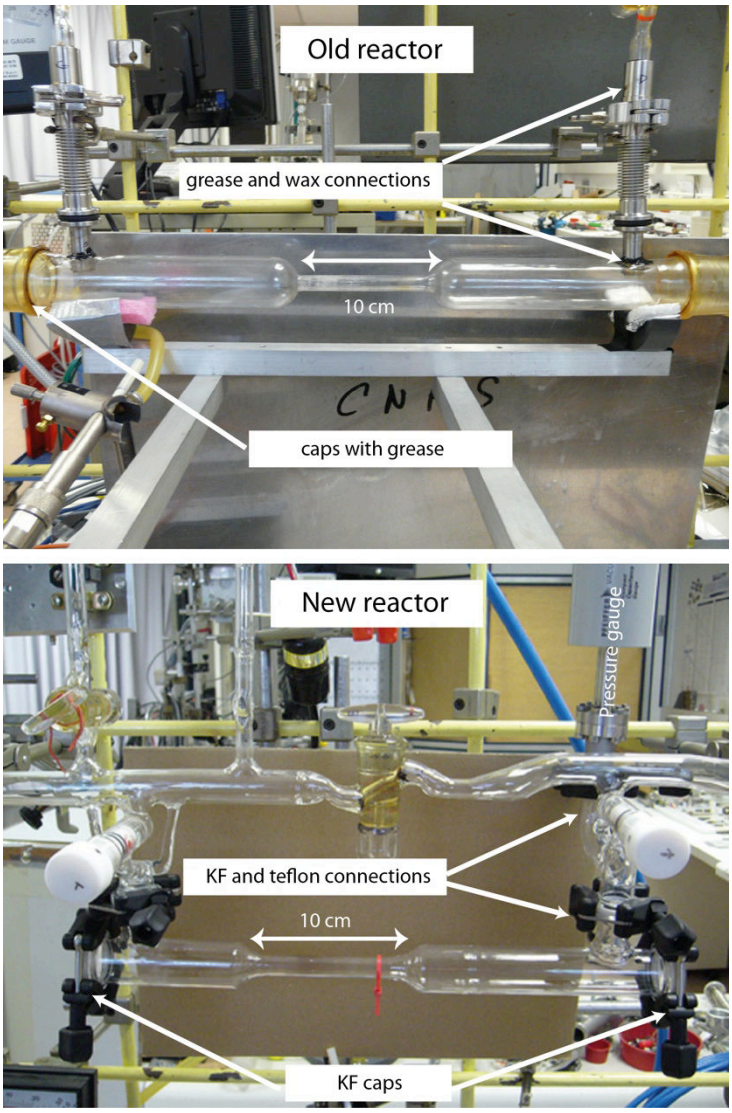

Figure 2.11. The Nebulotron old reactor vs. the new reactor.

2.3.2.2 The microwave generator and cavity

The microwave generator is from Opthos Instruments (MPG 4-470 model). It generates high frequency waves (2.45 GHz), transmitted through a coaxial cable to a cavity (Fig. 2.13). The forward power can be up to 120 W, and the reflected power is controlled on a second screen, and must be minimized.

The cavity acts as a resonant structure to increase the electric field in the gas flowing in the quartz tube. This particular cavity (a modified McCarroll type: McCarroll, 1970) must be tuned, using a stainless steel tuning screw and a ceramic coupling slider in order to match the impedance of the coaxial cable, thereby minimizing power reflected to the cavity. The original cavity had arms on both sides. One of them was removed to adapt the cavity to the Nebulotron II. This probably resulted in a less efficient coupling between the generator and

the cavity, the frequency modes in the cavity having been modified (McCarroll, 1970). In practice, this cavity is delicate to tune and the modification probably amplified the problem.

The cavity is cooled down with compressed air arriving in the discharge area (Fig. 2.12).

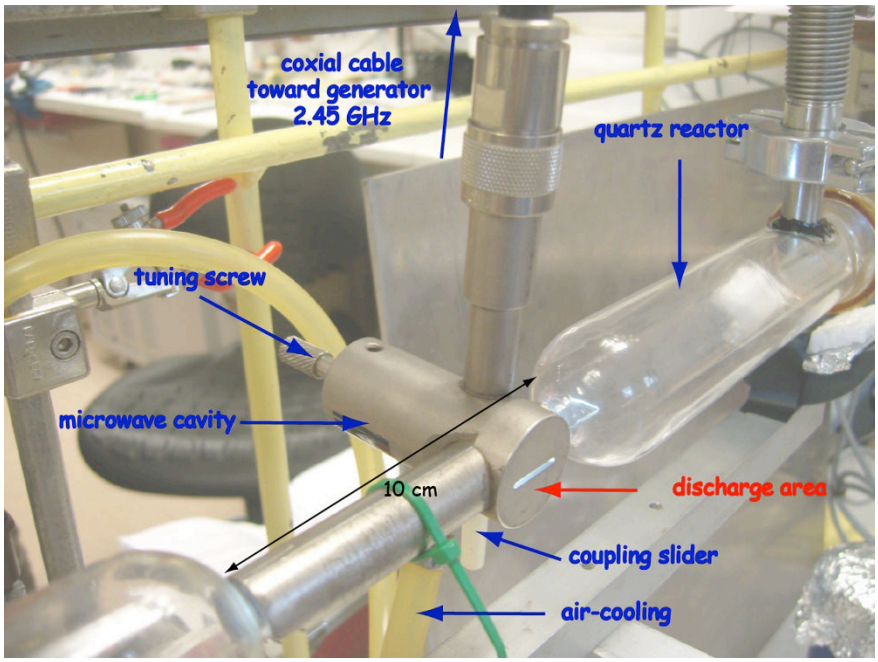

Figure 2.12. Microwave cavity onto the Nebulotron reactor.

2.3.3 Experimental conditions

2.3.3.1 Gas mixtures used

Two mass-flow controllers (Brooks, Delta Smart II) were used, one of 50 sccm and the other of 10 sccm, both calibrated on CO. The gases are mixed up after the mass-flow controllers (Fig. 2.11). I used 4 gas tanks with gases relevant of the solar nebula composition:

- tank 1: CO (quality 2.5 (CO=99.5%, Messer) for 2 years, then changed to quality 3.7 (99.97 %, Messer)
- tank 2: N_2 (high quality, 99.99995%, Messer)
- tank 3: Noble gas mixture (75% He, 15% Ne, 5% Ar, 3% Kr and 2% Xe, Air Liquide)
- tank 4: N_2 + noble gases mixture (50% N2, 20% Ne, 10% Ar, 10% Kr and 10% Xe, Messer)

The four different gas mixtures used, along with the flow rates, are reported in Table 2.5. The flow rates were small (10 sccm maximum) to maintain a pressure in the reactor of ~ 1 mbar. There was no valve between the reactor and the pump to control the total pressure when changing the gas flow rates. As a consequence, increasing the gas flow rates resulted in

an increase of the total pressure in the reactor, and thus likely changed the plasma characteristics. Because of that, the study of the gas ratios in the mixture was limited to small variations (less than one order of magnitude).

	gases	flow CO (sccm)	flow NG / N_2 (sccm)	total flow (sccm)	total pressure (mbar)	Xe/C (at.)	N/C (at.)
1	CO only	5		5	0.75		
		10		10	2.28		
2	CO - noble gases	5	1	6	0.8	0.004	
		5	3	8	0.98	0.012	
		5	4	9	1.11	0.016	
		5	5	10	1.19	0.020	
		8	1	9	0.97	0.0025	
		8	0.5	8.5	1.02	0.0013	
3	CO-N_2	5	1	6	0.82		0.4
4	CO-N_2-noble gases	5	1	6	0.7	0.02	0.2

Table 2.5. Gas mixtures used and the corresponding gas flows.

These mixtures were chosen in order to study (i) the nature of the solids with or without noble gases and nitrogen in the initial gas mixture, (ii) the noble gas incorporation into the solids, by varying the ratio noble gases/CO in the initial gas mixture, and (iii) the nitrogen incorporation into the solids and its isotopic fractionation.

H_2, the most abundant gas in the solar nebula, was not used because of technical and safety constraints. Moreover, matching the exact solar nebula composition in an experiment is quite difficult, especially for the noble gases. Indeed, in order to be able to measure Kr and Xe trapped in synthetic solids, we had to enhance greatly the Kr/C and Xe/C ratios in the experiments compared to the solar nebula (see Tables 2.1 and 2.2): in the Nebulotron, Xe/C ratio is 2000 to 3.10^5 higher than the canonic Xe/C ratio. Nebulotron Ar/C, O/C and N/C ratios better match the solar composition.

2.3.3.2 Controlled parameters

In order to study the nature of the solid organics and the trapping and isotopic fractionation of noble gases, the following experimental parameters were varied:

- the **duration of the discharge** (from 5 to 360 mn) to study the kinetics of the processes
- the **net power of the discharge** ($P_{net} = P_{forward} - P_{reflected}$; from 25 to 65 W). The power delivered to the discharge controls the overall electric state of the plasma by governing the electron density, the power density in the reactor ($W.cm^{-3}$) and as a consequence influences the gas temperature and the electron average energy. Increasing the power delivered to the discharge results in a larger ionization rate.
- the **gas ratios**, notably the noble gases/CO ratio to study the noble gas trapping efficiency.

I have conducted a series of experiment, in which I only varied one parameter at a time.

All the synthesized samples along with the experimental conditions are reported in Appendix A.

2.3.4 Plasma characteristics

No plasma modeling has been performed for the Nebulotron. Nonetheless, some orders of magnitude of the plasma characteristics can be found in the literature, but must be treated cautiously as a tiny change in the geometry of the reactor, in the pressure or in the nature of the gas can dramatically change the plasma characteristics. A comparison between plasma characteristics of the PAMPRE setup (modeled by Alves et al., 2012) and an estimation of the Nebulotron ones are given in Table 2.6.

	PAMPRE	**Nebulotron**
type of electric discharge	RF (13,56 MHz)	microwave (2.45 GHz)
size of the reactor (height * diameter)	40*30 cm	10*0.8 cm
volume of the plasma (cm^3)	740	2.5
injected power (W)	30	30
W/cm^3	0.04	12
pressure (mbar)	0.9	~ 1
Neutral temperature	300 - 350 K [a]	≥ 800 K (estimated[c,d])
Electron density (cm^{-3})	$2\ 10^8$ [a]	5.10^{10} - 1.10^{11} (estimated[d])
Average electron energy	2 eV [b]	2 eV (estimated[d])

[a] *Alcouffe et al. (2010)* [c] *Es-Sebbar et al. (2009)*
[b] *Alves et al. (2012)* [d] *Gries et al. (2009)*

Table 2.6. Qualitative comparison of plasma characteristics of the PAMPRE and the Nebulotron setups.

The Nebulotron is a microwave plasma. It is, thus, **very efficient** in terms of dissociation and ionization rates, notably because of the high power density in a small reactor (~12 $W.cm^{-3}$ for the Nebulotron relative to 0.04 $W.cm^{-3}$ in the PAMPRE setup). As a consequence, the neutral gas temperature is much higher than in the PAMPRE setup and is estimated to be ~ **1000 K**. Thus, the solid organics produced in the reactor certainly suffer from **pyrolysis**, but to a degree that is difficult to quantify.

These experimental conditions, debatable regarding the formation of organics in nebular environments, will be discussed in Chapter 3 in light of the characterization of the Nebulotron samples.

2.4 Synthesized solids

The synthesis of solid particles in the Nebulotron setup takes place on the walls of the quartz tube (Fig. 2.13). The dissociation of initial gases and the formation of reactive species result in the nucleation and in the polymerization of solid particles. These particles are deposited or grown onto the reactor surfaces, progressively forming thicker and thicker aggregate layers.

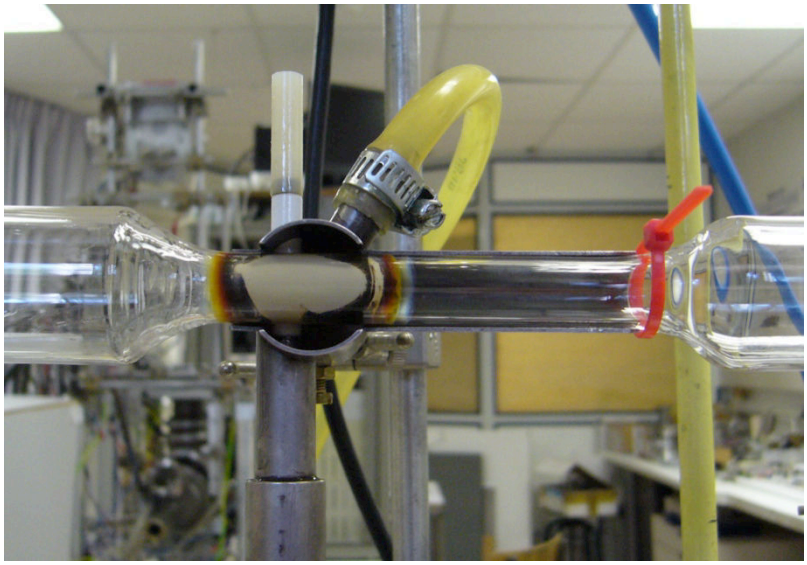

Figure 2.13. Picture of the Nebulotron reactor (new one) with the synthesized solids after a CO-N_2 experiment of 360 min, at 30W. The cavity length is 10 cm.

2.4.1 Sample extraction from the reactor and storage

The solids produced in the reactor are removed by scraping the sidewalls using a dedicated stainless spatula. In some experiments, as shown in the Fig. 2.14, the solids exhibited two colors: red on the edges of the discharge and black in the center. In this case, I tried to collect those two types of synthesized samples separately.

The recovered solids are very fine grained, except for the red part, which is much like a film. The extracted powders were stored in plastic or glass microvials at atmospheric pressure. Depending on the initial gas mixture composition, the synthesized solids have different colors (Fig. 2.14), probably due to their different chemical compositions.

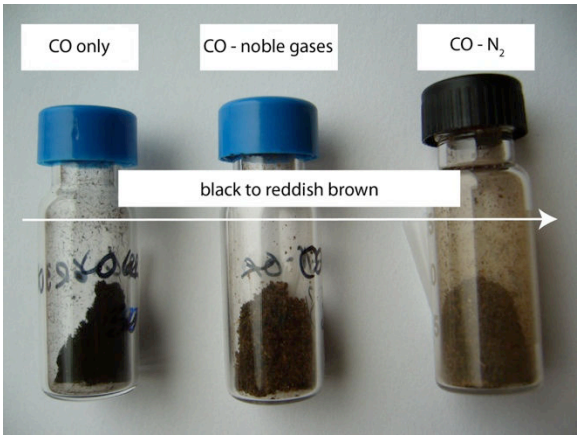

Figure 2.14. Different synthesized samples depending on the initial gas mixture composition.

2.4.2 Production rates

The solid production rates were calculated for each experiment. The mass of the solid that is recovered after each experiment gives a lower bound for the actual mass since some solids are left on the reactor's surfaces and since a part of the aerosols formed in the plasma are lost in the gas flow and pumped out. The leftover aerosols onto the reactor can be estimated to ~ 1-2 mg maximum, but the amount of the aerosols lost through pumping is unknown.

Regardless of the experimental conditions, the solid production rates ranged from 0.7 to 17.5 mg/h. The production rate mostly depended on the composition of the initial gas mixture (Fig. 2.15). Adding N_2 to the initial gas mixture greatly increases the solid production rate, whereas adding only noble gases to CO does not change the rate. This suggests that N_2 dissociation and ionization in the gas phase provides reactive species prone to polymerization. This recalls the large nitrogen incorporation in PAMPRE tholins (Sciamma-O'Brien et al., 2010).

For a given experimental condition, the solid production rate also depends on the duration of the discharge experiment, with a higher production rate when the experiment is longer. The trend follows a power law rather than a linear law (Fig. 2.15). Although this might suggest a snowball effect of the grain polymerization, a lack of reproducibility of the experiments may cause an over-interpretation of such a trend.

Overall, the solid production rates are satisfactory for ex-situ analysis since sufficient solid amounts are available.

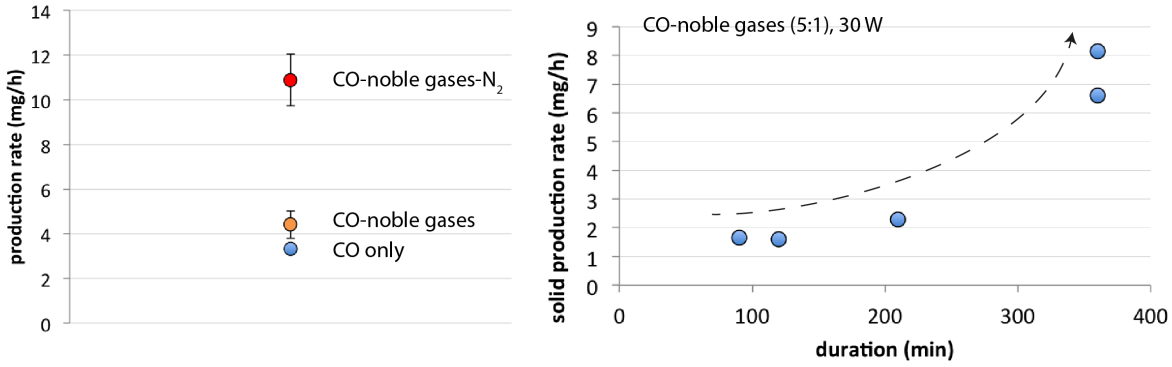

Figure 2.15. Solid production rate (mg/h) in the Nebulotron. Left: averages of samples produced in the same experimental conditions (360 min, 30 W) as a function of the initial gas mixture composition, for the new reactor. Right: for the CO-noble gases mixture (5:1, 30W) as a function of the experiment duration, on the old reactor.

2.4.3 Carbon and Nitrogen gas-to-solid yields

The gas-to-solid yield is a proxy of gas incorporation into solids and, thus, it is related to the plasma efficiency for dissociating molecules and to their ability to polymerize. The calculation of the carbon and nitrogen gas-to-solid yields in the Nebulotron has been done using the C and N wt. % in the solids (elemental analysis, see next chapter, section 3.2.3), the initial gas fluxes and the measure of the solid mass production rate:

$$Y\,(\%) = \frac{M_{solid}\,(mg/h)}{M_{gas}\,(mg/h)} \times 100 = \frac{P \times c}{(F \times M \times 6.10^4)\,/V_m} \qquad (9)$$

with P the solid production rate (mg/h), c the C or N content in the solids (wt. %), F the gas mass flow (sccm/min), M the C or N molar mass (g/mol), Vm the molar volume (22414 cc/g STP) and 6.10^4 the conversion factor for g/min to mg/h.

The calculated solid production rate is a lower bound since some of the formed organics have been pumped out. The calculated C and N yields are lower bounds as well.

Calculated carbon yields from pure CO gas to solids range from 0.2 to 4.2 %; which is about one order of magnitude smaller than in the PAMPRE setup (Sciamma-O'Brien et al., 2010). The production rate in the Nebulotron setup is indeed 10 times smaller than in the PAMPRE setup. The PAMPRE and the Nebulotron setups have similar power of discharge (30W) and pressure (1 mbar) and the average electron energy is likely to be the same in both experiments (Table 2.6). Thus, I suggest that this difference is partly due to the dissociation

energy difference between CH_4 and CO (4.4 eV and 11.11 eV respectively), the former being dissociated more easily in a plasma.

The nitrogen yield from N_2 gas to solids produced in a N_2-CO mixture ranges from 4.9 to 7.7 %. The N yield is almost twice the C yield, and again, this may be due to the electron energy distribution in the plasma, providing more electrons at 9.8 eV (N_2 dissociation energy) than at 11.11 eV (CO dissociation energy) – e.g. Fig. 2.8. In the PAMPRE setup, the N gas-to-solid yields are in the range 0.05 – 0.7 %, thus one order of magnitude lower than in the Nebulotron setup. This illustrates the better dissociation efficiency in the Nebulotron relative to the PAMPRE setup, likely due to an enhanced power density in the reactor (see Table 2.6).

Chapter 3

Characterization of organic solids synthesized in the Nebulotron

Table of contents

Carbon is one of the most abundant elements in the Universe and plays a central role in the chemistry associated to life on Earth. Carbon is also encountered as various inorganic phases in all astrophysical contexts (Ehrenfreund and Charnley, 2000). In meteorites, carbon is notably found as nanodiamonds, SiC, carbonates, graphite, amino-acids and polyaromatic compounds, the so-called "Insoluble Organic Matter" (IOM, Botta and Bada, 2002, Derenne and Robert, 2010, Huss et al., 2003). IOM has been extensively studied by a large number of analytic techniques because of its possible link with prebiotic molecules. Furthermore, IOM presents significant, sometime extreme, isotopic variations of H and N (Bonal et al., 2010, Briani et al., 2009, Remusat et al., 2010) and is also the main host of trapped noble gases in meteorites (Lewis et al., 1975, Ott, 2002, Ott et al., 1981). The chemical and physical structures of this IOM have recorded the conditions, process(es) and location(s) of its formation. Determining with precision its composition and structure may lead to constrain its original synthesis mechanism(s) and to get information on its astrophysical context. Such characterization was done quite successfully for IOM in meteorites, IDPs and Antarctic micrometeorites (AMMs) (Quirico et al., 2005, Bonal et al., 2007, Busemann et al., 2009, Derenne and Robert, 2010, Dobrică et al., 2011, Quirico et al., 2014, Dartois et al., 2013), although the conditions of the formation of this IOM and the impact aqueous and thermal alteration on the parent bodies is still actively debated (Alexander et al., 2010, Remusat et al., 2010).

We have attempted a physico-chemical characterization of organics synthesized during the Nebulotron experiments using several techniques. The goals of this characterization were 3-folds: (i) assessing the reproducibility of the experiments and the homogeneity of the Nebulotron synthesized solids, (ii) comparing the Nebulotron synthesized solids with extraterrestrial carbon materials using similar techniques, and (iii) exploring mechanisms of noble gas trapping and isotope fractionation in synthesized organics by better understanding their formation process in the plasma.

The first part of this chapter is dedicated to the brief description of the analytical methods used to characterize the Nebulotron-synthesized solids: microscopic imaging (SEM, TEM), Raman, FTIR and elemental analyses. In particular, TEM imaging and Raman spectroscopy give insights into the carbon microtexture and structure, respectively, of the Nebulotron synthesized organics; and FTIR and elemental analysis give insights into the chemical composition and speciation of C, H, O and N in the samples. The results are given in the second part of this chapter, where the morphology, carbon texture and structure and chemical composition of the Nebulotron grains are successively described. Limitations of the Nebulotron experimental setup are also discussed in the light of these results. The third part is dedicated to the comparison of the Nebulotron samples with chondritic IOMs. Finally, some perspectives and open questions raised by the Nebulotron samples – IOMs likeness are discussed.

3.1 Analytical methods used for the characterization of the Nebulotron-synthesized organics

3.1.1 Microscopy imaging

3.1.1.1 Optical microscopy

A few samples were observed under an optical microscope, with objectives up to x100 in both transmitted and reflected light. The homogeneity, the morphology and the size of the particles were checked.

3.1.1.2 Scanning electron microscopy (SEM)

- SEM principle

A SEM is composed of an electron gun, producing electrons up to 40 keV, which are focused through a series of lenses and diaphragms. The electron beam is synchronized by a cathodic oscilloscope, which deflect the beam in the x and y axes so that it scans in a raster fashion over a rectangular area of the sample surface.

The SEM uses the electron-sample interaction resulting in the emission of secondary electrons (SEI mode, inelastic scattering, low energy), backscattered electrons (BSE mode, elastic scattering, high energy), and X ray photons; all of them coming from different depths in the sample – fig 3.1.

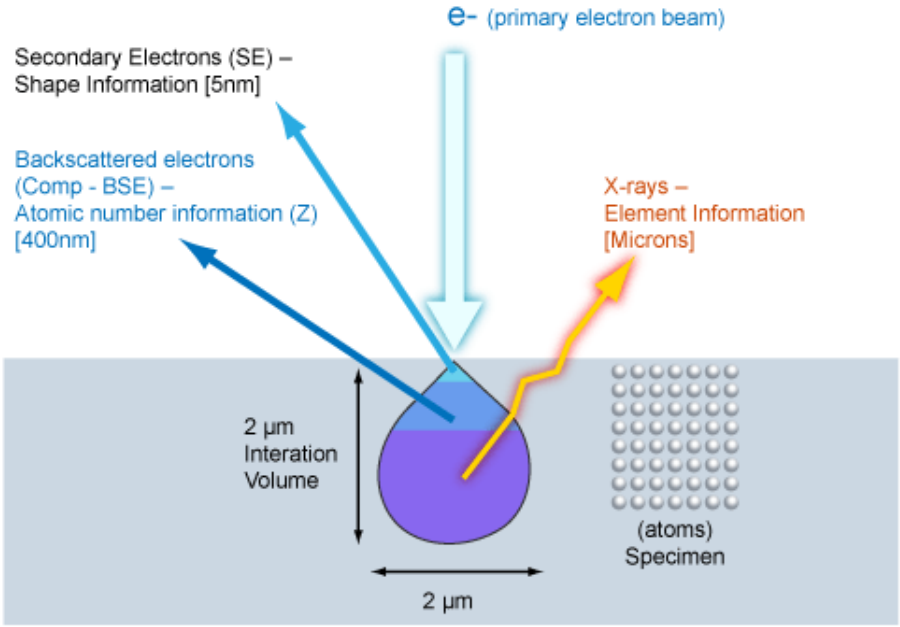

Figure 3.1. Electron-sample interaction volume, resulting in the emission of secondary and backscattered electrons and X-ray photons, used by SEM technique.

I have used the SEM installed at CRPG, a Jeol JSM 6510 instrument operating at 15 keV and in the SEI imaging mode in order to get a good representation of grain morphology and topography.

- Sample preparation

Synthesized grains were gently deposited on a double-sided carbon adhesive tape, attached to an inox support. Four samples could be imaged at the same time. The samples were not carbon-coated as we thought than the carbon content of the Nebulotron grains was sufficient to provide electrical conductivity. Several samples however were not sufficiently conductive, resulting in blurred images (see Appendix A for the samples that were studied with this technique).

3.1.1.3 Transmission electron microscopy (TEM)

The objective of this study was to determine the morphology and the texture of the carbon materials produced in the Nebulotron at the macro and microscales.

- TEM principle

A TEM consists of three main systems: an electronic column, a vacuum system and detectors. The electronic column is the fundamental feature of a TEM, allowing very large magnifications (up to x1000000) and high spatial resolutions (less than 1 nm for conventional TEM). Electrons are produced by an electron gun with a 200 kV acceleration tension. Electromagnetic lenses allow the convergence of the electron beam as well as the correction of asymmetrical distortions. A series of lenses and diaphragms provide either the image plane of the objective lens (bright field imaging mode – the electrons absorption and occlusion contrasts are imaged) or the focal plane of the objective lens (diffraction mode) – Fig. 3.2. Sample imaged with TEM must be very thin, so there is a minimal scattering of the electron beam through the sample. TEM thus provides a much higher spatial resolution than SEM, down to the atomic scale using electron beam energies of ~ 200 keV.

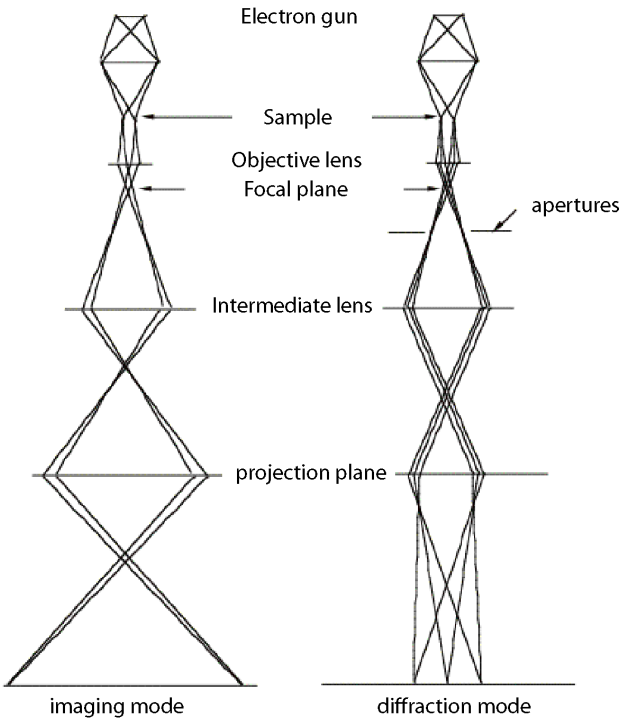

Figure 3.2. TEM imaging (bright field) and diffraction modes.

We have used the Philips CM20 (200 kV) instrument installed at the Service Commun de Microscopies Electroniques et Microanalyses X (SCMEM, Université de Lorraine, Nancy).

- Sample preparation

The Nebulotron samples were ultrasonically cleaned in ethanol and the suspension was deposited on a TEM copper grid (see Appendix A for the samples that were studied with this technique).

3.1.2 Raman spectroscopy

Raman spectroscopy, along with TEM, is a reference tool for studying the carbon structure of organic materials. It was applied successfully to terrestrial coals and kerogen, to synthetic soot and to extraterrestrial carbon compounds (Bonal et al., 2006, Busemann et al., 2007, Dobrică et al., 2011, Quirico et al., 2005, Quirico et al., 2009, Sadezky et al., 2005). It is a non-destructive technique and requires a small amount of sample (a few grains fro microRaman) and is easy to use. A few samples from the Nebulotron setup were analyzed by

Raman spectrometry at 514 and 244 nm (see Appendix A for the samples that were studied with this technique).

3.1.2.1 Raman spectroscopy: principle

Raman spectroscopy is a vibrational spectroscopy. When a beam of light reaches a sample surface, a part of this light is reflected or transmitted by the sample and only a small fraction light is scattered (10^{-3} of incident photons). This scattered fraction is dominated by elastic scattering (Rayleigh scattering); and only a tiny fraction is inelastic scattering (10^{-7} of incident photons): this is the Raman effect. The laser interacts with molecular vibrations resulting in the energy of the laser photons being shifted up or down (Stokes and anti-Stokes scattering – Fig. 3.3). It is customary to measure only the "Stokes" side of Raman spectra. The shift in energy gives information on the vibrational modes in the system. Raman scattering can be resonant if the energy of the incoming or scattering photon matches the transition energy of an allowed electronic transition, leading to the enhancement of the Raman cross section (Thomsen and Reich, 2000). In particular, in graphitic carbon, the Raman modes depend on the energy of the incident laser light and their frequencies shift when the laser energy is changed (Vidano et al., 1981). Such a behavior was interpreted to originate from a double-resonant Raman process (Thomsen and Reich, 2000). Electronic transitions may occur, as in graphitic carbon, producing a fluorescence background. This fluorescence background may completely mask the Raman signal in some cases, preventing any measurement.

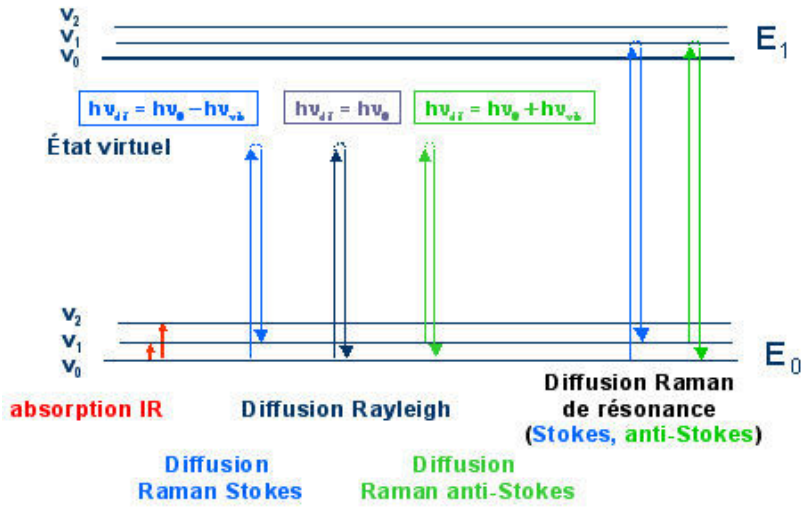

Figure 3.3. Diagram of the infra-red, Rayleigh and Raman scattering processes. In carbon materials, Raman scattering is resonant and correspond to an electronic transition.

3.1.2.2 Raman spectroscopy and disordered carbon compounds

The electronic structure of a carbon atom allows 3 types of hybridization, sp^1, sp^2 and sp^3, responsible of the polymorphism of carbon materials. The pure crystalline forms are graphite (pure sp^2), which is the usual form under normal pressure conditions and diamond (pure sp^3). Natural carbon assemblages rarely present only one type of hybridization. On the contrary, carbon mostly occurs as **disordered** and amorphous forms, displaying a mixture of sp^1, sp^2 and sp^3 hybridizations. These forms may present a local structural organization in a "random" disordered matrix. Polyaromatic compounds, like coal, soot or extraterrestrial IOM, are described as disordered carbon materials. These polyaromatic materials are generally characterized by a multi-scale organization of basic structural units (BSU; Oberlin et al., 1984, Bonal, 2006). These BSU are constituted of 2 or 3 layers formed by 4 to 10 aromatic rings (total size < 1 nm) and define the **structure and microtexture of the carbon material**.

Raman spectroscopy is very sensitive to the carbon structure, such as the size of BSUs and more generally to sp^2 clusters, to bond disorder and to the sp^2/sp^3 ratio (Beyssac et al., 2003, Beyssac and Lazzeri, 2012, Ferrari and Robertson, 2000, Tuinstra and Koenig, 1970). Carbon materials are dark and opaque, resulting in a large optical absorption coefficient. Thus the incident beam light only interacts with the very surface of the sample in the visible range. Raman spectra of carbon materials can be divided into first order bands (1100-1800 cm^{-1}) and second order bands (2300-3400 cm^{-1}), the latter generally being weak. Raman spectra of disordered carbons are notably different from the spectra of monocrystalline graphite: two main peaks are displayed in the 800-2000 cm^{-1} spectral range, the G peak at ~ 1580 cm^{-1} and the D (or D1) peak at ~ 1350 cm^{-1} (G stands for "graphite" and D stands for "defect"). The G peak is attributed to the in-plane vibration mode with symmetry E_{2g} (C=C bond vibration in cycles or oleifinic chains) and the D peak is tentatively attributed to the vibration mode with symmetry A_{1g} (aromatic rings breathing mode, Ferrari and Robertson, 2000) – Fig. 3.4. Three more defects peaks are reported for soot and highly disordered carbon materials: the D4, D3 and D2 peaks, at ~ 1200 cm^{-1}, ~ 1500 cm^{-1}, and ~ 1620 cm^{-1} respectively (Brunetto et al., 2011, Brunetto et al., 2009, Sadezky et al., 2005).

Some sp^2 clusters (here, polyaromatic units) are more easily excited by different incident radiation frequencies. The part of the material probed by Raman spectroscopy will thus depend on the incident frequency of the beam light. For example, nitrile functions and small polyaromatic domains are more sensitive to UV than to visible radiations. UV and visible Raman are thus complementary regarding the composition and the structure of the carbon material.

Several Raman parameters have been used to classify aromatic-rich carbonaceous materials, including the frequency (ω) and the full-width at half maximum (FWHM) for G and D peaks, and I_D/I_G intensity ratio (Beyssac et al., 2003, Beyssac and Lazzeri, 2012, Bonal, 2006, Brunetto et al., 2011, Brunetto et al., 2009, Busemann et al., 2007, Ferrari and Robertson, 2000, Lahfid et al., 2010, Sadezky et al., 2005, Sforna et al., 2014, Wopenka and Pasteris, 1993). Because the I_D/I_G ratio may not be accurate in some cases to determine the

graphitization/amorphization trajectory for disordered carbon compounds, more complicated tracers based on bands areas and intensities were built to retrieve in details information of the metamorphic history of natural carbon compounds (Lahfid et al., 2010, Sforna et al., 2014).

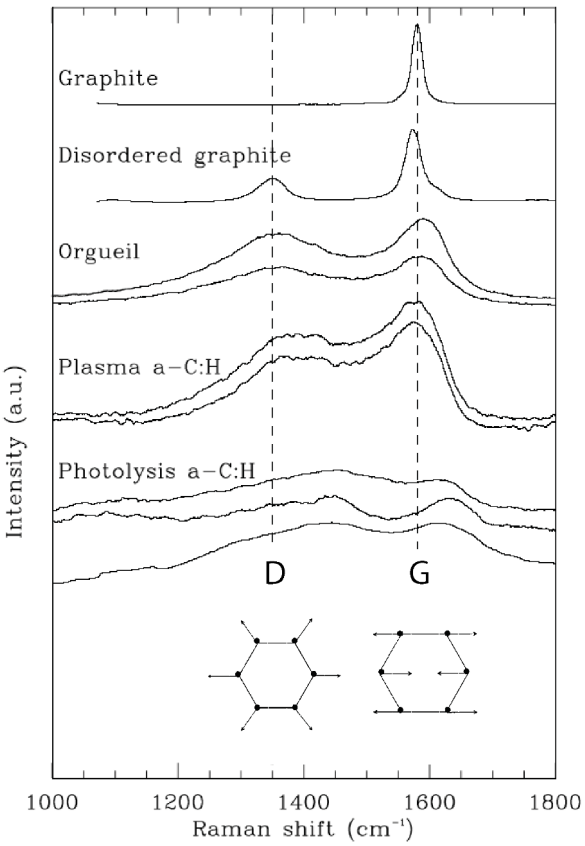

Figure 3.4. Raman spectra of (from top to bottom): (i) graphite; (ii) disordered graphite (G. Montagnac, data base of the ENS Lyon); (iii) carbonaceous fraction of the Orgueil meteorite; (iv) a-C:H produced in a hydrogen-dominated RF plasma; (v) UV photoproduced a-C:H from hexane and trans-2-butene precursors. The position of the G (for "graphitic") and D (for "defect") in (disordered) graphite are given by vertical dashed lines along with their vibration modes (adapted from Dartois et al., 2005 and Ferrari and Robertson, 2000).

3.1.2.3 Analytical methods

- Raman measurements with 514 nm excitation (Laboratoire GéoRessources, in collaboration with Jean Dubessy and Marie-Camille Caumon)

Raman microscopy was performed at Laboratoire Géoressources (Nancy, France) using a LabRam Raman spectrometer (Horiba Jobin-Yvon) equipped with a 600 gr/mm grating and a Spectra Physics Ar^+ laser that provided a 514 nm excitation wavelength. The laser beam was focused through a x80 objective, leading to a ~ 1 µm circular spot. The typical power on the sample and acquisition time were ~ 4 µW and 200 s, respectively. Several spectra were acquired on the same spot to check that there is no degradation of the sample by the laser beam (Quirico et al., 2008). Spectra were acquired in two spectral windows: 700-2200 cm^{-1} and 2200-3400 cm^{-1}. A diamond standard was used as a reference to calibrate the spectrometer.

Most of Nebulotron samples, notably the red ones and those with a high nitrogen content were found to fluoresce strongly when using green incident laser light and other visible wavelenghts (we have tested 457, 488, 660 and 785 nm without any success). Quirico et al., 2008 have found that UV Raman excitation (244 nm) on tholins (experimental aerosols formed in a N_2-CH_4 gas mixture in a plasma experiment) gave rise to Raman spectra with a high signal-to-noise ratio and that were unperturbed by fluorescence background. We thus tried UV Raman excitation on Nebulotron samples, and indeed, UV spectra were free of fluorescence effects.

- Raman measurements with 244 nm excitation (Laboratoire de Géologie de Lyon, in collaboration with Gilles Montagnac)

Raman spectroscopy using UV excitation was performed with a Horiba Jobin-Yvon LabRam system with a frequency-doubled Ar+ (244 nm) excitation, a 600 g/mm grating and a x40 objective at the Laboratoire de Géologie de Lyon (LGL, France). The width of the laser spot on the sample was ~ 5 µm. In this configuration, the laser power delivered to the sample was limited to 300 µW to avoid heating damage by the incident beam. Spectra were acquired in the 500-4000 cm^{-1} spectral range. Like for the 514 nm measurements, several spectra were acquired on the same spot to check the non-degradation of the sample by the beam light (Quirico et al., 2008). A diamond standard was used as a reference to calibrate the spectrometer.

- Sample preparation

Nebulotron grains were manually squeezed between two glass slides in order to get a roughly similar grain thickness. Those grains were directly observed with the optical microscope attached to the spectrometer.

- Fitting procedure

Retrieving quantitative information from Raman spectra, such as the position and intensities of the D and G bands as well as the I_D/I_G ratio, requires peak fitting. The first step is the baseline correction, which is generally linear for graphitic carbons. But the situation is more complex when the structural disorder increases, which is generally accompanied by an increasing contribution of fluorescence to the background. Several fitting strategies can be found in the literature. Depending on the structural disorder, one uses 3-band fitting (ordered graphitic carbon, Beyssac et al., 2003) or 5-band fitting (disordered carbons, Brunetto et al., 2009, Sadezky et al., 2005) procedures, using symmetric profiles (Lorentzian and/or Gaussian band profiles). Nonetheless, the 5-band model, which fits very well disordered carbons and which I have used for the Nebulotron samples, is more subject to high statistical uncertainties because of numerous degrees of freedom. Some authors prefer to use of fewer peaks but with asymmetric profiles (Bonal et al., 2006, Brunetto et al., 2011, Quirico et al., 2003). Such a model fits accurately carbon matter in type 1 and 2 chondrites

(Bonal et al., 2006). The choice of one fitting procedure is arbitrary, its quality only depending on the goodness-of-fit, controlled by the eye and by the low value of residuals between the model and the spectrum.

In my case, curve fitting and spectral parameters determination was performed on 514 nm spectra with the software Origin (OriginLab). Most Nebulotron samples presented a fluorescence background; that was subtracted assuming a linear base line between 800 and 2000 cm^{-1} (Fig. 3.5). The intensity was normalized to the G band intensity at ~ 1600 cm^{-1}. Then, the peaks were adjusted.

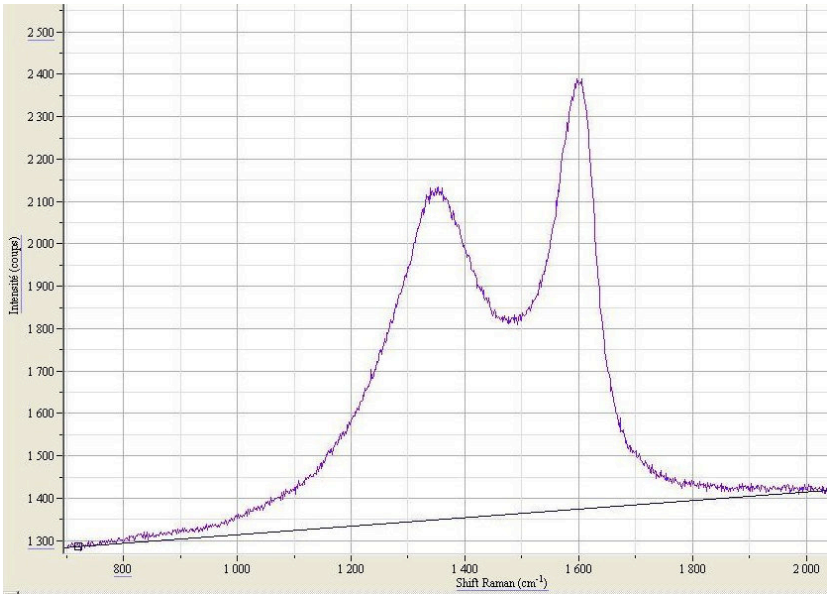

Figure 3.5: Subtraction of the fluorescence background by a linear baseline on a 514 nm Raman spectra of a Nebulotron sample.

Nebulotron samples gave two kinds of Raman spectra: the first ones were well fitted by a 2-band model, and the second ones clearly displayed more than 2 bands, and a 5-band model was more successful. In the 2-band model, the D peak is adjusted to a Lorentzian profile and the G band to an asymmetric Breit-Wigner-Fano profile in order to fit the valley between the D and the G peaks (LBWF fit, Bonal, 2006, Bonal et al., 2007, Bonal et al., 2006, Ferrari and Robertson, 2000). The 5-band model is based on Sadezky et al., 2005 (Fig.3.6), with the D, G, D2 and D4 peaks adjusted to Lorentzian profiles and the D3 peak to a Gaussian profile. The 5-bands model best fits most of the Nebulotron spectra; but in order to compare their spectral parameters to extraterrestrial organics ones (Bonal et al., 2007, Bonal et al., 2006, Busemann et al., 2007), I used a LBWF 2-band model when possible.

UV 244 nm spectra can be fitted adequately with a LBWF model as well (Bonnet, 2012, Quirico et al., 2014). However, the 244 nm spectra presented in this thesis were not fitted and are interpreted qualitatively.

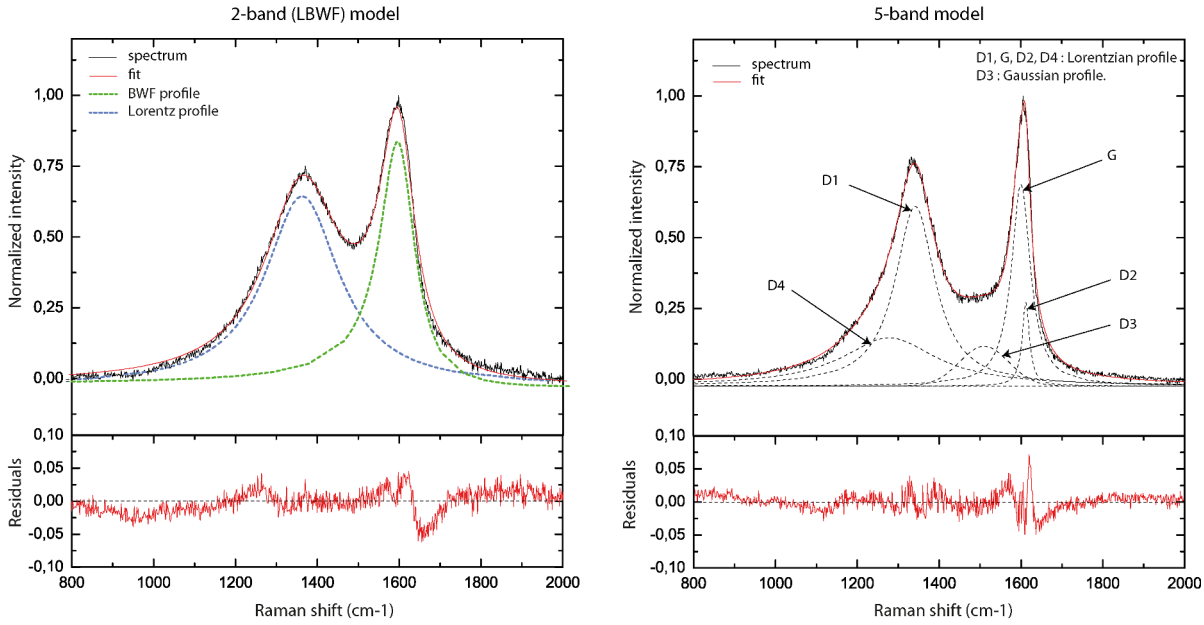

Figure 3.6. Examples of curve fitting models and associated residuals of 2 Nebulotron samples at 514 nm: (left) CO-11 spectrum and curve fit with a 5-bands combination (G, D1, D2 and D4: Lorentzian profile; and D3: Gaussian profile) – inspired by Sadezky et al., 2005. (right) CO-12 spectrum and curve fit with a 2-bands combination (D: Lorentzian profile; G: asymmetric shape modeled by a Breit-Wigner-Fano profile) – inspired by Bonal et al., 2006.

3.1.3 Elemental analysis

Elemental composition analyses (for C, H, O and N elements) of some of the Nebulotron samples were done at the Service d'Analyses Elémentaires at Université de Lorraine (Nancy, France) by the usual techniques of pyrolysis and combustion. Duplicate analysis of the 4 elements requires ~ 6 mg of sample. Such an amount was not available for all Nebulotron samples; only those produced in sufficient quantities were analyzed for C, H, O and N content (see Appendix A). Samples were not baked before analysis.

These analyses have pointed out the presence of relatively large H, O and N contents in the Nebulotron solids, which consequently can be identified as organic materials. The contamination by H and N is discussed later in this chapter.

3.1.4 Infrared spectroscopy

Infrared (IR) spectroscopy gives information on some functional groups present in the organic compounds. Like Raman spectroscopy, infrared spectroscopy is non-destructive and requires low amount of samples. This technique is briefly described here.

3.1.4.1 Basic principle of IR spectroscopy

IR spectroscopy is a vibrational spectroscopy, relying on the interaction between infrared light and a sample. Molecular bonds can be approximately modeled by harmonic oscillators, which vibrational frequencies depend on the masses of atoms and on the spring constant.

Most molecular vibrations of organics fall in the mid-IR domain (2.5 µm < λ < 25 µm / 400 - 4000 cm^{-1}) and the two main molecular vibration modes are stretching and bending modes. The frequency of the absorption (and thus the band position in IR spectra) is mainly determined by the reduced mass of the molecule, the bond strength and the neighboring atoms. A sample of a given chemical composition and structure will thus produce a set of specific absorption bands, allowing its characterization.

Nowadays, infrared spectroscopy is done via an interferometer, which allows the measurements of all IR frequencies in a minimum amount of time. The raw absorption by the samples is an interferogram; which is transformed into an absorption spectrum by applying a Fourier Transform.

3.1.4.2 Analytical methods

Several IR measurement sessions were conducted during the course of this thesis.

- Nancy measurements (Laboratoire GéoRessources, in collaboration with Odile Barrès)

Some samples were analyzed in transmission. The measurements were done using a Brucker Equinox 55 Fourier-Transform spectrometer coupled with a Brucker A590 microscope, equipped with a MCT detector cooled down with liquid nitrogen. Spectra were acquired in the spectral range 4000-600 cm^{-1} with a spectral resolution of 2 cm^{-1}. The spot size was in the range 20-100 µm.

In order to have bulk measurements, some of the Nebulotron samples were pressed into KBr (0.1 wt% sample in KBr powder) at 10 T/cm^2. The KBr pellets (diameter 13 mm) were analyzed with a Brucker Equinox 55 Fourier Transform spectrometer, equipped with a DTGS detector. With these analytical conditions, the spectra were acquired in the range 4000-400 cm^{-1}, with a 2 cm^{-1} spectra resolution. The IR beam diameter was 7 mm. A pure KBr pellet was measured as a reference.

- Grenoble measurements (Institut de Planétologie et d'Astrophysique de Grenoble, in collaboration with Eric Quirico)

The IPAG laboratory, in Grenoble, has an environmental cell equipped with turbo and primary pumps (typical vacuum ~ 10^{-6} mbar), and a heating element (up to 300 °C), which ensures the removing of adsorbed water on sample surfaces; and allows working with small quantities.

In a first step, measurements were performed by transmission microscopy directly on Nebulotron grains. Nebulotron grains were deposited on a diamond window (3x0.5 mm) and crushed by applying a second diamond window, in order to get a thin sample layer and a roughly identical thickness from one sample to another. The thickness was visually controlled with the microscope focus. Complementary measurements were performed with the environmental cell. Three Nebulotron samples spectra were acquired under vacuum at room temperature, then at 80 °C to control the water removal from sample surfaces. Spectra were finally acquired at 150 and 300°C, in order to check for any thermal degradation that could be visible in the IR spectra. Samples were kept for 15 min at the desired temperatures before the measurements. All the measurements were performed with a Brucker Hyperion 3000 FTIR spectrometer coupled to a microscope, with 4 cm^{-1} spectral resolution from 4000 to 600 cm^{-1}. The typical size of the spot was 50 µm.

3.1.4.3 Treatment and interpretation of IR spectra

In order to allow a qualitative comparison of the different Nebulotron sample spectra and a comparison of these spectra to other organic analogues and extraterrestrial matter, a baseline was subtracted (polynomial function that was adjusted with the eye as no quantitative interpretation has been done) and the spectra were normalized to the 1600 cm^{-1} peak (C=C).

Most of the organic functional group band positions are well documented in the literature, and the identification of specific organic group in the Nebulotron spectra is based on the common IR spectra description of natural and synthetic carbon materials (Dartois et al., 2004, Kebukawa et al., 2013, Orthous-Daunay et al., 2013, Painter et al., 1981, Ristein et al., 1998). In particular, the goal of this study was to see if Nebulotron organics are aliphatic or aromatic-rich, what is the speciation of oxygen (C=O, COOH, -OH?) and of nitrogen (-NH, -CN, -NO?). The bonds along with their spectral range that I have been using for the Nebulotron IR spectra interpretation are reported in Table 3.1.

Function	Formula	IR Vibrational mode	wavenumber (cm^{-1})
Carboxylic acid water, alcohol	OH	OH streching	3600-3000
Amine	NH (secondary) NH_2 (primary)	streching	3500-3100
Aromatic	C-H	CH streching	3050-3030
Aliphatic	CH_3	asym. streching	2955
	CH_2	asym. streching	2925
	CH_3	sym. streching	2865
Nitrile	CN		2260-2240
Carbonyl (aldehyde, ketone, ester, acids, amides)	C=O	C=O streching	~1700 (1650-1750 depending on the conjugation)
Alkene	C=C	streching	1660-1600 (weak)
Water	OH	bending	1635
Amine, Amide	NH	bending	1640-1550
Aromatic	C_6 (cycle)	cycle streching	1630-1600
Aliphatic	CH_2	bending	1460
	CH_3	asym bending	1450
	CH_3	sym bending	1380
Phenol	C-OH	C-O streching	1240
Ether, alcohol	C-O	C-O streching	1300-1000
Aliphatic, aromatic	CH_2, CH	bending	1000-700

Table 3.1. List of IR vibrational modes used to interpret the chemical composition of the Nebulotron organics.

3.2 Results and discussion

3.2.1 Microscope observations: morphology and size of the Nebulotron aerosols

3.2.1.1 Optical microscopy

A few Nebulotron samples were observed with an optical microscope. Nebulotron deposits present a color zonation ranging from dark and powdered solids in the center of the discharge to red-brown films on the discharge edge (Fig. 3.7).

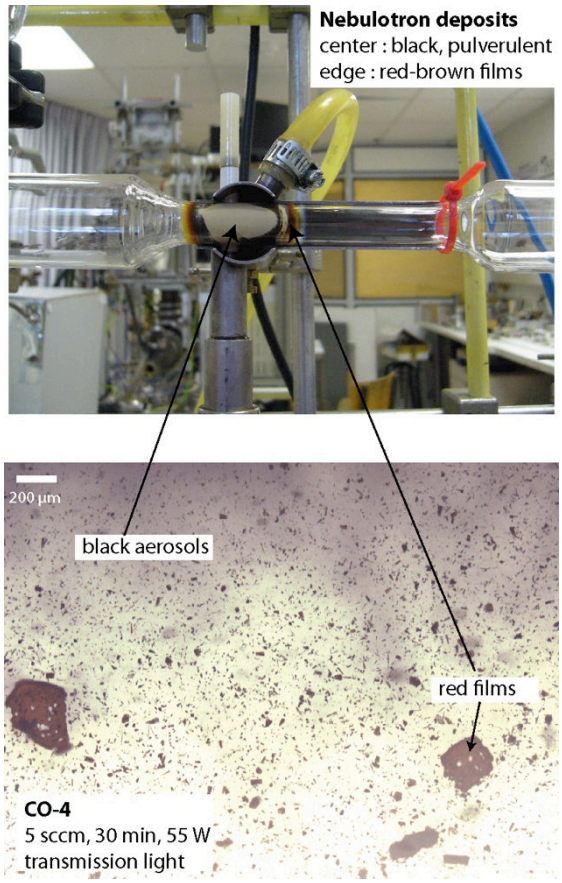

Figure 3.7. Picture of the Nebulotron deposits observed with an optical microscope and their formation area in the discharge tube.

The dark powdered solids have a stick-like morphology with sizes ranging from 1 µm to a few 100 µm, that seem to be aggregates of smaller grains. Dark grains are more porous and fluffy than brown films (Fig. 3.8).

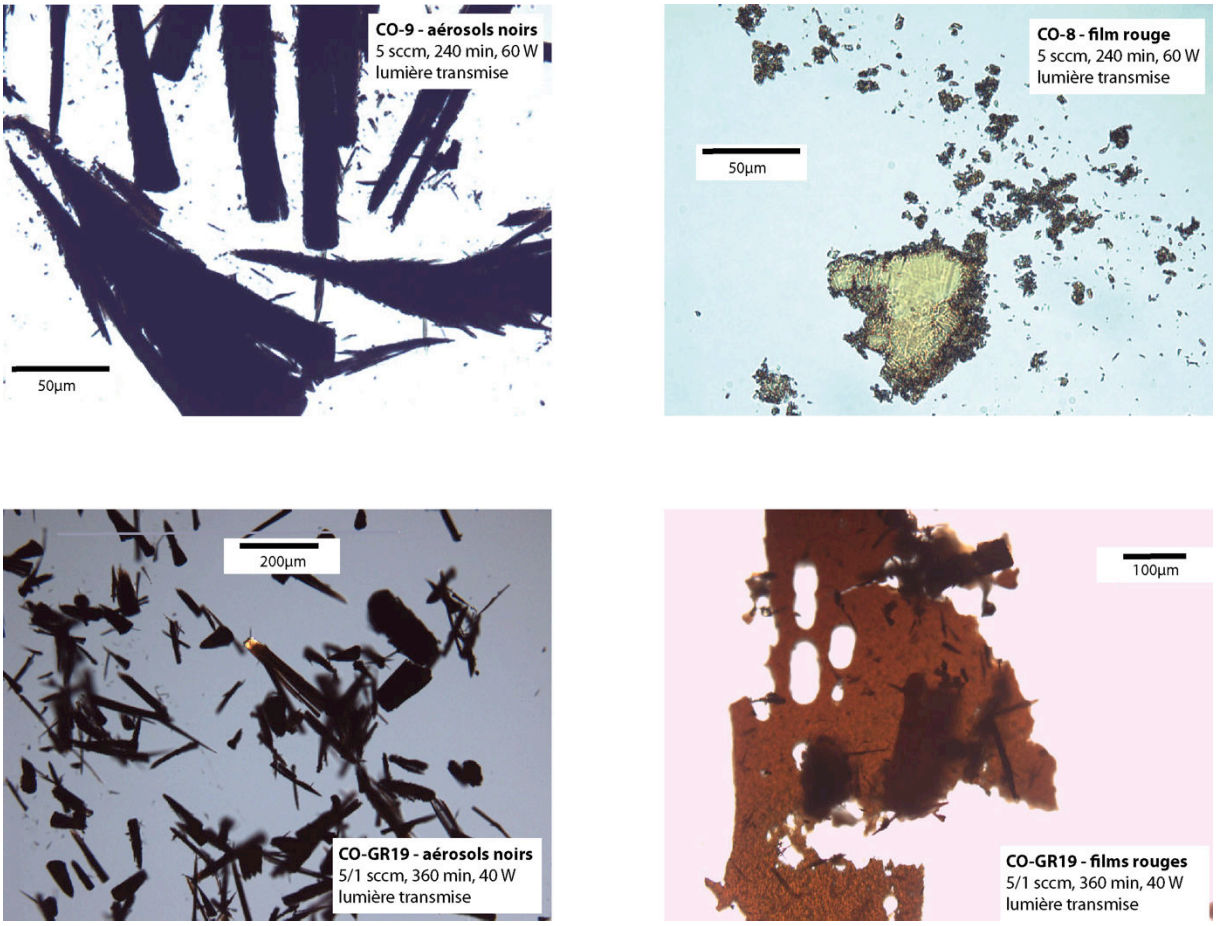

Figure 3.8: Microscopy images of dark and red-brown grains from the Nebulotron discharge. Scale bars are shown on the pictures.

3.2.1.2 SEM observations

A review of dark grain morphologies encountered in Nebulotron synthesized solids is presented in Fig. 3.9.

Dark grain morphologies range from filaments or needles (Fig. 3.9, CO-4, CO-3, CO-GR-19), to small feathers (Fig. 3.9, CO-6, CO-7) or to "ear of corn" shapes (Fig. 3.9, CO-9), of at least 50-100 µm-long. Filament, needle and ear of corn shaped grains seem to be aggregates of smaller features of about 1µm in size (Fig. 3.9, CO-6 or CO-9). The nucleation and growth mechanism of the carbon compounds in the plasma are likely responsible for such an acicular morphology. The presence of the SiO_2 surfaces of the reactor's walls probably enhanced the growth like a catalyst (Guo et al., 2000, Kamo et al., 1983).

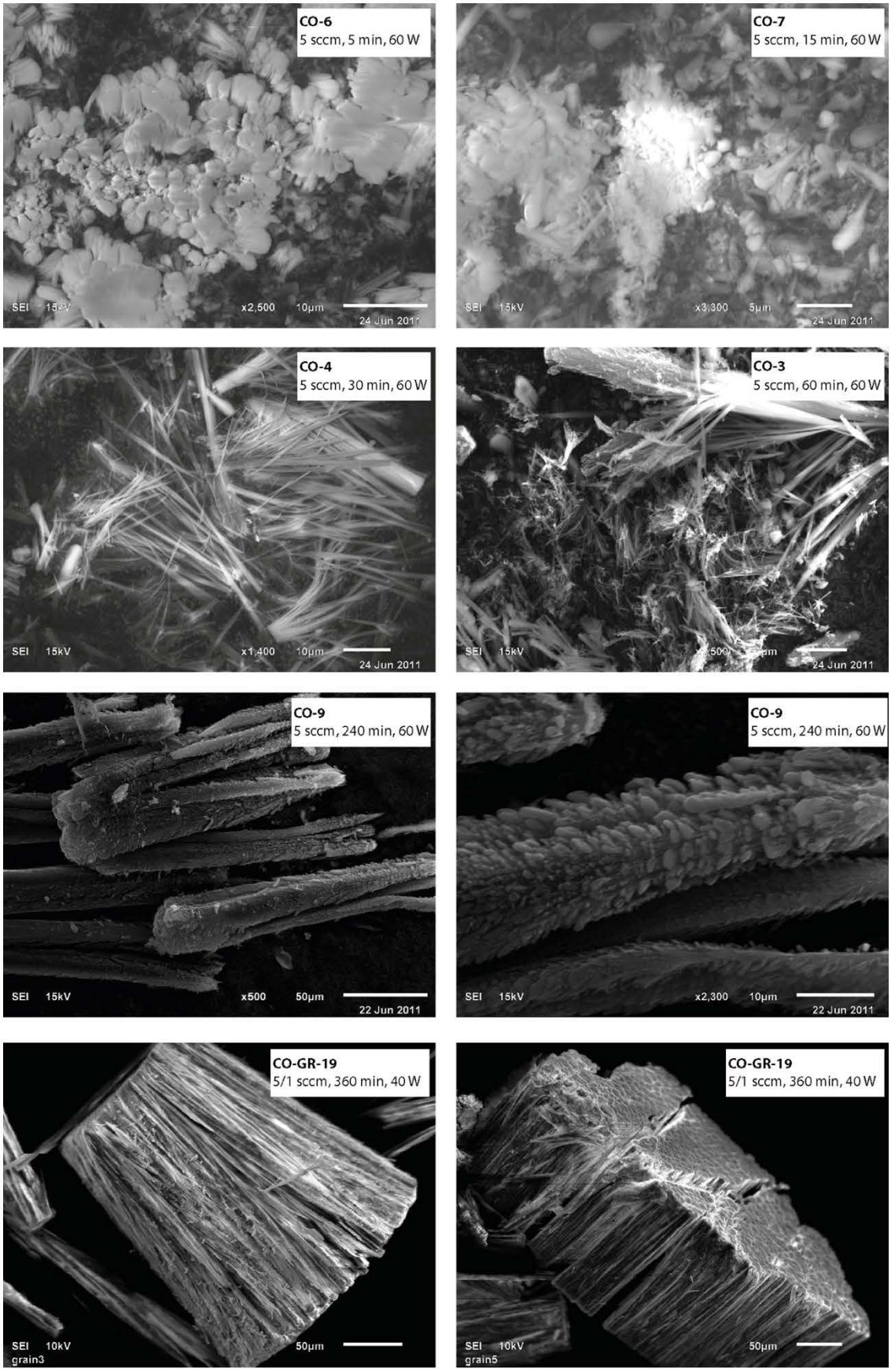

Figure 3.9. Various morphologies of dark grains (SEM pictures).

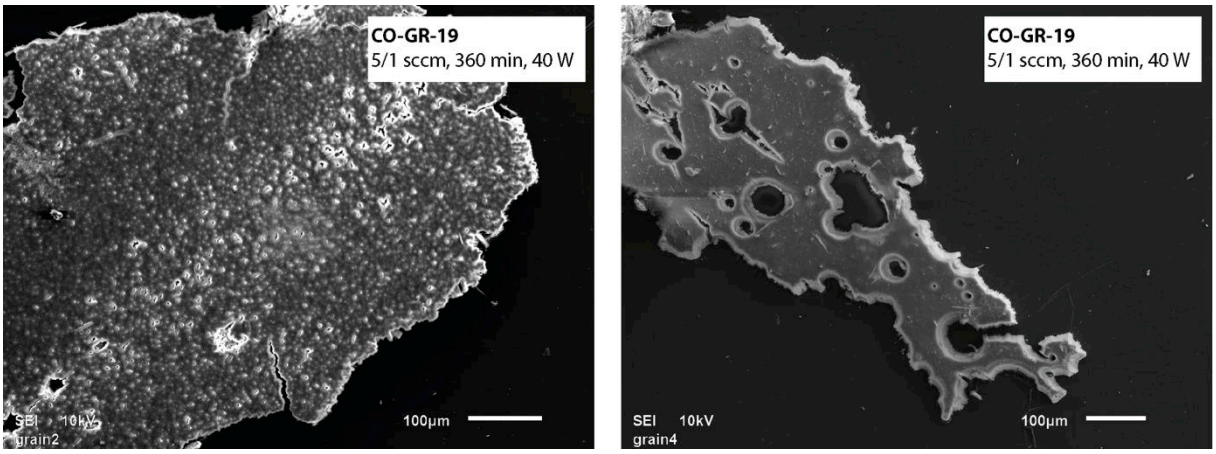

Figure 3.10. SEM pictures of red films synthesized in the Nebulotron.

Red films are compact and exhibit "flat" morphologies (Fig. 3.10), with some grains presenting circular holes, like bubbles. Such features were already described for tungsten surfaces sputtered by low energy He ions (1 - 50 eV) in plasmas (Nishijima et al., 2004). This type of grains was probably formed in high-temperature areas of the discharge, meaning that the air-compressed cooling is less efficient on the edges of the discharge. Such red grains are not present in all experiments and, when they are, they represent less than 15% of the total mass of recovered solids.

3.2.1.3 TEM observations

Four Nebulotron samples (dark grains) were imaged by TEM in bright field imaging mode. Some images are shown in Fig. 3.11. At the nano- to micro-scale, all samples appear to consist of "needle" and "feather" aggregates, confirming the SEM observations. The morphologies and shapes of the dark solids synthesized in the Nebulotron are probably due to a variety of processes, among them their growth on the walls of the quartz tube, playing the role of a substrate, the gas flow lines in the tube, sputtering by incoming ions and the pyrolysis inside the discharge (see 3.2.6 Section).

As a conclusion, grains synthesized in the Nebulotron (with the exception of the red ones) have a needle/feather shape, gathering in 50-200 µm aggregates of features of 1µm or less in size. This shape is likely to be strongly related to the nucleation and growth mechanisms in the plasma setup.

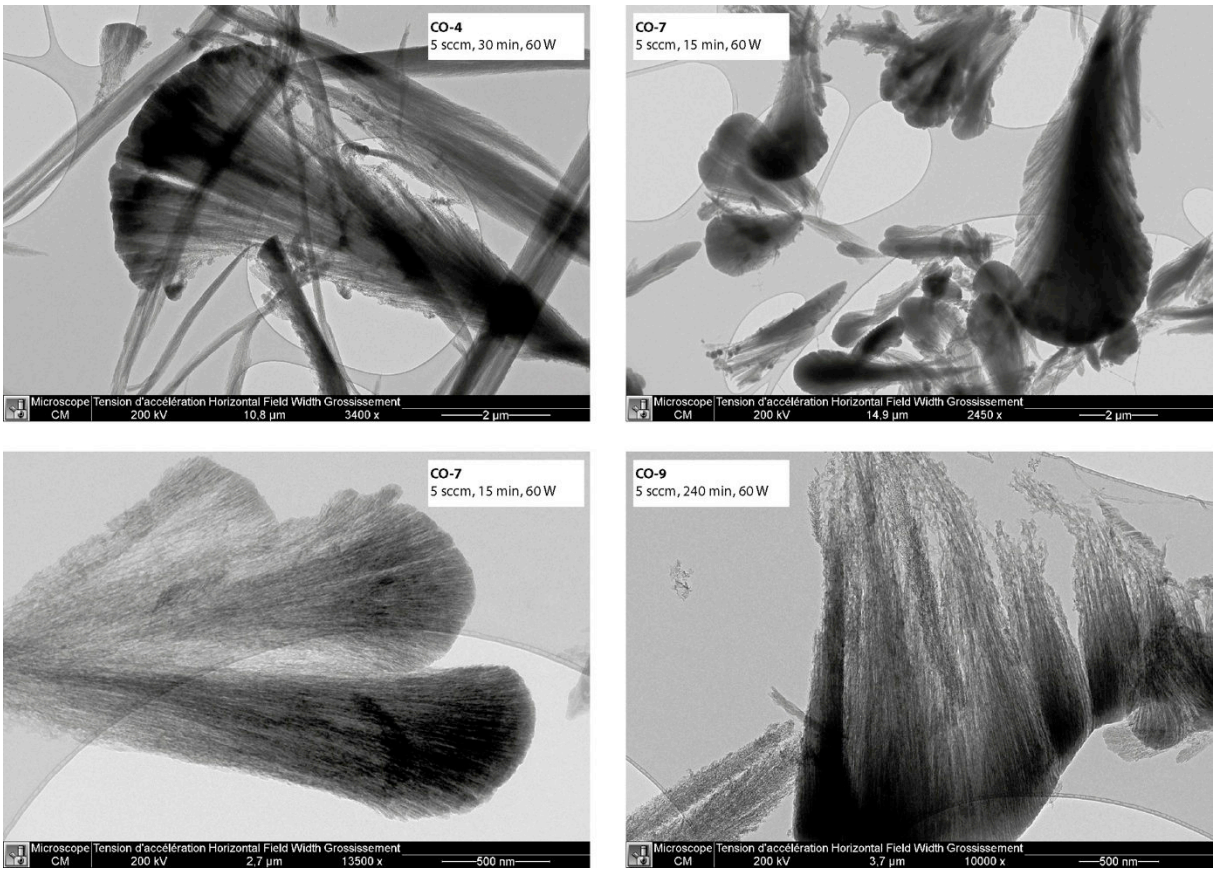

Figure 3.11. TEM pictures of 3 samples synthesized in the Nebulotron. Scale bars are shown on the pictures.

3.2.2 Carbon structural organization of the Nebulotron synthesized organics

3.2.2.1 Carbon microtexture with TEM imaging

In this part, TEM imaging and electron diffraction have been used to characterize the micro/nanostructure and texture of the carbon composing the Nebulotron samples. These observations show that the Nebulotron samples can be heterogeneous at the microscale, as they display several carbon textures (Fig. 3.12).

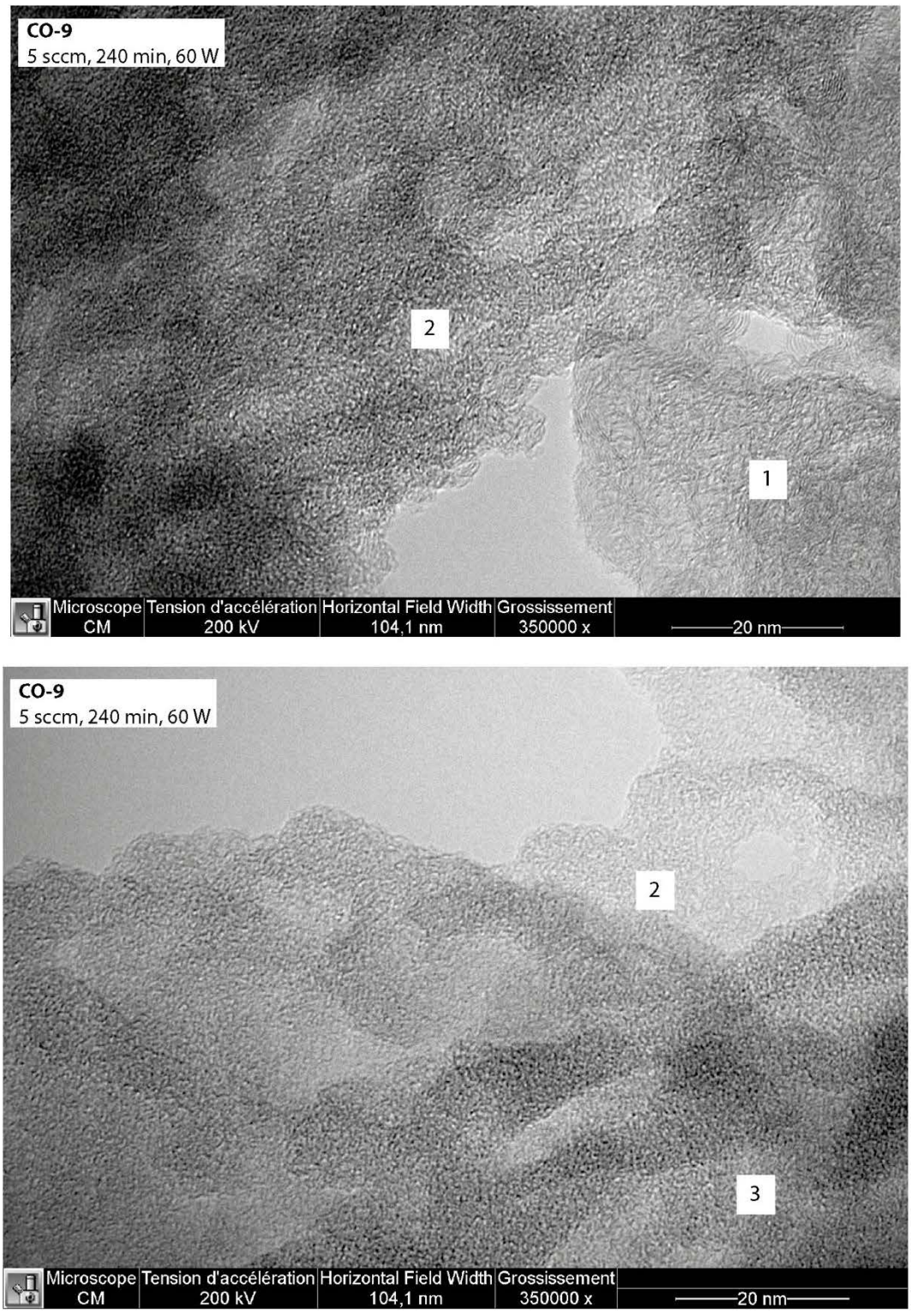

Figure 3.12. TEM pictures of Nebulotron samples with 3 identified carbon microtextures: (1) microporous, (2) concentric and (3) amorphous.

Three main carbon textures were identified: microporous (area 1), microporous with concentric tendency (area 2) and amorphous (area 3) textures.

- Microporous carbon (Fig. 3.13)

The first carbon texture encountered in the Nebulotron samples is a combination of microporous and "crumpled paper" textures (Moreno, 2006). This texture is characterized by the presence of localized coherent domains, displaying stacks of graphene layers (10 maximum), well distinguishable in the magnified area of Fig. 3.13. These graphene layers are quite short (~ 5 nm long), discontinuous and often twisted. These graphene domains surround pores of variable diameters (2 – 15 nm) and wall thicknesses (2 – 10 graphene layers).

The diffraction pattern confirms the turbostratic structure of the carbon, as the 002, 10 and 11 reflection rings are displayed. The 002 ring indicate the presence of graphene layer stack; and the 10 and 11 rings show the bi-dimensionality of the structure. The rings are diffuse showing the small diameter of the coherent domains. The rings are also uniform, pointing out that the graphene layers grew isotropically.

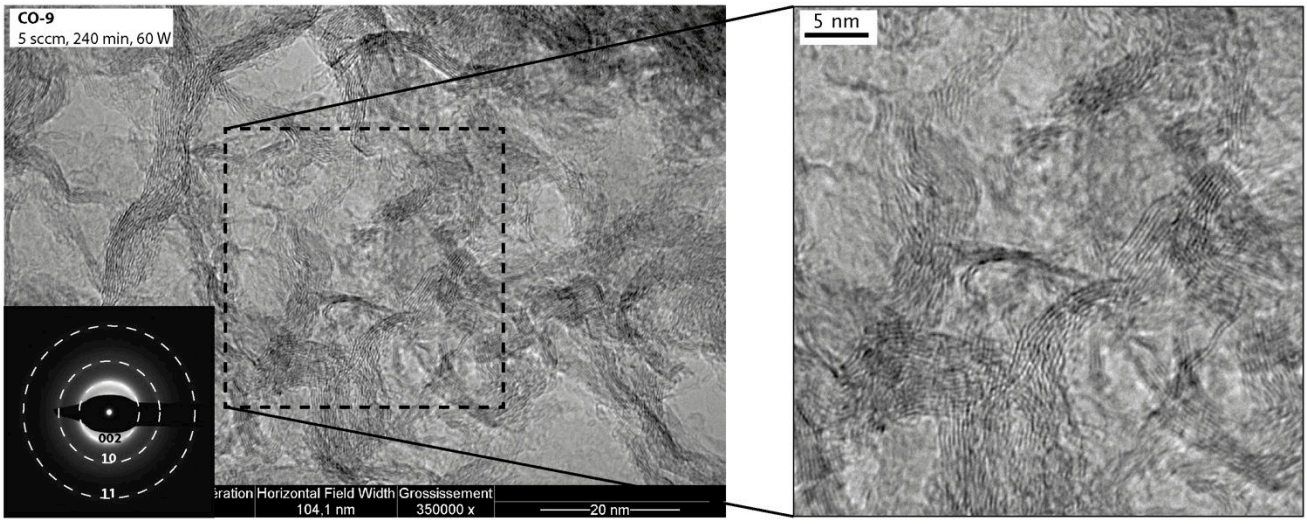

Figure 3.13. TEM picture with a diffraction pattern of Nebulotron sample CO-9.

- Microporous with concentric tendency (Fig. 3.14)

The second carbon texture found in the Nebulotron samples presents weaker nanostructures than the first one, displaying even shorter and more discontinuous graphene layers. It seems that concentric nanostructures are present (shown by the red arrows), forming aggregates of diameter from 5 to 10 nm. Pores are also present, but are smaller than in the first carbon texture (double red arrows).

This texture is typical of carbon blacks and soot nanoparticles (Moreno, 2006, Rouzaud and Clinard, 2002); although in the Nebulotron samples the concentric microtexture seems less developed.

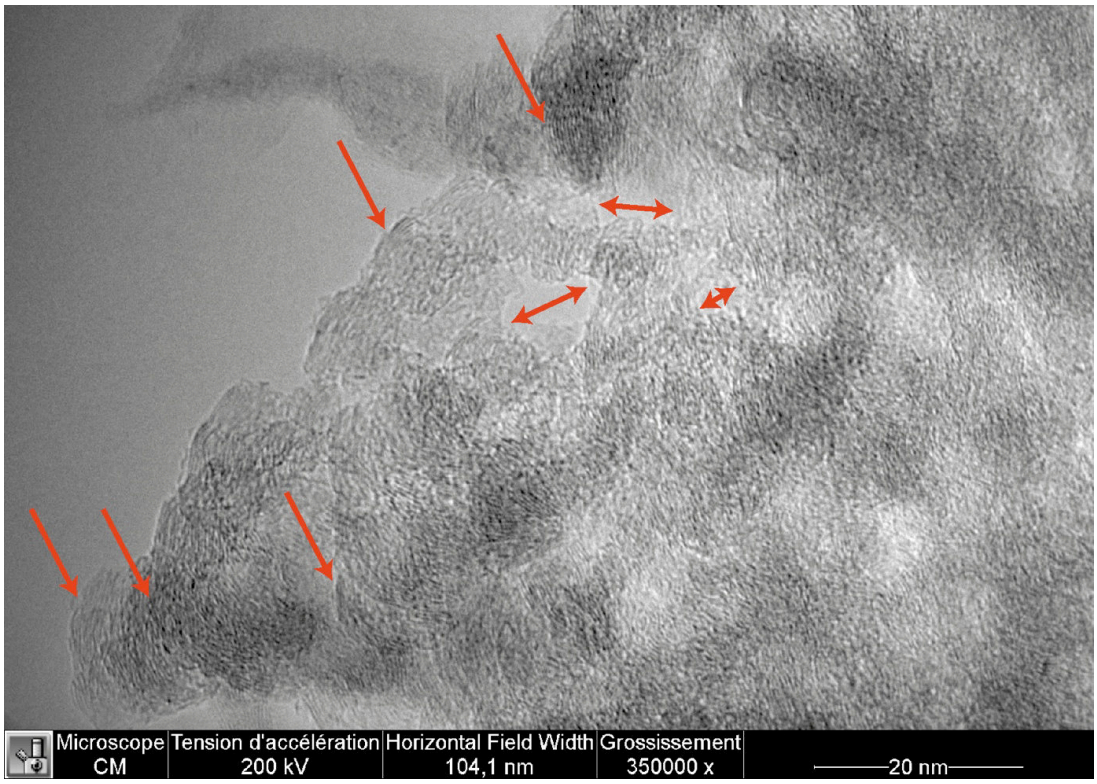

Figure 3.14. TEM picture showing a concentric carbon microtexture observed in Nebulotron sample CO-Ar-1.

- Amorphous carbon (Fig. 3.15)

Fig. 3.15 displays a carbon texture without any visible arrangement of graphene layers. The diffraction pattern is diffuse, without distinguishable rings. This is typical of amorphous carbon.

This carbon amorphous microtexture, along with the concentric microporous texture, and all the intermediates between the two, are the most commonly encountered textures in the four Nebulotron samples that were imaged with TEM.

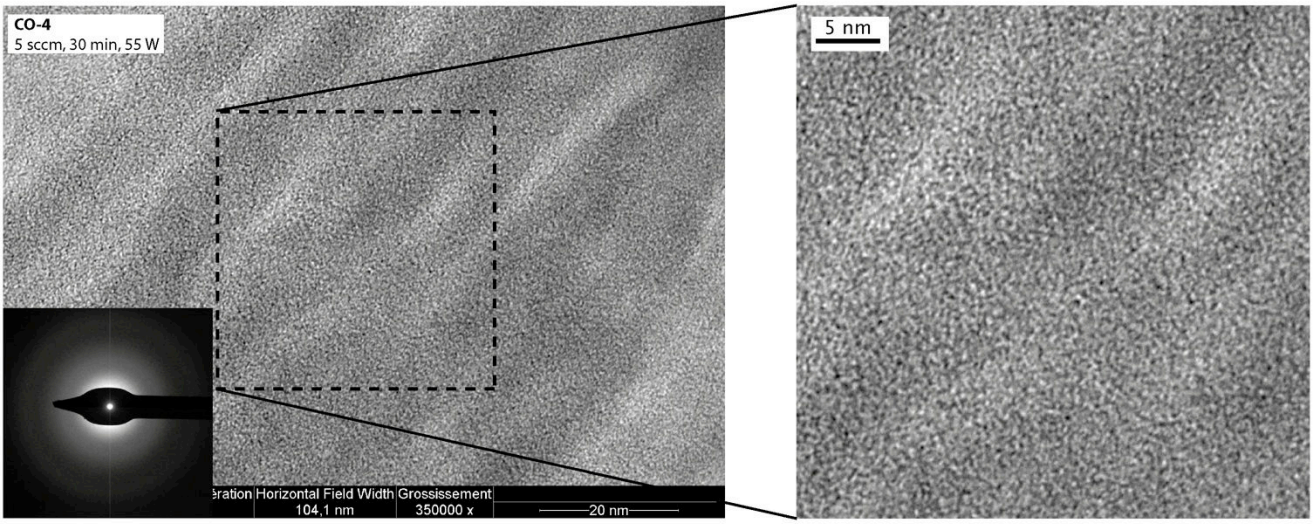

Figure 3.15. TEM picture and diffraction pattern of amorphous carbon - Nebulotron sample CO-4.

3.2.2.2 Carbon structure inferred by Raman microspectroscopy

Raman spectroscopy has been used to compare the Nebulotron samples among themselves in terms of Raman peak parameters (retrieving information on the carbon skeleton nature and structure).

- 514 nm measurements

The most representative Raman spectra that were obtained at 514 nm are displayed in Fig. 3.16, illustrating the variability of the Raman spectra and thus of the carbon structure.

First of all, the primarily observation from Fig. 3.16 points out:

- The occurrence of both the D and G peaks in the Nebulotron samples;
- the low degree of carbon structural organization, as the D and G bands are large (~ 200 cm^{-1} and 95 cm^{-1} respectively, with the exception of CO-9-a and CO-12 spectra, Busemann et al., 2007);
- the heterogeneity of some samples – CO-9 in this case, which displays 3 very different spectra (a, b and c), with variable FWHM of the D and the G peaks and variable I_D/I_G ratios.
- the variability among samples, shown by the relative peak intensities ratio and FWHMs of the D and G peaks.

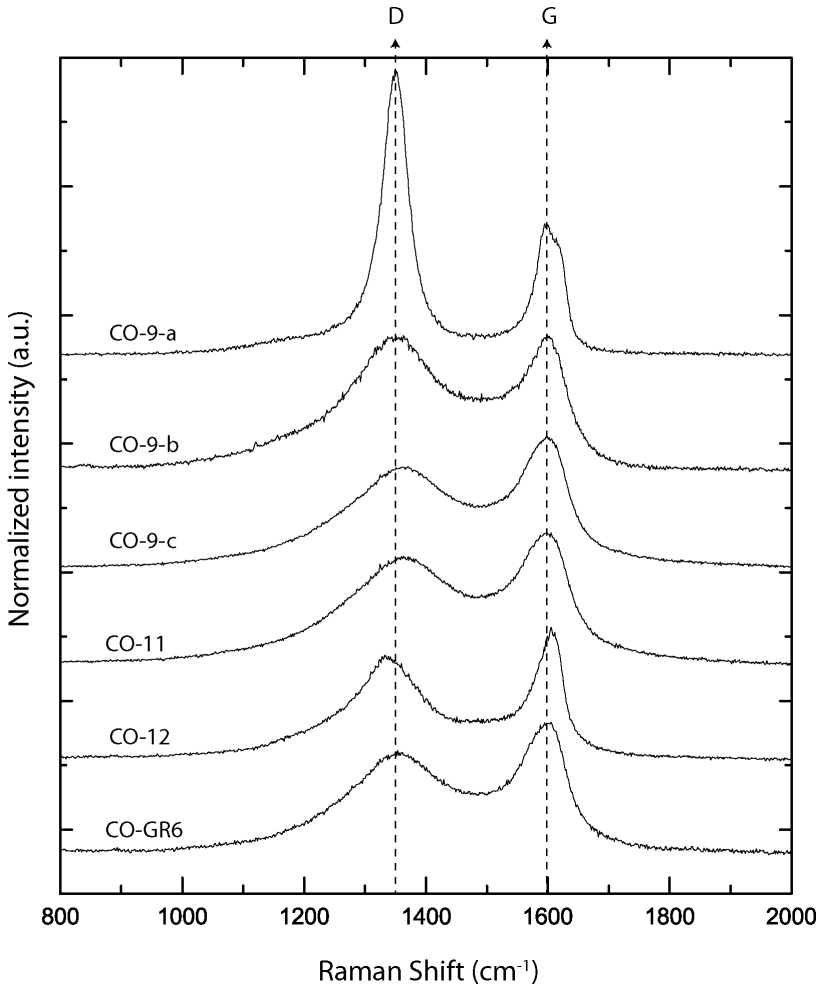

Figure 3.16. Representative Raman spectra of the Nebulotron samples analyzed at 514 nm. The baseline is subtracted and the intensity is normalized to the intensity of the G peak. The D and the G peak are materialized by the dote lines.

The fitting and the extraction of the Raman parameters (peak position, intensity and I_D/I_G ratio) of these spectra allow the quantification of these differences (Table 3.2 and Fig. 3.17).

	ω_G (cm^{-1})	FWHM-G (cm^{-1})	ω_D (cm^{-1})	FWHM-D (cm^{-1})	I_D/I_G
2-band model (LBWF)					
CO-9-903	1597.7	90.2	1349.4	191.5	1.02
CO9-900	1596.0	91.7	1358.7	215.1	0.80
CO-11-893	1595.8	105.4	1362.8	220.7	0.78
CO-11-895	1599.3	98.9	1356.9	196.3	0.75
CO11-891	1597.2	98.6	1361.0	225.9	0.85
CO12-884	1605.5	59.7	1337.0	139.9	0.75
COGR6-910	1597.4	88.2	1352.0	197.4	0.76
COGR6-909	1597.8	91.9	1354.5	202.1	0.75
5-band model					
CO9-901	1596.2	37.2	1349.7	49.8	2.46
CO12-884	1600.0	56.1	1341.5	118.1	0.89
average CO-11 spectra					
average	1597.4	101.0	1360.2	214.3	0.79
±	1.8	3.8	3.0	15.8	0.05

Table 3.2. Raman parameters extracted from curve fitting of Nebulotron samples. 2-band and 5-band models results are given, along with the average calculation of these parameters for the sample CO-11 (3 spectra).

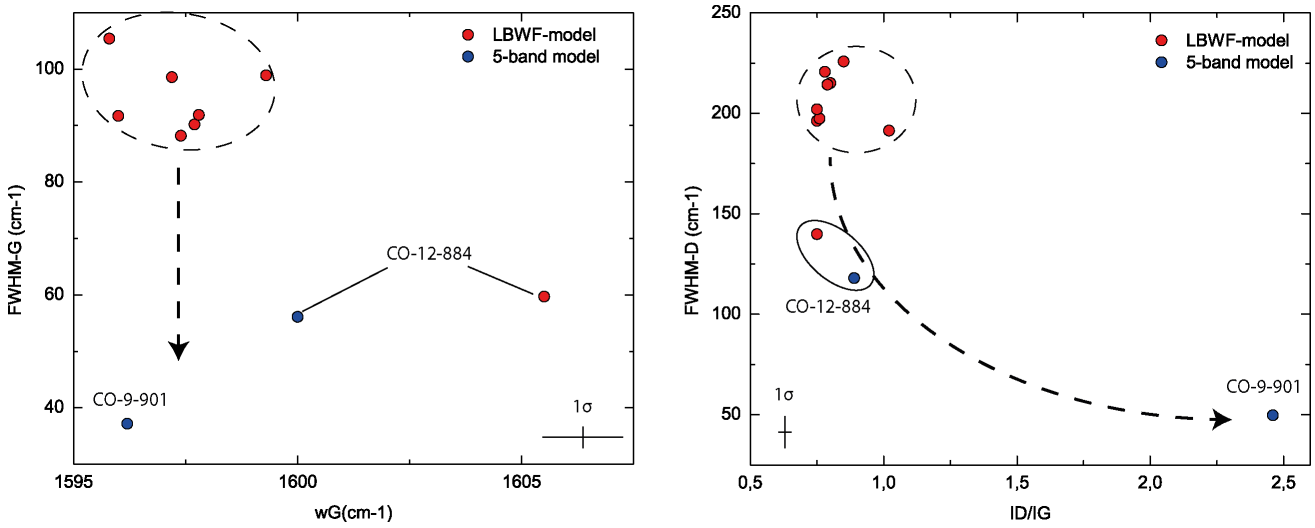

Figure 3.17. Raman parameters determined from the 2-band and 5-band fits. Left: FWHM-G vs. ω_G. Right: FWHM-D vs. I_D/I_G. Typical error bar (1σ) is given for each plot. CO-9-901 and CO-12-884 spectra plot outside the sample domain, probably because they have experienced higher temperatures. The arrows illustrate the growth of graphitic domains, with an increase of the I_D/I_G ratio and a decrease of the FWHM of the G and the D bands (Ferrari and Robertson, 2000, Busemann et al., 2007).

Nebulotron samples show relatively homogeneous Raman parameters, with the exception of the CO-9-901 (CO-9-a in Fig. 3.16) and the CO-12 samples, which display thinner D and G bands with a D band more intense than those of the other Nebulotron samples. These two samples definitely present a less disordered carbon structural organization compared to the other samples. This observation is consistent with TEM images of the CO-9 sample, showing a "crumpled paper" carbon microtexture, with areas presenting graphene layer stacks. This more graphitic structure is probably due to a more intense heating of these grains in the plasma. Indeed, when they are submitted to high temperatures or pressures, the structure of natural carbon compounds evolves towards the establishment of a layered structure until complete crystallization of graphite. The structure of carbon compounds might be a good indicator of thermal evolution under certain conditions and has been used as such to determine the maximum temperature seen by natural terrestrial carbon compounds such as kerogen (Lahfid et al., 2010) or by the organic macromolecule in meteorites (Bonal et al., 2006, Bonal et al., 2007, Busemann et al., 2007; Fig. 3.18).

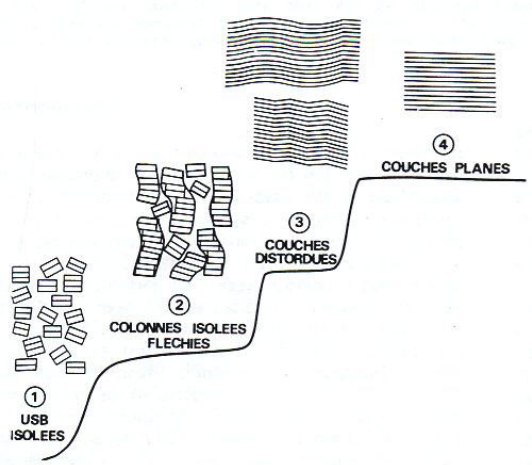

Figure 3.18: Progressive organization of carbon microtexture during heating treatment. When temperature rises, the BSU organization evolves toward a layered structure with less and less distortions. From Oberlin et al. 1984.

However, the thermal evolution of such natural materials occurs on timescales that are irrelevant for laboratory studies (10^6 years or more vs. several hours/days), in which the evolution kinetics might be rather different. The empirical thermometers based on Raman parameters in chondritic organics or in terrestrial kerogens are thus not very well adapted to decipher the maximum temperature experienced by the Nebulotron samples (Busemann et al., 2007, Bonal et al., 2007, Lahfid et al., 2010).

The dispersion of the G band position with incident beam light frequency has been used as an indicator of the annealing temperature of hydrogenated amorphous carbon films

(ta-C:H films) produced by plasma techniques (Ferrari and Robertson, 2001). Nebulotron samples from CO gas only may have a relatively close chemical composition as ta-C:H films except for the present of heteroatoms such as oxygen, which is absent from ta-C:H films. Although the dispersion of the G band position likely depends on the chemical composition of the precursor, notably on the presence of heteroatoms, it is the best temperature indicator found so far to apply to the Nebulotron samples. I have applied this tool on the present samples, taking into account the G band position at 514 nm and 244 nm. This results in an annealing temperature of ~ 500 °C for the more disordered Nebulotron samples and > 700 °C for the more ordered samples (CO-9; Fig. 3.19). Despite the fact that this indicator may not be strictly applied to the Nebulotron samples, it yields annealing temperatures that are reasonably consistent with the estimation of the neutral species temperature in the Nebulotron plasma (500 – 1000 °C, see Chapter 2).

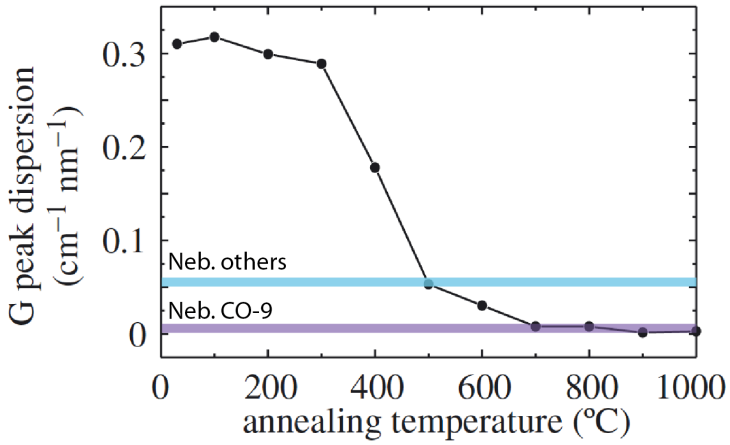

Figure 3.19: Empirical law between the G peak dispersion between 244 and 514 nm and the annealing temperature of hydrogenated amorphous tetrahedral carbons (ta-C:H, adapted from Ferrari and Robertson, 2001) along with the G peak dispersion between 244 and 514 nm for the Nebulotron samples.

In conclusion, all Nebulotron samples are relatively homogeneous in terms of Raman spectral parameters, with the exception of the CO-9 and CO-12 samples. The annealing temperatures determined from these Raman data are inferred to be ~ 500 °C and > 700 °C for the CO-9-901 and CO-12-884 samples, respectively. These results, along with the TEM imaging of the carbon microtextures, illustrate and further confirm that **the Nebulotron setup produces carbon materials at relatively high temperatures**. It also shows that the temperatures were not homogeneous inside the discharge, resulting in carbon structure heterogeneity.

- 244 nm measurements

Representative UV Raman spectra obtained on the Nebulotron samples and on tholins samples from the PAMPRE experiment are shown in Fig. 3.20. These spectra were not curve fitted and are interpreted qualitatively here.

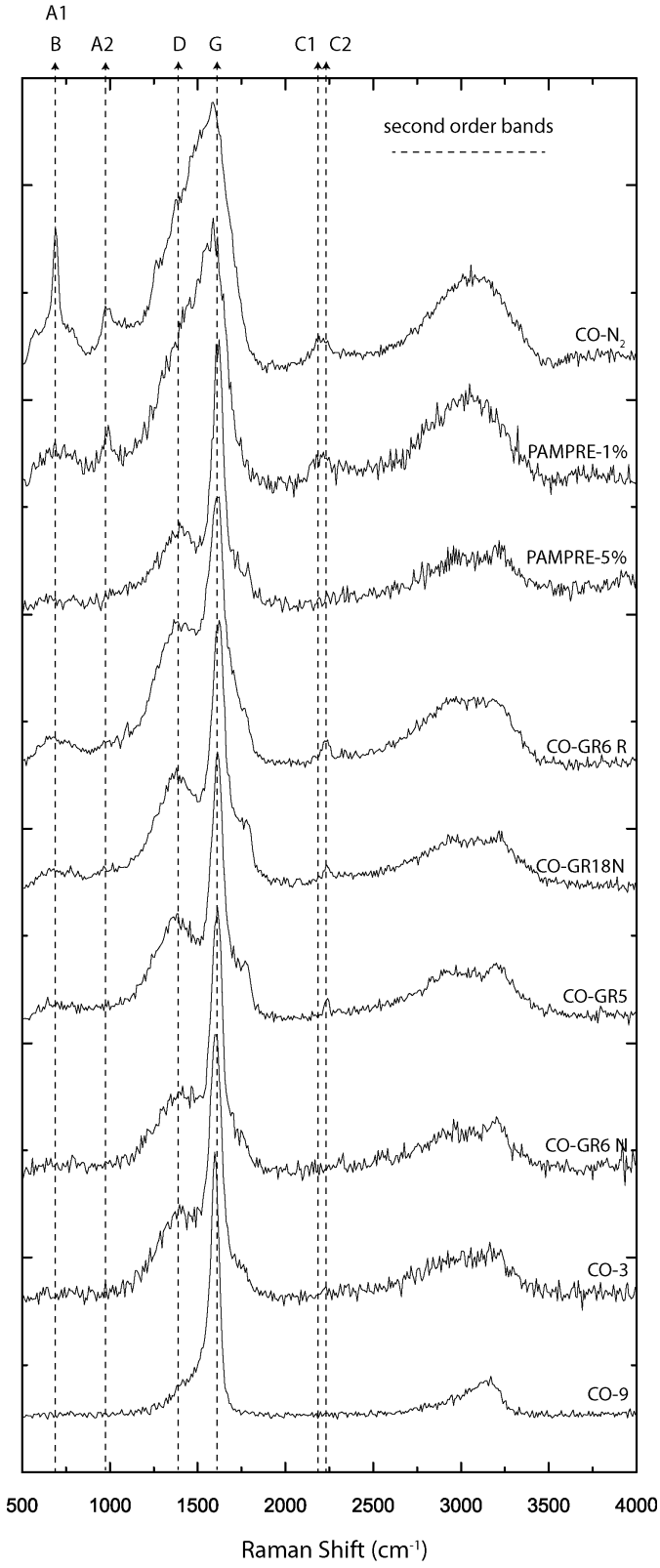

Figure 3.20. Representative UV-Raman spectra of 6 Nebulotron samples and 2 PAMPRE tholins in the 500-4000 cm^{-1} spectral range. Main bands: A1 and A2 [$C_3N_3H_3$, sp^2 carbon]; B [sp^3-bonded N center?]; D; G; C1 [N=C=N, sp^2 carbon] and C2 [–CN, sp^1 carbon] (Quirico et al., 2008, Ferrari et al., 2003).

The qualitative interpretation of these UV-Raman spectra is based on the interpretation of tholins, poly-HCN and carbon nitride UV-Raman spectra (Quirico et al., 2008, Ferrari et al., 2003, Bonnet, 2012).

In the first-order spectral range, UV-Raman spectra of Nebulotron and tholins samples point out:

- that UV Raman spectra are devoid of fluorescence and exhibit in the first order spectral range an intense and narrow G peak, whereas the D peak is weaker and appears as a shoulder towards low wavenumbers. A shoulder on the G peak towards higher wavenumbers is also present in most Nebulotron samples;
- a variability in the carbon structural organization of the different Nebulotron samples, shown by the different D and G peaks shapes and intensities;
- that the CO-9 sample displays a very different spectrum relative to the others, the D band being almost absent and the G band being very thin;
- the presence of resonant features: CO-GR5, CO-GR18N and CO-GR6R spectra exhibit the broad band B at ~ 680 cm^{-1} and the band C2 at ~ 2235 cm^{-1}, that are weak but nonetheless present. Such bands are related to nitrogen bonded to carbon (Quirico et al., 2008), meaning that those samples contain nitrogen although no N_2 was provided in the initial gas mixture. This is probably due to leaks in the experimental setup. This point will be discussed in the next section.
- that CO-N_2 and PAMPRE-1% (1%CH_4 - 99% N_2 initial gas mixture) spectra are very different from the other ones, displaying notably the A1, A2, C1 and C2 bands, presumably due to triazine rings and nitrile bonds, respectively (Quirico et al., 2008). The A1 band is extremely well developed in the CO-N_2 Nebulotron sample spectrum, similarly to HCN polymer spectrum (Dobrică et al., 2011, Quirico et al., 2008). This suggests that triazine rings are abundant in the chemical structure of this particular sample.

To conclude, nitrogen incorporation into Nebulotron samples can be detected by UV Raman spectroscopy, by identifying some particular bands due to C-N bonds, which are either double, triple or conjugated bonds (thus mostly sp^1 and sp^2 carbon hybridization). In particular, the CO-N_2 Nebulotron samples display typical nitrile and triazine features. This suggests that this sample bears many unsaturated bonds.

Most Raman data presented in this manuscript have been interpreted qualitatively. However, the Raman spectra collected for the Nebulotron samples are high quality data and their fully quantitative treatment and thorough analysis will help to draw a more detailed interpretation of the Nebulotron samples carbon structure.

3.2.3 Elemental analysis (C, H, O and N)

The C, H, N and O contents of the Nebulotron samples were analyzed when a sufficient amount was available (~ 6 mg). Weight %, atomic % and atomic ratios are given in Table 3.3 and in Figs. 3.21 and 3.22.

3.2.3.1 Atomic % and ratios

The most striking observation is the presence of H in large quantities (> 20 at. %) in the Nebulotron samples, as well as N (0.3 < at. % < 8) in samples produced from a gas mixture without N_2. Samples were not heated before elemental analysis, thus part of the H content measured in the Nebulotron samples may come from water adsorption. This also suggests the presence of uncontrolled sources of N_2 and H_2O, most likely coming from air leaks in the setup for the N source or from H_2O desorption from the walls of the reactor for the H source, confirming the previous UV Raman results (Fig.3.20). This point is discussed in the next section. Nonetheless, one can note that with the new reactor (italic values in Table 3.3), the H and N contents are greatly reduced compared to the old reactor; suggesting a much better control on the H_2O and N_2 contaminations in the new experimental setup.

The elemental composition (atomic ratios) is shown in Fig. 3.21 as a function of the type of the initial gas mixture (CO only, CO+Noble gases "CO-GR" and CO+N_2 (+ Noble Gases) "CO-N2"). The following tendencies are observed:

H vs. C: The H content varies inversely relative to the C content (Fig. 3.21.a). The samples having the largest C content (~ 60 at. % or more) and the least H content (<25 at. %) have been produced with a higher energy delivery. Such high C and low H contents are then consistent with **pyrolysis or carbonization** in the Nebulotron due to high temperatures induced by the high power density in the reactor (blue arrow). Indeed, pyrolysis will results in the loss of H (and O and N as well) and will tend to concentrate elemental carbon in the residual solid (Bonnet, 2012, Uzun et al., 2007). On the other hand, the CO-GR samples have higher H contents associated with lower C contents. Unless, the noble gas tank has H_2 or H_2O impurities (not known), this tendency might be due to the high **sputtering** power of the noble gases, (Choi et al., 1993, Stuart and Wehner, 1962) which could result in more H_2O degassing from the reactor walls than in runs with a CO-only gas mixture (red arrow). Adding N_2 to the initial gas mixture results in lower H and C contents, likely due to the incorporation of N both in the skeleton instead of C and in terminal functional groups instead of H (green arrow).

O vs. C: The O content follows the same tendency as H as a function of the C content (Fig. 3.21.b). Pyrolysis, due to high temperatures in the plasma, will result in an O loss and a relative gain in C (blue arrow). Adding noble gases to the initial gas mixture results in a slight increase of the O content, likely due to sputtering of H_2O from the reactor walls. Then oxygen in the Nebulotron samples may come from the initial CO gas and also from H_2O desorption in the reactor. The O content is even more increased when N_2 is added to the initial mixture, associated to a C content decrease. This might be due, again, to the fact that N takes the C place in the organic skeleton. This also suggests that N might be linked to O.

N vs. C: The N content is variable in CO-only and CO-GR samples, from 0.3 to 8 at. %; the higher values likely due to leaks in the setup and the lower values to low efficiency of primary pumping (Fig. 3.21.c). When N_2 is added to the initial gas mixture, the N content

largely increases, up to 22 at.% (note: the pool at N=17 at.% was produced with a CO-N_2-NG mixture, containing 50% less N2 than in the CO-N_2 mixture).

O vs. H: The O content increases as the H content increases in 1:1 to 1:2 proportions (Fig. 3.21.d). This clearly confirms the role of H_2O in the O and H incorporation into the Nebulotron samples, or adsorbed water For the CO-only and the CO-GR samples, pyrolysis/sputtering tendencies can be seen again.

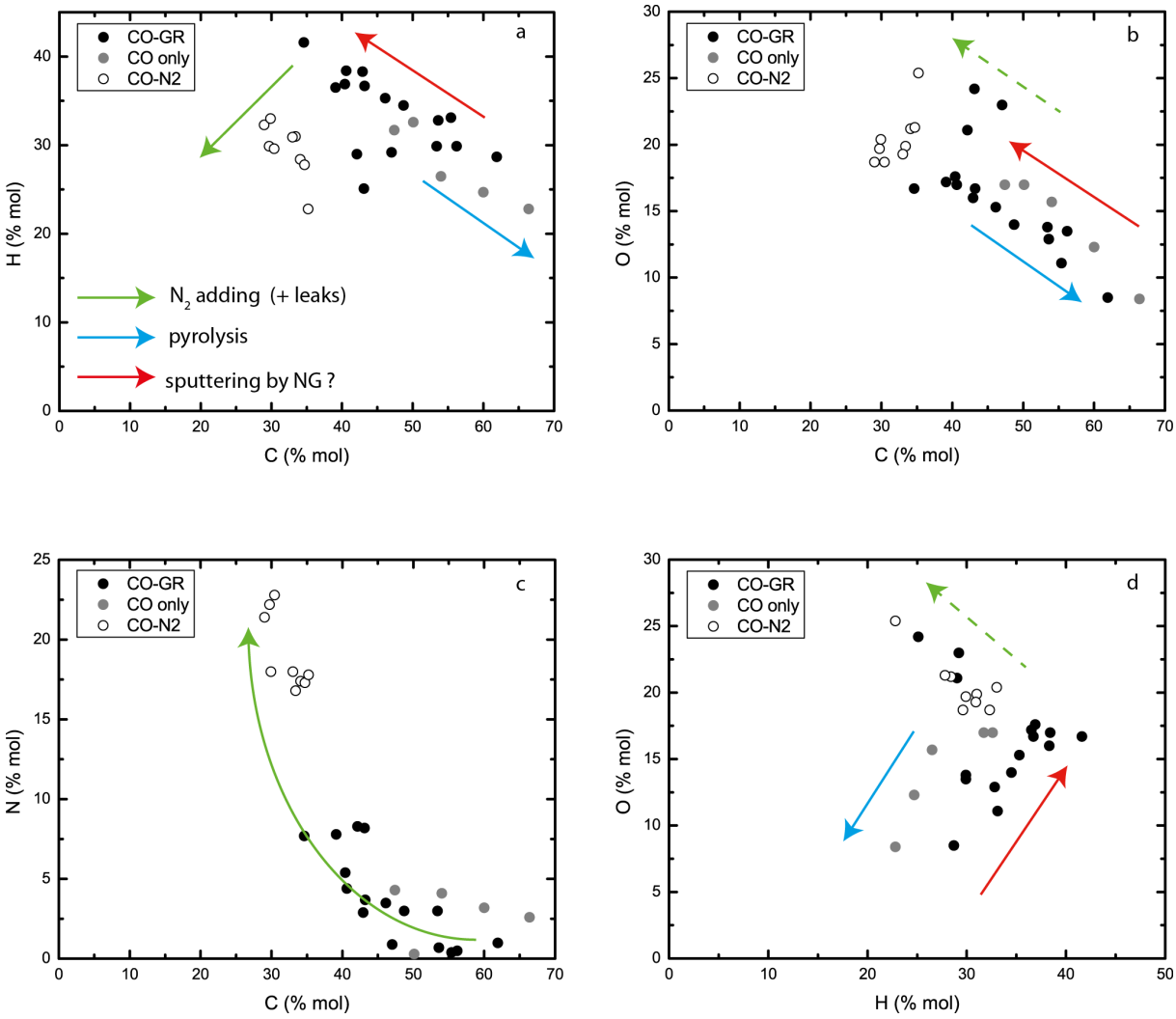

Figure 3.21. Elemental composition (in at. % of C, H, O and N) of Nebulotron samples. (a) H vs. C, (b) O vs. C, (c) N vs. C and (d) O vs. H. The arrows illustrate the evolution of the elemental composition with pyrolysis in the plasma (blue), the N_2 addition in the initial gas mixture (green) and the noble gas addition in the initial gas mixture (red), probably favoring surface sputtering.

Table 3.3: Elemental composition of Nebulotron samples

		C (wt%)	H (wt%)	N (wt%)	O (wt%)[†]	C (% mol)	H (% mol)	N (% mol)	O (% mol)	N/C	H/C	O/C
initial gas mixture : CO and Noble Gas mix (He, Ne, Ar, Kr and Xe)												
CO-GR3		60.5	4.5	4.9	30.2	42.9	38.3	2.9	16.0	0.07	0.89	0.37
CO-GR5		50.0	5.0	12.9	32.1	34.6	41.6	7.7	16.7	0.22	1.20	0.48
CO-GR6N		66.0	3.9	4.7	21.6	49.7	35.2	3.0	12.2	0.06	0.71	0.25
CO-GR8N		55.1	4.2	8.7	32.0	40.4	36.9	5.4	17.6	0.13	0.91	0.44
CO-GR9		68.6	3.2	4.5	20.0	54.6	30.6	3.1	11.9	0.06	0.56	0.22
CO-GR10N		56.8	4.5	7.2	31.6	40.6	38.4	4.4	17.0	0.11	0.95	0.42
CO-GR11N		62.7	4.0	5.5	27.8	46.1	35.3	3.5	15.3	0.08	0.77	0.33
CO-GR13		59.3	4.2	6.0	30.5	43.2	36.7	3.7	16.7	0.09	0.85	0.39
CO-GR16N		52.7	4.1	12.2	31.0	39.1	36.5	7.8	17.2	0.20	0.93	0.44
COGR18		49.5	2.8	11.4	33.2	42.1	29.0	8.3	21.1	0.20	0.69	0.50
CO-GR18N		49.5	2.4	11.0	37.1	43.1	25.1	8.2	24.2	0.19	0.58	0.56
CO-GR19N		58.0	3.0	1.3	35.6	47.8	29.7	0.9	21.7	0.02	0.62	0.45
COGR29		70.1	3.6	1.1	22.4	53.6	32.8	0.7	12.9	0.01	0.61	0.24
COGR30		78.2	3.0	1.4	14.3	61.9	28.7	1.0	8.5	0.02	0.46	0.14
COGR31		70.8	3.1	0.7	22.7	56.2	29.9	0.5	13.5	0.01	0.53	0.24
COGR32		73.8	3.7	0.6	19.8	55.4	33.1	0.4	11.1	0.01	0.60	0.20
initial gas mixture : CO only												
CO-3		61.0	3.4	6.4	29.2	47.4	31.7	4.3	17.0	0.09	0.67	0.36
CO-9		80.5	2.3	3.7	9.0	68.3	23.4	2.7	5.7	0.04	0.34	0.08
CO-11		65.9	2.7	5.8	23.4	54.7	26.9	4.1	14.5	0.08	0.49	0.27
CO-12		73.0	2.5	4.5	20.0	60.0	24.7	3.2	12.3	0.05	0.41	0.21
CO-28		63.5	3.5	0.5	28.7	50.1	32.6	0.3	17.0	0.01	0.65	0.34
initial gas mixture : CO and N2												
CO-N2 20R		35.5	3.3	30.6	30.6	29.0	32.3	21.4	18.7	0.74	1.12	0.65
CO-N2-20N		35.2	3.0	30.7	32.6	29.4	29.6	22.0	20.4	0.75	1.01	0.69
CO-N2-20B		36.0	2.9	31.5	30.5	30.2	29.4	22.7	19.2	0.75	0.97	0.63
CO-GR21N	with noble gases	40.1	2.8	23.9	33.1	34.2	28.4	17.4	21.1	0.51	0.83	0.62
CO-GR21R	with noble gases	37.0	3.4	26.0	33.6	29.9	33.0	18.0	20.4	0.60	1.10	0.68
COGR34	with noble gases	39.5	3.1	23.1	31.5	33.4	31.0	16.8	19.9	0.50	0.93	0.60
COGR35	with noble gases	40.6	2.7	23.6	33.3	34.7	27.8	17.3	21.3	0.50	0.80	0.62
COGR36	with noble gases	39.4	3.1	25.0	30.7	33.0	30.9	18.0	19.3	0.54	0.94	0.58
COGR37	with noble gases	38.4	2.1	22.7	36.9	35.2	22.8	17.8	25.4	0.51	0.65	0.72

italic: new Nebulotron reactor

When plotting the O/C ratio vs. H/C ratio, a strong O:H correlation is even more visible: the sample data points plot around a 1:2 slope straight line (Fig. 3.22). This confirms the important role of water in controlling the proportions of H and O in the Nebulotron samples. Nonetheless, the scattering around this line suggests that not all the O and H atoms are in adsorbed water onto the Nebulotron sample surfaces. In particular, the CO-N_2 samples plot above this line, showing a higher O/H ratio and suggesting that the speciation of O atoms in these samples might be different. One can note that the H/C ratio increases when noble gases or N_2 are added to CO in the gas mixture. As mentioned above, this is likely due to a higher sputtering rate of water form the reactor surfaces. H/C ranges in 0.3 – 1.2, thus the Nebulotron organics are likely to contain oleifinic or aromatic carbon rather than aliphatic carbon only.

The N/C ratio increases dramatically up to 0.7 when N_2 is added to the mixture, whereas it is less than 0.2 for CO only and CO-GR samples. Again, samples having a N/C ratio ranging from 0.1 to 0.2 are likely to have been contaminated by air in the reactor when they were produced, suggesting the presence of leaks in the setup.

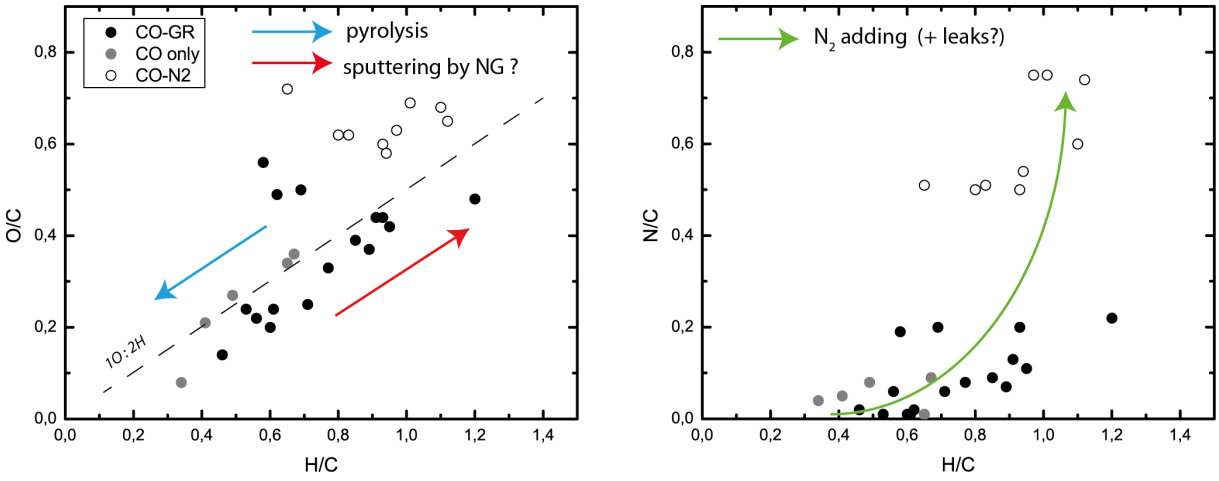

Figure 3.22. Atomic ratios O/C (left) and N/C (right) ratios as a function of H/C ratio for the Nebulotron samples. The arrows illustrate the evolution of the elemental composition with pyrolysis in the plasma (blue), increase of N_2 (green) and of noble gases (red) contents in the gas mixture, probably favoring surface sputtering.

3.2.3.2 Bulk formula and number of unsaturation

I have calculated the bulk formula of the Nebulotron organics knowing the C, H, O and N contents (Table 3.4). Such a representation reveals that the Nebulotron samples are C and H-rich, both accounting for 78 to 85 % of all atoms in CO-only and CO-GR samples; and for 60 % in CO-N_2 samples. In the latters, N is indeed not a minor heteroatom. The (C+N)/total atoms ratio is rather constant (0.5-0.6) for all the Nebulotron samples, either

with or without N_2 in the initial mixture, confirming the C-N balance in the chemical structure of the organics.

The bulk formula, along with the valence of atoms, can be used to calculate the unsaturation number, i.e. the number of double and triple bonds and of cycles. The unsaturation degree U.D. is defined as the difference between the maximum and the minimum number of bonds for a bulk formula with k atoms:

$$U.D. = \left(\sum_k \frac{n_{val\,k}}{2}\right) - (k-1) = n_C - \frac{n_H}{2} + \frac{n_N}{2} + 1$$

where the first member is the maximum number of bonds and the second member is the minimum number of bonds with k atoms. The final result is simply based on the number of C, H and N atoms.

The U.D. for the Nebulotron samples varies from 66 up to 85 for 100 carbon atoms, the latter being found for CO-N_2 samples. Thus, **the Nebulotron samples are composed of extremely unsaturated compounds**. The U.D. for a benzene molecule is 67% and this molecule may be the main structural component responsible for the unsaturation in CO-GR samples in the old reactor. Otherwise, CO-only samples have a U.D. of ~ 80% and CO-N_2 samples of ~ 85%. Such high U.D. may only be explained by the presence of large polycyclic units (up to 5 or more cycles like big PAHs) or by the presence of conjugated C-N or N-heterocycles. Indeed, pyridine (C_5H_5N) has a U.D. of 80% and polycyclic compounds based on pyridine cycles, like triazine, N-bearing PAHs or even nucleic bases have larger U.D. (Demarais et al., 2014) This suggests that **a large fraction of the N is incorporated into cycles in the Nebulotron samples**, in structure based on pyridine cycles. This confirms the interpretation of UV Raman spectra (previous section).

	gas mixture	C	H	N	O	D.U.
ALL SAMPLES (average)	CO-only	100	51	5	25	78
old + new reactor	CO-GR	100	73	8	34	69
	CO-N2	100	93	60	64	85
OLD REACTOR	CO-only	100	48	6	23	80
	CO-GR	100	81	12	40	66
	CO-N2	100	105	71	66	84
NEW REACTOR	CO-GR	100	57	1	25	73
	CO-N2	100	83	51	63	85

Table 3.4. Bulk formulas of Nebulotron organics for 100 carbon atoms depending on the initial gas mixture and on the old vs. new Nebulotron reactor along with the degree of unsaturation D.U.

3.2.4 Chemical functions and speciation: Infrared spectroscopy

3.2.4.1 Main chemical functions

The main organic functional groups identified in the Nebulotron IR spectra are marked in Fig. 3.23 (CO only), Fig. 3.24 (CO-GR) and Fig. 25 (CO-N2) (see Table 3.1 for the vibrational modes attribution).

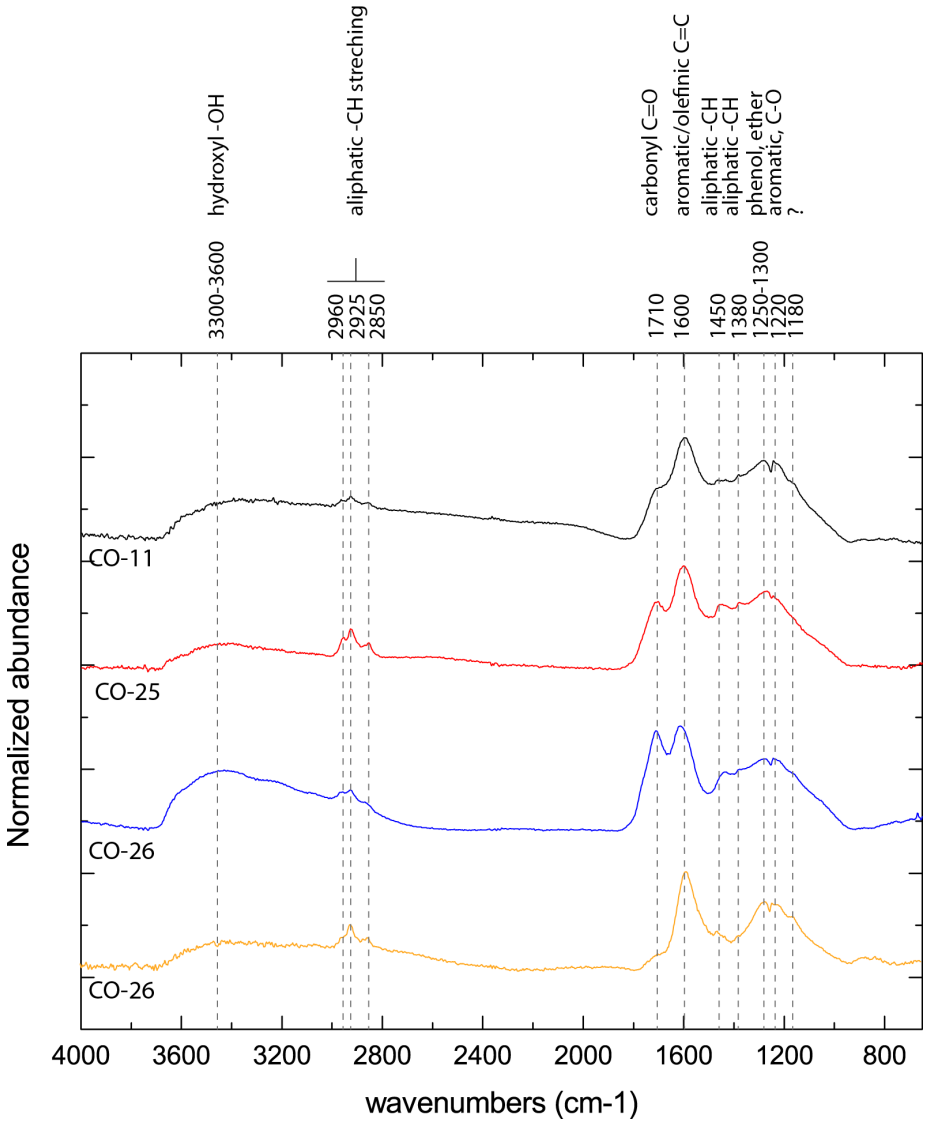

Figure 3.23: IR microspectroscopy spectra (Grenoble measurements) of Nebulotron CO samples (starting gas mixture CO only).

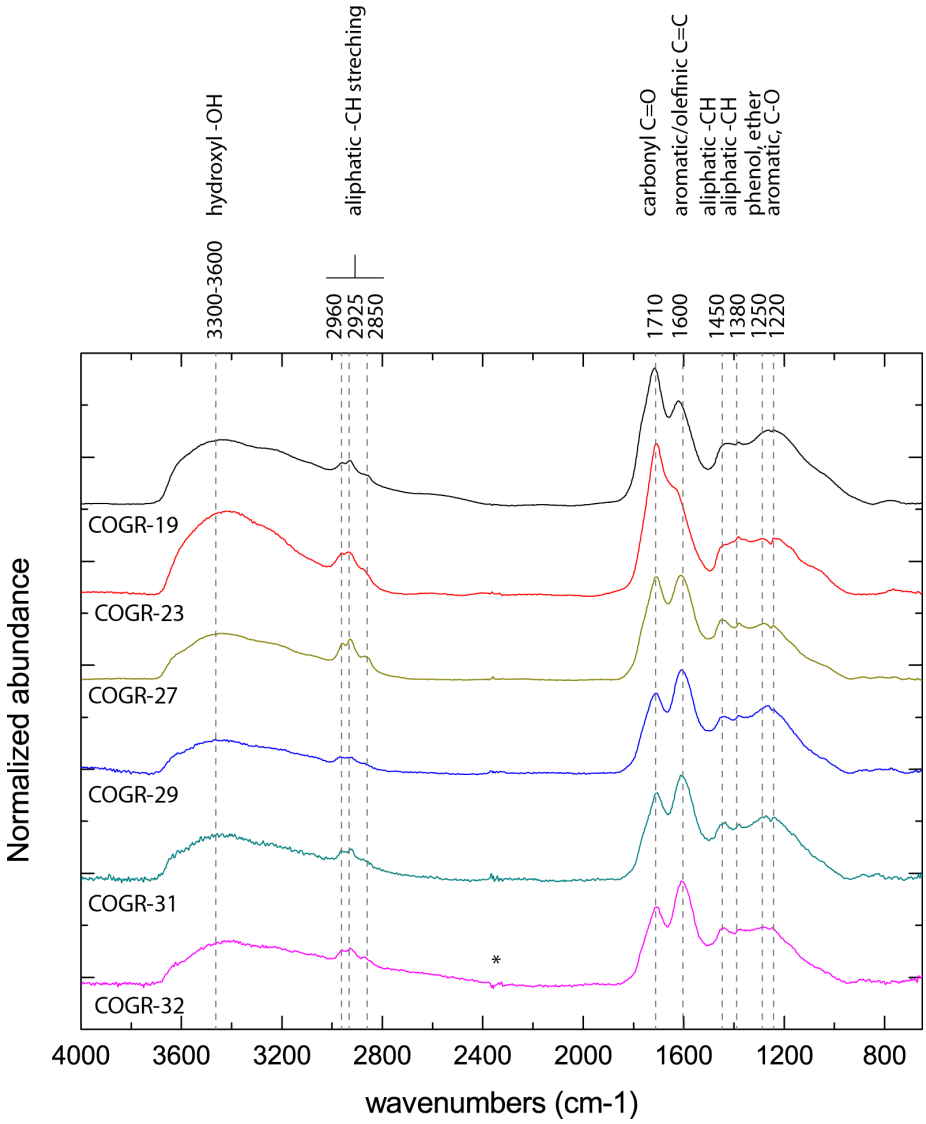

Figure 3.24. IR microspectroscopy spectra (Grenoble measurements) of Nebulotron CO-GR samples (starting gas mixture CO+Noble gases).

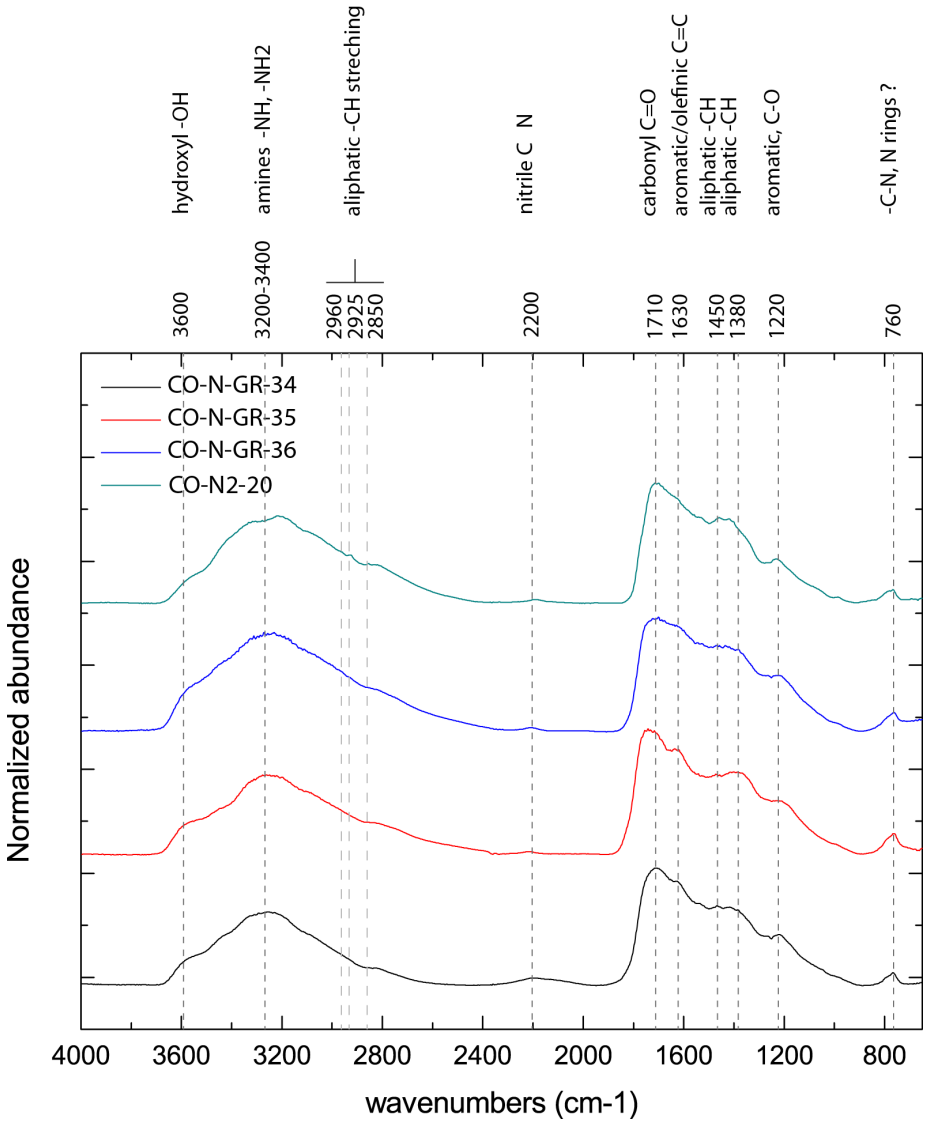

Figure 3.25. IR microspectroscopy spectra (Grenoble measurements) of Nebulotron CO-N-GR samples (starting gas mixture CO+N_2+Noble gases, except for the CO-N_2-20 sample, which was produced with a CO+N_2 gas mixture).

Saturated vs. Unsaturated carbons: both alkane (stretching and bending modes) and alkene/aromatic signatures are found in all the Nebulotron samples, although aliphatic groups are less well seen in the 3000-2800 cm^{-1} region the CO-N-GR samples. Aromatic C=C bonds are identified by the ~ 1600 cm^{-1} band, observed in all the Nebulotron sample spectra. Double-bonded carbons (olefinic C=C) might also be present. According to Dartois et al., 2005, the vibrational mode of olefinic C=C appears at higher wavenumbers than aromatic carbon, i.e. 1640 cm^{-1} rather than 1600 cm^{-1}, respectively. In the CO-N-GR spectra the position of the C=C band is at higher wavenumbers (~ 1620-1630 cm^{-1})(Fig. 3.25), and the bands around 1600 cm^{-1} are less well defined. C=N bonds (imine) are also expected to be in the 1610-1660 cm^{-1} range (Dartois et al., 2005, Bonnet, 2012). As the CO-N-GR samples

contain large amounts of nitrogen, the unsaturated IR region around 1600-1630 cm^{-1} can be due to the presence of both C=C and C=N bonds. According to these IR data, hydrogen atoms present in the Nebulotron solids take part to CH, CH_2 and CH_3 groups. As no CH bonds are present in any of the gases used to produce the Nebulotron solids, it means that water dissociation in the plasma, along with CO, results in the formation of CH radicals that participate in the aerosols' growth. The aliphatic/aromatic ratio cannot be inferred from these IR data, as the spectra were not quantitatively treated. Nonetheless, the calculation of the degree of unsaturation in the Nebulotron samples suggests that the aliphatic/aromatic ratio should be small. Further peak fitting and consequent quantification on the Nebulotron samples spectra will permit the calculation of the degree of ramification of the chemical structure, the total aliphatic/olefinic-aromatic ratio and will give detailed picture of the aliphatic structure (Orthous-daunay, 2011, Orthous-Daunay et al., 2013).

Oxygen-rich groups: As the main starting gas is CO, the solids are O-rich, as attested by the elemental analysis, as well as the IR spectra. The mode position at 1700 cm^{-1} indicates that the terminal C=O group is dominant in all the Nebulotron samples. The ratio C=O/C=C is variable, from >1 to <1 (Figs. 3.23, 24 and 25). This likely originates in the temperature formation of the solids in the plasma, a variable depending on the experimental conditions and on the gas mixture (Quirico et al., 2009, Fridman, 2008). All spectra also exhibit a strong absorption in the 3200-3600 cm^{-1} region, due to OH bonds, either from water adsorption or from acid, alcohol or phenol groups. As pointed out by elemental analysis, water adsorption onto Nebulotron organics surfaces is very likely and might be responsible for this 3400 cm^{-1} large band. Nonetheless, the water OH band at 1635 cm^{-1} is not clearly identified. If present, it might be partly hidden by the intense C=O and C=C bands in the unsaturated region. A phenolic C-O contribution is present in the CO-GR and CO-only spectra at ~ 1250 cm^{-1}, but not in the CO-N-GR and CO-N2 samples. The phenolic groups thus might also contribute to the strong absorption in the 3400 cm^{-1} region. A small contribution of ether C-O bonds to the 1220 cm^{-1} band might be present.

Nitrogen-rich groups: Although some CO-only and CO-GR samples have a non-negligible N content (up to 13 % at.), no N-H or C-N vibration modes are clearly identified in their IR spectra; which are very different from the CO-N-GR and CO-N_2 spectra. In the latters, indeed, both N-H (amine + amide?) and C-N (nitrile) bonds are present in the 3400-3200 cm^{-1} and ~ 2200 cm^{-1} regions respectively. Due to the presence of NH bonds, the band around 3300 cm-1, is much larger and more intense than in the CO-only and CO-GR spectra; partly hiding the OH absorption at ~ 3600-3400 cm^{-1}. The unsaturated region (1800-1550 cm^{-1}) is also very different in the CO-N-GR and CO-N_2 samples compared to the CO-only and CO-GR samples: the signal saturates easily and the bands seem larger or more numerous. This might be due to the presence of NH bending vibration modes in the 1550-1640 cm^{-1} range or to double C=N bonds (imine) also absorbing in this wavenumber region (Dartois et al., 2005). A peak is systematically seen in the Nebulotron N-rich samples at ~ 760 cm^{-1}, in the aliphatic and aromatic bending region. Such an absorption, not observed in tholins for example (Gautier et al., 2012, Quirico et al., 2008), is poorly documented in the literature but might be to a C-N bond in a cycle, maybe specific to an O-rich environment. This could

be confirmed by ^{13}C and ^{15}N solid-state Nuclear Magnetic Resonance measurements on those samples.

Conclusions: IR spectra of the Nebulotron samples demonstrate the presence of both aliphatic and aromatic carbon bonds. Oxygen is mainly bonded to carbon in ketone (C=O) and phenolic (C-OH) groups, as well as bonded to hydrogen in hydroxyl (O-H) groups. Nitrogen-bearing functional groups are identified in CO-N-GR and CO-N_2 samples only. Nitrogen is involved in amine, nitrile and likely in amide and imine groups. IR spectra treatment using typical peak fitting methods in spectral ranges of interest would permit a quantification of the relative abundance of some chemical functions in the Nebulotron samples, such as the C=O/C=C ratio, the aliphatic/aromatic ratio or the CH_3/CH_2 ratio, that were used to describe in details the chemical structure of some chondritic IOMs (Orthous-Daunay et al., 2013). ^{13}C and ^{15}N solid-sate nuclear magnetic resonance measurements would certainly help to better describe the molecular structure of the Nebulotron organics.

3.2.4.2 Thermal degradation test

Three Nebulotron samples (CO-28, CO-GR-29 and CO-N-GR34) were analyzed under vacuum in the environmental cell in Grenoble. Samples CO-28 and CO-GR-29 did not show clear spectral differences between atmospheric pressure and vacuum, nor during their heating at 80°C, 150°C and 300°C, suggesting that the large absorption feature in the range 3200-3600 cm^{-1} is more likely due to tightly bonded OH rather than water adsorption. Sample CO-N-GR34 (Fig. 3.26, black arrow) showed a thinner band at ~ 3300 cm^{-1} under vacuum relative to atmospheric pressure; suggesting H_2O desorption when put under vacuum. Subsequent heating up to 300°C did not produce any evident spectral difference. The thermal degradation tests under vacuum thus resulted in few spectral changes. This confirms that Nebulotron solids were produced at higher temperatures than 300°C and are thus **refractory organics**.

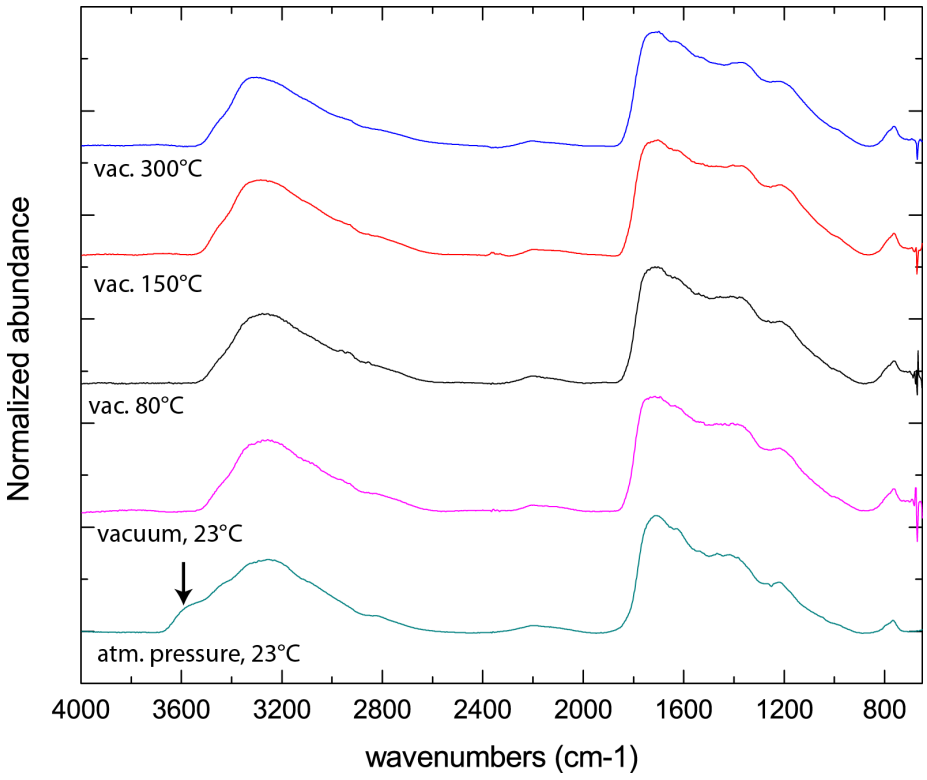

Figure 3.26: Spectral evolution of the sample CO-N-GR34, from atmospheric pressure to vacuum, and then from room temperature to 300°C under vacuum. The black arrow shows the disappearing of the absorption at ~ 3600 cm^{-1} when the sample is put under vacuum, likely due to H_2O desorption.

3.2.4.3 "Flash pyrolysis" test

A test of "flash heating" was performed on two Nebulotron samples (CO-GR29 and CO-N-GR34) at ~ 1200°C for 4 to 8 seconds, at atmospheric pressure under N_2 flux and in a graphite crucible. This was done in order to check whether any chemical structure evolution occurs when these organic materials are exposed to thermal shocks that are similar to what might happen in the young solar protoplanetary disk, during chondrules formation events for instance (Ciesla, 2006, Desch et al., 2012, Hewins, 1997).

FTIR spectra of these "high temperature shocked" samples were then acquired. Not surprisingly, the samples lost H, N and O, as indicated by the disappearance of the aliphatic, amine and C=O bands (Fig. 3.27). The –OH groups at ~ 3600 cm^{-1}, the C=C bonds at ~ 1600 cm^{-1} and the ether bonds (C-O) at ~ 1200-1300 cm^{-1} are still present. The final material in then essentially aromatic associated with C-O bonds. Such an evolution likely signs the presence of O2 during the heating experience, resulting in a combustion event rather than in a pyrolysis event. Interestingly, the final heated CO-N-GR34 sample (initially containing a lot of N) presents a much more intense nitrile band at 2200 cm^{-1} relative to the non-heated sample. This suggests that either the initial N in the sample is present essentially in amine

and amide groups, and/or N from the N_2 gas buffering the heating experiment, is remobilized into nitrile groups. N-heterocycles (if represented by the 760 cm^{-1} feature) also disappear.

Thermal annealing under vacuum of photoproduced a-C:H (analogue of the interstellar carbon dust, Dartois et al., 2005) and tholins (Bonnet, 2012) up to 1000 K resulted in similar materials with final compounds being mostly aromatic and having lost aliphatic, C=O, and nitrogen-bearing functions.

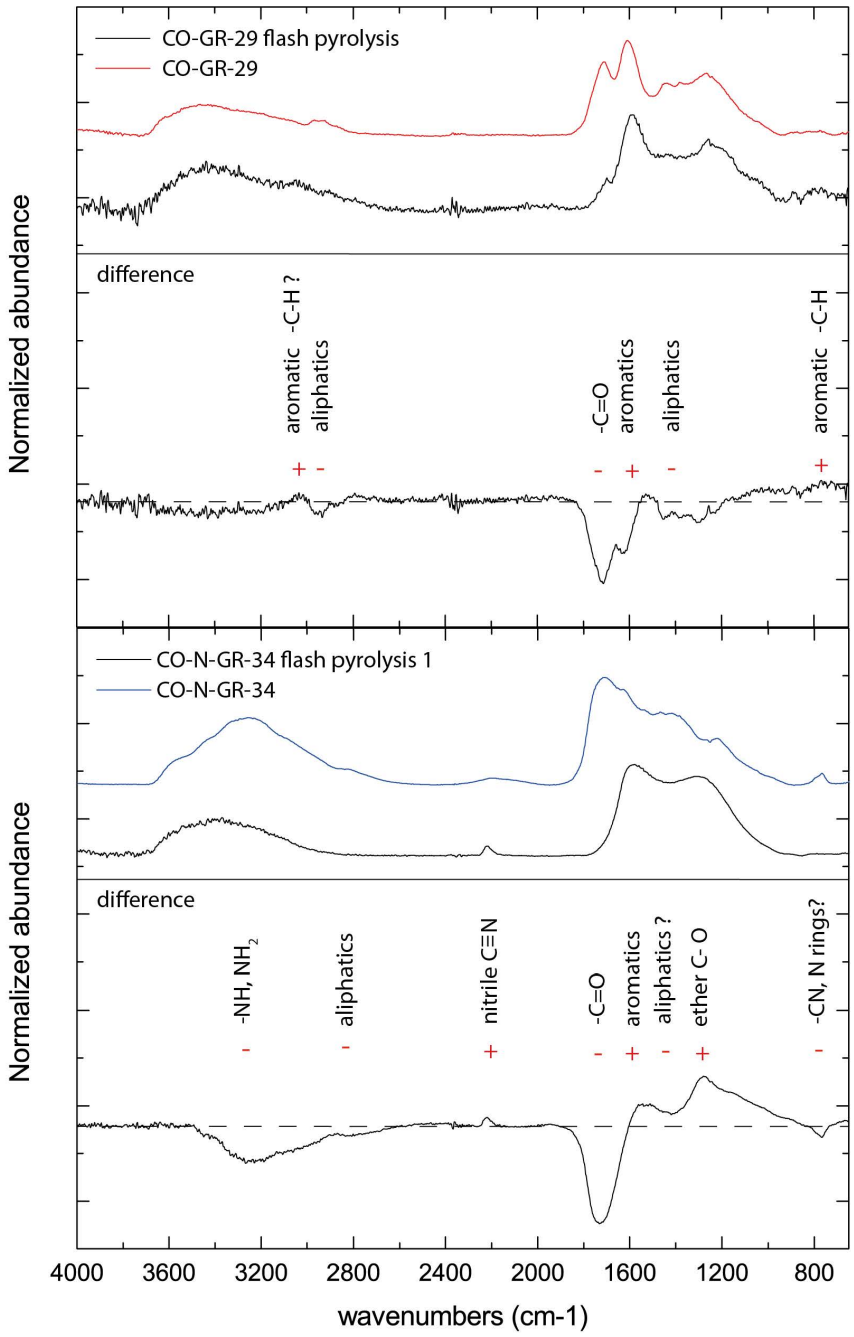

Figure 3.27. FTIR spectra of the CO-GR29 (top) and CO-N-GR34 (bottom) samples before and after the 1200°C flash heating, and the calculated difference between the two. Minus signs mark the disappearance/intensity decrease of some bands, whereas the plus signs mark the appearance/intensity increase of other bands.

3.2.4.4 Influence of the initial experimental conditions on the chemical structure of Nebulotron solids

No systematic study of the chemical composition and structure with FTIR as a function of plasma experimental parameters (duration, noble gas partial pressure and power input) has been done on the CO-GR samples. Only one or two spectra were acquired for each condition. The conclusions thus are to be taken with care.

- Power input

Increasing the discharge power input in the Nebulotron setup results in an increase of the neutral gas temperature in the plasma and of the reactor walls. This increase could be expected to result in a modification of the chemical composition of the Nebulotron solids, as observed for the Raman and TEM data (previous section, sample CO-9). Nonetheless, the two samples, produced at 30 and 60 W in the new reactor, do not seem to show clear chemical and functional group differences, with the exception of different relative intensities of the C=O band at ~ 1700 cm^{-1} and the C=C band at ~ 1600 cm^{-1} (Fig. 3.28). Thus, the discharge power input does not much change the chemical structure of the Nebulotron solids.

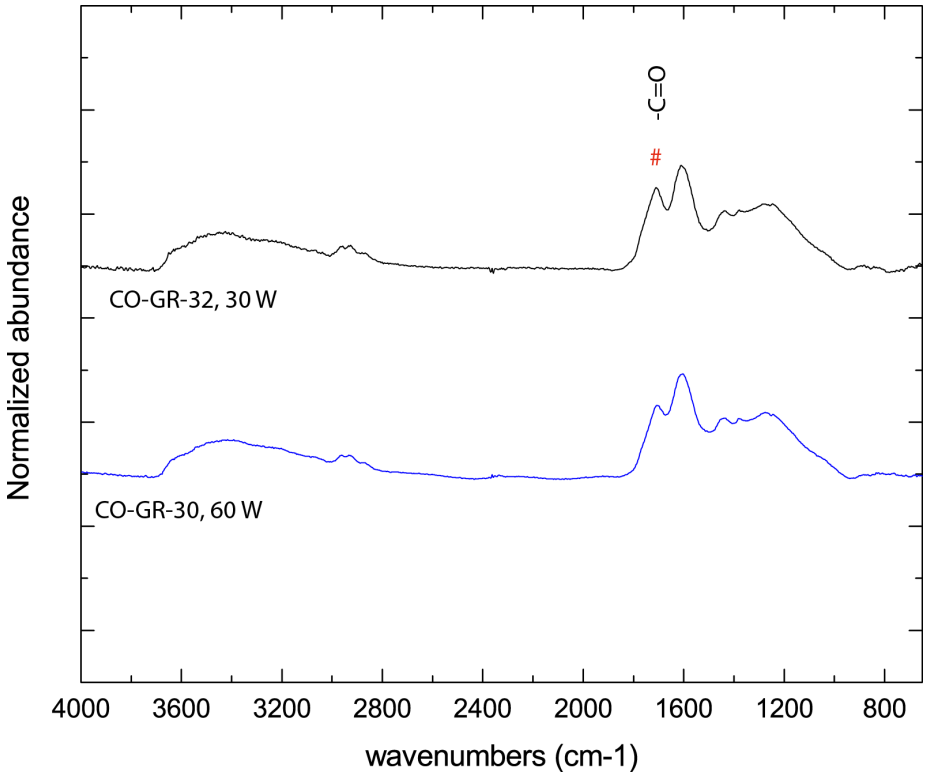

Figure 3.28. FTIR spectra of samples CO-GR-32 and CO-GR-30, produced at 30 W and 60 w respectively. The # symbol marks where the visible difference between the two spectra occurs at 1700 cm^{-1}.

- Duration and noble gas partial pressure in the initial gas mixture

The FTIR spectra of CO-GR samples exhibit no visible difference as a function of the experiment duration and the noble gas % in the initial gas mixture. Nonetheless, a variation in the relative intensities of the C=O and C=C absorption features in the CO-GR spectra presented in Fig. 3.24 is clearly observed, notably for the samples 19, 23 and 27, all produced in the old reactor. The COGR-23 and 27 were produced under the same experimental conditions, and the difference between the two is rather likely due to contamination of the plasma gases or to bad control of the plasma discharge leading to strong thermal heterogeneity in the reactor.

3.2.5 Conclusions of the analytical section

From this physical and chemical characterization, some inferences about the general features of Nebulotron samples can be drawn:

- Nebulotron organics are aerosols that are formed in the gas phase and grow up onto the reactor surfaces, resulting in **fluffy and feather-like grain morphologies**.
- The few Nebulotron samples that were observed with a TEM displayed carbon microtextures typical of **turbostratic carbon** materials, with some variability at the micron scale from microporous texture with a few graphene layers organization to completely amorphous texture. This disorganized carbon texture is confirmed by the 514 nm Raman study and the quantification of the D and G bands parameters. The Raman study also allows for a rough estimate of the maximum temperature seen by the Nebulotron samples, which is expected to be **500°C minimum** for most samples.
- Bulk elemental compositions for the Nebulotron samples point to a surprisingly high abundance of hydrogen atoms, which is enhanced when adding noble gases and/or N_2 to the initial gas mixture. The hydrogen source is suspected to be water molecules that are desorbed from the walls of the reactor by the sputtering action of N_2 and noble gases, as well as the heating of the reactor by the plasma itself.
- The C, H, O and N contents in the Nebulotron samples are likely to be controlled by the composition of the starting gas mixture, as well as by the level of contamination and by the plasma gas temperature causing pyrolysis of the formed solids. The degree of unsaturation (U.D.) of Nebulotron samples is very high, up to 85 for 100 carbon atoms. This suggests a **polyaromatic structure**, along with **N-bearing heterocycles** for the CO-N_2 and CO-N-GR samples in particular. This also supports the presence of triazine rings in those Nebulotron samples, as inferred by UV Raman interpretation.
- FTIR spectra confirm the presence of aromatic carbon, but also of aliphatic functional groups. Oxygen likely is incorporated in ketones, hydroxyl and phenolic groups. Nitrogen is present as amine/amide, nitrile and N-rings. Nebulotron samples are thus **highly functionalized macromolecules**.
- Both physical and chemical characterization of the Nebulotron samples also exposed some **limitations of the experimental setup**: leaks contaminate the initial gas mixture; the reactor releases water to the gas phase; the temperature in the plasma is not

homogeneous and the reproducibility of the chemical composition and speciation of the solids is somewhat rough. These points are discussed in the next subsection.

3.2.6 Limitations of the Nebulotron setup

3.2.6.1 Water desorption, leaks and incorporation of H and N into organic solids

On the H content in the Nebulotron solids: Although no gaseous hydrogen was used in the starting gas mixtures, hydrogen is present in the solids formed in the Nebulotron plasma in large quantities (up to 40 at. %). This hydrogen may come from several different sources:

(i) from H_2 and/or H_2O gas impurities in gas tanks used to make the initial gas mixtures. The CO tank that was first used in the present work was a 2.5 quality tank (99.5 % pure CO), with $H_2 < 100$ ppm and $H_2O < 50$ ppm according to the quality certification. In particular, H_2 is easily dissociated in the plasma ($E_d = 4.5$ eV). The CO tank was changed during the thesis to a 3.7 quality tank, with H_2 and H_2O impurities was reduced by factors of 20 and 10, respectively. The H contents in the Nebulotron samples have somewhat decreased after changing the tank, but the decrease may also be due to the installation of the new reactor soon after.

(ii) from H emission by the quartz of the reactor when heated. Indeed, OH groups are part of the quartz network, but in low quantities (< 5 ppm, Sloots, 2008). These OH groups diffuse out of the quartz at high temperatures, and might be ionized in the plasma and be incorporated into reactive network in the gas phase. Nonetheless, because of the low OH content in quartz, I suspect that this process is not the main H source in the Nebulotron setup.

(iii) from water adsorbed on the reactor's surfaces. Indeed, after each experiment, the reactor was opened to atmospheric pressure. When the solids were recovered, the reactor was rinsed with water first and then with ethanol. The reactor was then connected again to the vacuum line and pumped out. However, the pumping system on the Nebulotron setup is a primary pump, allowing for a limit vacuum of $\sim 5.\ 10^{-3}$ mbar. Because the reactor was not baked before starting a new experiment, the primary pumping only likely was likely to leave water adsorbed on the reactor's walls. These H_2O molecules were then desorbed during the experiment, either by diffusion because of the high temperature of the gas in the plasma, or by noble gases, CO or N_2 sputtering onto the surfaces (cf. section 3.2.3.1). Quantifying the H source contamination is difficult. H_2O ($+H_2$) probably did not exceed 1 % in the total gas mixture that flowed in the setup. Although the dissociation energy of H_2O is quite high (9.5 eV), H_2O is very reactive and the formation of OH groups or H radicals certainly enhanced the polymerization of molecules in the plasma. However, when the H partial pressure is too high in the plasma, the growth of aerosols tends to be inhibited (Sciamma-O'Brien et al., 2010). Such an effect was observed once in the Nebulotron setup: the CO-N-GR 37 sample was formed in an CO-N_2-noble gases mixture experiment, that was preceded by a N_2-noble gases plasma, dedicated to desorb a maximum of water from the reactor's wall. Indeed, the

CO-N-GR 37 sample displays a much lower H/C ratio than other CO-N-GR samples that were produced without a "cleaning" N_2-NG plasma. Moreover, the production rate for the CO-N-GR 37 experiment was almost doubled compared to other similar experiments. This suggests that water desorption from the reactor, either by doing a cleaning plasma, or baking the reactor or pumping to a secondary vacuum prior to the experiment, would lead to a better control on the hydrogen content in the final synthetic solids.

(iv) from (either physical or chemical) H_2O adsorption onto the Nebulotron samples. The Nebulotron samples were not baked prior to elemental analyses, thus if water was adsorbed onto Nebulotron organics, it likely resulted in a biased high H content. The Nebulotron samples have a very large specific surfaces (up to 500 m^2/g, A. Razafitianamaharavo, personal communication) and thus are prone to H_2O adsorption. Plasma synthetic particles are also well known to have dangling and reactive bonds onto their surface, which are prone to react when put in contact with the atmosphere. Such a process would also be responsible for an enhanced H content in the Nebulotron samples as well as for the presence of hydroxyl groups in their chemical structure.

On the N content in the Nebulotron solids: the second point to discuss is the presence of N atoms in the Nebulotron samples (up to 8 at. %) that were formed in gas mixtures lacking N_2. As for H, N contamination may come from different sources:

(i) from N_2 impurities in gas tanks. As mentioned above, the first CO tank used in this thesis was a 2.5 quality, with N_2 content up to 600 ppm. Later on, the 3.7 quality CO tank had a N_2 content of lower than 20 ppm. When looking at the elemental compositions of the Nebulotron samples, an N content decrease is clearly marked, with N at. % lower than 1% after the CO tank was changed (Fig. 3.29). As a result, the N_2 impurity in the first CO gas tank might be a significant source for the N incorporation into Nebulotron solids produced in CO-only and CO-noble gases mixtures. However, the variability of the N/C ratio during the use of the first CO tank points to an additional source of nitrogen.

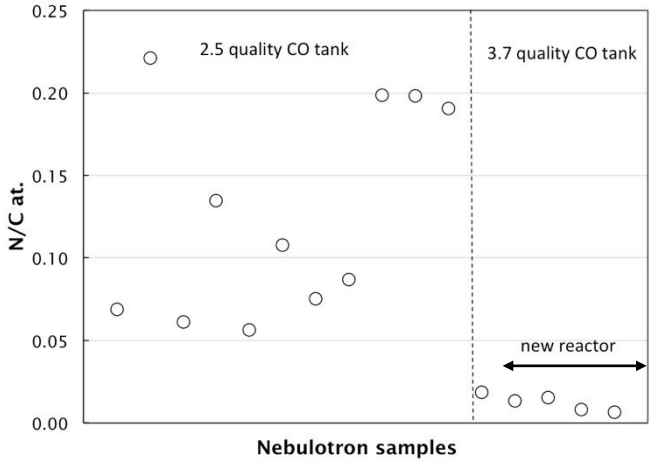

Figure 3.29. Evolution of the N/C ratio in Nebulotron samples as a function of production time. The CO gas tank change is marked on the graphic.

(ii) from leaks into the Nebulotron setup. Indeed, the large N content in the Nebulotron samples, up to 8% at., are likely due to air entry into the setup through leaks. The Nebulotron line is old and in particular, the old reactor was connected to the line via fragile metal/glass cylindrical connections filled with black wax to ensure a good airtightness. Obviously, the airtightness was not so good. Leaks might also come from grease valves on the line and reactor setups. The N/C ratio is even lower in the experiments done with the new reactor setup (Fig. 3.29), which has no more grease valves (or black wax) nearby the quartz reactor, which was changed too (cf. Chapter 2).

As in the case of hydrogen, although the atmosphere in the Nebulotron setup was not controlled at the beginning of this work, leaks in the setup have now been removed and the N content in the Nebulotron organics is consequently much lower and better controlled.

3.2.6.2 A high temperature process

The Raman study, as well as the elemental composition analysis on the Nebulotron samples confirmed that the plasma temperature is high, the solids having experienced at least 500°C. Such a high temperature was predicted by the high power density in the Nebulotron setup (see Chapter 2). Moreover, the temperature is not homogeneous in the reaction area, as solids formed on the edge of the plasma have seen much higher temperature than those in the center of the plasma, likely due to a cooling deficiency on the reactor's edges.

Although the Raman study can give a rough estimation of the formation temperature of the Nebulotron samples, the temperature throughout the plasma is not well known in the Nebulotron setup. This temperature is a consequence of the plasma configuration and cannot be controlled easily, as a simple tiny modification in the gas pressure and composition or power input can change dramatically the temperature distribution. It results in the sample pyrolysis in the plasma, a process that likely competes with the formation of aerosols. Nonetheless, despite a high temperature formation, the Nebulotron organics are not carbonized and display complex chemical compositions and speciation, with non-negligible H, O and N contents. The Nebulotron experiment thus shows that functionalized and complex molecules can be formed at high temperatures.

3.2.6.3 Experimental reproducibility

The elemental compositions, the IR and the Raman spectra point to a variability among Nebulotron samples that were produced under the same conditions. This variability is very likely to be due to the three factors mentioned above: the uncontrolled sources of N and H, the temperature heterogeneity and temperature variability. Yet, the Nebulotron samples produced in the new reactor appear much more reproducible, according to elemental and FTIR analyses (Table 3.3, Figs. 3.23, 3.24 and 3.25).

3.2.6.4 The new reactor: towards a better control on experiments?

The three points raised above clearly point to the limitations of the Nebulotron setup. In order to circumvent these limitations, a new reactor was built to reduce leaks and contamination problems. Few experiments have been performed on this new setup, but these ones indeed are much more reproducible and display lower H and N contents than before. Further studies are now required to get a fine control on the chemical and physical structure of the synthetic organics.

Along with improvements in the pre and post-experiments cleaning and baking procedures, the new Nebulotron setup, in its present configuration, offers the possibility of producing large amounts of O- and N-rich organic material with reproducible chemical and physical structures. Notably, Nebulotron organic materials have interesting properties that can make them analogues of extraterrestrial materials like IOM in chondrites or cometary organics.

3.3 Nebulotron organics: IOM analogues?

The Nebulotron produces complex organic materials in conditions that are designed to mimic protoplanetary disk (PPD) environments (e.g. ionization, CO-N_2 gas mixture). In this section, I compare the characteristics of the Nebulotron organics, with those of chondritic IOM, keeping in mind that: (i) laboratory materials are formed generally in conditions and on timescales that are different from those of IOM formation, and (ii) extraterrestrial organics, and in particular IOM, have undergone thermal and aqueous alteration since their formation.

3.3.1 The chondritic IOM: molecular and structural specificities

The chemical structure of the chondritic IOM has been studied by both destructive and non-destructive techniques (see Chapter 1 for references). IOMs from 'unheated' chondrites (type 1 and type 2) have an average bulk formula $C_{100}H_{70}O_{20}N_3S_3$ (Alexander et al., 2007, Hayatsu et al., 1977). The degree of unsaturation of IOM is about 67%, pointing out a highly unsaturated material. Spectroscopic, TEM and GCMS studies have shown that carbon atoms are included in small aromatic units (1-4 rings) that are linked by short (2-9 carbon atoms) and branched aliphatic chains, resulting in a high degree of cross-linking. Oxygen is the most abundant element after C and H, and is included in carbonyl and carboxyl groups, as well as in ether and aliphatic alcohols. Nitrogen is a minor element in IOM and thus difficult to analyze. It seems that hetero-aromatic cycles and nitriles are the main N-bearing groups in IOM and that more labile functions, as amine or amide, are absent (Remusat et al., 2005). Sulfur appears in various speciation forms: aliphatic, heterocyclic and oxidized sulfur (Orthous-Daunay et al., 2010b). In the Murchison meteorite, all these results led to a model of the IOM molecular structure (see Fig. 1.9, Derenne and Robert, 2010). The IOM carbon textures, inferred from TEM observations, presents variability at the micro scale, from amorphous to rare organized areas (Bonal, 2006, Derenne et al., 2005). This results in a

disordered carbon structure, which level of disorder, provided by quantification of Raman parameters, has been used to identify the degree of thermal processing of the chondrite parent bodies (Bonal, 2006, Quirico et al., 2014). In particular, organics from primitive chondrites have I_D/I_G ratios between 0.8 and 1.

3.3.2 Comparison with Nebulotron organics

3.3.2.1 Elemental composition

Bulk elemental compositions of numerous IOMs from different classes of chondrites were measured by Alexander et al., 2007. Bulk formula of Nebulotron samples and some chosen IOMs are given in Table 3.5. Overall, CO-GR and CO-only Nebulotron samples have similar C, H, N and O atomic proportions as "unheated" IOM from CI and CM chondrites or cometary organics, whereas CO-N-GR samples display much higher N content than IOMs.

Nebulotron synthetic organics	gas mixture	C	H	N	O	S
ALL SAMPLES (average)	CO-only	100	51	5	25	
old + new reactor	CO-GR	100	73	8	34	
	CO-N2	100	93	60	64	
OLD REACTOR	CO-only	100	51	5	25	
	CO-GR	100	81	12	40	
	CO-N2	100	105	71	66	
NEW REACTOR	CO-GR	100	57	1	25	
	CO-N2	100	83	51	63	
Extraterrestrial organics						
Chondritic IOM - "unheated" (type 1 and 2)[a]	Orgueil (CI)	100	67	3	18	3
	Murchison (CM)	100	59	3	18	2
	Bells (CM)	100	69	3	21	5
	EET92042 (CR)	100	75	4	17	3
Chondritic IOM - "heated" (type 3 or more)[a]	Kaba (CV ox)	100	31	1	30	
	Allende (CV ox)	100	17	0.5	13	
	Vigarano (CV red)	100	18	0.8	11	
	Kainsaz (CO-3.1)	100	16	0.6	12	
	Semarkona (OC-3.00)	100	48	1.5	29	7
	Krymka (OC-3.2)	100	35	1	15	3
	Tieschitz (OC-3.6)	100	16	1	14	
comet Halley CHON particles[b]		100	80	4	20	2
N-rich IDPs and UCAMMs		100	30-200 ?[c]	10-30[d,e]	?	?

[a] data from Alexander et al. 2007, [b] Kissel and Krueger 1987, [c] Aleon et al. 2001, [d] Aleon et al. 2003, [e] Dartois et al. 2013

Table 3.5. Bulk formula of the Nebulotron samples and a few chondritic IOMs as well as comet Halley CHON particles (Alexander et al., 2007, Kissel and Krueger, 1987).

Bulk IOM and Nebulotron samples H/C, N/C and O/C ratios are compared in Fig. 3.30. Overall, Nebulotron samples span a much larger range of N/C and O/C ratios than IOM, and to a less extent of H/C. However, some of the Nebulotron samples (notably those

produced in the new reactor with CO only and CO+NG mixtures and with limited contamination) plot in the IOM field. Hence, the Nebulotron samples produced with CO gas only (without N_2) seem compatible with the bulk elemental composition of IOMs.

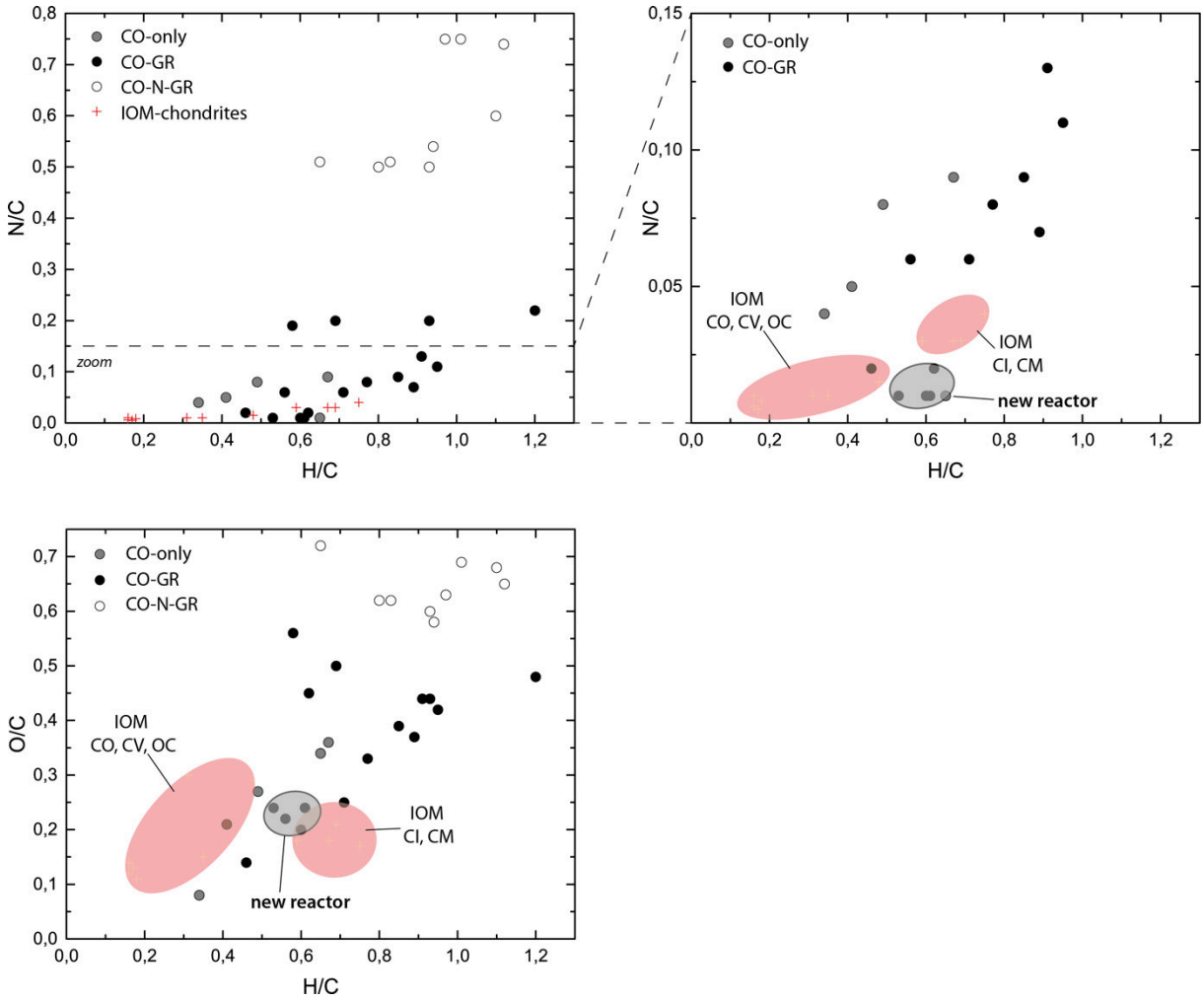

Figure 3.30. Atomic N/C and O/C ratios as a function of H/C ratio for the Nebulotron samples and for the chondritic IOM. The latter falls into two groups (i) CI and CM of types 1 and 2, and (ii) type 3 or more, as for CO, CV and OC chondrites (Alexander et al., 2007).

The Nebulotron samples CO-N-GR and CO-N_2 have a N/C ratio that is 20 times higher than the bulk N/C ratio of chondritic IOMs, although they were formed in a gas mixture having a canonical N/C ratio (Table 3.5 and Fig. 3.30). In line with the present observations, Bonnet, 2012 has tested the possibility that thermodegraded N-rich tholins could represent analogues of IOM precursor(s) but obtained too high N contents compared to IOMs'. If the IOM precursor(s) was initially N-rich, other processes than thermodegradation (pressure shocks? oxidation shocks?) are required to lose the N even more. Alternatively, the present data suggest that N-poor organics could not be formed upon ionization in a canonical

atmosphere ($CO+N_2$) but were instead produced in a CO atmosphere containing only traces of N_2. For instance, N_2 might not have been the main N-bearing species (Caselli and Ceccarelli, 2012). These possibilities are, however, speculative as the protosolar nebula gas was rich in **H_2**, in addition to CO and N_2, and a high pressure of H_2 might have impacted the incorporation of N into solid organics.

Interestingly, rare N-rich polyaromatic organic phases have been identified in UCAMMs and in some IDPs, with N/C ratios up to 0.3 (Table 3.5, Aléon et al., 2003, Dartois et al., 2013, Floss et al., 2010). Bonnet, 2012 suggests that N-rich organics like tholins, might be the precursors of IDP and UCAMM organics that evolved upon thermal degradation up to 500°C. Other authors have proposed that N-rich and polyaromatic UCAMMs precursors were formed within the N_2-rich subsurface of comets in the Oort cloud by cosmic-ray irradiation (Dartois et al., 2013).

From the present Nebulotron experiment and assuming that H_2 does not play a role in N incorporation into organic solids, a canonical-like atmosphere of CO and N_2 experiencing modest irradiation (ions with energies of 10-50 eV), strong ionization by UV photons or electrons (here by electrons) as well as subsequent heating might have produced such N-rich organics.

3.3.2.2 C, O and N-speciation

FTIR spectra of chondritic IOMs (Orthous-Daunay et al., 2013) and three Nebulotron samples are compared in Fig. 3.31.

The main chemical functional groups that were identified in IOM are alkyl (CH_2 and CH_3), carbonyl (C=O) and aromatic (C=C). The same functional groups are also observed in the Nebulotron samples produced from CO or CO-Noble gas mixtures (Fig. 3.31). Given the molecular complexity of IOM, the relative abundances of the above functional groups are generally used to quantify the variability of IOM from one chondrite to another one (Orthous-Daunay et al., 2013). Such quantification was not done for the Nebulotron samples. Here, the comparison between the Nebulotron samples and IOMs was carried out by visual inspection of their of FTIR spectra. Like IOMs, the Nebulotron samples display large chemical heterogeneities, as pointed out by the relative abundances of the three functional groups highlighted above. The Nebulotron samples seem to have low alkyl abundances (green in Fig. 3.31) relative to aromatics (blue in Fig. 3.31), in a ratio which is comparable to the one measured for Tagish Lake (ungrouped) and Cold Bokkeveld (CM2), i.e., alkyl/aromatic ratio < 0.3 (Orthous-Daunay et al., 2013). With the exception of a few samples like CO25, the Nebulotron organics display a C=O absorption feature (orange in Fig. 3.31) that is at a minimum equal to, but generally more intense than the C=C feature (blue in Fig. 3.31). This is not observed in IR spectra of IOMs in which the C=O feature is systematically less intense than the C=C feature at 1600 cm^{-1}, except for Cold Bokkeveld.

Overall, the Nebulotron samples (from CO or CO-Noble gases mixtures) IR spectra look like IOM spectra because they display the same functional groups. But in details, the relative abundances of these groups are different from those of IOM of type 1-2 chondrites,

suggesting that the molecular structures of the Nebulotron samples and of these particular IOMs are also different.

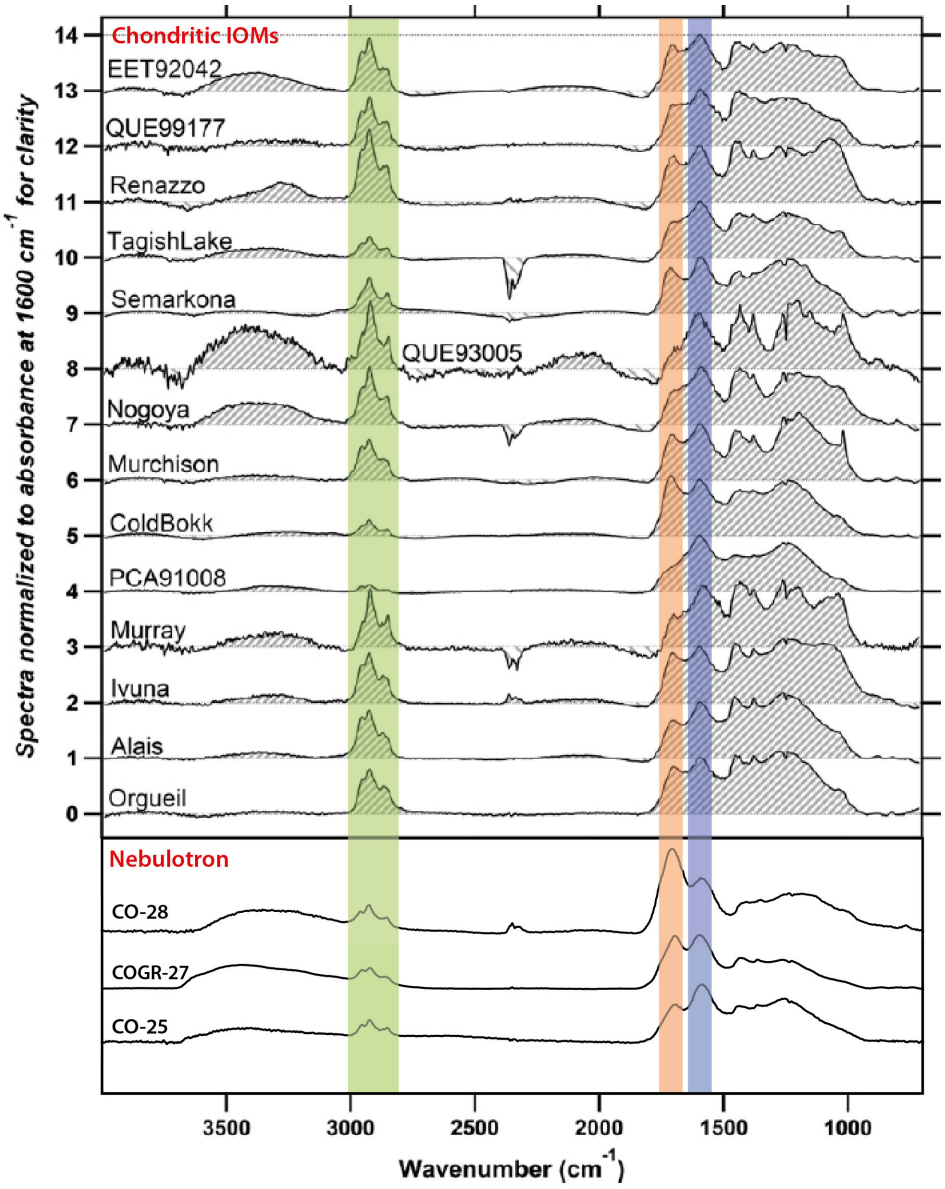

Figure 3.31. FTIR spectra of chondritic IOMs (adapted from Orthous-Daunay et al., 2013) and of three Nebulotron samples (CO25, COGR27 and CO28). Those Nebulotron samples display spectra qualitatively closer to spectra of IOMs than the other samples. The spectral domains that are highlighted are: alkyl (CH_3, CH_2, *green*), carbonyl (C=O, *orange*) and aromatic (aromatic C=C, *blue*) functional groups.

3.3.2.3 Carbon microtexture and structure

Carbon textures of three chondritic IOMs, of an experimental soot sample and of two Nebulotron samples determined by TEM imaging are shown in Fig. 3.32.

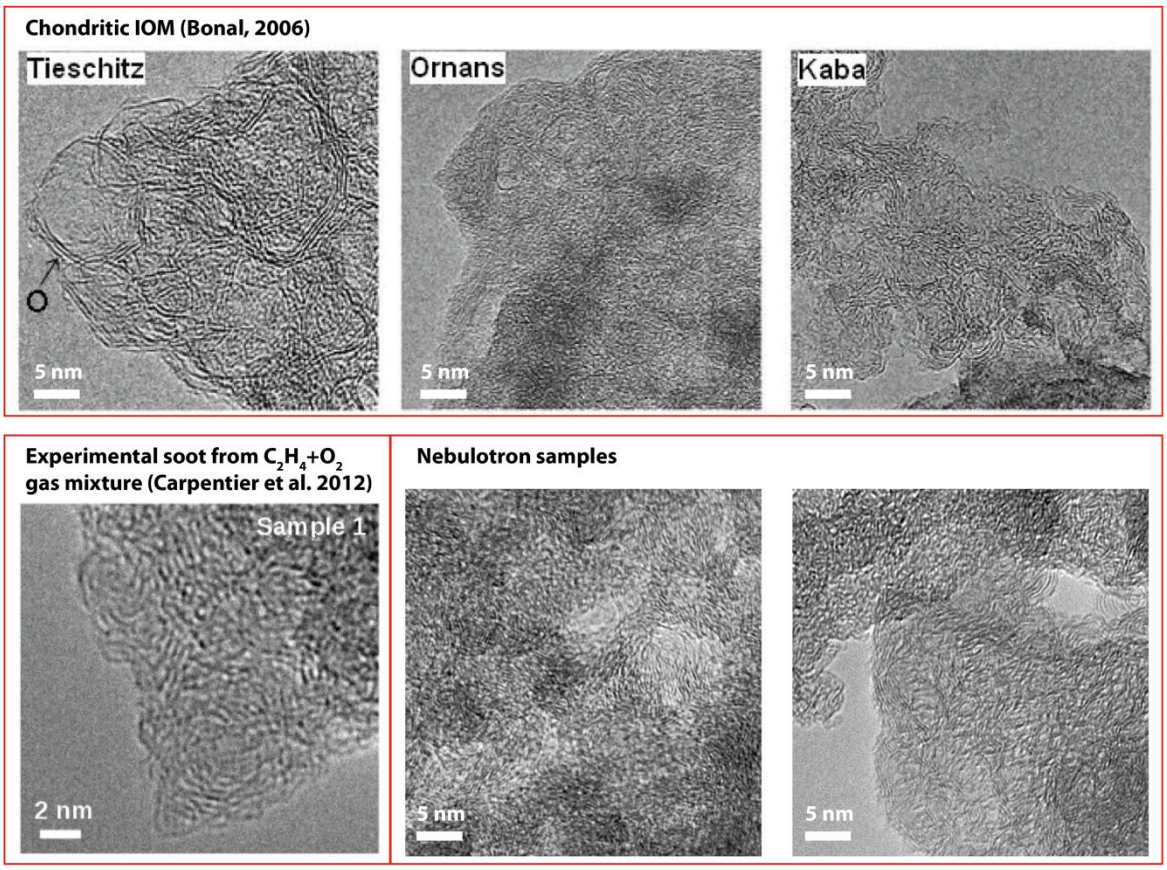

Figure 3.32. TEM observations of carbon textures in chondritic IOMs (Bonal, 2006), in an experimental soot formed in a flame composed of C_2H_4 and O_2 (Carpentier et al., 2012) and in Nebulotron samples.

Several carbon textures are encountered in IOMs: microporous, layered or onion-like textures (Bonal, 2006, Vis et al., 2002). Such carbon textures resemble to those observed in soot formed in the laboratory (Carpentier et al., 2012). Some of these textures were identified in the Nebulotron samples, except for clear onion-like structures. One key parameter to describe in detail the carbon texture is the length of the layers and of the coherent domains with high-resolution TEM, generally used to derive the size of the aromatic moieties (Derenne et al., 2005). Such quantification on the Nebulotron samples has not been done yet. Hence, although the textures are similar, the size of the aromatic units in the Nebulotron samples cannot be inferred here and the comparison with IOMs stays limited.

The carbon structure is inferred by Raman spectroscopy and the quantification of structural indicators such as the position of the D and the G bands, their width and their relative intensities. A compilation of the Raman parameters obtained on chondritic organics (matrix pieces or extracted IOM), IDPs and UCAAMs, experimental soot and irradiated organics in the laboratory is presented in Fig. 3.33.

From the study of thermally processed chondrites and "primordial" IDPs and UCAMMs, a metamorphism trend was inferred which corresponds to an increase of the I_D/I_G ratio and of the G band position associated with a decrease of the FWHM of the D and the G bands (Dartois et al., 2013, Dobrică et al., 2011). Thermal processing results in a material that is more organized. On the other hand, ion irradiation in the keV range (solar wind particles or cosmic-rays in the solar nebula for instance) mostly results in disorder generation. Quirico et al., 2009 suggested that a precursor effect could be superimposed on the metamorphism/irradiation trends, causing the scattering of the Raman spectral parameters of the organic compounds in chondrites, IDPs and UCAMMs.

In the FWHM-G vs. w_G diagram, most of the Nebulotron samples plot in the domain defined by chondritic organics and IDPs/UCAMMs, but on the edges and rather toward thermally processed materials than towards pristine ones. However, the I_D/I_G ratio of most of the Nebulotron samples is <1, which is similar to UCAMMs and less processed chondrites. FWHM-G seems to be a reliable parameter of ordering in very disordered carbon materials (Busemann et al., 2007). The Nebulotron samples have FWHM-G that plot well in the FWHM-G range occupied by chondritic organics, suggesting a similar level of ordering (or disordering). Interestingly, the Nebulotron samples plot far from the materials that were irradiated with keV-ions, illustrating that ions in the Nebulotron plasma, which are low-energy ones, do not affect the carbon structure of the organics growing in the plasma setup. Experimental soots display a large variation in their Raman spectral parameters, likely depending on their formation conditions (Brunetto et al., 2009, Sadezky et al., 2005). Some of the chondritic IOMs plot in the area defined by diesel soot (Sadezky et al., 2005), consistent with the fact that the carbon texture of some IOMs looks like soot textures (see the above section).

These 514 nm Raman spectral data suggest that some of the Nebulotron samples (the less thermally processed ones) display a carbon structure that is very similar to the one of chondritic IOMs. The level of disorder is likely to be the same in the Nebulotron samples and in the IOMs. A precise quantification of the UV-Raman spectra of the Nebulotron samples should allow a more pertinent comparison with extraterrestrial organics.

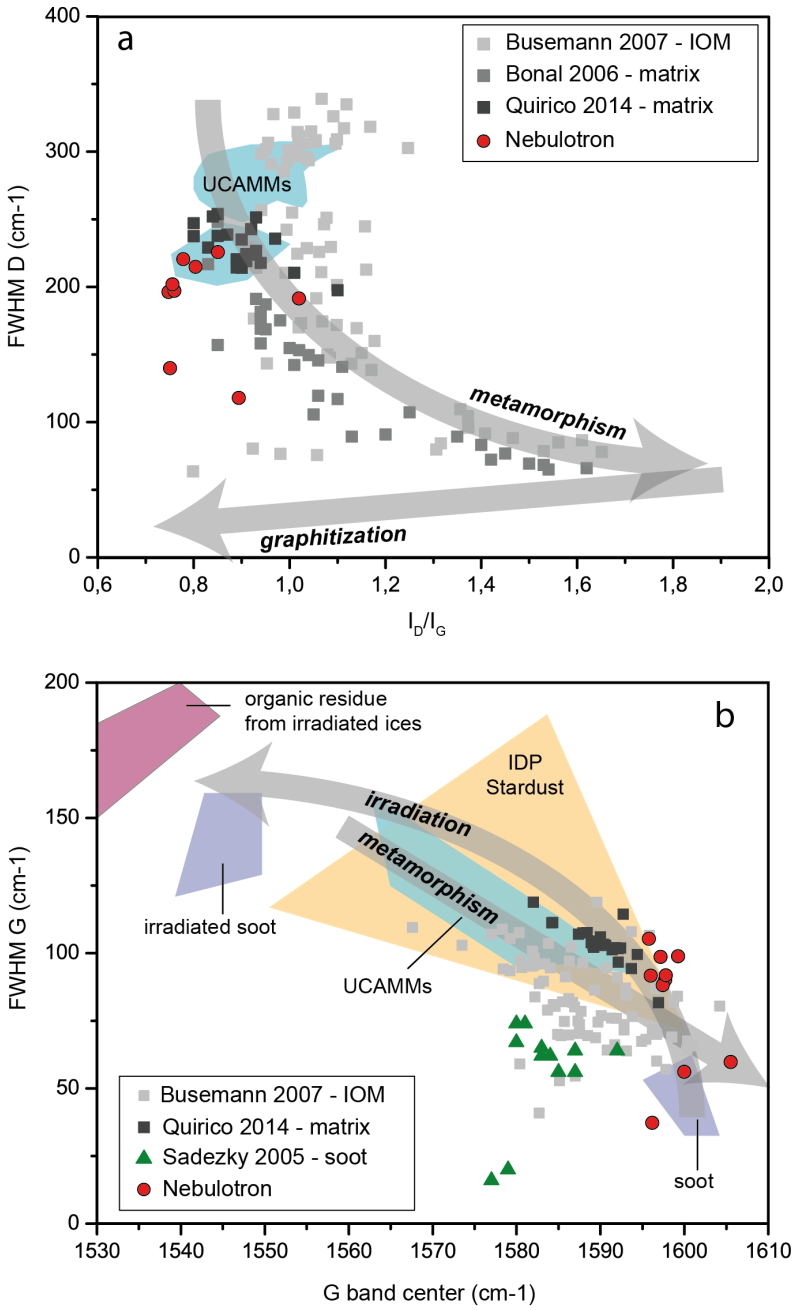

Figure 3.33. Comparison of 514 nm Raman spectral parameters of Nebulotron samples with those of organics from cosmomaterials. Chondrites: matrix (Bonal, 2006, Quirico et al., 2014), and extracted IOMs (Busemann et al., 2007). Antarctic micrometeorites (UCAMMs, blue area: Dartois et al., 2013, Dobrică et al., 2011). IDPs and Stardust grains (orange area: Quirico et al., 2005, Rotundi et al., 2008, Sandford et al., 2006). Laboratory soot (green triangles: Sadezky et al., 2005, purple area: Brunetto et al., 2009). Irradiated organic materials (soot: Brunetto et al., 2009, organic residue from irradiated ices: Baratta et al., 2004). (a) FWHM-D vs. I_D/I_G and (b) FWHM-G vs. w_G. The grey arrows illustrate the evolution of the Raman spectral parameters with metamorphism and irradiation with high energy ions (keV) (Bonal et al., 2006, Brunetto et al., 2009, Busemann et al., 2007).

3.3.2.4 An insoluble and refractory material

The kerogen-like IOM in chondrites is insoluble, by definition, in acids and organic solvents (methanol, chloroform, Gardinier et al., 2000, Orthous-daunay, 2011). IOM is also a refractory organic material: its chemical structure is not significantly modified when heated up to 300°C under vacuum (Orthous-Daunay et al., 2010a) and at least a very small part of IOM is very refractory as most trapped noble gases (Ar, Kr and Xe) are extracted at temperatures higher than 600°C (Huss et al., 1996).

A rough solubility test was performed on three Nebulotron samples (CO-GR18, CO-25 and CO-N2-3), by dissolving 5 mg of aerosols into 5 mL of (i) distilled water and (ii) methanol. The suspensions were ultrasonicated for 30 min and then centrifuged. The supernatant was transferred into another tube and 5mL of solvent was added again to the insoluble fraction. Both tubes were ultrasonicated and centrifuged for a second time. The results are shown in Fig. 3.34. Although the soluble/insoluble fractions were not weighted after methanol evaporation, the material seems mostly insoluble as most of it stays in the bottom of the tubes. A fraction of CO-N2 and COGR18 samples is nonetheless soluble because the supernatant solution is colored, whereas the supernatant of CO-25 sample is clear. The former samples are N-rich, which may explain their enhanced solubility compared to CO25 sample.

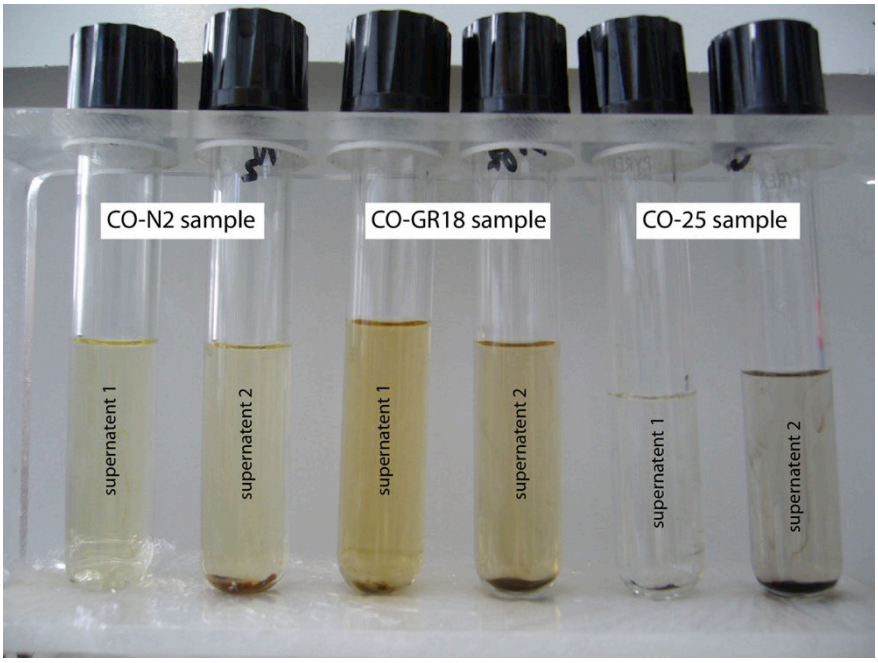

Figure 3.34. Dissolution experiments in methanol for three Nebulotron samples: CO-N_2-3 (left), CO-GR-18 (middle) and CO-25 (right). The picture is taken after the second centrifugation of the two tubes.

The Nebulotron organics are also refractory, as attested by the thermal degradation studied with FTIR (see section 3.2.4.2). At least up to 300°C, no significant modification is seen in the chemical structure of the Nebulotron organics. However, the heating was performed for short durations (15 min) and may not be representative of the kinetics of the thermal degradation on such samples. It is worth noting that noble gases, e.g. xenon, are extracted at rather low temperature in Nebulotron samples (400°C) compared to the high-temperature release of Xe in chondritic organics, e.g. ~ 1000°C (see Chapter 5). This difference suggests that either the trapping process in the plasma does not reproduce the process of the Q-gases trapping, or that it requires a secondary process in the protoplanetary disk or on the parent bodies that enables the high-temperature extraction of heavy noble gases in chondrites. Overall, the refractory pattern of the IOM is relatively well reproduced by the Nebulotron samples, regarding the thermal sensitivity of the chemical structure seen by IR spectroscopy.

3.4 Conclusions and perspectives

The physical and chemical characterization of the Nebulotron samples has shown that these carbon-rich materials are complex organic compounds with a high level of disorder and carbon textures that are similar to those found in soot. This study also pointed out the presence of unexpected sources of hydrogen and nitrogen in the experimental setup that are likely resolved with the new reactor design. Finally, these results confirmed that the organic synthesis occurs at high temperatures in the Nebulotron setup, i.e. > 800 K.

From the comparison between the Nebulotron samples and the chondritic IOM, we can infer that they share common features, such as the elemental composition, a polyaromatic structure with highly substituted aromatic moieties, the O-rich groups, the disorder level of the carbon structure and texture and the solubility behavior. The combination of these features are not generally encountered in other laboratory analogues, and notably in organic residues from irradiated ices that are soluble and display different Raman spectral parameters that IOMs (Muñoz Caro and Schutte, 2003, Nuevo et al., 2011) or in a-C:H films that generally have a low aromaticity and in any case do not bear oxygen atoms (Dartois et al., 2004, Dartois et al., 2005). This suggests that the Nebulotron samples might be pertinent laboratory analogues for extraterrestrial organics such as IOMs and cometary C-rich grains. In details, the molecular structure of the Nebulotron samples, as well as their carbon structure, might be different from those of the IOMs or other extraterrestrial organics, and further quantification of TEM, IR and Raman data is required to demonstrate this.

As pointed out above, a perfect laboratory analogue might never be produced, but the closer they match the cosmomaterials, the more we may learn of their astrophysical context. In particular, laboratory analogues are needed to prepare space missions dedicated to the observation of Mars, asteroids or comets. They will be essential then to interpret the data coming from these missions. In such a context, the Nebulotron setup offers the possibility to produce large amounts (>50 mg) of analogue materials that can be used for further measurements and experiments such as thermal degradation experiments (Bonnet, 2012),

light-scattering measurements (Hadamcik et al., 2009) or reflectance spectro-photo-goniometric measurements (Beck et al., 2012). Such measurements are currently used to interpret the composition of the surface of asteroids (Beck et al., 2012, Cloutis et al., 1994) or comets (Hadamcik and Levasseur-Regourd, 2003, Hadamcik et al., 2007, Hadamcik et al., 2013).

The comparison between the chemical and structural features of the Nebulotron samples with those of IOMs raises several questions:

(i) **why chondritic IOMs are N-poor?**

The CO-N_2 Nebulotron samples were produced from a gas mixture having a canonical C/N ratio. As shown in the above section, these samples have much higher N content than chondritic IOM, which is N-poor. This discrepancy suggests that IOM precursors may have formed in a N-depleted environment, or, alternatively, nitrogen from N-rich precursors was lost by secondary processes, while keeping alkyl functional groups. Thermal annealing alone is not sufficient to lose enough nitrogen from N-rich precursors and cause a dramatic decrease of the alkyl abundance in the residue (Bonnet, 2012). On the other hand, IDPs and UCAMMs, that are thought to be of cometary origin, have large nitrogen amounts. This suggests that the precursors of chondritic IOMs and cometary organics were chemically different (Orthous-Daunay et al., 2013, Quirico et al., 2014).

(ii) **Where and when the polyaromatic structure of the IOM was acquired?**

Laboratory analogues that are formed at low or ambient temperatures, representative of the interstellar medium (ISM) or the outer solar system, are generally less complex, lack sufficient aromaticity and are not refractory enough (Dartois et al., 2005). Small Polycyclic Aromatic Hydrocarbons (PAHs), ubiquitous in the ISM and observed in some PPD (Chiar et al., 2013, Kamp and Kamp, 2011, Tielens, 2005), might be precursors of chondritic and cometary IOMs, but experiments are lacking. The Nebulotron experiment suggests that such a polyaromatic structure can result from a formation of organic compounds at high temperatures, i.e. > 800 K, starting from a canonical gas composition. Such high temperatures are found in the inner part of disk, and material processed in this hot region could be transported in the outer solar system (Ciesla, 2007). Such a process is not incompatible with a production of organics in the outer solar system as well, in particular if several IOM precursors exist in the PPD before the accretion of the final parent bodies. In any case, modeling is required to infer the residence times of the C-rich compounds in the different parts of the disk when transported inward or outward and the fraction of surviving materials taking into account their production and destruction processes (that are different in the different parts of the disk – pyrolysis, irradiation by UV/cosmic rays, etc.…).

(iii) **Where and when the deuterium-rich isotopic composition was acquired?**

It has been proposed that the large D enrichments measured in some carbonaceous chondrites (Bonal et al., 2013, Alexander et al., 2007) and in comets (Bockelée-Morvan et al., 1998, Jehin et al., 2009), and more generally in the solar system reservoirs compared to the protosolar nebula, are the result of ion-molecule chemistry, that took place at low (typically

< 40K) temperatures in the ISM or in the outer part of the solar system (Watson, 1974, Alexander et al., 2010, Remusat and et al., 2009, Remusat et al., 2010). Therefore, organics found in chondrites could have also formed at low temperature, but the refractory nature of these compounds can hardly be reconciled with that possibility. Alternatively, the refractory and polyaromatic core of these organics could have formed prior to deuteration, in a different environment and possibly close to the Sun, as suggested by the present experiments. Such a hypothesis calls for a high temperature synthesis. The presence of D-rich radicals in the IOM of the Orgueil meteorite supports this hypothesis (Remusat and et al., 2009). Interestingly, recent results have suggested that D enrichments observed in organics could also occur at higher temperatures, i.e. > 100 K (Thi et al., 2010). The modification of the isotopic composition on the parent body complicates the discussion, as the deuterium exchange between presumably D-rich organic molecules and an initially D-poor water ice on the parent body is not well constrained (Alexander et al., 2010, Bonal et al., 2013). Further work is needed to understand the relationships between the deuterium enrichment origin and conservation and the processes leading to the formation of refractory organics either in the ISM or in the PPD.

(iv) **Where and when the ^{15}N-rich isotopic composition was acquired?**
This point is addressed in Chapter 4.

(v) **How to explain the large noble gas content of the chondritic organic compounds and their isotopic fractionation relative to the Sun? How far is it related to the IOM formation process?**
This point is addressed in Chapter 5.

Chapter 4

Nitrogen isotopic fractionation during plasma synthesis of organic solids

Table of contents

4.1 Introduction

Nitrogen is ubiquitous in the solar system and exists as different species. Its main forms in the solar system are molecular nitrogen N_2 and ammonia NH_3, which are found in the present-day planetary atmospheres according to their oxidation degree. Nitrogen is also found in small N-bearing organic compounds such as HCN, which has been detected in Titan's atmosphere, comets' tails and in the interstellar medium (ISM). In meteorites, the macromolecular organic matter (IOM) is the main reservoir of nitrogen. Nitrogen isotopic analyses have been carried out on various solar system objects and nitrogen compounds, revealing a very large range for $^{15}N/^{14}N$ isotopic ratios through the solar system. While ^{15}N is largely depleted in the Sun, hence in the protosolar nebula ($^{15}N/^{14}N=2.27\pm0.03\times10^{-3}$, from solar wind nitrogen measurement from the Genesis mission; Marty et al., 2011, Marty et al., 2010), it is enriched in all other solar system bodies and in ISM compared to the solar reference. In comets and in the ISM, nitriles seem to concentrate ^{15}N (Hily-Blant et al., 2013, Bockelée-Morvan et al., 2008), although recent measurements of cometary NH_2^+ suggest that there is a single nitrogen isotopic composition in cometary N-bearing compounds (Rousselot et al., 2014). The largest ^{15}N-enrichments in the solar system measured so far are found in Titan's atmospheric HCN ($^{15}N/^{14}N=1.7\pm0.2\times10^{-2}$, Vinatier et al., 2007) and in the CB/CH-like chondrite Isheyevo ($^{15}N/^{14}N$ in situ up to $1.9\pm0.1\times10^{-2}$, Briani et al., 2009).

Two main models account for the formation of large ^{15}N-enrichments: (i) ion-molecule reactions under specific cold, yet dense environments (ISM or the outer solar system, Terzieva and Herbst, 2000, Aléon, 2010) and (ii) N_2 photodissociation and self-shielding in the upper atmosphere of the solar nebula, as previously proposed for CO (Clayton, 2002, Lyons et al., 2009). The large ^{15}N-enrichment observed in Titan's atmosphere has been interpreted as resulting from N_2 photodissociation associated with self-shielding. More recently, accidental predissociation during N_2 photodissociation has also been proposed as a potential mechanism responsible for the large ^{15}N-enrichments in solar system objects (Chakraborty et al., 2012, Chakraborty et al., 2013, Muskatel et al., 2011).

These nitrogen isotope variations in the solar system raise two questions:

- In meteorites, nitrogen is hosted by large and complex organic molecules, thus, how these ^{15}N-enrichments resulting from either of these fractionation mechanisms are propagated into more complex organic molecules through a chemical network, and what is the degree of conservation of the enriched isotopic composition?
- In Titan's atmosphere, aerosols produced from the photodissociation of N_2 and CH_4 are expected to represent a substantial nitrogen reservoir, thus, what is the nitrogen isotopic of these photo-produced aerosols?

To address these two questions, we have performed laboratory experiments using the Nebulotron and the PAMPRE plasma setups, dedicated to simulate photochemical processes. We aimed at investigating the nitrogen isotopic composition of N-rich organic aerosols

produced in a ionized environment from two gas mixtures composed of CO-N_2 and CH_4-N_2, in proportions that are representative of the compositions of the solar nebula and the atmosphere of Titan, respectively. The results are presented in the next section. This study has been published in EPSL (Kuga et al., 2014).

4.2 Nitrogen isotopic fractionation during abiotic synthesis of organic solid particles

Earth and Planetary Science Letters 393 (2014) 2–13

Contents lists available at ScienceDirect

Earth and Planetary Science Letters

www.elsevier.com/locate/epsl

Nitrogen isotopic fractionation during abiotic synthesis of organic solid particles

Maïa Kuga [a,*], Nathalie Carrasco [b,c], Bernard Marty [a], Yves Marrocchi [a], Sylvain Bernard [d], Thomas Rigaudier [a], Benjamin Fleury [b], Laurent Tissandier [a]

[a] CRPG-CNRS, Université de Lorraine, 15 rue Notre Dame des Pauvres, 54500 Vandoeuvre-les-Nancy, France
[b] Université de Versailles St Quentin, LATMOS, Université Paris 6 Pierre et Marie Curie, CNRS, 11 bvd d'Alembert, 78280 Guyancourt, France
[c] Institut Universitaire de France, 103 Boulevard Saint-Michel, 75005 Paris, France
[d] IMPMC, MNHM, UPMC, UMR CNRS 7590, 61 rue Buffon, 75005 Paris, France

ARTICLE INFO

Article history:
Received 23 December 2013
Received in revised form 14 February 2014
Accepted 15 February 2014
Available online xxxx
Editor: T.M. Harrison

Keywords:
nitrogen isotopes, organics
plasma
Solar System
Titan's atmosphere
early Earth

ABSTRACT

The formation of organic compounds is generally assumed to result from abiotic processes in the Solar System, with the exception of biogenic organics on Earth. Nitrogen-bearing organics are of particular interest, notably for prebiotic perspectives but also for overall comprehension of organic formation in the young Solar System and in planetary atmospheres. We have investigated abiotic synthesis of organics upon plasma discharge, with special attention to N isotope fractionation. Organic aerosols were synthesized from N_2–CH_4 and N_2–CO gaseous mixtures using low-pressure plasma discharge experiments, aimed at simulating chemistry occurring in Titan's atmosphere and in the protosolar nebula, respectively. The nitrogen content, the N speciation and the N isotopic composition were analyzed in the resulting organic aerosols. Nitrogen is efficiently incorporated into the synthesized solids, independently of the oxidation degree, of the N_2 content of the starting gas mixture, and of the nitrogen speciation in the aerosols. The aerosols are depleted in ^{15}N by 15–25‰ relative to the initial N_2 gas, whatever the experimental setup is. Such an isotopic fractionation is attributed to mass-dependent kinetic effect(s).
Nitrogen isotope fractionation upon electric discharge cannot account for the large N isotope variations observed among Solar System objects and reservoirs. Extreme N isotope signatures in the Solar System are more likely the result of self-shielding during N_2 photodissociation, exotic effect during photodissociation of N_2 and/or low temperature ion-molecule isotope exchange. Kinetic N isotope fractionation may play a significant role in the Titan's atmosphere. On the Titan's night side, ^{15}N-depletion resulting from electron driven reactions may counterbalance photo-induced ^{15}N enrichments occurring on the day's side. We also suggest that the low $\delta^{15}N$ values of Archaean organic matter (Beaumont and Robert, 1999) are partly the result of abiotic synthesis of organics that occurred at that time, and that the subsequent development of the biosphere resulted in shifts of $\delta^{15}N$ towards higher values.

1. Introduction

Organic compounds are widely distributed in the Solar System, from very simple to more complex molecules. In contrast to what happen on Earth where organic matter has been mostly synthesized by life since the Archaean, and possibly, the Hadean, eon(s), the formation of organic compounds is generally assumed to result from abiotic processes in the Solar System. Extraterrestrial organics are found mostly as amino-acids and kerogen-like material in primitive meteorites and as organic haze in planetary atmospheres such as Titan's. Among such organic molecules, the nitrogen-bearing ones are of particular prebiotic interest, as nitrogen is a key element of proteins and nucleic acids. Furthermore, nitrogen seems to play a pivotal role during the production of organic aerosols in the N_2-rich atmosphere of Titan (Israël et al., 2005; Carrasco et al., 2013).

Nitrogen has two stable isotopes, ^{14}N and ^{15}N. The $^{15}N/^{14}N$ ratio (3.676×10^{-3} for the terrestrial atmospheric N_2) is often expressed in permil deviation to terrestrial atmospheric N_2 isotope composition (AIR) as $\delta^{15}N = [(^{15}N/N)_{sample}/(^{15}N/^{14}N)_{AIR} - 1] \times 1000$ (in ‰). Relative abundances of ^{14}N and ^{15}N fractionate upon physical, chemical and biological transformations of N-bearing

* Corresponding author.
E-mail address: mkuga@crpg.cnrs-nancy.fr (M. Kuga).

http://dx.doi.org/10.1016/j.epsl.2014.02.037
0012-821X/

compounds. Remarkably, the isotopic composition of nitrogen presents dramatic variations among Solar System objects and reservoirs, which are not fully understood. N_2 was probably the main N-bearing species in the protosolar nebula (PSN, Grossman, 1972) and was ^{15}N-poor ($^{15}N/^{14}N = 2.27 \pm 0.03 \times 10^{-3}$, that is, $\delta^{15}N = -383 \pm 8‰$; Marty et al., 2011) whereas all other objects and reservoirs of the Solar System (with the exception of a few like Jupiter's atmosphere) are richer in ^{15}N by several hundreds to thousands of permil. Most meteorite families and the inner planetary bodies including the Earth have comparable $\delta^{15}N$ values within a few tens of ‰ whereas cometary CN and HCN are enriched in ^{15}N by a factor of 3 relative to the PSN value (Bockelée-Morvan et al., 2008). ^{15}N enrichments can be dramatic at the micron scale in meteoritic organics, with $\delta^{15}N$ values up to 5000‰ (Briani et al., 2009). Some of these enrichments may be related to atmospheric processing, as proposed for the atmosphere of Mars ($\delta^{15}N_{N2} = +660‰$, Owen et al., 1977), but in other cases these ^{15}N enrichments relative to the PSN nitrogen require other types of extensive isotope fractionation that are poorly understood.

Exothermic ion-molecule reactions at low temperature might have led to extensive N isotope fractionation under specific cold yet dense environments (e.g., dense cores, outer Solar System, Terzieva and Herbst, 2000; Rodgers and Charnley, 2008; Aleon, 2010; Hily-Blant et al., 2013). Alternatively, photodissociation of N_2 associated or not to self-shielding (Clayton, 2002; Lyons et al., 2009; Chakraborty et al., 2013), might have led to ^{15}N-rich radicals prone to incorporation into forming organics. Such a photochemical induced fractionation has been invoked to address the ^{15}N-rich HCN relative to N_2 in Titan's atmosphere (Vinatier et al., 2007; Liang et al., 2007; Croteau et al., 2011). However, those theoretical studies have focused on the isotopic composition of very simple gaseous N-bearing compounds, and the propagation and conservation of such a large N isotopic fractionation upon polymerization of organic solids has not yet been fully investigated.

Several experimental works have simulated the synthesis of gaseous and solid organic compounds in gas mixtures similar to Titan's atmosphere (see Coll et al., 2013, for a review) early Earth's atmosphere (Miller, 1953; Chang et al., 1983) or the PSN (Dzizckniec and Lumkin, 1981; Kerridge et al., 1989), either by UV photons or by electron energy deposition. However, only a few of them have focused on the nitrogen incorporation into refractory organics from N_2 dissociation (Trainer et al., 2012; Gautier, 2013), and the extent of related N isotope fractionation is essentially undocumented.

Whatever the original mechanism of isotope selection, N_2 dissociation and nitrogen compound ionization are believed to play an important yet not fully understood role. Plasmas were used in the present study because of the strong covalent bond of N_2, which needs energies above 9.8 eV (<120 nm) to break. Recent experimental simulations have used VUV photons as incident energy but production of aerosols was not reported (Imanaka and Smith, 2010; Peng et al., 2013). So far, electron energy deposition stays the easiest energy source to simulate aerosol productions from irradiated gas mixtures. Here, we investigate the isotopic fractionation of nitrogen during synthesis of solid organics by plasma discharge using N_2–CH_4 and N_2–CO gaseous mixtures as proxies of Titan's atmosphere and the PSN, respectively.

2. Experimental methods

2.1. Aerosols production setups

Two experimental plasma setups were used for this study in order to produce nitrogen-rich aerosols: (i) the PAMPRE experiment (LATMOS, Guyancourt, France), designed to investigate Titan's ionosphere processes; and (ii) the Nebulotron experiment (CRPG, Nancy, France), dedicated to simulate young solar nebula processes. Main experimental conditions and plasma characteristics are described below and in Table 1.

Table 1
Qualitative comparison of the two plasma setups used in this study.

	PAMPRE	Nebulotron
Gas mixture	N_2 (90–99%)–CH_4	N_2 (20%)–CO
Type of electric discharge	RF (13.56 MHz)	microwave (2.45 GHz)
Size of the reactor (height ∗ diameter)	40 ∗ 30 cm	10 ∗ 0.8 cm
Volume of the plasma (cm^3)	740	2.5
Injected power (W)	30	30
W/cm^3	0.04	12
Pressure (mbar)	0.9	∼1
Neutral temperature	300–350 K[a]	⩾1000 K (estimated[c,d])
Electron density (cm^{-3})	2×10^8[a]	5×10^{10}–1×10^{11} (estimated[d])
Average electron energy	2 eV[b]	2 eV (estimated[d])

[a] Alcouffe et al. (2010).
[b] Alves et al. (2012).
[c] Es-Sebbar et al. (2009).
[d] Gries et al. (2009).

2.1.1. The PAMPRE experiment

The PAMPRE (for *Production d'Aérosols en Microgravité par Plasma REactif*) experiment consists of a stainless steel reaction chamber, where a radiofrequency discharge (RF, 13.56 MHz) is generated between two electrodes in a metallic cage confining the plasma (Sciamma-O'Brien et al., 2010; Szopa et al., 2006, Fig. 1a).

A gas mixture of high purity N_2 and CH_4 is flowed continuously through the plasma discharge in which electrons dissociate and ionize N_2 and CH_4. This initiates chemical reactions and molecular growth that results in the production of hydrocarbons and N-bearing molecules that eventually end up forming solid particles. These solid particles grow up in suspension in the plasma and fall in a glass vessel surrounding the metallic cage. After typical runs of 8 h, the produced solid particles, orange to brown in color, are collected for ex-situ analysis.

In this work, experiments were performed with a continuous 55 sccm (standard cubic centimeter per minute) N_2–CH_4 gas flow, containing 1%, 2%, 5% and 10% CH_4 in N_2. These gas proportions are representative of the composition of Titan's atmosphere (Niemann et al., 2005; Waite et al., 2005). For all experimental conditions, the injected RF power was fixed to 30 W, the pressure in the reactor was 0.9 mbar and the neutral gas temperature, measured by Alcouffe et al. (2010), ranged from 310 to 340 K depending on experimental conditions (Tables 1 and 2).

2.1.2. The Nebulotron experiment

The second experimental setup used in this study, the Nebulotron (CRPG–CNRS), consists of a vacuum glass line in which adjustable gas mixtures can be flowed through a microwave (2.45 GHz) plasma discharge (Robert et al., 2011). The aim of this setup is to simulate processes occurring in a CO–N_2 atmosphere. CO and N_2 are believed to have been the main gaseous species hosting C and N in the protosolar nebula (Grossman, 1972). The experimental setup consists of a quartz reactor (Fig. 1b) where a gas mixture of CO (purity 99.5%) and N_2 (purity 99.995%) is flowed continuously through the plasma discharge at a pressure of 1 mbar. As for the PAMPRE experiment, electrons dissociate and ionize N_2 and CO. In this setup however, organic aerosols grow up on the quartz tube surfaces that are cooled down by compressed air. After a typical 6 hours-long experiment, the plasma is turned off and the glass line is pumped out for 12 hours before opening the reactor to atmospheric pressure. The orange to dark solids are then recovered by gently scratching the quartz tube and stored in microvials for

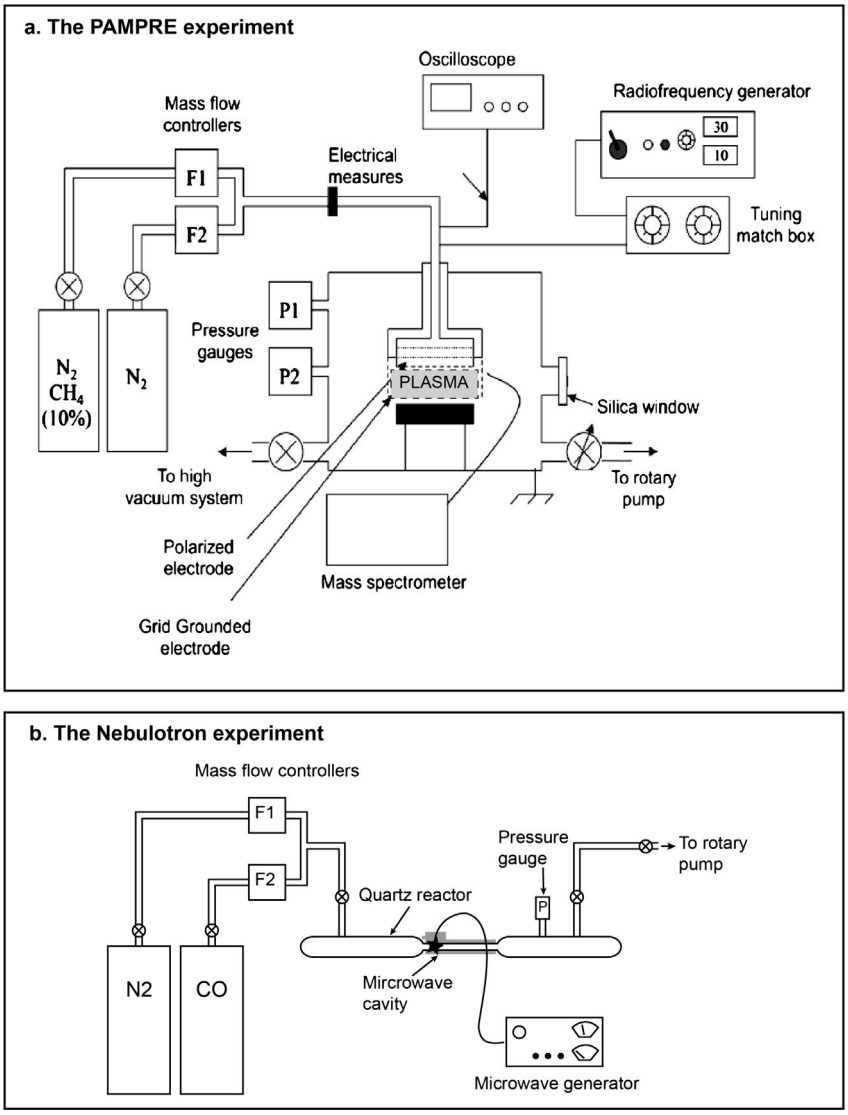

Fig. 1. Schematics of the PAMPRE (a) and the Nebulotron (b) experimental setups.

Table 2
Experimental conditions of aerosol production in the PAMPRE and Nebulotron setups.

a. The PAMPRE experiment (N_2–CH_4)

%CH_4 i	%CH_4 ss[a]	Gas flow rate (sccm)	Power input (W)	Pressure (mbar)	Aerosols production rate (mg h^{-1})[a]
1	0.18 ± 0.01	55	30	0.9	18
2	0.42 ± 0.01	55	30	0.9	32
5	1.80 ± 0.03	55	30	0.9	33
10	5.53 ± 0.05	55	30	0.9	4

b. The Nebulotron experiment (N_2–CO)

%CO i	%CO ss	Gas flow rate (sccm)	Power input (W)	Pressure (mbar)	Aerosols production rate (mg h^{-1})
80	nm	6	30	1	6

nm = not measured, i = initial, ss = at steady state, sccm = standard c^3/min.
[a] Sciamma O'Brien et al. (2010).

ex-situ analysis. As for the PAMPRE setup, not all the solids produced can be collected and the mass production rates presented here (Table 2) must be considered as minimum values. No leak has been detected on the Nebulotron reactor when isolated from the pumping group and from the gas injection system. Nonetheless, contrary to the PAMPRE setup, this one is not fitted with a secondary turbo pump, allowing a 10^{-2} mbar limit vacuum only. This does not allow for sufficient desorption of water adsorbed on the reactor walls. This expected water contamination is discussed in Section 3.1. So far, the electronic features of the Nebulotron plasma setup have not been characterized yet but, as the volume of the plasma is much smaller than for the PAMPRE experiment, with a similar input power (30 W, Table 1), the temperature of neutral gases and the electron density in the Nebulotron setup are expected to be higher than in the PAMPRE plasma (Fridman, 2008; Es-Sebbar et al., 2009; Gries et al., 2009).

Here, a 6 hour-long experiment was performed with a 30 W injected power and a 6 sccm CO–N_2 gas mixture containing 80% CO in N_2 (Table 2). This experimental C/N ratio is comparable to what is estimated for the protosolar nebula (Lodders, 2003).

2.2. Elemental composition analysis of the aerosols

The elemental composition (C, H, N and O) of the Nebulotron aerosols has been analyzed at the Service d'Analyses Elementaires (Université de Lorraine, France) by combustion and pyrolysis tech-

niques. The PAMPRE aerosol elemental composition was measured and reported previously by Sciamma-O'Brien et al. (2010).

2.3. Carbon- and nitrogen-edge XANES analysis

Measurements were done using the STXM (*Scanning Transmission X-Ray Microscopy*) located on beamline 5.3.2.2 (Polymer STXM beamline – Kilcoyne et al., 2003) at the Advanced Light Source (ALS, Berkeley, USA). This beamline uses soft X-rays (250–600 eV) generated via a bending magnet while the electron current in the storage ring is held constant in top-off mode at 500 mA at a storage ring energy of 1.9 GeV. The microscope chamber was evacuated to 0.1 mbar after sample insertion and back-filled with helium. The energy calibration was carried out using the well-resolved 3p Rydberg peak at 294.96 eV of gaseous CO_2 for the C K-edge. In order to obtain partly X-ray transparent samples which do not completely absorb the incident light at the C and N K-edges, the PAMPRE and Nebulotron aerosols have been finely ground and deposited on SiN windows. The C- and N-XANES data shown here have been collected following the procedures for X-ray microscopy studies of radiation sensitive samples recommended by Wang et al. (2009). Alignment of images of stacks and extraction of XANES spectra were done using the aXis2000 software (ver2.1n). Normalization and determination of spectral peak positions were determined using the Athena software package (Ravel and Newville, 2005). Extensive databases of reference C- and N-XANES spectra are available for organic compounds (e.g., Leinweber et al., 2007; Solomon et al., 2009).

2.4. Nitrogen isotope analysis techniques

2.4.1. Nitrogen isotopic ratio in the N_2 initial gases

Two N_2 tanks were used in the PAMPRE experiment: pure N_2 and a N_2–CH_4 mixture (90–10%), which were mixed up in the flow in order to get 1, 2, 5 and 10% CH_4 in the initial gas mixture. One tank of pure N_2 was used in the Nebulotron setup, which was mixed up with pure CO. The isotopic compositions of the two pure N_2 tanks (PAMPRE and Nebulotron) were obtained by filling a glass vessel with N_2 gases from the respective tanks and by analyzing it by dual-inlet technique on a MAT253 mass-spectrometer at CRPG (Nancy, France).

The N_2–CH_4 tank used in the PAMPRE experiment could not be directly measured because of its high CH_4 content. In order to remove CH_4 from the N_2, an aliquot of this mixture was oxidized during 45 min in a CuO furnace at 900 °C to oxidize CH_4 into CO_2, which was then removed by adsorption on a cold trap held at −172 °C. The CuO furnace was then cooled down to 450 °C and the purified N_2 gas was transferred to a Cu furnace at 600 °C in order to trap residual oxygen that could still be present in the line. The yield of the purification was close to 100% thus implying no isotope fractionation effect during purification. The purified N_2 was then measured by dual-inlet mass spectrometry for its isotopic composition.

Data were normalized against the NSVEC-air standard (International Atomic Energy Agency, Vienna, Austria). Blanks were negligible and errors (±0.04‰ on $\delta^{15}N$, 1σ) include external reproducibilities on the standards and on the samples obtained following 10 analyses of each gas.

2.4.2. Bulk nitrogen content and isotopic ratio of aerosols by EA-IRMS

Bulk measurements of nitrogen content and isotopic ratio of aerosols were performed with an elemental analyzer (EuroVector) coupled to an isotope ratio mass spectrometer (IsoPrime, GV Instruments) at CRPG (Nancy, France). N_2 (purity 99.999%) was used as the reference gas. The elemental analyzer was calibrated with urea (46.65% N), glutamic acid (9.52% N) and ammonium sulphate (21.2% N) for nitrogen in the range of 0.04–0.18 mg. Certified nitrogen isotopic standards (IAEA-N-1, $\delta^{15}N = 0.4 \pm 0.2$‰ and USGS-25, $\delta^{15}N = -30.4 \pm 0.4$‰, International Atomic Energy Agency, Vienna, Austria) were used to calibrate the mass spectrometer and correct sample isotopic ratios. Two aliquots of each aerosol sample was analyzed and bracketed by several standards (elemental and isotopic standards) analysis. The external reproducibility of isotopic standards was 0.2‰ (1σ) on the $\delta^{15}N$ values.

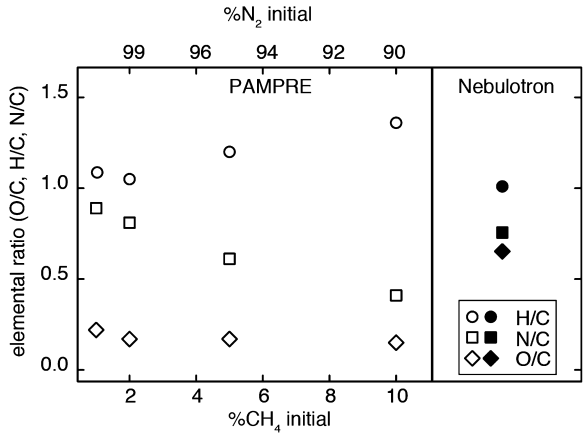

Fig. 2. Elemental composition of the PAMPRE (open symbols) and Nebulotron (filled symbols) experiments. Elemental ratios of the PAMPRE aerosols are presented as a function of the initial CH_4 concentration in the gas mixture (data from Sciamma-O'Brien et al., 2010). Error bars are smaller than the symbol sizes.

2.4.3. Stepwise pyrolysis extraction and static mass spectrometry

We used a static stepwise pyrolysis extraction and a static mass spectrometry method (Marty and Humbert, 1997) in order to check the evolution of the nitrogen isotopic composition of aerosols during their thermal degradation. Aerosols were wrapped in Pt foil and pre-heated at 100 °C for 24 h under high vacuum ($<10^{-8}$ mbar) before extraction. Aerosols were thermally degraded by stepwise pyrolysis up to 950 °C (3 to 5 steps, each of 20 min long) in a double-walled quartz tubing furnace (Yokochi et al., 2009). Extracted gases were purified by oxidation through a CuO furnace at 800 °C. Most oxidized gases were removed using a cold trap held at −172 °C, and only NO_x compounds and minor amounts of CO and organic volatiles remained in the purification line. The CuO furnace was then cooled to 450 °C to reduce NO_x to N_2. Purified N_2 was then expanded and analyzed in a mass spectrometer working in static mode (Marty and Humbert, 1997; Marty and Zimmermann, 1999). $\delta^{15}N$ external reproducibility on air standards was 1.8‰ (1σ). Blanks were less than 1% of the samples. Two samples from the PAMPRE experiment (1% and 5% CH_4) and an aliquot of the Nebulotron aerosols were analyzed with this technique (Fig. 5).

3. Results

3.1. Elemental composition of aerosols: H/C, N/C and O/C ratios

Fig. 2 shows the H/C, N/C and O/C ratios of the Nebulotron aerosols, as well as the previously reported data by Sciamma-O'Brien et al. (2010) for the PAMPRE aerosols. Interestingly, the H/C values of the PAMPRE aerosols increase while their N/C values decrease with increasing CH_4 concentration in the initial gas mixture. The oxygen content of these aerosols is interpreted as resulting from water adsorption and/or from partial oxidation in air after recovery (Sciamma-O'Brien et al., 2010). In contrast to the PAMPRE aerosols, the Nebulotron aerosols are characterized by a high O/C ratio, consistently with the high initial concentration of CO. As no

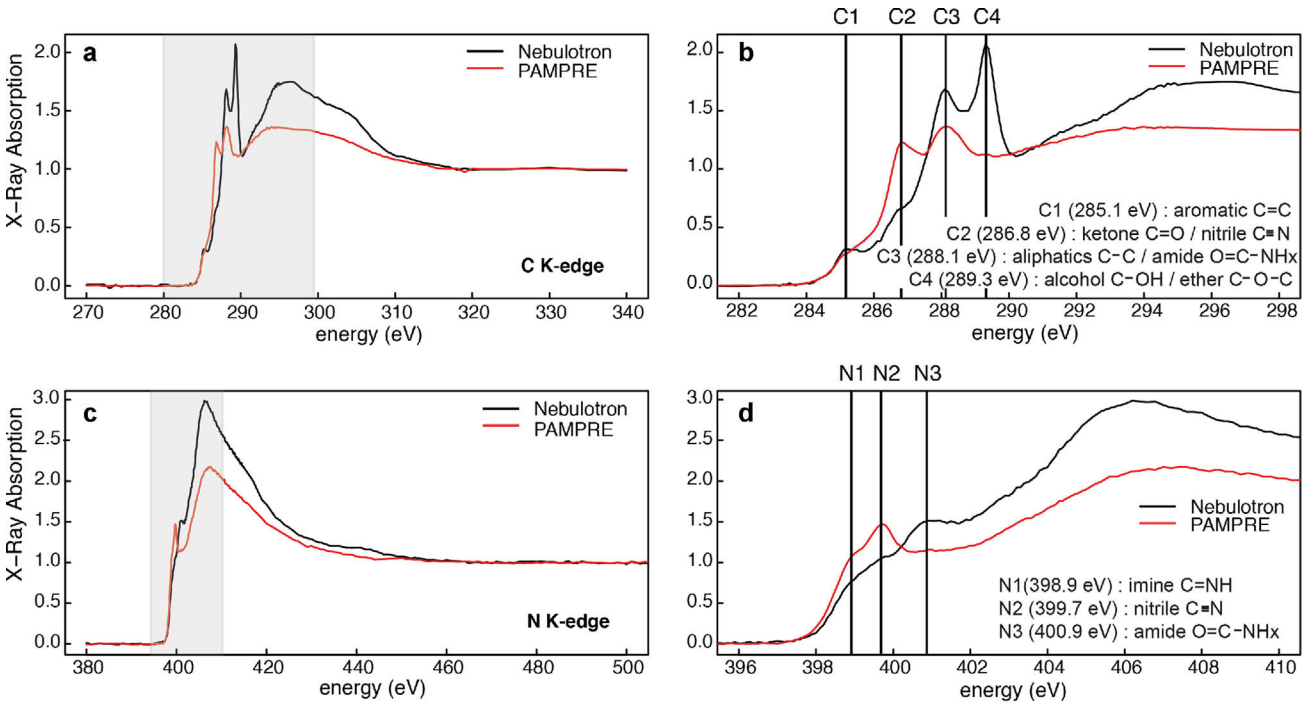

Fig. 3. XANES spectra and band assignment in the C and N K-edges ((a) and (c) respectively) of the PAMPRE (5% initial CH_4) and Nebulotron aerosols. (b) and (d) are a zoom of the shaded area in the (a) and (c) plots respectively.

hydrogen was present in the CO–N_2 gas mixture of the Nebulotron experiment, the high H/C value of the Nebulotron aerosols may only come from water contamination. Indeed, as suggested before, the complete removing of the water adsorbed on the reactor walls would have required baking the reactor and secondary pumping. Moreover, solids that are produced in plasmas are known to be highly reactive: water adsorption on the Nebulotron solids when put out to the atmosphere cannot be excluded. The Nebulotron and the PAMPRE aerosols exhibit similar N/C ratios despite an initial N_2 concentration in the Nebulotron experiment ~5 times lower than in the PAMPRE one. This highlights a nitrogen incorporation from gas to solid much more efficient in the Nebulotron setup than in the PAMPRE one, probably due to the higher energy to volume ratio in the former relative to the PAMPRE one (Table 1).

3.2. STXM based XANES spectroscopy: carbon and nitrogen speciation

Synchrotron-based XANES spectroscopy at the C and N K-edges provides key insights on carbon and nitrogen speciation in the PAMPRE and Nebulotron aerosols. These two aerosol mixtures are spectroscopically very homogeneous: over 20 particles of each aerosol, 19 exhibit very similar C- and N-XANES spectra. Representative C- and N-XANES spectra are shown in Fig. 3.

At the C K-edge, the low intensity of the absorption feature that can be seen in both samples at 285.1 eV (C1) is commonly attributed to electronic transitions of aromatic or olefinic carbon groups (C=C) (Bernard et al., 2010a; Bernard et al., 2010b). This is consistent with the previous chemical studies which have pointed out an organic structure dominated by methyl groups and sp^2 carbons; and a lack or low abundance of any protonated aromatic or heteroaromatic rings in the PAMPRE aerosols (Quirico et al., 2008; Derenne et al., 2012). The peak at 286.8 eV (C2), identified in C-XANES spectra of both samples, is generally assigned to electronic transitions of ketonic or phenolic groups (C=O) and/or nitrile groups (C≡N) (Cody et al., 2008; Solomon et al., 2009). Both functions may be present within Nebulotron areosols, while only nitrile groups contribute to this peak in spectra of PAMPRE aerosols as attested by Infra-Red spectroscopy data (Quirico et al., 2008; Gautier et al., 2012). The peak at 288.1 eV (C3), also seen in spectra of both types of aerosols, is usually assigned to electronic transitions of amidyl groups (CO–NH_x) (Cody et al., 2008; Nuevo et al., 2011) and/or aliphatics (CH_{1-3}) (Bernard et al., 2012a; Bernard et al., 2012b; Buijnsters et al., 2012). In contrast to the sharp and intense peak that can be seen in the spectra of the Nebulotron aerosols, for which both of these functionalities may contribute, the broader absorption feature located at 288.1 eV in spectra of the PAMPRE aerosols can only be related to the absorption of various types of aliphatics, mostly connected to nitrogen atoms as indicated by FTIR and NMR data (Quirico et al., 2008; Gautier et al., 2012; Derenne et al., 2012). Finally, the peak located at 289.3 eV (C4), only observed in spectra of Nebulotron aerosols, is attributed to electronic transitions of hydroxylated- or ether-linked C species (Cody et al., 2008; Solomon et al., 2009), confirming the oxidized nature of these aerosols.

These results notably show that a part of the hydrogen incorporated into the Nebulotron aerosols is linked to carbon atoms in aliphatic and aromatic functions. This confirms the dissociation of a hydrogenated molecule, most probably H_2O, and further active chemistry to form C–H bonds into the plasma. Even if H_2O partial pressure in the plasma is small, hydrogen is probably very efficiently incorporated into the organic structure, for which hydrogen is necessary to build organic bonds and for polymerization. The presence of terminal −OH functions (C4 peak) in the Nebulotron aerosols' spectra likely traces oxidation and water adsorption on the aerosols' surface when they are extracted from the reactor.

At the N K-edge, three main peaks have been identified in the N-XANES spectra of the PAMPRE and Nebulotron aerosols at 398.1 eV (N1), 399.7 eV (N2) and ~401 eV (N3) (Mitra-Kirtley et al., 1993; Mullins et al., 1993; Leinweber et al., 2007; Cody et al., 2008; Nuevo et al., 2011). These peaks can be attributed to electron transitions of imine (C=N), nitrile (C≡N) and amidyl groups (CO–NH_x), respectively. Nitrogen-bearing heterocycles may also contribute to those peaks (Mitra-Kirtley et al., 1993, and references therein). Saturated amines have been identified in the PAMPRE aerosols in FTIR data (Quirico et al., 2008; Gautier et al., 2012). In XANES spectra, saturated amines generally appear at ~406 eV

Table 3
Nitrogen isotopic composition in initial gas mixtures and aerosols from the PAMPRE and Nebulotron experiments from EA-IRMS measurements.

Experimental setup	Initial gas mixture	δ^{15}N (‰) initial N_2[a]	σ	δ^{15}N (‰) aerosols	σ	Δ^{15}N (‰) aerosols[b]	σ
PAMPRE	CH_4–N_2 (10–90)	−3.18	0.04	−17.8	0.2	−14.6	0.2
PAMPRE	CH_4–N_2 (5–95)	−3.42	0.04	−24.6	0.2	−21.2	0.2
PAMPRE	CH_4–N_2 (2–98)	−3.56	0.04	−26.0	0.2	−22.4	0.2
PAMPRE	CH_4–N_2 (1–99)	−3.60	0.04	−28.1	0.2	−25.5	0.2
Nebulotron	CO-N_2 (80-20)	−3.4	0.2	−26.2	0.2	−22.8	0.2

[a] The δ^{15}N of N_2 of the initial the gas mixture for the four PAMPRE experiments has been calculated by mass balance between the δ^{15}N of the two tanks which are -3.65 ± 0.04‰ and -3.18 ± 0.04‰ for the N_2 tank and the No–CH, tank respectively.
[b] Δ^{15}N gas − aerosols = δ^{15}N aerosols − δ^{15}N gas.

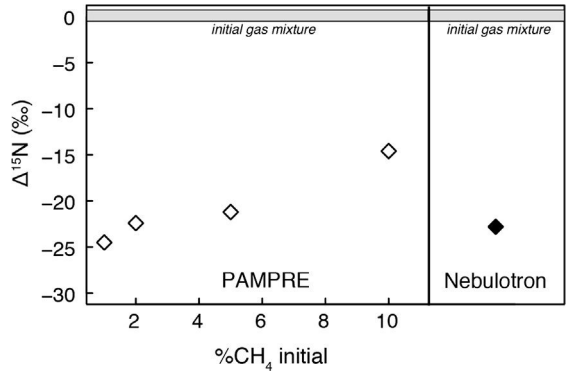

Fig. 4. Bulk nitrogen isotopic composition of the PAMPRE (open diamonds) and Nebulotron (filled diamonds) aerosols, expressed as a Δ^{15}N (in ‰) relative to the isotopic composition of the initial N_2 gas (represented by the shaded area). Δ^{15}N of the PAMPRE aerosols is presented as a function of the initial CH_4 concentration in the gas mixture. Error bars (1σ) are smaller than the symbol sizes.

(Mitra-Kirtley et al., 1993; Mullins et al., 1993) and their contribution to the Nebulotron and the PAMPRE aerosols spectra is certainly masked by the diffuse absorption observed at the same energy likely corresponding to highly delocalized excited states or to the overlapping contribution of electronic and atomic resonances (Feshbach resonances, Stöhr, 1992).

Interestingly, although nitrogen in the Nebulotron aerosols appears to be mainly within amidyl groups whereas the PAMPRE aerosols are richer in imine and nitrile groups, nitrogen seems entirely linked to C or H atoms, as no N–O functionalities have been identified. This suggests that –NH and –CN bonds are favored despite the high oxygen content in the starting gas mixture of the Nebulotron. Thus, the volatile precursors of the nitrogen incorporation into the aerosols might be comparable in the Nebulotron and the PAMPRE experiments.

3.3. Nitrogen isotopic composition of aerosols

Because the nitrogen isotopic ratio of initial N_2 in the experimental gas mixtures is slightly different from that of air ($\delta^{15}N = 0$‰ by definition), we use the Δ notation, which represents the difference between the isotopic composition of the products (aerosols) and that of the reactant (initial gas mixture):

$$\Delta^{15}N = \delta^{15}N\text{-aerosols} - \delta^{15}N\text{-initial gas (in ‰)}$$

The δ^{15}N values measured by EA-IRMS for the experimental aerosols from the PAMPRE and the Nebulotron setups and the corresponding Δ^{15}N values are reported in Table 3.

All aerosols show a systematic depletion in the heavier nitrogen isotope ^{15}N compared to the initial gas N_2, with Δ^{15}N ranging from −15 to −25‰ whatever the setup used (Fig. 4). Previous Δ^{15}N values of −3 to −17‰ for nitrogen trapped in plasma-synthesized organics were reported by Kerridge et al., 1989. However, neither these data nor the experimental setup were discussed. Step-heating data (Table 4, Fig. 5) confirm such negative values and show overall a good homogeneity for N isotope fractionation, except for the lowest temperature step of the Nebulotron experiment (Fig. 5, top panel), which value is closer to air and may result from atmospheric nitrogen contamination.

Overall, isotopic data from step-heating and bulk measurements show a remarkable consistency, implying that these organic aerosols are globally isotopically homogeneous, whatever the setup production and the oxidation degree of the initial gas mixture.

4. Discussion and implications

4.1. Origin of the nitrogen isotopic fractionation in plasma experiments

The PAMPRE and the Nebulotron aerosols share comparable ^{15}N depletions relative to the initial N_2 gas around −20‰, although experimental setups have different geometry, carbon source and electric discharge characteristics. This heavy isotope depletion is relatively large compared to the natural nitrogen isotopic variations observed in terrestrial organic molecules or geological objects, for which δ^{15}N lower than −10‰ are rare (Coplen et al., 2002). No such ^{15}N-depleted values were reported for abiotic and open-system experiments comparable to the PAMPRE and Nebulotron simulations performed in the present study.

However, the experimental nitrogen isotopic fractionation measured in this study is small compared to the large isotopic variations that are observed in planetary atmospheres, e.g., Titan, or among primitive reservoirs and objects of the Solar System, To explain such variations, several studies have focused on the dissociation of N_2 by photons in the far UV range (Liang et al., 2007; Croteau et al., 2011; Lyons et al., 2009; Chakraborty et al., 2013). Photodissociation of N_2 could lead in principle to large ^{15}N enrichments (several 100 to several 1000‰) either by (i) isotopic selective photoabsorption and further self-shielding of N_2 in a dense atmosphere (Liang et al., 2007; Lyons et al., 2009) and/or by (ii) indirect (also called accidental) predissociation of N_2 excited states (Lorquet and Lorquet, 1974; Lefebvre-Brion and Field, 2004; van de Runstraat et al., 1974; Muskatel et al., 2011). In contrast, in the present study, (i) the N isotope fractionation leads to compounds depleted, and not enriched, in ^{15}N, and (ii) the isotopic effect is much more modest than expected to account for N isotope variations in the Solar System.

In plasmas, N_2 dissociation mostly occurs via (i) electron impact at electron energies above the dissociation threshold of N_2 (9.8 eV) and (ii) heavy particles collisions (Fridman, 2008; Alves et al., 2012). As electron energy of impacting electrons is continuous and not quantified as for photons, several excited states of atoms and molecules can be reached by electron impact in plasmas. As a result, electron impact cross-sections of N_2 dissociation are not as structured as photoabsorption cross-sections (Zipf and McLaughlin, 1978). Because of the continuous distribution of electron energies, $^{14}N_2$ and $^{14}N^{15}N$ dissociation rates should not be

Table 4
Nitrogen isotopic composition in aerosols from the PAMPRE and Nebulotron experiments from step-heating and static mass-spectrometry measurements.

Sample	Mass (μg)	Extraction temperature (°C)	N (moles) $\times 10^8$	σ	% of total N extracted	δ^{15}N air (‰)	σ
PAMPRE (5% CH_4) (N_2–CH_4)	66	150	0.024	0.001	0.07	−24.5	2.8
		420	1.40	0.04	4.0	−23.8	2.4
		650	4.30	0.12	12.2	−20.5	2.0
		900	19.5	0.5	55.4	−26.9	2.1
		950	10.0	0.3	28.4	−20.0	2.2
						−24.1[a]	**2.1**
PAMPRE (1% CH_4) (N_2–CH_4)	47	185	0.004	1.10^{-4}	0.01	*−16.91*[b]	*24.3*
		500	4.16	0.11	8.5	−28.6	2.1
		900	33.0	0.9	67.8	−29.9	2.8
		930	11.5	0.3	23.6	−29.4	2.4
						−29.7	**2.7**
Nebulotron (CO–N_2)	79	150	0.001	3.10^5	0.01	*−1.4*	*47.4*
		420	0.59	0.02	3.6	−18.9	2.5
		650	10.8	0.3	65.7	−23.7	2.2
		800	1.52	0.04	9.2	−25.5	2.0
		930	3.53	0.1	21.5	−27.3	2.1
						−24.4	**2.1**

[a] Bold values: δ^{15}N weighted average upon heating-steps.
[b] Italic values: extracted nitrogen was too low and blank contribution exceeded 10% of the analyzed nitrogen.

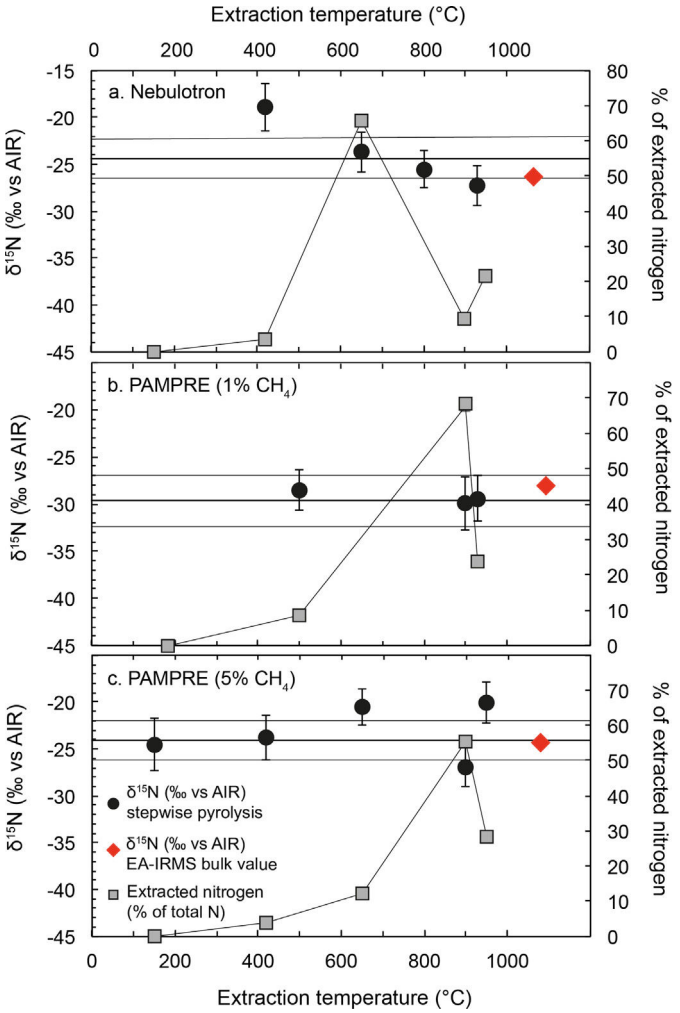

Fig. 5. Nitrogen isotopic composition (δ^{15}N in ‰, left axis, *dark circles*) and quantity of released nitrogen (in % of total nitrogen extracted, right axis, *gray squares*) as a function of pyrolysis temperature of the Nebulotron and the PAMPRE aerosols. *Solid lines*: weighted average and standard deviation of the nitrogen isotopic ratios over all extraction steps. *Red diamonds*: EA-IRMS bulk δ^{15}N measurements (error bars (1σ) are smaller than the symbol size).

different. Moreover, atoms and molecules in plasma are not subjected to self-shielding, as electrons are isotropically produced by the electric discharge, in contrast to what occur in photon-induced reactions.

Although indirect predissociation of N_2 might be invoked, this scenario has never been documented in plasma electron energy ranges (0–20 eV) relevant to the present study. In any case, this dissociation mechanism is quite rare in plasma, and isolated events may certainly not affect the final nitrogen isotopic composition of aerosols, even with an isotopic fractionation of a few thousands of ‰ (Muskatel et al., 2011).

Hence, other processes are responsible for the ^{15}N-depletion observed in the Nebulotron and PAMPRE aerosols. These ^{15}N-depleted values may result from one or several fractionation processes all along the reaction chain that leads to aerosol formation favoring the light ^{14}N isotope to be produced in the plasma by N_2 dissociation and/or isotopically light molecules to be incorporated into the aerosols via polymerization of gaseous precursors. Because the two setups and both type of aerosols are very different (e.g., elemental abundances and XANES characteristics) the fractionation process(es) must be independent of the chemistry and the oxidation degree of the environment.

Kinetic Isotopic Fractionation (KIF, O'Neil, 1986; Li et al., 2009) is likely to occur during such experiments, as the plasmas used in the present study are out of equilibrium. Chemical reactions occurring in the gas phase and during aerosol polymerization are largely controlled by kinetic competitions (Fridman, 2008). KIF during aerosol polymerization was already invoked to account for the ^{13}C isotopic fractionation observed in plasma-synthesized carbonaceous solids (Des Marais et al., 1981; Chang et al., 1983).

KIF is a mass-dependent fractionation process. Considering two molecules, A–^{14}N and B–^{15}N, isotopically substituted, and assuming, to a first approximation, a Maxwell–Boltzmann distribution of velocities in the gas phase in our plasma setups, the KIF α factor can be written as:

$$\alpha = \frac{k_B}{k_A} \approx \frac{\langle v_B \rangle}{\langle v_A \rangle}$$

with k being the reaction coefficient and v the average relative velocity within the gas.

The molecular velocity v will be proportional to $T^{1/2}$ and $m^{-1/2}$, with T and m being the gas temperature and the mass of

the molecule, respectively. For an isothermal gas, α is then equal to:

$$\alpha = \frac{k_B}{k_A} \approx \sqrt{\frac{m_A}{m_B}}$$

An ε value (in ‰) commonly defines the isotopic enhancement (or depletion depending on the value of α relative to 1) related to an isotopic fractionation factor α as:

$$\varepsilon = (\alpha - 1) \times 1000$$

ε is the theoretical equivalent of our experimental Δ^{15}N mentioned above.

As a result, the ^{14}N-substituted molecules will react faster than the ^{15}N-substituted ones. Furthermore, the isotopic fractionation ε will be larger if low mass molecules are reacting.

The Nebulotron and the PAMPRE aerosols have N isotopic fractionations between −15 and −25‰ relative to initial N_2. Considering a KIF occurring during the aerosols' growth and using the equations above, such a ^{15}N-depletion is compatible with involved N-bearing molecules with masses ranging theoretically between 19 and 33 amu. HCN ($m = 27$, $\varepsilon = -18$‰) and CH_2NH ($m = 29$, $\varepsilon = -17$‰), two molecules identified in the PAMPRE gas phase (Gautier et al., 2011; Carrasco et al., 2012), can contribute to the formation of C≡N, C=NH and C–NH_2 bonds identified in both the PAMPRE and the Nebulotron aerosols. These two molecules seem to be the main precursors for the nitrogen incorporation into the aerosols in the two setups. Except for the 10% CH_4-PAMPRE aerosol ($\Delta^{15}N \sim -15$‰), all the analyzed aerosols exhibit Δ^{15}N lower than −21‰ in both the PAMPRE and the Nebulotron setups. In such an "aerosol growth isotopic fractionation" model, this requires the involvement of molecules than can yield a larger ^{15}N-depletion than the one theoretically provided by HCN and CH_2NH. This can be provided by smaller molecules like NH_3 ($m = 17$, $\varepsilon = -28$‰) or even atomic N ($m = 14$, $\varepsilon = -34$‰), two species that are highly reactive too and that were identified in the PAMPRE experiment as well (Alves et al., 2012; Carrasco et al., 2012). On the other hand, the 10% CH_4-PAMPRE aerosols at −14.6‰ require a heavier molecule than HCN (or CH_2NH) that could imprint a less ^{15}N-depleted signature. In the PAMPRE setup context, one could think of acetonitrile (CH_3CN, $m = 41$, $\varepsilon = -12$‰) or even larger N-bearing molecules with 4, 5 or more carbon atoms that were identified in the gas phase of the PAMPRE experiment (Gautier et al., 2011; Carrasco et al., 2012).

We thus suggest that the ^{15}N-depleted isotopic composition of the experimental aerosols relative to the initial N_2 is due to a KIF during the aerosol growth by polymerization of N-bearing molecules, mainly HCN and/or CH_2NH. The strong relationship that is observed between the PAMPRE aerosols nitrogen isotopic composition and the initial CH_4 concentration at which they were produced (Fig. 4) requires the involvement of other N-bearing molecules that will enhance (at low CH_4%) or reduce (at high CH_4%) the ^{15}N-depleted signature of HCN and CH_2CN; namely NH_3 (or N) and CH_3CN (or even larger N-bearing molecules), respectively. Such a hypothesis is in good agreement with FTIR and High Resolution Mass Spectrometry (HRMS) data obtained on the PAMPRE aerosols (Gautier et al., 2012; Gautier, 2013), which clearly show an increase of the saturated amine (C–NH_2 bonds) content and an increase of light N-rich compounds incorporated into the aerosols as the initial CH_4% decreases.

Isotopic fractionation during synthesis of organic aerosols in plasma is thus consistent with kinetic isotopic fractionation (KIF). KIF is not specific to plasma and is likely to occur in every abiotic system, whether it is an electron, photon or temperature dominated environment. However, larger isotope effects in specific conditions such as photodissociation in the far UV light range may hide its ^{15}N-depleted typical signature.

4.2. Cosmochemical and planetary implications

- *Nitrogen in meteoritic organics*

Most of the organic compounds encountered in primitive meteorites are insoluble poly-aromatic macromolecules, referred as the so-called "Insoluble Organic Matter" (IOM, Derenne and Robert, 2010). Bulk nitrogen isotopic compositions of these organics show little variations and are very close to the terrestrial value of $\delta^{15}N = 0$‰, although some rare compounds exhibit extreme isotopic heterogeneities at very fine scales ("hot-spots", Busemann et al., 2006; Briani et al., 2009; Bonal et al., 2010). The process, timing and location of the formation of these large isotopic fractionations are still not resolved, but are probably closely related to the processes having led to the formation of these meteoritic organic compounds, processes that are still poorly understood (Alexander et al., 2007; Bonal et al., 2010; Hily-Blant et al., 2013).

The Nebulotron organic aerosols were experimentally produced from a gas mixture relatively close to the protosolar gases (N_2–CO *with* H_2O *contamination*). As discussed above, the use of an electric discharge to dissociate N_2 does not allow the production of very large isotopic fractionations as expected for UV photons. Thus, the reactions occurring in the Nebulotron setup do not explain the extreme ^{15}N-enrichments observed at the micron scale in the IOM nor the bulk nitrogen isotopic composition of these organics (enriched by ∼600‰ relative to the protosolar nebula composition). In this case, processes such as N_2 photodissociation/self-shielding or low temperature ion-molecule reactions seem more suitable to address these large ^{15}N-enrichments.

- *Titan's aerosols*

On Titan, the dissociation in the ionosphere of the two main gases N_2 and CH_4 results in an efficient integration of nitrogen in the gas products, as shown by the detection of numerous N-containing neutrals and ions by instruments on board Cassini, both on the dayside and the night side (Cui et al., 2009; Nixon et al., 2013). Aerosols are initiated in the upper atmosphere, where a dusty plasma chemistry occurs (Lavvas et al., 2013) possibly supporting the significant nitrogen amount detected in Titan's aerosols close to the surface by the Huygens probe (Israël et al., 2005). The PAMPRE experiment seems well representative of the chemistry occurring in Titan's atmosphere, as both gas and solid products are consistent with Cassini data (Gautier et al., 2011; Carrasco et al., 2012; Carrasco et al., 2013).

Although the dominant energy source available for N_2 dissociation in the upper Titan's atmosphere is solar radiation, suprathermal electrons may play a significant role in the neutral and ion chemistry occurring in Titan's atmosphere. Indeed, electron impact may account for ∼10% of the total N_2 dissociation rate during dayside, at an altitude of ∼1000 km, where initiation of aerosol growth is expected (Lavvas et al., 2011). On the nightside, solar photons cannot operate and electrons are the main source for ionization and dissociation of atmospheric molecules, despite a lower density than for the dayside (Cravens et al., 2009; Ågren et al., 2009).

Based on the present experimental KIF data, isotopic effects in the non-photonic dissociation of N_2 and further aerosol synthesis are not expected to play a major role in determining the large ^{15}N-enrichment of HCN relative to N_2 ($\Delta^{15}N \sim 4200$‰) in Titan's upper atmosphere (Vinatier et al., 2007; Liang et al., 2007; Niemann et al., 2010). However, the PAMPRE nitrogen isotopic data may give new constraints for nitrogen isotopic modeling in Titan's atmosphere, knowing that nitrogen isotopic composition of Titan's aerosols has not been measured yet. N_2 photodissociation and self-shielding isotopic effects calculated by Liang et al. (2007)

resulted in a factor of ~2.4 too large $^{15}N/^{14}N$ ratio for HCN ($^{15}N/^{14}N = 4.35 \times 10^{-2}$, Liang et al., 2007) compared to the observations ($^{15}N/^{14}N = 1.79 \pm 0.26 \times 10^{-2}$, Vinatier et al., 2007). These authors thus suggested that an additional source of unfractionated atomic nitrogen, produced by ion/electron-impact induced N_2 dissociation was required to counterbalance the too large effect of self-shielding. Isotopic effects described in the present study may contribute to counterbalance the calculated self-shielding ^{15}N-enrichment. We can roughly quantify by a simple mass balance calculation the importance of KIF for nitrogen isotopes in Titan's atmosphere. Assuming a −20‰ isotopic kinetic effect with 10% of electron-impact dissociated N_2 on the dayside (Lavvas et al., 2011) and 100% of electron-impact dissociated N_2 on the nightside, such a calculation provides a final $^{15}N/^{14}N$ ratio of 2.25×10^{-2}, dividing by 2 the discrepancy between the HCN isotopic ratio calculated by the self-shielding model and the measured one. This mass-balance suggests that KIF may play a role in the nitrogen isotopes balance in Titan's atmosphere. Besides, as first pointed out by Croteau et al. (2011), photoionization, photodissociation and non-photonic dissociation of N_2 provide distinct nitrogen isotopic fractionation signatures. The results of the present work may thus allow discriminating between putative aerosol formation pathways when nitrogen isotopic measurements in Titan's aerosols and organic molecules will become feasible.

- *Organics on early Earth*

The Earth's Archaean atmosphere (3.8 to 2.5 Ga ago) was anoxic and mainly consisted of N_2 and CO_2, with possibly minor amounts of H_2 and CH_4 (Zahnle, 1986; Pavlov et al., 2001; Tian et al., 2005; Wordsworth and Pierrehumbert, 2013; Charnay et al., 2013; Marty et al., 2013). In the presence of methane, a Titan-like hydrocarbon haze might have existed before widespread oxygenation around 2.5 Ga ago (Zahnle, 1986; Sagan and Chyba, 1997; Domagal-Goldman et al., 2008; Tian et al., 2011; Zerkle et al., 2012). Organic aerosol formation in such mildly reduced atmospheres has been demonstrated experimentally (Trainer et al., 2006; DeWitt et al., 2009). The formation of organic aerosols may also account for the isotopic fractionation of xenon in the ancient atmosphere (Hébrard and Marty, 2014) evidenced from the analysis of ancient sedimentary rocks (Pujol et al., 2011).

Without an ozone layer, the EUV photons from the Sun might have triggered atmospheric photochemical reactions such N_2 photodissociation and organic production. Even though the present experimental atmospheres (N_2–CH_4 and N_2–CO–H_2O) do not represent early Earth's atmosphere composition, it seems reasonable to assume that, in the expected mildly oxidized early Earth's atmosphere, active incorporation of nitrogen into organic aerosols have occurred as the result of photochemistry or lightning. The isotopic composition of Earth's atmospheric N_2 has not changed since the Archaean era, 3.5–3 Ga ago (Marty et al., 2013), confirming that the thin Earth's atmosphere has not been prone to nitrogen isotopic self-shielding as it is expected for Titan (Liang et al., 2007; Croteau et al., 2011). Thus, the present experimental results suggest strongly that, in the absence of such dramatic isotopic enrichments, nitrogen fixation into abiotic Archaean haze from atmospheric N_2 would have acquired a ^{15}N-depletion down to −25‰.

In the Archaean, the atmospheric production of abiotic organic matter and its delivery to oceans and continental areas might have been low, but comparable to that produced by early biological activity (Kasting and Catling, 2003). Later, on the Neoarchaean Earth, abiotic organic haze might have co-existed with life and biogenic organic production (Zerkle et al., 2012). ^{15}N-depleted abiotically formed aerosols could directly account for a significant fraction of sedimentary organics and thus leave their isotopic imprint in Archaean geological records. In line with this possibility, negative $\delta^{15}N$ values in the range of −11 to −6.2‰ measured in Paleoarchaean kerogens and metasedimentary rocks have been attributed to nitrogen cycle operated by microorganisms in a reducing environment (Beaumont and Robert, 1999; Pinti et al., 2001, Fig. 6). Alternatively, the present experimental results suggest that these low $\delta^{15}N$ might be in part of abiotic origin. The progressive oxygenation of the Earth's atmosphere, leading to a haze-free atmosphere, resulted in an oceanic nitrogen cycle dominated by the biomediated denitrification process, and $\delta^{15}N$ of organic matter evolved toward positive values (Boyd, 2001, Fig. 6). Considering the very negative $\delta^{15}N$ of the abiotic organics synthetized in the present study, the gradual enrichment in ^{15}N of organic matter from the Archaean to Present might also be the result of a transition from abiotic production to biotic one, and may therefore trace the temporal development of the biosphere.

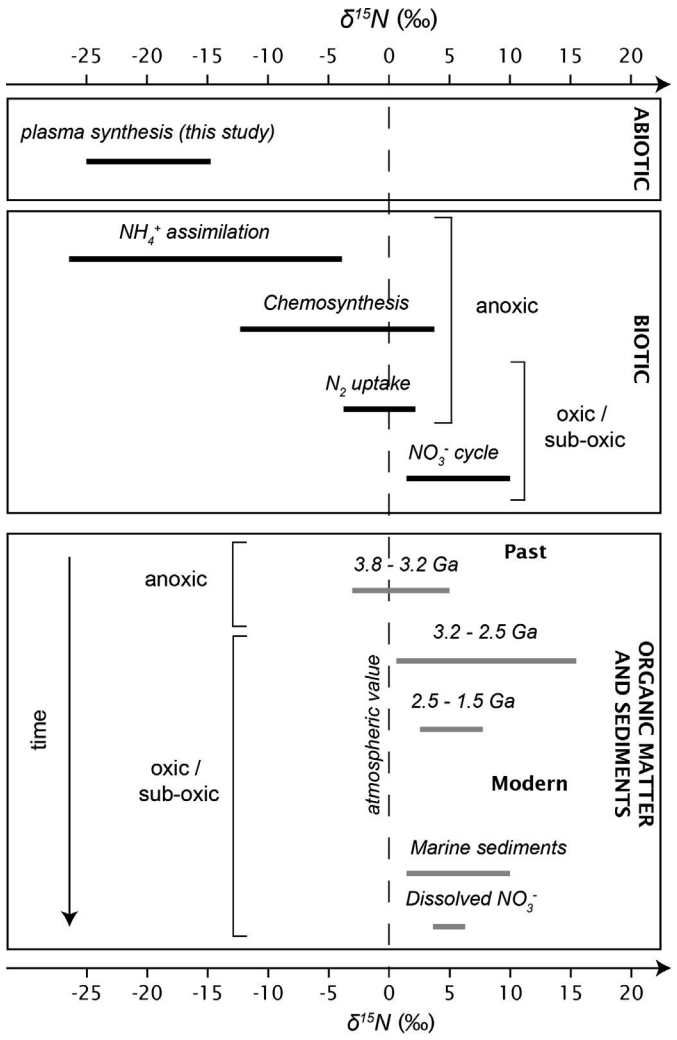

Fig. 6. Variations in the nitrogen isotopic composition of organic matter and biomass resulting from abiotic (this study, top box) and the main biomediated (middle box) processes. For comparison, $\delta^{15}N$ measured in old kerogen and modern marine sediments are given (bottom box). Sources of the data: NH_4^+ assimilation (Hoch et al., 1992; Macko et al., 1987; Waser et al., 1998), chemosynthesis (Brooks et al., 1987; Conway et al., 1994), N_2 uptake (Macko et al., 1987; Zerkle et al., 2008), NO_3^- cycle (Macko et al., 1987; Mariotti et al., 1981; Boyd, 2001), past kerogen data (compilation from Thomazo and Papineau, 2013, average $\delta^{15}N \pm \sigma$), modern marine sediments and dissolved NO_3^- (Peters et al., 1978; Sweeney et al., 1978).

5. Conclusions

We have analyzed the nitrogen content, the N speciation and the N isotopic composition in organic aerosols synthetized by plasma from two starting gas mixtures containing N_2: N_2–CH_4 (PAMPRE setup) and N_2–CO (Nebulotron setup). This study demonstrates the efficient incorporation of nitrogen into the synthesized solids, independently of the oxidation degree and the N_2 content of the starting gas mixture. Both the PAMPRE and the Nebulotron aerosols show a comparable ^{15}N depletion of about $-20‰$ relative to the initial N_2. The experimental organic solids were found to be isotopically homogeneous, with negligible air contamination. This isotopic signature is attributed to mass-dependent kinetic isotopic fractionation, which could occur at any step in the synthesis of aerosols but most likely during polymerization. Such kinetic isotopic fractionation is too small and goes in the wrong direction to account for the large ^{15}N enrichments observed in some primitive Solar System materials compared to the protosolar $^{15}N/^{14}N$ value. Processes such as specific isotopic effects associated to N_2 photodissociation, self-shielding, or isotopic exchange at very low temperature remain the best candidates. Nonetheless, in environments where these processes do not occur, as in Titan's atmosphere on the nightside or in early Earth's atmosphere, kinetic isotopic effects may imprint a ^{15}N-depleted signature. Such negative $\delta^{15}N$ values may characterize abiotic production of organics during the Archaean eon, rather than specific metabolic pathways.

Acknowledgements

We thank L. Zimmermann (CRPG, Nancy) and V. Busigny (IPGP) for their help with the nitrogen isotopes measurements by stepwise pyrolysis and the N_2–CH_4 purification, respectively. C. France-Lanord kindly put at disposition the CRPG stable isotope facility. We are grateful to P. Cartigny for helpful discussions and to G. Cernogora for the "plasma lessons" and for his wise scientific comments. M.K. gratefully acknowledges support from the French Ministry of Higher Education through a PhD grant. This study was partly funded by the French Programme National de Planétologie (PNP) and by the European Research Council under the European Community's Seventh Framework Program (FP/7 2007–2013, grant agreement number 267255 to B.M.). We thank two anonymous reviewers for constructive comments, and T.M. Harrison for efficient editorial handling. This is CRPG contribution no. 2304.

References

Ågren, K., Wahlund, J.E., Garnier, P., Modolo, R., Cui, J., Galand, M., Müller-Wodarg, I., 2009. On the ionospheric structure of Titan. Planet. Space Sci. 57, 1821–1827. http://dx.doi.org/10.1016/j.pss.2009.04.012.

Alcouffe, G., Cavarroc, M., Cernogora, G., Ouni, F., Joli, A., Boufendi, L., Szopa, C., 2010. Capacitively coupled plasma used to simulate Titan's atmospheric chemistry. Plasma Sources Sci. Technol. 19, 015008. http://dx.doi.org/10.1088/0963-0252/19/1/015008.

Aleon, J., 2010. Multiple origins of nitrogen isotopic anomalies in meteorites and comets. Astrophys. J. 722, 1342. http://dx.doi.org/10.1088/0004-637X/722/2/1342.

Alexander, C.M.O.D., Fogel, M., Yabuta, H., Cody, G.D., 2007. The origin and evolution of chondrites recorded in the elemental and isotopic compositions of their macromolecular organic matter. Geochim. Cosmochim. Acta 71, 4380–4403. http://dx.doi.org/10.1016/j.gca.2007.06.052.

Alves, L.L., Marques, L., Pintassilgo, C.D., Wattieaux, G., Es-sebbar, E., Berndt, J., Kovacevic, E., Carrasco, N., Boufendi, L., Cernogora, G., 2012. Capacitively coupled radio-frequency discharges in nitrogen at low pressures. Plasma Sources Sci. Technol. 21, 045008. http://dx.doi.org/10.1088/0963-0252/21/4/045008.

Beaumont, V., Robert, F., 1999. Nitrogen isotope ratios of kerogens in Precambrian cherts: a record of the evolution of atmosphere chemistry?. Precambrian Res. 96, 63–82. http://dx.doi.org/10.1016/S0301-9268(99)00005-4.

Bernard, S., Benzerara, K., Beyssac, O., Brown Jr., G.E., 2010a. Multiscale characterization of pyritized plant tissues in blueschist facies metamorphic rocks. Geochim. Cosmochim. Acta 74, 5054–5068. http://dx.doi.org/10.1016/j.gca.2010.06.011.

Bernard, S., Beyssac, O., Benzerara, K., Findling, N., Tzvetkov, G., Brown Jr., G., 2010b. XANES, Raman and XRD study of anthracene-based cokes and saccharose-based chars submitted to high-temperature pyrolysis. Carbon 48, 2506–2516. http://dx.doi.org/10.1016/j.carbon.2010.03.024.

Bernard, S., Horsfield, B., Schulz, H.-M., Wirth, R., Schreiber, A., Sherwood, N., 2012a. Geochemical evolution of organic-rich shales with increasing maturity: A STXM and TEM study of the Posidonia Shale (Lower Toarcian, northern Germany). Mar. Pet. Geol. 31, 70–89. http://dx.doi.org/10.1016/j.marpetgeo.2011.05.010.

Bernard, S., Wirth, R., Schreiber, A., Schulz, H.-M., Horsfield, B., 2012b. Formation of nanoporous pyrobitumen residues during maturation of the Barnett Shale (Fort Worth Basin). Int. J. Coal Geol. 103, 3–11. http://dx.doi.org/10.1016/j.coal.2012.04.010.

Bockelée-Morvan, D., Biver, N., Jehin, E., Cochran, A.L., Wiesemeyer, H., Manfroid, J., Hutsemékers, D., Arpigny, C., Boissier, J., Cochran, W., Colom, P., Crovisier, J., Milutinovic, N., Moreno, R., Prochaska, J.X., Ramirez, I., Schulz, R., Zucconi, J.-M., 2008. Large excess of heavy nitrogen in both hydrogen cyanide and cyanogen from Comet 17P/Holmes. Astrophys. J. Lett. 679, L49. http://dx.doi.org/10.1086/588781.

Bonal, L., Huss, G.R., Krot, A.N., Nagashima, K., Ishii, H.A., Bradley, J.P., 2010. Highly 15N-enriched chondritic clasts in the CB/CH-like meteorite Isheyevo. Geochim. Cosmochim. Acta 74, 6590–6609. http://dx.doi.org/10.1016/j.gca.2010.08.017.

Boyd, S.R., 2001. Ammonium as a biomarker in Precambrian metasediments. Precambrian Res. 108, 159–173. http://dx.doi.org/10.1016/S0301-9268(00)00162-5.

Briani, G., Gounelle, M., Marrocchi, Y., Mostefaoui, S., Leroux, H., Quirico, E., Meibom, A., 2009. Pristine extraterrestrial material with unprecedented nitrogen isotopic variation. Proc. Natl. Acad. Sci. 106, 10522–10527. http://dx.doi.org/10.1073/pnas.0901546106.

Brooks, J.M., Kennicutt, M.C., Fischer, C.R., Macko, S.A., Cole, K., Childress, J.J., Bidigare, R.R., Vetter, R.D., 1987. Deep-sea hydrocarbon seep communities: Evidence for energy and nutritional carbon sources. Science 238, 1138–1142. http://dx.doi.org/10.1126/science.238.4830.1138.

Buijnsters, J.G., Gago, R., Redondo-Cubero, A., Jimenez, I., 2012. Hydrogen stability in hydrogenated amorphous carbon films with polymer-like and diamond-like structure. J. Appl. Phys. 112, 093502. http://dx.doi.org/10.1063/1.4764001.

Busemann, H., Young, A.F., Alexander, C.M.O.D., Hoppe, P., Mukhopadhyay, S., Nittler, L.R., 2006. Interstellar chemistry recorded in organic matter from primitive meteorites. Science 312, 727–730. http://dx.doi.org/10.1126/science.1123878.

Carrasco, N., Gautier, T., Es-sebbar, E.-t., Pernot, P., Cernogora, G., 2012. Volatile products controlling Titan's tholins production. Icarus 219, 230–240. http://dx.doi.org/10.1016/j.icarus.2012.02.034.

Carrasco, N., Westlake, J., Pernot, P., Waite Jr., H., 2013. Nitrogen in Titan's atmospheric aerosol factory. In: Trigo-Rodriguez, J.M., Raulin, F., Muller, C., Nixon, C. (Eds.), The Early Evolution of the Atmospheres of Terrestrial Planets. Springer, New York, pp. 145–154. http://dx.doi.org/10.1007/978-1-4614-5191-4_11.

Chakraborty, S., Jackson, T.L., Muskatel, B.H., Ahmed, M., Thiemens, M.H., Levine, R.D., 2013. Huge Isotope effect in VUV photodissociation of N2: Implications for meteorite data. In: 44th Lunar Planet. Sci. Conf., http://www.lpi.usra.edu/meetings/lpsc2013/pdf/1043.pdf.

Chang, S., Des Marais, D.J., Mack, R., Miller, S.L., Strathearn, G., 1983. Prebiotic organic syntheses and the origin of life. In: Schopf, J.W. (Ed.), Earth's Earliest Biosphere: Its Origin and Early Evolution. Princeton University Press, pp. 53–92.

Charnay, B., Forget, F., Wordsworth, R., Leconte, J., Millour, E., Codron, F., Spiga, A., 2013. Exploring the faint young Sun problem and the possible climates of the Archean Earth with a 3-D GCM. J. Geophys. Res., Atmos. 118, 10,414–10,431. http://dx.doi.org/10.1002/jgrd.50808.

Clayton, R.N., 2002. Solar System: Self-shielding in the solar nebula. Nature 415, 860–861. http://dx.doi.org/10.1038/415860b.

Cody, G.D., Ade, H., Alexander, M.O.D., Araki, T., Butterworth, A., Fleckenstein, H., Flynn, G., Gilles, M.K., Jacobsen, C., Kilcoyne, A.L.D., Messenger, K., Sandford, S.A., Tyliszczak, T., Westphal, A.J., Wirick, S., Yabuta, H., 2008. Quantitative organic and light-element analysis of Comet 81P/Wild 2 particles using C-, N-, and O-μ-XANES. Meteorit. Planet. Sci. 43, 353–365. http://dx.doi.org/10.1111/j.1945-5100.2008.tb00627.x.

Coll, P., Navarro-González, R., Szopa, C., Poch, O., Ramírez, S.I., Coscia, D., Raulin, F., Cabane, M., Buch, A., Israël, G., 2013. Can laboratory tholins mimic the chemistry producing Titan's aerosols? A review in light of ACP experimental results. Planet. Space Sci. 77, 91–103. http://dx.doi.org/10.1016/j.pss.2012.07.006.

Conway, N., Kennicutt, M., Van Dover, C., 1994. Stable isotopes in the study of marine chemosynthetic-based ecosystems. In: Lajtha, K., Michener, R.H. (Eds.), Stable Isotopes in Ecology and Environmental Science. Blackwell Scientific, pp. 158–186.

Coplen, T.B., Hopple, J., Boehike, J., Peiser, H., Rieder, S., 2002. Compilation of minimum and maximum isotope ratios of selected elements in naturally occurring terrestrial materials and reagents. U.S. Geological Survey.

Cravens, T.E., Robertson, I.P., Waite Jr., J.H., Yelle, R.V., Vuitton, V., Coates, A.J., Wahlund, J.E., Agren, K., Richard, M.S., De La Haye, V., Wellbrock, A., Neubauer, F.M., 2009. Model-data comparisons for Titan's nightside ionosphere. Icarus 199, 174–188. http://dx.doi.org/10.1016/j.icarus.2008.09.005.

Croteau, P., Randazzo, J.B., Kostko, O., Ahmed, M., Liang, M.-C., Yung, Y.L., Boering, K.A., 2011. Measurements of isotope effects in the photoionization of N2 and

implications for Titan's atmosphere. Astrophys. J. Lett. 728. http://dx.doi.org/10.1088/2041-8205/728/2/l32.

Cui, J., Yelle, R.V., Vuitton, V., Waite Jr., J.H., Kasprzak, W.T., Gell, D.A., Niemann, H.B., Müller-Wodarg, I.C.F., Borggren, N., Fletcher, G.G., Patrick, E.L., Raaen, E., Magee, B.A., 2009. Analysis of Titan's neutral upper atmosphere from Cassini Ion Neutral Mass Spectrometer measurements. Icarus 200, 581–615. http://dx.doi.org/10.1016/j.icarus.2008.12.005.

Derenne, S., Coelho, C., Anquetil, C., Szopa, C., Rahman, A.S., McMillan, P.F., Corà, F., Pickard, C.J., Quirico, E., Bonhomme, C., 2012. New insights into the structure and chemistry of Titan's tholins via 13C and 15N solid state nuclear magnetic resonance spectroscopy. Icarus 221, 844–853. http://dx.doi.org/10.1016/j.icarus.2012.03.003.

Derenne, S., Robert, F., 2010. Model of molecular structure of the insoluble organic matter isolated from Murchison meteorite. Meteorit. Planet. Sci. 45, 1461–1475. http://dx.doi.org/10.1111/j.1945-5100.2010.01122.x.

Des Marais, D.J., Donchin, J.H., Nehring, N.L., Truesdell, A.H., 1981. Molecular carbon isotopic evidence for the origin of geothermal hydrocarbons. Nature 292, 826–828. http://dx.doi.org/10.1038/292826a0.

DeWitt, H.L., Trainer, M.G., Pavlov, A.A., Hasenkopf, C.A., Aiken, A.C., Jimenez, J.L., McKay, C.P., Toon, O.B., Tolbert, M.A., 2009. Reduction in haze formation rate on prebiotic Earth in the presence of hydrogen. Astrobiology 9, 447–453. http://dx.doi.org/10.1089/ast.2008.0289.

Domagal-Goldman, S.D., Kasting, J.F., Johnston, D.T., Farquhar, J., 2008. Organic haze, glaciations and multiple sulfur isotopes in the Mid-Archean Era. Earth Planet. Sci. Lett. 269, 29–40. http://dx.doi.org/10.1016/j.epsl.2008.01.040.

Dzizckniec, M., Lumkin, G.R., 1981. Plasma synthesis of carbonaceous material with noble gas tracers. In: 12th Lunar Planet. Sci. Conf., http://www.lpi.usra.edu/meetings/lpsc1981/pdf/1087.pdf.

Es-Sebbar, E.-t., Benilan, Y., Jolly, A., Gazeau, M., 2009. Characterization of an N2 flowing microwave post-discharge by OES spectroscopy and determination of absolute ground-state nitrogen atom densities by TALIF. J. Phys. D, Appl. Phys. 42, 135206. http://dx.doi.org/10.1088/0022-3727/42/13/135206.

Fridman, A., 2008. Plasma Chemistry. Cambridge University Press.

Gautier, T., 2013. Experimental simulation of Titan's aerosols formation. Université de Versailles-Saint Quentin en Yvelines. http://tel.archives-ouvertes.fr/tel-00878846.

Gautier, T., Carrasco, N., Buch, A., Szopa, C., Sciamma-O'Brien, E., Cernogora, G., 2011. Nitrile gas chemistry in Titan's atmosphere. Icarus 213, 625–635. http://dx.doi.org/10.1016/j.icarus.2011.04.005.

Gautier, T., Carrasco, N., Mahjoub, A., Vinatier, S., Giuliani, A., Szopa, C., Anderson, C.M., Correia, J.-J., Dumas, P., Cernogora, G., 2012. Mid- and far-infrared absorption spectroscopy of Titan's aerosols analogues. Icarus 221, 320–327. http://dx.doi.org/10.1016/j.icarus.2012.07.025.

Gries, T., Vandenbulcke, L., de Persis, S., Aubry, O., Delfau, J.L., 2009. Diagnostics and modeling of CH_4–CO_2 plasmas for nanosmooth diamond deposition: Comparison to experimental data. J. Vac. Sci. Technol., B 27, 2309–2320. http://dx.doi.org/10.1116/1.3231447.

Grossman, L., 1972. Condensation in the primitive solar nebula. Geochim. Cosmochim. Acta 36, 597–619. http://dx.doi.org/10.1016/0016-7037(72)90078-6.

Hébrard, E., Marty, B., 2014. Coupled noble gas-hydrocarbon evolution of the early Earth atmosphere upon solar UV irradiation. Earth Planet. Sci. Lett. 385, 40–48. http://dx.doi.org/10.1016/j.epsl.2013.10.022.

Hily-Blant, P., Bonal, L., Faure, A., Quirico, E., 2013. The 15N-enrichment in dark clouds and Solar System objects. Icarus 223, 582–590. http://dx.doi.org/10.1016/j.icarus.2012.12.015.

Hoch, M.P., Fogel, M.L., Kirchman, D.L., 1992. Isotope fractionation associated with ammonium uptake by a marine bacterium. Limnol. Oceanogr. 37, 1447–1459.

Imanaka, H., Smith, M.A., 2010. Formation of nitrogenated organic aerosols in the Titan upper atmosphere. Proc. Natl. Acad. Sci. 107, 12423–12428. http://dx.doi.org/10.1073/pnas.0913353107.

Israël, G., Szopa, C., Raulin, F., Cabane, M., Niemann, H., Atreya, S., Bauer, S., Brun, J.-F., Chassefière, E., Coll, P., 2005. Complex organic matter in Titan's atmospheric aerosols from in situ pyrolysis and analysis. Nature 438, 796–799. http://dx.doi.org/10.1038/nature04349.

Kasting, J.F., Catling, D., 2003. Evolution of a habitable planet. Annu. Rev. Astron. Astrophys. 41, 429–463. http://dx.doi.org/10.1146/annurev.astro.41.071601.170049.

Kerridge, J.F., Mariner, R., Flores, J., Chang, S., 1989. Isotopic characteristics of simulated meteoritic organic matter: 1—Kerogen-like material. Orig. Life Evol. Biosph. 19, 561–572.

Kilcoyne, A., Tyliszczak, T., Steele, W., Fakra, S., Hitchcock, P., Franck, K., Anderson, E., Harteneck, B., Rightor, E., Mitchell, G., 2003. Interferometer-controlled scanning transmission X-ray microscopes at the advanced light source. J. Synchrotron Radiat. 10, 125–136. http://dx.doi.org/10.1107/S0909049502017739.

Lavvas, P., Galand, M., Yelle, R., Heays, A., Lewis, B., Lewis, G., Coates, A., 2011. Energy deposition and primary chemical products in Titan's upper atmosphere. Icarus 213, 233–251. http://dx.doi.org/10.1016/j.icarus.2011.03.001.

Lavvas, P., Yelle, R.V., Koskinen, T., Bazin, A., Vuitton, V., Vigren, E., Galand, M., Wellbrock, A., Coates, A.J., Wahlund, J.-E., Crary, F.J., Snowden, D., 2013. Aerosol growth in Titan's ionosphere. Proc. Natl. Acad. Sci. 110, 2729–2734. http://dx.doi.org/10.1073/pnas.1217059110.

Lefebvre-Brion, H., Field, R.W., 2004. Photodissociation dynamics. In: The Spectra and Dynamics of Diatomic Molecules. Academic Press, San Diego, pp. 469–549. http://dx.doi.org/10.1016/B978-012441455-6/50010-X. Chapter 7.

Leinweber, P., Kruse, J., Walley, F.L., Gillespie, A., Eckhardt, K.-U., Blyth, R.I., Regier, T., 2007. Nitrogen K-edge XANES – an overview of reference compounds used to identify 'unknown' organic nitrogen in environmental samples. J. Synchrotron Radiat. 14, 500–511. http://dx.doi.org/10.1107/S0909049507042513.

Li, L., Cartigny, P., Ader, M., 2009. Kinetic nitrogen isotope fractionation associated with thermal decomposition of NH3: Experimental results and potential applications to trace the origin of N_2 in natural gas and hydrothermal systems. Geochim. Cosmochim. Acta 73, 6282–6297. http://dx.doi.org/10.1016/j.gca.2009.07.016.

Liang, M.-C., Heays, A.N., Lewis, B.R., Gibson, S.T., Yung, Y.L., 2007. Source of nitrogen isotope anomaly in HCN in the atmosphere of Titan. Astrophys. J. Lett. 664, L115. http://dx.doi.org/10.1086/520881.

Lodders, K., 2003. Solar System abundances and condensation temperatures of the elements. Astrophys. J. 591, 1220. http://dx.doi.org/10.1086/375492.

Lorquet, A.J., Lorquet, J.C., 1974. Isotopic effects in accidental predissociation. The case of the $C2\Sigma + u$ state of N^{+2}. Chem. Phys. Lett. 26, 138–143. http://dx.doi.org/10.1016/0009-2614(74)89104-9.

Lyons, J.R., Bergin, E.A., Ciesla, F.J., Davis, A.M., Desch, S.J., Hashizume, K., Lee, J.E., 2009. Timescales for the evolution of oxygen isotope compositions in the solar nebula. Geochim. Cosmochim. Acta 73, 4998–5017. http://dx.doi.org/10.1016/j.gca.2009.01.041.

Macko, S.A., Fogel, M.L., Hare, P.E., Hoering, T.C., 1987. Isotopic fractionation of nitrogen and carbon in the synthesis of amino acids by microorganisms. Chem. Geol., Isot. Geosci. Sect. 65, 79–92. http://dx.doi.org/10.1016/0168-9622(87)90064-9.

Mariotti, A., Germon, J., Hubert, P., Kaiser, P., Letolle, R., Tardieux, A., Tardieux, P., 1981. Experimental determination of nitrogen kinetic isotope. fractionation: some principles; illustration for the denitrification and nitrification processes. Plant Soil 62, 413–430.

Marty, B., Chaussidon, M., Wiens, R., Jurewicz, A., Burnett, D., 2011. A 15N-poor isotopic composition for the Solar System as shown by Genesis solar wind samples. Science 332, 1533–1536. http://dx.doi.org/10.1126/science.1204656.

Marty, B., Humbert, F., 1997. Nitrogen and argon isotopes in oceanic basalts. Earth Planet. Sci. Lett. 152, 101–112. http://dx.doi.org/10.1016/S0012-821X(97)00153-2.

Marty, B., Zimmermann, L., 1999. Volatiles (He, C, N, Ar) in mid-ocean ridge basalts: assesment of shallow-level fractionation and characterization of source composition. Geochim. Cosmochim. Acta 63, 3619–3633. http://dx.doi.org/10.1016/S0016-7037(99)00169-6.

Marty, B., Zimmermann, L., Pujol, M., Burgess, R., Philippot, P., 2013. Nitrogen isotopic composition and density of the Archean atmosphere. Science 342, 101–104. http://dx.doi.org/10.1016/10.1126/science.1240971.

Miller, S.L., 1953. A production of amino acids under possible primitive earth conditions. Science 117, 528–529. http://dx.doi.org/10.1126/science.117.3046.528.

Mitra-Kirtley, S., Mullins, O.C., Van Elp, J., George, S.J., Chen, J., Cramer, S.P., 1993. Determination of the nitrogen chemical structures in petroleum asphaltenes using XANES spectroscopy. J. Am. Chem. Soc. 115, 252–258. http://dx.doi.org/10.1021/ja00054a036.

Mullins, O.C., Mitra-Kirtley, S., Van Elp, J., Cramer, S.P., 1993. Molecular structure of nitrogen in coal from XANES spectroscopy. Appl. Spectrosc. 47, 1268–1275.

Muskatel, B.H., Remacle, F., Thiemens, M.H., Levine, R.D., 2011. On the strong and selective isotope effect in the UV excitation of N2 with implications toward the nebula and Martian atmosphere. Proc. Natl. Acad. Sci. 108, 6020–6025. http://dx.doi.org/10.1073/pnas.1102767108.

Niemann, H., Atreya, S., Bauer, S., Carignan, G., Demick, J., Frost, R., Gautier, D., Haberman, J., Harpold, D., Hunten, D., 2005. The abundances of constituents of Titan's atmosphere from the GCMS instrument on the Huygens probe. Nature 438, 779–784. http://dx.doi.org/10.1038/nature04122.

Niemann, H., Atreya, S., Demick, J., Gautier, D., Haberman, J., Harpold, D., Kasprzak, W., Lunine, J., Owen, T., Raulin, F., 2010. Composition of Titan's lower atmosphere and simple surface volatiles as measured by the Cassini–Huygens probe gas chromatograph mass spectrometer experiment. J. Geophys. Res. 115, E12006. http://dx.doi.org/10.1029/2010JE003659.

Nixon, C., Teanby, N., Anderson, C., Vinatier, S., 2013. Nitrogen in the stratosphere of titan from Cassini CIRS infrared spectroscopy. In: Trigo-Rodriguez, J.M., Raulin, F., Muller, C., Nixon, C. (Eds.), The Early Evolution of the Atmospheres of Terrestrial Planets. Springer, New York, pp. 123–143.

Nuevo, M., Milam, S., Sandford, S., De Gregorio, B., Cody, G., Kilcoyne, A., 2011. XANES analysis of organic residues produced from the UV irradiation of astrophysical ice analogs. Adv. Space Res. 48, 1126–1135. http://dx.doi.org/10.1016/j.asr.2011.05.020.

O'Neil, J.R., 1986. Theoretical and experimental aspects of isotopic fractionation. In: Reviews in Mineralogy and Geochemistry, pp. 1–40.

Owen, T., Biemann, K., Rushneck, D.R., Biller, J.E., Howarth, D.W., Lafleur, A.L., 1977. The composition of the atmosphere at the surface of Mars. J. Geophys. Res. 82, 4635–4639. http://dx.doi.org/10.1029/JS082i028p04635.

Pavlov, A.A., Brown, L.L., Kasting, J.F., 2001. UV shielding of NH_3 and O_2 by organic hazes in the Archean atmosphere. J. Geophys. Res., Planets 106, 23267–23287. http://dx.doi.org/10.1029/2000JE001448.

Peng, Z., Gautier, T., Carrasco, N., Pernot, P., Giuliani, A., Mahjoub, A., Correia, J.J., Buch, A., Bénilan, Y., Szopa, C., Cernogora, G., 2013. Titan's atmosphere simulation experiment using continuum UV–VUV synchrotron radiation. J. Geophys. Res., Planets 118, 778–788. http://dx.doi.org/10.1002/jgre.20064.

Peters, K., Sweeney, R., Kaplan, I., 1978. Correlation of carbon and nitrogen stable isotope ratios in sedimentary organic matter. Limnol. Oceanogr. 23, 598–604.

Pinti, D.L., Hashizume, K., Matsuda, J.-I., 2001. Nitrogen and argon signatures in 3.8 to 2.8 Ga metasediments: Clues on the chemical state of the Archean ocean and the deep biosphere. Geochim. Cosmochim. Acta 65, 2301–2315. http://dx.doi.org/10.1016/S0016-7037(01)00590-7.

Pujol, M., Marty, B., Burgess, R., 2011. Chondritic-like xenon trapped in Archean rocks: A possible signature of the ancient atmosphere. Earth Planet. Sci. Lett. 308, 298–306. http://dx.doi.org/10.1016/j.epsl.2011.05.053.

Quirico, E., Montagnac, G., Lees, V., McMillan, P.F., Szopa, C., Cernogora, G., Rouzaud, J.-N., Simon, P., Bernard, J.-M., Coll, P., Fray, N., Minard, R.D., Raulin, F., Reynard, B., Schmitt, B., 2008. New experimental constraints on the composition and structure of tholins. Icarus 198, 218–231. http://dx.doi.org/10.1016/j.icarus.2008.07.012.

Ravel, B., Newville, M., 2005. ATHENA, ARTEMIS, HEPHAESTUS: data analysis for X-ray absorption spectroscopy using IFEFFIT. J. Synchrotron Radiat. 12, 537–541. http://dx.doi.org/10.1107/s0909049505012719.

Robert, F., Derenne, S., Thomen, A., Anquetil, C., Hassouni, K., 2011. Deuterium exchange rate between and organic CH bonds: Implication for D enrichment in meteoritic IOM. Geochim. Cosmochim. Acta 75, 7522–7532. http://dx.doi.org/10.1016/j.gca.2011.09.016.

Rodgers, S.D., Charnley, S.B., 2008. Nitrogen isotopic fractionation of interstellar nitriles. Astrophys. J. 689, 1448. http://dx.doi.org/10.1086/592195.

Sagan, C., Chyba, C., 1997. The early faint Sun paradox: Organic shielding of ultraviolet-labile greenhouse gases. Science 276, 1217–1221. http://dx.doi.org/10.1126/science.276.5316.1217.

Sciamma-O'Brien, E., Carrasco, N., Szopa, C., Buch, A., Cernogora, G., 2010. Titan's atmosphere: An optimal gas mixture for aerosol production?. Icarus 209, 704–714. http://dx.doi.org/10.1016/j.icarus.2010.04.009.

Solomon, D., Lehmann, J., Kinyangi, J., Liang, B., Heymann, K., Dathe, L., Hanley, K., Wirick, S., Jacobsen, C., 2009. Carbon (1s) NEXAFS spectroscopy of biogeochemically relevant reference organic compounds. Soil Sci. Soc. Am. J. 73, 1817–1830. http://dx.doi.org/10.2136/sssaj2008.0228.

Stöhr, J., 1992. NEXAFS Spectroscopy. Springer.

Sweeney, R., Kaplan, I., Liu, K.-K., 1978. Oceanic nitrogen isotopes and their uses in determining the source of sedimentary nitrogen. In: Robinson, B.W. (Ed.), Stable isotopes in the Earth Sciences. In: DSIR Bull., pp. 9–26.

Szopa, C., Cernogora, G., Boufendi, L., Correia, J.J., Coll, P., 2006. PAMPRE: A dusty plasma experiment for Titan's tholins production and study. Planet. Space Sci. 54, 394–404. http://dx.doi.org/10.1016/j.pss.2005.12.012.

Terzieva, R., Herbst, E., 2000. The possibility of nitrogen isotopic fractionation in interstellar clouds. Mon. Not. R. Astron. Soc. 317, 563–568. http://dx.doi.org/10.1046/j.1365-8711.2000.03618.x.

Thomazo, C., Papineau, D., 2013. Biogeochemical cycling of nitrogen on the Early Earth. Elements 9, 345–351. http://dx.doi.org/10.2113/gselements.9.5.345.

Tian, F., Kasting, J., Zahnle, K., 2011. Revisiting HCN formation in Earth's early atmosphere. Earth Planet. Sci. Lett. 308, 417–423. http://dx.doi.org/10.1016/j.epsl.2011.06.011.

Tian, F., Toon, O.B., Pavlov, A.A., De Sterck, H., 2005. A hydrogen-rich early Earth atmosphere. Science 308, 1014–1017. http://dx.doi.org/10.1126/science.1106983.

Trainer, M.G., Jimenez, J.L., Yung, Y.L., Toon, O.B., Tolbert, M.A., 2012. Nitrogen incorporation in CH_4–N_2 photochemical aerosol produced by far ultraviolet irradiation. Astrobiology 12, 315–326. http://dx.doi.org/10.1089/ast.2011.0754.

Trainer, M.G., Pavlov, A.A., DeWitt, H.L., Jimenez, J.L., McKay, C.P., Toon, O.B., Tolbert, M.A., 2006. Organic haze on Titan and the early Earth. Proc. Natl. Acad. Sci. 103, 18035–18042. http://dx.doi.org/10.1073/pnas.0608561103.

van de Runstraat, C.A., de Heer, F.J., Govers, T.R., 1974. Excitation and decay of the C2Σ + u state of N + u in the case of electron impact on N2. Chem. Phys. 3, 431–450. http://dx.doi.org/10.1016/0301-0104(74)87010-2.

Vinatier, S., Bézard, B., Nixon, C.A., 2007. The titan 14N/15N and 12C/13C isotopic ratios in HCN from Cassini/CIRS. Icarus 191, 712–721. http://dx.doi.org/10.1016/j.icarus.2007.06.001.

Waite, J.H.J., Niemann, H., Yelle, R.V., Kasprzak, W.T., Cravens, T.E., Luhmann, J.G., McNutt, R.L., Ip, W.-H., Gell, D., De La Haye, V., 2005. Ion neutral mass spectrometer results from the first flyby of Titan. Science 308, 982–986. http://dx.doi.org/10.1126/science.1110652.

Wang, J., Morin, C., Li, L., Hitchcock, A., Scholl, A., Doran, A., 2009. Radiation damage in soft X-ray microscopy. J. Electron Spectrosc. Relat. Phenom. 170, 25–36. http://dx.doi.org/10.1016/j.elspec.2008.01.002.

Waser, N., Harrison, P., Nielsen, B., Calvert, S., Turpin, D., 1998. Nitrogen isotope fractionation during the uptake and assimilation of nitrate, nitrite, ammonium, and urea by a marine diatom. Limnol. Oceanogr. 43, 215–224.

Wordsworth, R., Pierrehumbert, R., 2013. Hydrogen–nitrogen greenhouse warming in Earth's early atmosphere. Science 339, 64–67. http://dx.doi.org/10.1126/science.1225759.

Yokochi, R., Marty, B., Chazot, G., Burnard, P., 2009. Nitrogen in peridotite xenoliths: lithophile behavior and magmatic isotope fractionation. Geochim. Cosmochim. Acta 73, 4843–4861. http://dx.doi.org/10.1016/j.gca.2009.05.054.

Zahnle, K.J., 1986. Photochemistry of methane and the formation of hydrocyanic acid (HCN) in the Earth's early atmosphere. J. Geophys. Res., Atmos. 91, 2819–2834. http://dx.doi.org/10.1029/JD091iD02p02819.

Zerkle, A.L., Claire, M.W., Domagal-Goldman, S.D., Farquhar, J., Poulton, S.W., 2012. A bistable organic-rich atmosphere on the Neoarchaean Earth. Nat. Geosci. 5, 359–363. http://dx.doi.org/10.1038/ngeo1425.

Zerkle, A.L., Junium, C.K., Canfield, D.E., House, C.H., 2008. Production of 15N-depleted biomass during cyanobacterial N2-fixation at high Fe concentrations. J. Geophys. Res., Biogeosci. 113, G03014. http://dx.doi.org/10.1029/2007jg000651.

Zipf, E.C., McLaughlin, R.W., 1978. On the dissociation of nitrogen by electron impact and by E.U.V. photo-absorption. Planet. Space Sci. 26, 449–462. http://dx.doi.org/10.1016/0032-0633(78)90066-1.

Chapter 5

Noble gas trapping and isotopic fractionation in Nebulotron organics

Table of contents

5.1 Introduction

For the heavy noble gases (Ar, Kr and Xe), the Q component dominates the trapped noble gas inventory of primitive meteorites. Phase Q is an ill-defined structure concentrated in the acid-residue, the latter mostly consisting of macromolecular organics (e.g. IOM, Lewis et al., 1975, Busemann et al., 2000, Ott et al., 1981). Only a tiny fraction of such a residue is the host of trapped heavy noble gases, with high concentrations up to 5×10^{-9} mol per gram of acid residue for ^{132}Xe (Busemann et al., 2000), which is the largest observed for any natural material. These Q-gases are elementally and isotopically different from solar gases from which they presumably evolved, showing a strong enrichment in heavy elements and isotopes (Huss et al., 1996, Busemann et al., 2000). The exact origin and the history of Q-gases still present a puzzle.

There have been a variety of attempts to simulate noble gas trapping and fractionation by Q, for example: noble gas trapping in ices (Wacker and Anders, 1984, Notesco et al., 2003), adsorption onto carbon surfaces (Wacker et al., 1985, Marrocchi et al., 2005, Marrocchi and Marty, 2013), noble gas trapping into irradiated Si-smokes (Nichols et al., 1992) and ion implantation experiments with a variety of ion energies into amorphous carbon surfaces, nanodiamonds, Pyrex or low-Z metals (Frick et al., 1979, Dzizckniec et al., 1981, Marrocchi et al., 2011, Bernatowicz and Fahey, 1986, Bernatowicz and Hagee, 1987, Ponganis et al., 1997, Fukunaga and Matsuda, 1997, Matsuda et al., 1991, Hohenberg et al., 2002, Huss et al., 2008, Koscheev et al., 2001). Experimental conditions involving adsorption or condensation of neutral noble gases did not yield any detectable isotopic fractionations whereas trapping of ionized noble gases during ion implantation experiments was associated with significant isotopic fractionations. Noble gas ionization energies might have played an important role in establishing the fractionated elemental pattern of Q-gases, as elemental ratios from He/Xe to Kr/Xe in Q relative to the solar composition seem to correlate with ionization energy (Göbel et al., 1978, Frick et al., 1979, Fukunaga and Matsuda, 1997, Rai et al., 2003, Ott, 2014). Such observations are strong arguments for the involvement of noble gas ions in the formation of the fractionated elemental and isotopic pattern of Q-gases relative to the solar composition. However, the physical mechanism(s) by which this might happen is still poorly understood and experiments simulating nebular environments are lacking to provide constraints.

In order to improve our understanding of the noble gas trapping and fractionation mechanism(s), we have performed noble gas trapping experiments in gaseous atmospheres mimicking the solar nebula composition, i.e., a mixture of CO, N_2 and noble gases (He, Ne, Ar, Kr and Xe), under varying conditions. For this purpose, the Nebulotron setup was used, with a plasma providing the required energy to ionize the noble gases and initiate an organic chemistry from CO and N_2 dissociation (see Chapter 2 and 3). The heavy noble gases (Ar, Kr and Xe) trapped into the solids produced in the discharge were analyzed by static-mass spectrometry, which is described in the first section of this Chapter. The noble gas concentrations and isotopic compositions and their dependence onto the experimental

parameters are presented and discussed in the second and the third parts, respectively. Finally, some implications for the origin of the Q-gases are outlined in the last section.

5.2 Analytical methods for noble gas measurements

The elemental and isotopic compositions of the noble gases trapped in the Nebulotron samples, as well as the isotopic composition of the noble gas tank used in the experiments, were analyzed by static mass-spectrometry at CRPG (Nancy, France). I have mainly analyzed Xe abundances and isotopes, while Kr and Ar were only analyzed when sufficient quantities were available.

5.2.1 Noble gas static-mass spectrometry

5.2.1.1 Principles

The present-day standard noble gas mass spectrometers consist of an electron impact source, an electro-magnetic sector filter and a combination of Faraday cups and secondary electron multipliers (SEMs) as collectors. Noble gases are in very low abundance in natural samples and their analysis requires a high detection efficiency, which necessitates ultra-high vacuum techniques and in most cases static mass spectrometry (Reynolds, 1956). This means that all of the gas available is admitted into the mass spectrometer with the valves to the vacuum pumps closed (opposite to dynamic mass spectrometry, typically used for stable isotope analysis of C, H, N, O and S and ICP-MS techniques). Most noble gas mass spectrometers use either modified Nier-type sources or Baur-Signer sources, both of which depend on a tungsten filament to create an electron beam, which then ionize gas molecules in a ionization chamber by electron bombardment. The filament operates at a current of around 2.5 A and emits the electron beam at a current ("trap current") that is generally of the order of 10 – 800 µA, depending on the gas analyzed. Those sources have a very good ionization-extraction-transport yield, which ensures a good sensitivity for all noble gases. After being transferred to the detection area through the flight tube, ions are collected either by Faraday cups, which directly measure the ion current thanks to 10^{11} to 10^{12} Ω resistances and are generally used for large gas quantities, or, alternatively by SEMs. SEMs amplify the detected signal by emitting an electron cascade by 2000 V conversion dynodes connected to a resistance with a large ohmic value (generally 10^{13} Ω). Depending on their gain, SEMs can amplify the signal by up to 6 orders of magnitude compared to Faraday cups and are thus used to analyze small gas quantities, notably ^{36}Ar, ^{38}Ar and all Kr and Xe isotopes. There are two ways of measuring different isotopes of a same element, depending on the number of available collectors: "peak-jumping" and "multicollection" modes. Some instruments have a single collector (or one Faraday cup and one SEM only; e.g., the VG5400 mass spectrometer used during this thesis) and the measurement of the ion current on all masses of interest is performed in "peak-jumping" mode, i.e. the magnetic field strength is changed sequentially to focus ion beams of different masses on a single collector. Instruments equipped with multiple collectors (like the ARGUS and the HELIX-MC Plus used during this thesis) allow ion beams of different isotopes to be measured simultaneously: this is the "multi-collection" mode. Multicollection is expected to improve the precision of isotope ratio measurements

because (i) all the fluctuations due to the ion production or external sources (e.g. temperature) affect all the ion currents simultaneously, and (ii) the analytical time is reduced so that more analytical cycles can be carried out. The latter point is of importance for the analysis of Kr and Xe isotopes as both gases have numerous isotopes (6 and 9 stable isotopes, respectively) and their atoms have short life times in the mass spectrometer due to their high ionization cross-sections compared to He, Ne and Ar atoms.

5.2.1.2 Calibration with air standards

The mass spectrometer must be calibrated in order to convert the ion currents into gas amounts and to correct the isotope ratios for the instrumental mass discrimination. For this purpose, standards of known isotopic composition and with known quantities of noble gases are required and the calibration is performed relative to these standards. At CRPG, each purification line is equipped with gas standards that are composed of laboratory air, which has a known an elemental and isotopic composition. The standards for Ar consist of thoroughly purified laboratory air. The standards for Xe consist of purified air in which most Ar has been eliminated by cycling the air gas several times on a cold finger at liquid N_2 temperature. During this step, we assume that all Xe atoms are conserved and are thus devoid of any isotopic fractionation. The purified air-Ar and Xe are then diluted and stored in bottles connected to the purification line via calibrated pipettes (~ 0.2 cm^3), which ensure the delivery of identical aliquots of standard gas. Since Kr has a condensation temperature in between that of Ar and Xe, the preparation of the Xe standard cannot ensure a total conservation of all initial Kr atoms and, in addition, causes a fractionation of the Kr/Xe ratio. This elemental fractionation depends on the standard fabrication procedure (Reika Yokochi, personal communication). R. Yokochi has measured a loss of Kr atoms of 73% in her case (Yokochi, 2005). As a consequence, the Kr content of the Xe-standard is not precisely known so we cannot accurately determine the Kr content of unknown samples. However, the isotopic composition of air Kr is assumed to be unmodified during this step and the Kr isotopic composition of the Xe standard can be used to correct Kr isotope ratios measured in samples.

The Ar content of the Ar-standard has been calibrated with the international standard MMhb-1 displaying a very well known ^{40}Ar concentrations (Samson and Alexander Jr, 1987).

The Xe content of the Xe standard was intercalibrated with the Ar-standard (which was produced without the use of traps, and thus shows no elemental fractionation compared to the air composition) and the sensitivity was found to be the same within errors, confirming that no Xe fractionation occurred during the standard preparation.

5.2.1.3 Abundance and isotopic ratio determination

Signal extrapolation

While Nier-type sources have a good ionization yield, the signal changes over time as the gas is gradually consumed. Usually this is accounted by performing an extrapolation to the instant the gas was inlet into the mass spectrometer. In my case, an exponential

approximation of the decrease of the signal yielded the best match to the data (15 to 20 cycles accounted for one analysis of each isotope, Fig. 5.1).

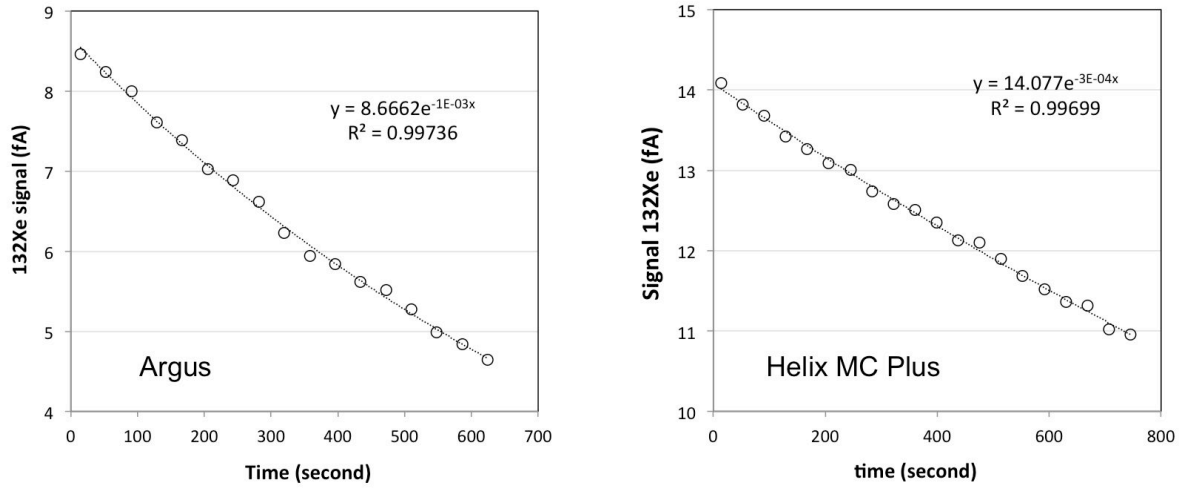

Figure 5.1. Signal of ^{132}Xe vs. time in an Argus (left) and in an Helix MC Plus (right) spectrometer (300 µA trap current). The signals are extrapolated to t=0 in order to account for gas consumption by ionization of the gas during measurement. One can note that the decrease of the signal is much more important in the Argus than in the Helix mass spectrometer, due to the low volume of the Argus one.

Sensitivity calculation and abundance determination

The sensitivity (S, usually expressed in A/Torr) of a mass spectrometer measures its ability to produce an electric signal (in ampere A) as a function of a gas pressure ($P_{spectro}$ in torr) introduced into the analyzer. The sensitivity is determined from the analysis of known standards and is used to determine the noble gas content of an unknown sample. The sensitivity is calculated following this equation:

$$S = \frac{I_{standard}}{P_{spectro}(torr)} = \frac{I_{standard}}{P_{pipette}(torr) \times d} = \frac{I_{standard} \times 1.432}{P_{pipette}(mbar) \times d} \quad (1)$$

Where $I_{standard}$ is the signal intensity of the standard aliquot measured on the collectors (ampere) and d the dilution factor for the standard aliquot, which can be calculated because all the volumes of the purification line, as well as the volume of the mass spectrometer, are calibrated and well known. The sensitivity is expressed in normal conditions of pressure and temperature. Since we measure the pressure in the standard bottle in mbar, we have to convert it into torr by using a factor equal to 1.432.

The gas amount (in moles) in a sample is then calculated from the signal intensity (in A) measured on the collectors:

$$n_{sample}(moles) = \frac{I_{sample}(A) \times v_{initial}(cm^3) \times 29.5(mol/torr/cm^3)}{d \times S(A/torr)} \quad (2)$$

where $v_{initial}$ is the starting volume in which the sample gas is extracted and d stands for the dilution factor of the sample gas from the starting volume to the mass spectrometer. When there is a blank contribution, it must be subtracted from the sample abundance in order to get the final sample gas amount.

Determination and correction of isotopic ratios for mass bias

The raw isotopic ratio (either for standards or for samples) was determined as following:

(i) calculation of the isotopic ratio (denominator 130 or 132 for Xe, 84 for Kr and 36 for Ar) for each cycle of an analysis;

(ii) calculation of the isotopic ratios averaged over all cycles because isotopic ratios were found to be constant most of the time over all cycles (Fig. 5.2).

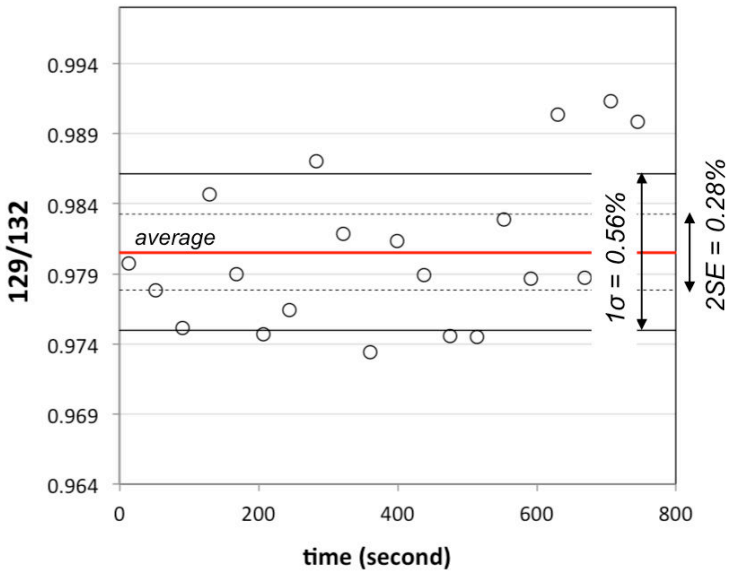

Figure 5.2. Example of the determination of the raw $^{129}Xe/^{132}Xe$ ratio by calculating the isotope ratios averaged over all cycles. σ = standard deviation $= \sqrt{\frac{1}{N-1}\sum_1^n (x_i - \bar{x})^2}$; SE = standard error $= \frac{s}{\sqrt{n}}$ (where n is the number of measurements, here the number of cycles). In this case, the 95% confidence interval on the average value is 0.28% (2 SE). Each point represents the isotopic ratio determined for one cycle.

The standards display an isotope discrimination relative to their true isotopic value (i.e. air composition, Fig. 5.3) of about -3‰/amu for Xe isotopes in the Helix MC Plus. In this particular mass spectrometer, ^{128}Xe and ^{136}Xe were measured simultaneously in multicollection mode, with ^{128}Xe measured on L2, ^{132}Xe on Ax and ^{136}Xe on H2 (all other isotopes are measured by peak jumping on the Ax). Fig. 5.3 illustrates that the SEMs do not have the same gain and that a correction to remove this instrumental bias is needed.

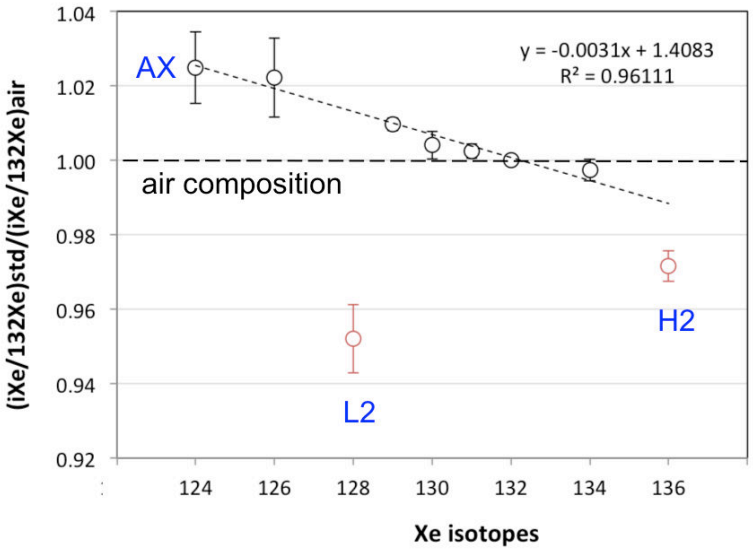

Figure 5.3. Example of the instrumental mass fractionation in the Helix MC Plus for Xe standards of atmospheric isotopic composition (average and standard deviation of 60 standard aliquots). The black circles represent the Xe isotopes measured on the Ax SEM. The red circles (^{128}Xe and ^{136}Xe) represent the isotopes measured on the other SEM, L2 and H2 detectors, respectively. The regression line through the "Ax isotopes" illustrates the mass fractionation from the true value (i.e. air) relative to the measured one, which is of the order of -3‰/amu. The isotopes measured on other SEM collectors fall off this mass fractionation line.

For the samples, the instrumental discrimination must then be corrected by using the following equation:

$$R_{corrected} = R_{raw} \times \frac{R_{air}}{R_{standard}} \tag{3}$$

where R_{raw} is the isotopic ratio of the sample calculated from the average over all the analytical cycles, $R_{standard}$ is the average ratio of all standards measured under the same conditions as the sample and R_{air} is the isotopic ratio of air, which is the true value for the standard isotopic composition. This equation can be applied only if the blank contribution is negligible, i.e. $< 1\%$ of the sample signal. Otherwise, one has to take into account the blank contribution and its isotopic ratio to correct the sample ratio by using this equation:

$$R_{blankcorrected} = \frac{(R_{sample} \times {}^{132}Xe_{sample}) - (R_{blank} \times {}^{132}Xe_{blank})}{{}^{132}Xe_{sample} - {}^{132}Xe_{blank}} \times \frac{R_{air}}{R_{standard}} \tag{4}$$

The mount of blank and its isotopic ratio can be either an average of several blanks if several blanks have been analyzed in the same conditions, or the data for one blank. Since in my case, the Nebulotron samples were rather Xe-rich, the blank correction was often negligible and the first correction formula was used.

5.2.1.4 Error propagation

The error on a measurement is the difference between the measured value and the true value. Errors are part of the measurement process and must be propagated when the final result is calculated from different measured quantities. This is the case when the abundance and the isotope ratios are determined (Eqns. (2), (3) and (4)).

If the final result is a function u calculated from several measured quantities x, y, z,… that are independent, each of them having a mean value and an error σ:

$$u = f(x,y,z,\ldots)$$

Then the error on u can be determined as:

$$\sigma_u = u \times \sqrt{\left(\frac{\partial u}{\partial x}\right)^2_{y,z} \times \sigma_x^2 + \left(\frac{\partial u}{\partial y}\right)^2_{x,z} \times \sigma_y^2 + \left(\frac{\partial u}{\partial z}\right)^2_{x,y} \times \sigma_z^2} \quad (5)$$

Error propagation on the isotopic ratios

If the blank contribution is negligible for the sample measurements, Eqn. (3) is used to calculate the final isotopic ratio. In this case, the relative error on the final isotopic ratio reduces to:

$$\sigma_{Rcorr} = R_{corr} \times \sqrt{\left(\frac{\sigma_{Rraw}}{R_{raw}}\right)^2 + \left(\frac{\sigma_{Rstandard}}{R_{standard}}\right)^2} \quad (6)$$

where (σ_{Rraw}) is the "**internal error**" calculated on the raw ratio of the sample, taken as the standard error of the mean over all analytical cycles ('SE', see Fig. 5.2) and ($\sigma_{standard}$) is the "**external error**" or the "**standard reproducibility**", taken as the standard deviation of all the standards measurements ('σ' see Fig. 5.2). The latter was used instead of the standard error of the mean of the standards because the samples (at least in my case) were analyzed only once. Hence, the standard deviation was most suited to describe the analytical uncertainty. External errors are reported in Table 5.1.

When the blank contribution was too large, the final isotopic ratio of the sample was corrected for the blank contribution and the standard deviation using Eqn. (4) and the final error on this ratio was evaluated with Eqn. (5), by calculating all the partial derivative terms.

Error propagation on the abundance

The abundance is determined by measuring several different quantities (Eqn. (2)), so Eqn. (5) is used to calculate the final error on the mole quantity in the sample. In practice,

the standard deviation on the sensitivity measurements is largely dominant over to the other errors (on the volume calibration, the dilution factor and the intensity value) so the final relative error on the noble gas abundance in a sample was systematically derived the relative error on the sensitivity:

$$\frac{\sigma_{nsample}}{n_{sample}} = \frac{\sigma_S}{S} \tag{7}$$

5.2.2 Elemental and isotopic analysis on Nebulotron solids (Ar, Kr and Xe)

During this thesis, three analytical sessions (S1, S2 and S3 in the following) have been done, on two different purification lines and three different mass spectrometers. Extraction and purification methods did not vary very much and are described in the following section. The analytical conditions for the three sessions are reported in a second part.

5.2.2.1 Noble gas extraction and purification

In general, the noble gases are present in low concentrations in geological materials and even in synthetic materials, such ad the Nebulotron-synthesized samples, i.e., at the ppm level or lower for Xe and Kr atoms. Hence, it is necessary to extract and separate the noble gases from their host phase before analysis.

Extraction method

The noble gases trapped in the samples synthesized in the Nebulotron setup were extracted by heating the samples in a double-walled quartz furnace that was developed at CRPG (Yokochi, 2005). A horizontal quartz tube, heated by a classical furnace, was associated with a vertical induction furnace also made of quartz (Fig. 5.4). In the latter, a Mo crucible was used to transfer the heat to the sample.

Once the samples were introduced into the furnace, the system was baked at ~ 100°C under ultra vacuum. The quartz tube was used for step heating in the range of 150-800°C, whereas heating at higher temperature was achieved in the induction furnace. The Nebulotron samples were heated up to 1400°C in order to completely degrade the carbon structure. The temperature of the horizontal quartz furnace was monitored with an accuracy of ~ 50°C using a thermocouple located outside the tube. To calibrate the temperature of the induction furnace, we used an optical pyrometer with a precision of ± 100°C. Some samples were heated in two steps, one at 150°C to check for any atmospheric gas adsorbed onto the surfaces of the sample and one at 1400°C to extract all the gases trapped into the sample. A second heating step at 1400°C was systematically performed to ensure the total extraction of the gases. Some samples were heated in 3 to 5 steps between 150°C and 1400°C in order to determine the thermal release behavior of the noble gases. Each heating step lasted 20 min to 30 min.

Before introduction into the furnace, a fraction of the Nebulotron samples was weighted (50 µg to 1 mg) on a precise weighing scale and wrapped in platinum foils or in small nickel crucibles, previously degassed at 800°C under ultra vacuum.

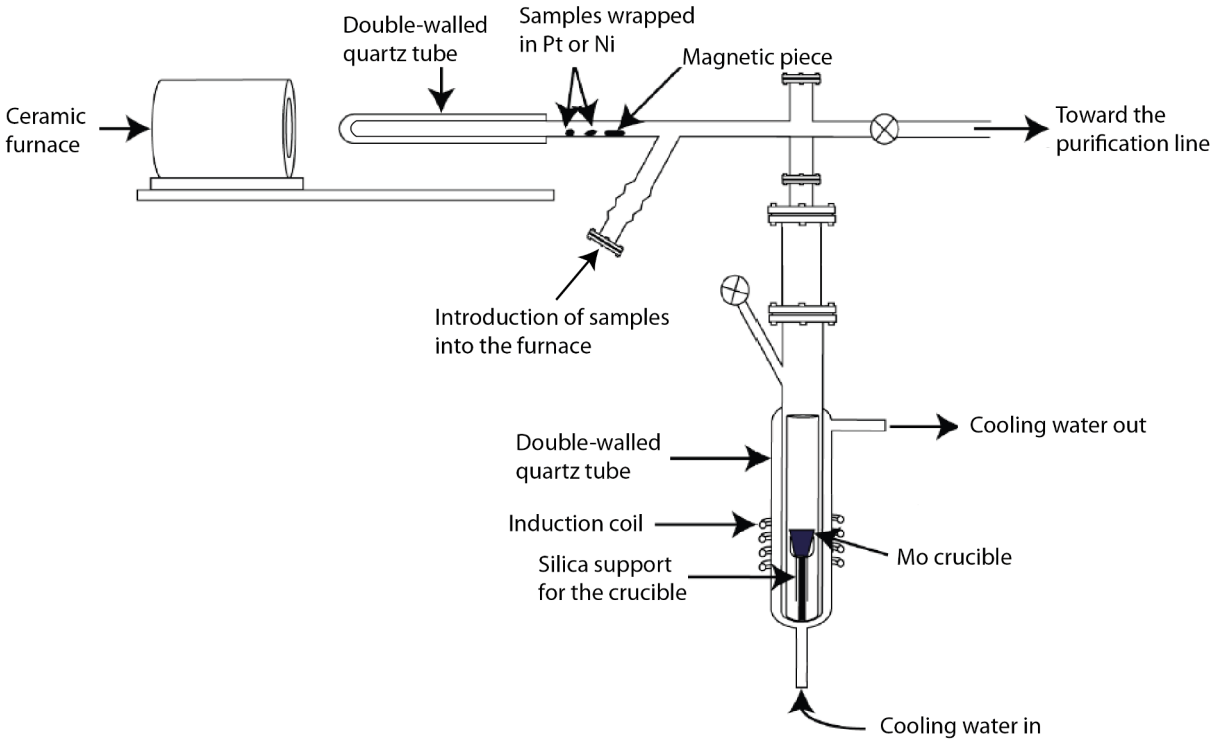

Figure 5.4. Extraction system: quartz furnace associated with an induction furnace for sample heating from 150°C up to 1400°C.

Purification

It is necessary to purify the extracted gases in order to admit pure, or as near-pure as possible, noble gases into the mass spectrometer. Noble gas purification methods rely on the non-reactivity of the noble gases and chemically remove active species (CO, CO_2, N_2, O2, H_2O, H_2, hydrocarbons, etc.…) from the extracted gases. Generally, active metal surfaces (Ti or Zr), commonly called "getters", combine with the reactive gases either by adsorption or chemisorption at hot (500-700°C) and ambient temperatures. In the noble gas laboratory at CRPG, all purification lines are homemade and equipped with at least 4 getters (Ti sponge), used both hot and cold, active charcoal traps (used for Ne and Ar analysis) and ion pressure gauges.

For the analysis of the noble gases trapped in the Nebulotron samples, I used a standard purification procedure. The first getter, located at the furnace exit, was used at 650°C for 15 min then at room temperature for 10 min, to ensure a maximum trapping of H_2 molecules produced upon heating within the furnace. All other getters (up to 4) were used hot and cold for 5 min each. The final gas pressure in the purification line was monitored with an ion-gauge and was adjusted by dilution in order to admit a reasonable noble gas quantity into the mass spectrometer ($P < 10^{-6}$ mbar in order to prevent the source from being damaged).

Cryoseparation

When various noble gases are present in the extracted gases from the sample, it may be necessary to separate them in order to admit single noble gas aliquots into the mass spectrometer for suitable analysis, in particular if one of them is overabundant relative to the other(s).

In my case, I intended to analyze Ar separately from Xe (and Kr) in the analytical session S2. For that purpose, the gases released from the sample were put in contact with a finger made of Pyrex plunged into an external liquid nitrogen bath (T=77K): Xe and a portion of Kr atoms were condensed while all Ar atoms remained in the gas phase. The Ar fraction was purified and analyzed first. Subsequently, the Xe fraction (with a portion of Kr) was desorbed, purified and admitted into the mass spectrometer for analysis.

5.2.2.2 Analytical sessions

Three mass spectrometers were used during this thesis: a VG5400 (Micromass) as well as an Argus and Helix MC Plus (ThermoFisher), with different analytical conditions each time. Details for each analytical session are reported in Table 5.1.

Table 5.1. Experimental and analytical conditions for each noble gas analytical sessions.

Session	S1	S2	S3
date	June 2012	January 2013	September 2013
spectrometer	**VG5400**	**Argus**	**Helix MC Plus**
collectors available	1 Faraday, 1 SEM	5 Faraday, 1 SEM	5 Faraday, 5 SEM
mass resolution	200	200	750 / 1500
analyzed noble gases	Kr, Xe	Ar, Xe	Kr, Xe
trap current (µA)	200	270	300
collectors that were used	SEM	Faraday (Ar), SEM (Xe)	SEMs
analysis mode	peak jumping	peak jumping	peak jumping (Ax) / multicollection (L2 and H2)
number of samples analyzed	7	16	13
wrapping	platinum	nickel	nickel
stepwise heating extraction	2 to 5 steps (300 - 1400°C)	2 to 5 steps (150 - 1250°C)	2 to 3 steps (150 - 1100°C)
number of Xe/Kr standard aliquots	11*	36*	60
mean sensitivity 132Xe (A/torr) - 1 pipette = 4.3 10^{-15} moles	9.6×10^{-4} ± 5.2 %	2.3×10^{-4} ± 2.3 %	4.2×10^{-4} ± 0.8 %
number of Ar standard aliquots	-	22	-
mean sensitivity 40Ar (A/torr) - 1 pipette = 4.5 10^{-12} moles	-	1.5×10^{-3} ± 2.3 %	-
average Xe content in Nebulotron samples (moles)	130Xe : 4.1± 0.1×10^{-16}	132Xe : 8.1± 0.1×10^{-14}	132Xe : 4.4± 0.1×10^{-14}
Hot blanks (> 800°C, moles)	130Xe : 8.8×10^{-19}	132Xe : 1.9×10^{-17} 40Ar : 2.1×10^{-13}	132Xe : 1.7×10^{-17}
standard deviation on Xe standards isotope ratios (min - max)	129/130 : 0.17 % 134/130 : 0.98 %	130/132 : 0.26 % 128/132 : 0.57 %	129/132 : 0.16 % 126/132 : 1.04 %
standard deviation on Kr standards isotope ratios	82/84 : 1.03 %	-	82/84 : 0.55 %
standard deviation on Ar standards isotope ratios (min-max)	-	40/36 : 0.28 % 38/36 : 0.69 %	-

* several standard concentrations were used

5.2.2.3 Data correction and reduction for the S2 session (Argus)

In order to match the (unknown) sample concentrations, standard aliquots with different Xe concentrations were analyzed to get a calibration curve. I realized, by doing this, that the background contribution from the mass spectrometer was important for some Xe isotopes and impacted the Xe isotope ratios (notably $^{128}Xe/^{132}Xe$ and $^{130}Xe/^{132}Xe$ ratios) of the standards having a small signal. A mixing line was observed between the isotopic composition of the mass spectrometer blank and that of the standard, resulting in a offset of up to 35% from the true value (air composition) for small ^{132}Xe signals (Fig. 5.5).

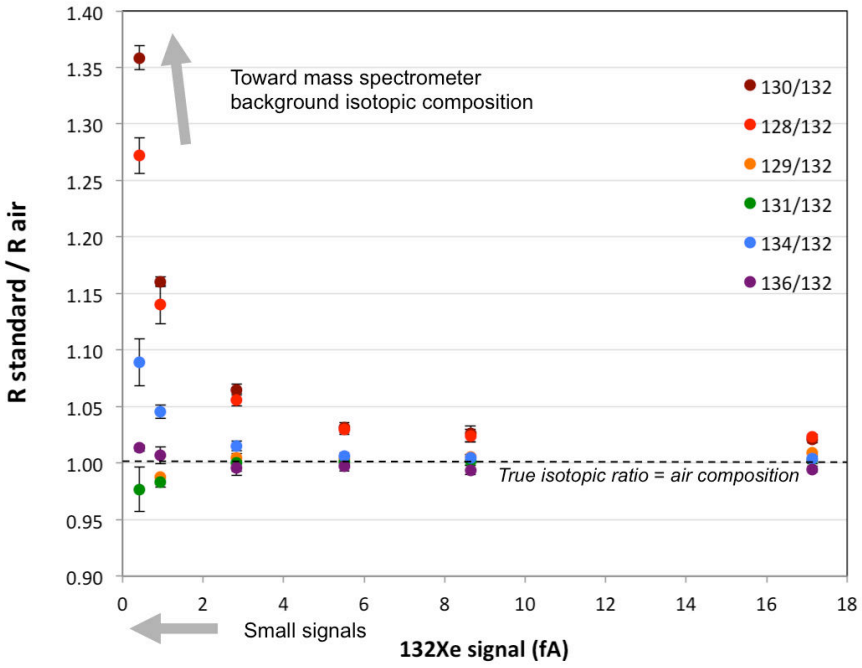

Figure 5.5. Mixing lines between the Xe standard and the Argus spectrometer background for each isotopic ratio relative to air ($(^{i}Xe/^{132}Xe)std/(^{i}Xe/^{132}Xe)air$) as a function of the signal of ^{132}Xe measured.

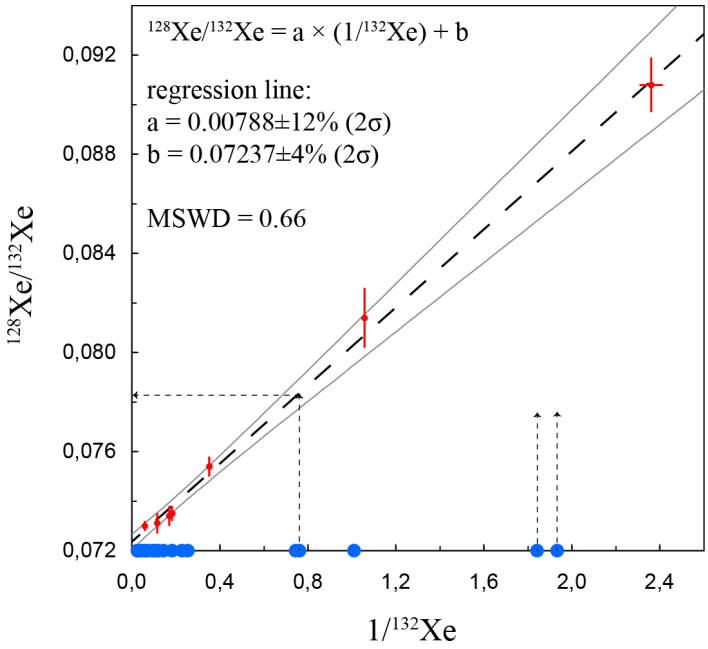

Figure 5.6. Mixing line between the standard and the Argus background for the $^{128}Xe/^{132}Xe$ ratio calculated with the standard calibration line (red dots with 1σ error crosses): the slope and the intercept were calculated by applying an error-weighted regression line to the standard isotopic ratios measured for each standard concentration. This calculated line was then used to determine the 'true' isotopic ratio for the standard to be used to correct the sample isotopic ratio (illustrated by the dotted arrows). The blue circles represent the $1/^{132}Xe$ ratio measured in the Nebulotron samples and furnace blanks.

The Xe concentrations measured in the Nebulotron samples were in the range of concentrations chosen for the standards (Fig. 5.6). In order to correct the Xe isotopic ratios for each sample, I have determined the equation of the mixing line between the standard and the mass spectrometer background based on the isotopic ratios measured for each standard aliquot, and this was done for each Xe isotope (example for $^{128}Xe/^{132}Xe$ is shown in Fig. 5.6). The 'true' standard ratio was then calculated thanks to the regression line for the ^{132}Xe signal measured for each sample i (8) and this ratio was used to correct the corresponding sample i (9):

$$\left(\frac{^{128}Xe}{^{132}Xe}\right)^{i}_{std} = a \times \left(\frac{1}{^{132}Xe}\right)^{i}_{sample} + b \tag{8}$$

$$\left(\frac{^{128}Xe}{^{132}Xe}\right)^{i}_{corr} = \frac{\left(\frac{^{128}Xe}{^{132}Xe}\right)^{i}_{meas}}{\left(\frac{^{128}Xe}{^{132}Xe}\right)^{i}_{std}} \times \left(\frac{^{128}Xe}{^{132}Xe}\right)_{air} \tag{9}$$

These two calculations were applied to each Xe isotopic ratio. The errors were propagated to the final corrected sample isotopic ratio, and took into account the uncertainties on the slopes and intercepts from the regression lines. In fact, this method is correct only if the blank contribution is exactly the same for the standards and the samples. This was not the case in my study because the samples were affected by a blank contribution from the furnace that did not exist for the standards (the blank from the purification line and from the mass spectrometer were the same for both). However, for most samples (those having a ^{132}Xe signal > 0.8 fA), the blank contribution from the furnace was less than 1%. Hence, I assumed that this method is appropriate. For the other analytical sessions (S1 and S3), the mass spectrometer background was negligible and no such correction had to be performed.

5.2.3 Isotopic composition of the noble gas tank

In order to look for any isotopic fractionation displayed by the noble gases trapped in the solids organics synthesized in the Nebulotron setup, the initial isotopic composition of the noble gases used in the experiments had to be precisely determined. The Xe isotopes in the tank containing the He, Ne, Ar, Kr and Xe gas mixture were thus analyzed.

The tank (150 bar, 11 L) contains 67 moles of gas atoms, with 5.3×10^{-2} moles of ^{130}Xe atoms. The usual Xe quantities used in static mass spectrometry are ~ 10^{-16} moles of ^{130}Xe. In order get a large dilution factor, we used an empty and clean stainless steel tank of 10.7 L capacity, connected to two pipettes of 0.3 cm^3 each, one located between the noble gas tank and the dilution tank and the second between the dilution tank and the purification line. The small volumes available on the purification line were further used to ensure a final dilution factor of 1.6×10^{-13}. The ^{130}Xe gas quantity that was introduced into the mass spectrometer was thus ~ 8.5×10^{-15} moles. Such a quantity was relatively large and could be analyzed by Faraday cups. The Xe isotopes (^{128}Xe to ^{136}Xe) in the gas tank were analyzed using the “old” Helix MC installed at CRPG in 2005, which is equipped with Faraday cups only. The measurements were done in “peak-jumping” mode with the H1 Faraday cup.

Six aliquots of the gas tank were analyzed along with 18 standard aliquots. The final isotopic composition of Xe in the gas tank is given in Table 5.2.

Table 5.2. Xe isotope ratio for one noble gas tank used for Nebulotron experiments, obtained with the "old" Helix MC.

TANK (n=6)	128/132	± 1σ	129/132	± 1σ	130/132	± 1σ	131/132	± 1σ	134/132	± 1σ	136/132	± 1σ
B2	-	-	-	-	-	-	0.7858	0.0013	-	-	-	-
B3	0.0687	0.0019	0.9834	0.0029	0.1621	0.0019	0.7842	0.0016	0.3916	0.0018	0.3214	0.0020
B4	0.0664	0.0012	0.9784	0.0014	0.1608	0.0012	0.7885	0.0014	0.3934	0.0014	0.3245	0.0010
B5	0.0657	0.0013	0.9775	0.0017	0.1610	0.0012	0.7851	0.0012	0.3934	0.0009	0.3228	0.0013
B6	0.0669	0.0012	0.9781	0.0012	0.1612	0.0010	0.7853	0.0013	0.3942	0.0012	0.3247	0.0011
B7	0.0666	0.0011	0.9795	0.0015	0.1603	0.0012	0.7868	0.0014	0.3935	0.0011	0.3243	0.0010
weighted average	**0.0667**		**0.9787**		**0.1609**		**0.7859**		**0.3937**		**0.3240**	
2 SE (95%)	0.0011		0.0013		0.0011		0.0011		0.0010		0.0010	
STANDARD (n=18)												
average	0.0668		0.9761		0.1609		0.7843		0.3939		0.3250	
2 SE (95%)	0.0007		0.0014		0.0007		0.0007		0.0009		0.0014	
TANK/STANDARD	0.999		1.003		1.000		1.002		1.000		0.997	
2 σ	0.019		0.002		0.008		0.002		0.003		0.005	

The gas tank displays a mass fractionation of -0.9 ± 0.5 ‰/amu for Xe isotopes according to the error-weighted regression line (Fig. 5.7). This is a very small fractionation and for convenience, I will assume an air-like composition in the following sections.

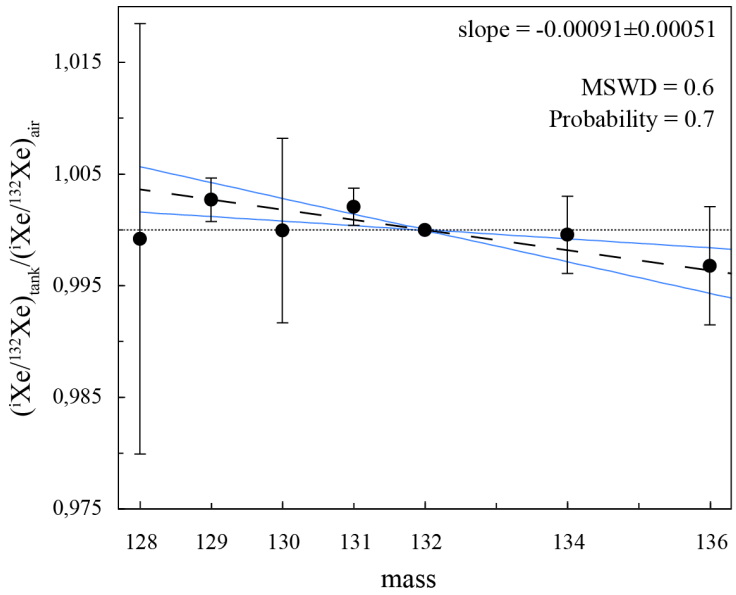

Figure 5.7. Xe isotopic composition of the gas tank (black dots) relative to the Xe standard (^{132}Xe=1) as a function of mass. Error bars are 2σ. The regression line and its 2σ envelope are shown. The dotted line represents the air composition (≡1, unfractionated).

5.3 Results

Experimental conditions and Xe concentrations and isotopic fractionation for all Nebulotron samples are reported in Table 5.3.

5.3.1 Xe concentration and trapping efficiency

The concentration of ^{132}Xe trapped in the Nebulotron samples ranges from 2.0×10^{-12} to 2.4×10^{-9} mol/g (Table 5.3). Some samples were analyzed several times, and the Xe concentration was variable. For example, the standard deviation around the mean ^{132}Xe concentration in the COGR18N sample is 60%. This may reflect that the samples themselves are not homogeneous. Moreover, these measurements have been done in different analytical sessions and the analytical conditions might have played a role in the observed abundance variability.

The gas-to-solid yield, i.e. the fraction of Xe trapped into the solids relative to the Xe in the gas phase integrated over the total experiment duration (the Nebulotron setup works in 'dynamic' mode) was calculated for each sample, based on the known Xe flow rate in the starting gas mixture, the duration of the experiment and the total mass of solids recovered. This yield is a minimum value because a fraction of the solids may have been pumped out during the experiment. The Xe gas-to-solid yields in our experiments span a large range, as for the concentrations, from 2.8×10^{-11} to 7×10^{-7} (moles into the solid/moles in the gas). The trapping efficiency can also be quantified based on Henry's law and assuming that Xe trapping follows a linear behavior (H in Table 5.3). The use of such a parameter is debatable in plasma experiments because a cold plasma is out of equilibrium by definition (Fridman, 2008). Nonetheless, several authors have used it to describe the noble gas trapping efficiency in electric discharge experiments (Marrocchi et al., 2011, Fukunaga and Matsuda, 1997, Frick et al., 1979). In order to compare our experimental results with the previous ones, the Henry coefficient H was calculated for the Nebulotron samples (Table 5.3). The H coefficients are in the range 0.1 – 71 ccSTP/g/bar, which again illustrates the large Xe concentration variability in the Nebulotron samples.

The Xe concentrations in experimental 'blanks' (e.g. Nebulotron samples produced from CO gas only) were also measured. These samples displayed ^{132}Xe concentrations of $7.1\pm3\times10^{-14}$ mol/g. Trapped Xe in these 'blank' samples likely originated from air adsorbed onto the surfaces or from residual Xe that was present in the Nebulotron setup during the experiment. These samples have 50 times less Xe than the Xe-poorest Nebulotron sample (COGR8N, Table 5.3). Hence, Xe measured in the Nebulotron organics produced from CO-noble gas mixtures is definitely derived from Xe in the gas flow and not from adsorbed air.

Table 5.3. Experimental conditions, Xe concentrations (mol/g) and isotopic fractionation (%/amu) in Nebulotron samples. Henry's coefficient (cc/g/bar) was calculated for each sample. Uncertainties (1) are ±5% for the mass of solid recovered and ±5% for the ^{132}Xe concentration.

sample	duration (min)	input power (W)	net power (W)	Xe fraction in the gas flow (‰)	$P^{132}Xe$ ($\times 10^{-7}$ bar)	mass of solids recovered (mg)	^{132}Xe ($\times 10^{-12}$ mol/g)	$H^{132}Xe$ (cc STP/g/bar)	isotopic fractionation (%/amu)	±2σ
'partial pressure' experiments										
COGR12	120	60	40	1.2	3.2	11.2	38.3	2.7	0.75	0.14
COGR10	120	60	43	8.9	27	2.8	130.0	1.1	0.79	0.15
COGR23	120	70	40	3.3	7.5	3.1	30.3	0.9	1.21	0.13
COGR11N	120	62	42	10	32	4.7	53.1	0.4	0.90	0.12
COGR11N	120	62	42	10	32	4.7	26.7	0.2	0.89	0.17
COGR17N	120	60	40	10	23	3.2	154.9	1.5	0.79	0.11
COGR3	120	60	40	2.2	5.8	6.1	7.1	0.3	1.04	0.24
COGR3	120	60	40	2.2	5.8	6.1	4.5	0.2	-	-
COGR5	120	60	40	7.5	20	1.4	20.6	0.2	0.60	0.18
COGR5	120	60	40	7.5	20	1.4	79.0	0.9	-	-
'duration' experiments										
COGR18N-a	360	65	43	3.3	7.5	48.8	152.5	4.6	0.73	0.14
COGR18N-b	360	65	43	3.3	7.5	48.8	420.3	12.6	0.88	0.12
COGR18N-c	360	65	43	3.3	7.5	48.8	293.5	8.8	0.81	0.11
COGR18N	360	65	43	3.3	7.5	48.8	144.7	4.3	1.16	0.41
COGR18	360	65	43	3.3	7.5	48.8	66.3	2.0	1.08	0.11
COGR19N-b	360	62	38	3.3	7.5	39.7	570.3	17.0	0.73	0.12
COGR23	120	70	40	3.3	7.5	3.1	30.3	0.9	1.21	0.13
COGR6N	210	60	40	3.3	7.5	8.0	6.8	0.2	1.58	0.29
COGR1	60	60	45	3.3	7.5	0.2	2.0	0.1	0.60	0.83
'discharge power' experiments										
COGR9N	120	90	65	3.3	7.5	7.5	53.7	1.6	1.92	0.14
COGR8N	120	40	28	3.3	7.5	6.0	21.8	0.7	0.71	0.16
COGR23	120	70	40	3.3	7.5	3.1	30.3	0.9	1.21	0.13
COGR18	360	65	43	3.3	7.5	48.8	66.3	2.0	1.08	0.11
COGR18N-a	360	65	43	3.3	7.5	48.8	152.5	4.6	0.73	0.14
COGR18N-b	360	65	43	3.3	7.5	48.8	420.3	12.6	0.88	0.12
COGR18N-c	360	65	43	3.3	7.5	48.8	293.5	8.8	0.81	0.11
COGR18N	360	65	43	3.3	7.5	48.8	144.7	4.3	1.16	0.41
COGR29	360	32	31	3.3	7.5	25.2	108.0	6.7	0.96	0.11
COGR30	360	60	60	3.3	7.5	25.4	2390.0	71.4	2.02	0.10
COGR31	360	30	30	3.3	7.5	30.6	550.0	46.2	0.92	0.10

italic = duplicate samples

5.3.2 Elemental fractionation

The Ar content was tentatively measured in some of the Nebulotron samples but in most cases, the blank contribution from the induction furnace (~ 2×10^{-13} moles of ^{40}Ar) was much larger than the Ar released from the Nebulotron samples. Therefore, I took the Ar mole quantity in the furnace blanks as an upper limit for the Ar content in the Nebulotron samples. Then, I calculated a ^{36}Ar/^{132}Xe ratio by taking the sample that displayed the maximum ^{132}Xe content during the same analytical session (even in this sample the Ar blank contribution was too high for suitable analysis) to get **an upper limit for the ^{36}Ar/^{132}Xe ratio for all the Nebulotron samples**.

The Kr content was also tentatively analyzed in some of the Nebulotron samples. In this case, while the blank contribution was high as well, four samples displayed blank contributions of less than 20%. However, the Xe standard used for correcting the analyses is not calibrated for its Kr content. I thus arbitrarily applied a depletion factor of 0.3 relative to the air Kr/Xe ratio to calculate the Kr content in the standard bottle and then a ^{84}Kr sensitivity (see previous section and Yokochi, 2005). Hence, I could calculate a ^{84}Kr/^{132}Xe ratio for the samples displaying a low blank contribution.

Finally, I evaluated the elemental ratios ^{36}Ar/^{132}Xe and ^{84}Kr/^{132}Xe of the Nebulotron samples relative to the same ratios in the flowing noble gas mixture, assuming air-like isotopic abundances for Kr atoms and Xe atoms (see section 4.2.3). This yielded the elemental fractionation factors α_{Ar} and α_{Kr} relative to Xe and to the starting gas composition:

$$\alpha_{Ar} = \frac{\left(\frac{^{36}Ar}{^{132}Xe}\right)_{solid}}{\left(\frac{^{36}Ar}{^{132}Xe}\right)_{gas}} \tag{10}$$

$$\alpha_{Kr} = \frac{\left(\frac{^{84}Kr}{^{132}Xe}\right)_{solid}}{\left(\frac{^{84}Kr}{^{132}Xe}\right)_{gas}} \tag{11}$$

The noble gas elemental fractionation factors calculated for the Nebulotron samples are reported in Fig. 5.8. They display a relative large α_{Kr} range, over more than one order of magnitude, with an average of 0.048±0.043. The upper limit for α_{Ar} in the Nebulotron samples is 0.049, which is indistinguishable from α_{Kr}.

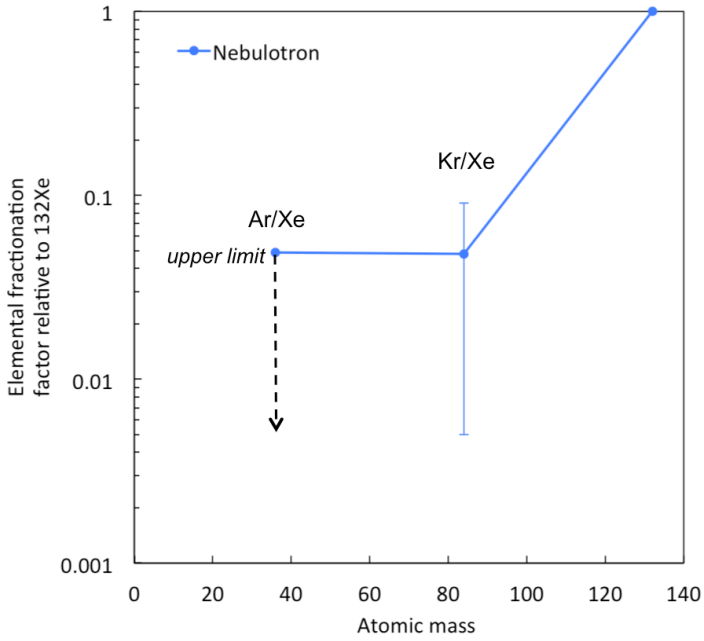

Figure 5.8. Noble gas (Ar, Kr and Xe) elemental fractionation measured in the Nebulotron samples. The fractionation factor for Ar is an upper limit (see text). The error bar on the $^{84}Kr/^{132}Xe$ ratio represents the standard deviation of four analyses.

5.3.3 Isotopic fractionation

5.3.3.1 Xenon and Krypton isotopic fractionation

Trapped Xe isotopes have been measured in all analyzed Nebulotron samples, whereas Kr isotopes were measured only in a few samples (only in the analytical sessions S1 and S3). In the following, the δ notation is used to describe the isotopic deviation of the Nebulotron samples from the air composition:

$$\delta\left(\frac{^{i}Xe}{^{132}Xe}\right) = \left(\frac{\left(\frac{^{i}Xe}{^{132}Xe}\right)_{sample}}{\left(\frac{^{i}Xe}{^{132}Xe}\right)_{air}} - 1\right) \times 1000 \tag{12}$$

$$\delta\left(\frac{^{i}Kr}{^{84}Kr}\right) = \left(\frac{\left(\frac{^{i}Kr}{^{84}Kr}\right)_{sample}}{\left(\frac{^{i}Kr}{^{84}Kr}\right)_{air}} - 1\right) \times 1000 \tag{13}$$

Xenon isotopic fractionation

Xenon isotopic fractionation factors (%/amu) relative to the composition of the flowing gas mixture are reported in Table 5.3. (Xe isotope ratios, corrected for the blank contribution and standard fractionation, are given in Appendix B).

All the Nebulotron samples produced from CO+Noble gases (±N_2) mixtures present large mass-dependent isotopic fractionations, resulting in Xe isotopic compositions significantly enriched in heavy isotopes relative to the flowing gas mixture (Fig. 5.9).

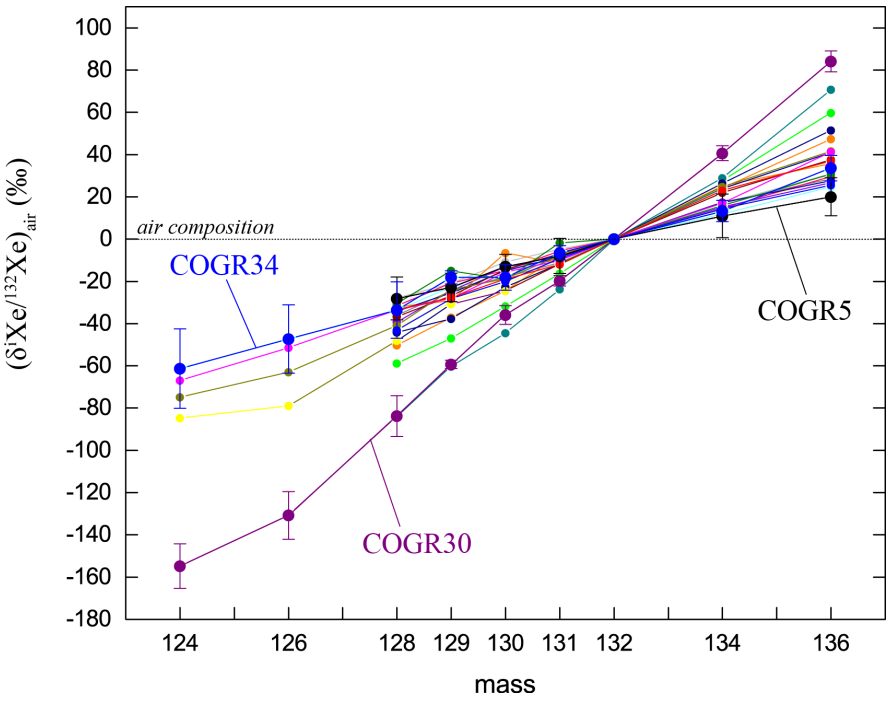

Figure 5.9. Xenon isotopic composition in Nebulotron samples (in δ notation). Uncertainties (1σ) are listed for samples COGR5, COGR34 and COGR30. Uncertainties for other samples are similar but not shown for visibility.

Isotopic fractionation factors were calculated by applying a linear and error-weighted regression through the Xe isotope ratios ($^{128\text{-}136}$Xe or $^{124\text{-}136}$Xe when ^{124}Xe and ^{126}Xe were measured) of Nebulotron samples normalized to ^{132}Xe and to the starting gas composition (Fig. 5.9). These regression calculations yielded Xe isotopic fractionation factors in the range 0.60-2.02 %/amu relative to the starting composition, with most Nebulotron samples recording an isotopic fractionation factor around 0.7-0.8 %/amu (Table 5.3. and Fig 5.9). Two samples display a much larger Xe isotopic fractionation, of about 2 %/amu. These two samples (COGR9 and COGR30) were produced with a higher power input in the discharge. The dependence on this experimental parameter is discussed in the next subsection.

Krypton isotopic fractionation

Seven Nebulotron samples displayed reliable Kr isotope ratios. Krypton isotopes are fractionated relative to the starting gas composition as well, showing an enrichment in heavy isotopes (Table 5.4. and Fig. 5.10).

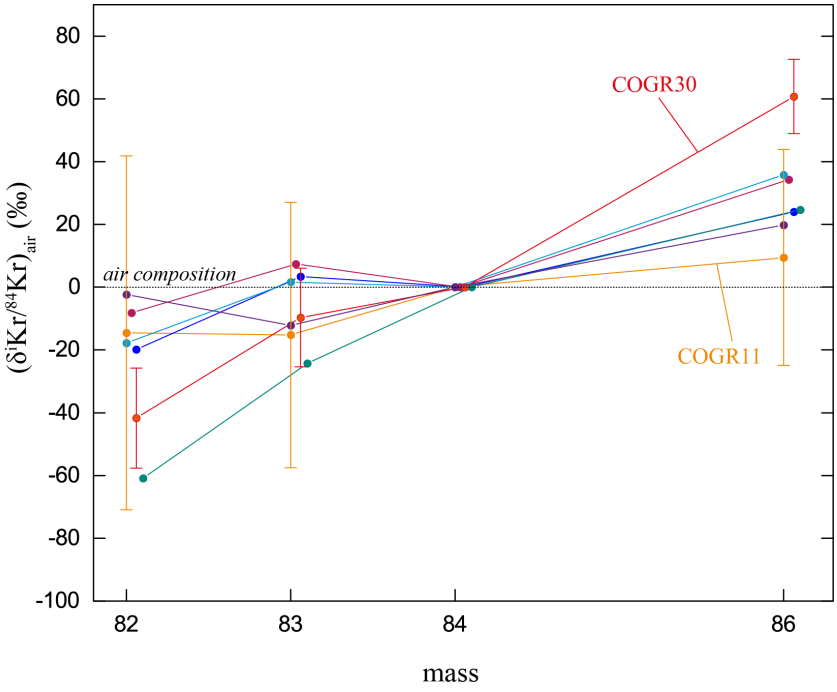

Figure 5.10. Krypton isotopic compositions in the Nebulotron samples. The points are slightly shifted along the mass axis for visibility. Error bars (1σ) are shown for two samples only for clarity.

The Kr isotopic fractionations (linear regressions on $^{82\text{-}86}$Kr isotopes normalized to ^{84}Kr and to the starting gas mixture) are in the range 0.70 – 2.57 %/amu, with an average of 1.34±0.7 %/amu (Table 5.4). Krypton isotopes are thus ~ 30% more fractionated relative to the starting composition than Xe isotopes.

Table 5.4. Kr isotopic fractionation factors (%/amu) for the Nebulotron samples.

sample	Kr isotopic fractionation (%/amu)	±2σ
S1 - VG5400		
COGR11-a	0.7	2.7
COGR5	0.97	1.8
COGR11-b	0.93	1.4
S3 - Helix MC		
COGR18	2.05	1.4
COGR29	1.42	0.95
COGR30	2.57	0.9
COGR31	0.71	0.6

5.3.3.2 A mass-dependent fractionation

Two mass-dependent fractionation laws describe the partitioning of isotopes: equilibrium and kinetic fractionations (Bigeleisen and Mayer, 1947, Urey, 1947, Young et al., 2002). These laws are characterized by the exponent β relating the fractionation factors α for two isotope ratios, such that $\alpha_{2/1} = \alpha_{3/1}^{\beta}$. This relationship yields fractionation curves in three-isotope diagrams. The system can be linearized if the δ' notation is used: $\delta' = 1000 \times \ln(R_{sample}/R_{standard})$ were R is the isotopic ratio, e.g., $^{i}Xe/^{132}Xe$ for Xe (Hulston and Thode, 1965). In three-isotope space, the mass fractionation curves in terms of δ' are straight lines of the form:

$$\delta'^{2/1} = \beta \times \delta'^{3/1} - \beta \times \left(\delta'^{3/1}\right)_{ref} - \left(\delta'^{2/1}\right)_{ref} \quad (14)$$

where β is the slope and the intercept is zero because here, ref is the air composition and $\delta'_{ref} = 0$.

The Xe isotopic ratios of the Nebulotron sample were drawn in three-isotope diagrams using the δ' notation (Fig. 5.11). All data points plot on a fractionation line with a slope that is equal within errors to equilibrium and kinetic mass-dependent fractionation factors determined for Xe isotopes with the β factors given in Young et al., 2002. Hence, **the Xe isotopic fractionation observed in the Nebulotron samples is mass-dependent**.

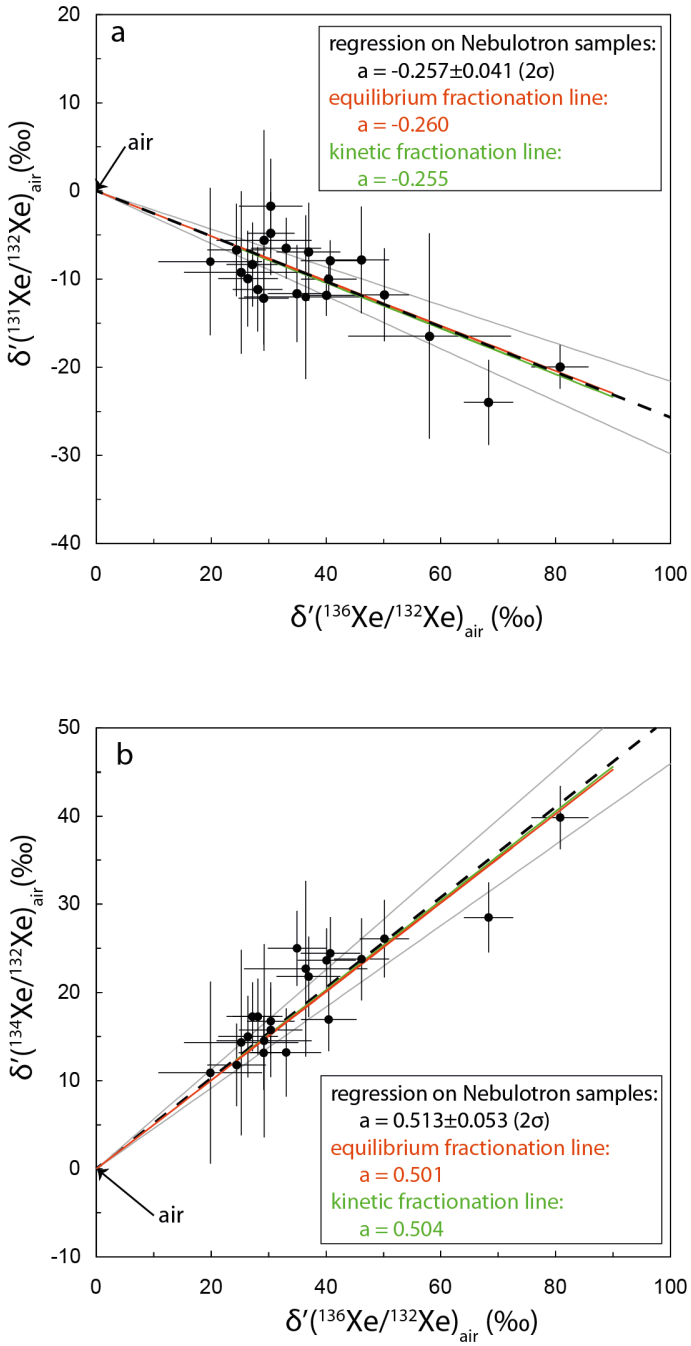

Figure 5.11. Xenon three-isotope diagrams. The linearized δ' notation was used ($\delta' = 1000 \times \ln(R_{sample}/R_{standard})$ were R is the isotopic ratio $^{i}Xe/^{132}Xe$) in order to obtain straight lines and to be able to apply a linear regression to the data set (Young et al., 2002). The black doted-line is the regression line on the Nebulotron samples (forced to zero). The red and green lines are equilibrium and kinetic fractionation lines, respectively. (a) $\delta'^{131}Xe$ vs. $\delta'^{136}Xe$ and (b) $\delta'^{134}Xe$ vs. $\delta'^{136}Xe$. Data-point error bars are 1σ.

Xe isotopic fractionation factors span a range of 0.60-2.02%/amu for the Nebulotron samples. The overall mass dependence is thus greater than $m^{1/2}$ (0.4%/amu, Fig. 5.12). Most samples have an isotopic fractionation factor of ~ 0.8%/amu, which is rather consistent with a m^{1} mass-dependent process (0.8%/amu, Fig. 5.12). Two Nebulotron samples have a Xe isotopic fractionation of about 2%/amu. Such large isotopic fractionation factors require a m^{2} or m^{3} dependence mass fractionation. This may reflect a change in the fractionation process

or a change in the relative importance of several fractionation processes: this is discussed below.

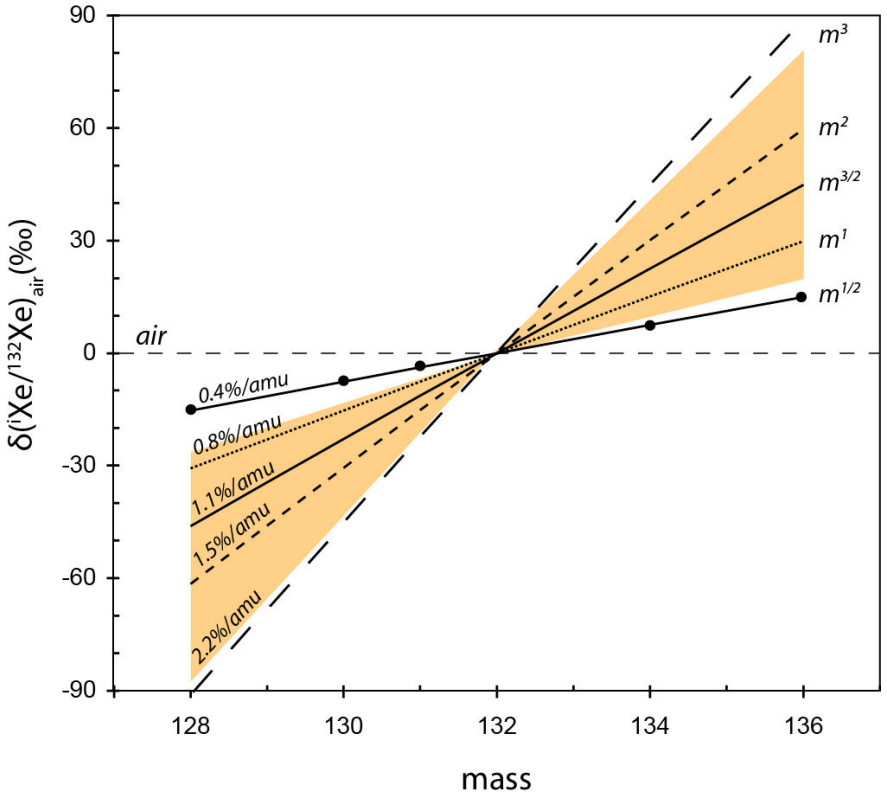

Figure 5.12. Xe isotopic fractionations for all the Nebulotron samples (orange area) assuming a mass-dependent fractionation laws with isotopic fractionation depending on $m^{1/2}$, m^{1}, $m^{3/2}$, m^{2} and m^{3}. Isotopic fractionation factors in ‰/amu are given for each law.

5.3.4 Dependence on the experimental parameters

The dependence of Xe trapping and isotopic fractionation on three experimental parameters was explored: i) the noble gas partial pressure in the gas flow, ii) the experiment duration, and iii) the power input given to the discharge.

5.3.4.1 Noble gas partial pressure

Some experiments were performed with a variable noble gases/CO ratio in the gas flow, from 0:100 to 50:50. The concentration and isotopic fractionation of trapped Xe atoms into the Nebulotron samples for these 'partial pressure' experiments are reported in Table 5.3.

The concentration of trapped Xe in the Nebulotron samples does not follow a linear trend as a function of the partial pressure of Xe, which would have been expected if the system had followed Henry's law (Fig. 5.13). The extreme dispersion of the data points

suggests that the equilibrium between the gas and the solid phases in the Nebulotron setup does not control the trapping of Xe atoms into solids. However, the variation of the partial pressure of Xe in the gas flow was limited by the mass-flow controller capacity (10 sccm) and by the total gas pressure in the setup (kept at ~ 1 mbar for all experiments). The noble gas partial pressure thus ranged over less than one order of magnitude, which might be too small to see a difference in the trapped Xe concentrations. Moreover, as outlined above, the Nebulotron samples do not seem homogeneous regarding the Xe concentrations, which certainly explains some of the dispersion observed in Fig. 5.13.

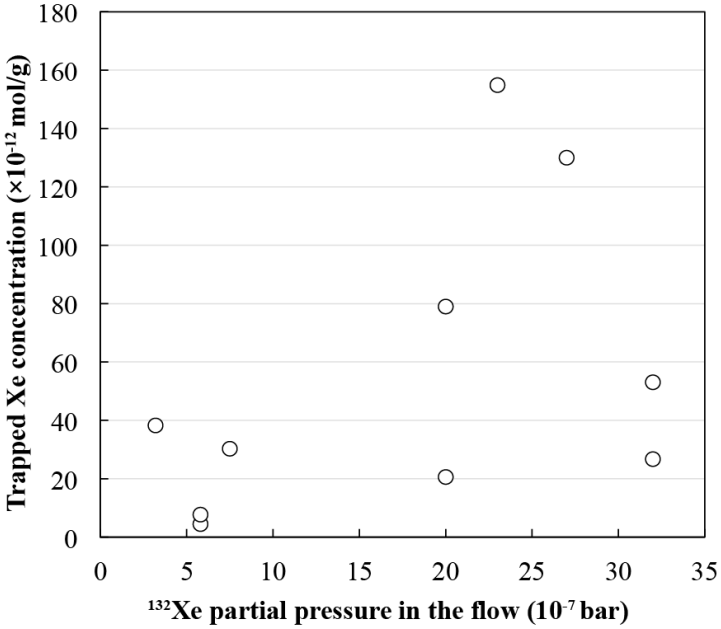

Figure 5.13. Trapped Xe concentration as a function of Xe partial pressure during the experiment.

5.3.4.2 Duration

One hour to six hour-long experiments were performed, with the same noble gas partial pressure and discharge power (Table 5.3).

Trapped Xe concentrations in the Nebulotron samples increase (exponentially) over several orders of magnitude for longer experiment durations (Fig. 5.14). However, the dispersion of the data is large, in particular for the 360 min points, preventing any reliable conclusion.

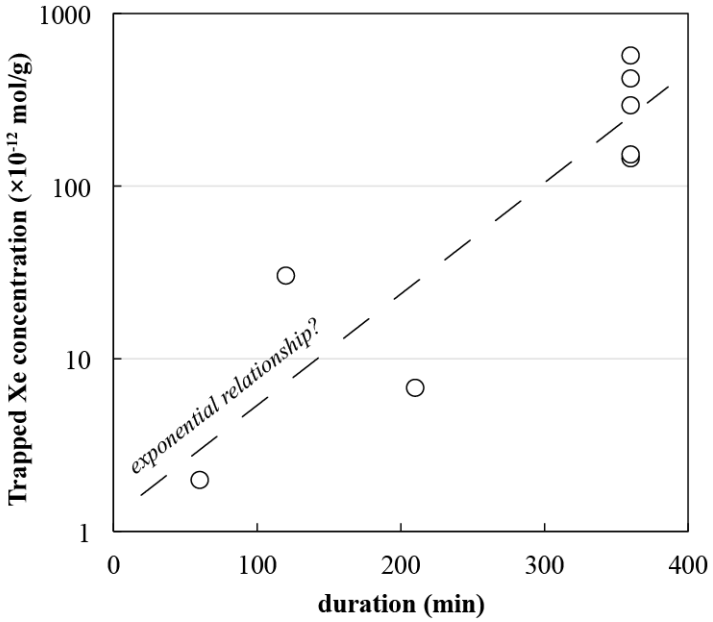

Figure 5.14. Trapped Xe concentrations in the Nebulotron samples as a function of the duration of the experiments.

5.3.4.3 Power delivered to the discharge

The last parameter that was varied in the present study was the power delivered to the discharge. Xenon concentration and isotopic fractionation as a function of the power of the discharge are reported in Table 5.3 and Fig. 5.15.

The Xe isotopic fractionation factor is strongly correlated with the net power delivered to the discharge, irrespective of the duration of the experiment. The two experiments performed at 60 W exhibited a Xe isotopic fractionation factor twice as large as the other experiments. The concentration of trapped Xe into the solids is less well correlated with the discharge power, but the solids produced at 60 W are nonetheless more Xe-rich than the others. Hence, **a larger power delivered to the discharge results in the increase of both the trapped Xe concentration and isotopic fractionation factor measured in the solids**. This raises the question of the role of the power input to the discharge.

When the power delivered to the plasma increases, the overall state of the plasma changes: (i) the gas temperature rises because the power density increases in the reaction volume, (ii) the electron density increases together with the ion density to maintain the neutrality, and (iii) as a consequence of the two first points, the neutral density decreases (same flow rate); hence the electron energy and the kinetic energy of ions are expected to increase too.

The larger Xe concentration and isotopic fractionation factors would thus be a consequence of the larger density and kinetic energy of ions in the plasma: **this would confirm the primordial role of Xe ions in the trapping and fractionation processes**.

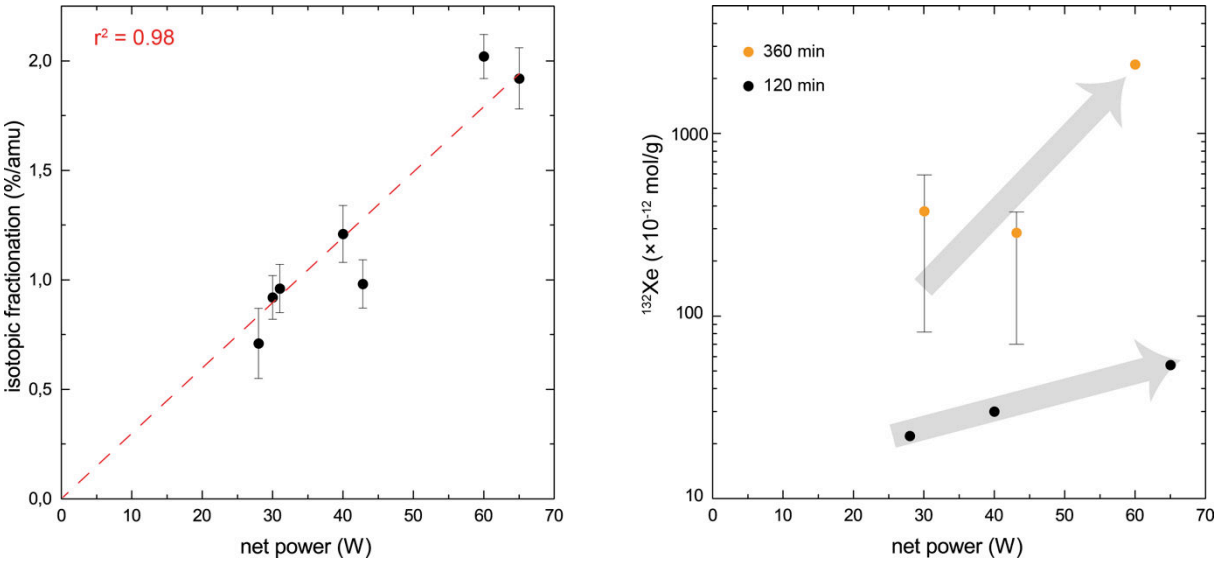

Figure 5.15. Xe isotopic fractionation factor (‰/amu, left) and concentration (mol^{132}Xe/g, right) as a function of the net power delivered to the plasma. Averages and standard deviations of Xe concentrations in COGR29 and COGR31 and in all COGR18 duplicates are shown for 30W and 43W, respectively.

5.3.5 Thermal release pattern

Four Nebulotron samples have been analyzed by stepwise pyrolysis from 150°C to 1400°C (3 to 5 steps, Fig. 5.16). No gas was released in the 150°C step, demonstrating that if air was adsorbed onto the surfaces of the Nebulotron samples, it was degassed during the baking step. While the thermal release pattern is not identical for the four Nebulotron samples, **all of them show a maximum gas release at 300-400°C** (30% to 90% of total Xe). This indicates that the trapped Xe atoms are not strongly retained in the carbon structure, but nonetheless enough not to be lost by diffusion or desorption. Except for sample CO-GR11, other Nebulotron samples released non-negligible Xe quantities above 500°C, up to 50% of the total gas for sample CO-GR3.

The released Xe is enriched in heavy isotopes relative to air for the four Nebulotron samples (Fig.5.16). With the exception of sample CO-GR6, **the isotopic composition of Xe does not change with the extraction temperature within errors** (1 sigma), demonstrating that Xe isotopes are homogeneously distributed within the samples. The ^{136}Xe/^{130}Xe ratio decreases with the extraction temperature in sample CO-GR6, with an air-like isotopic ratio at 1400°C. Such a behavior is not well understood at the time of writing.

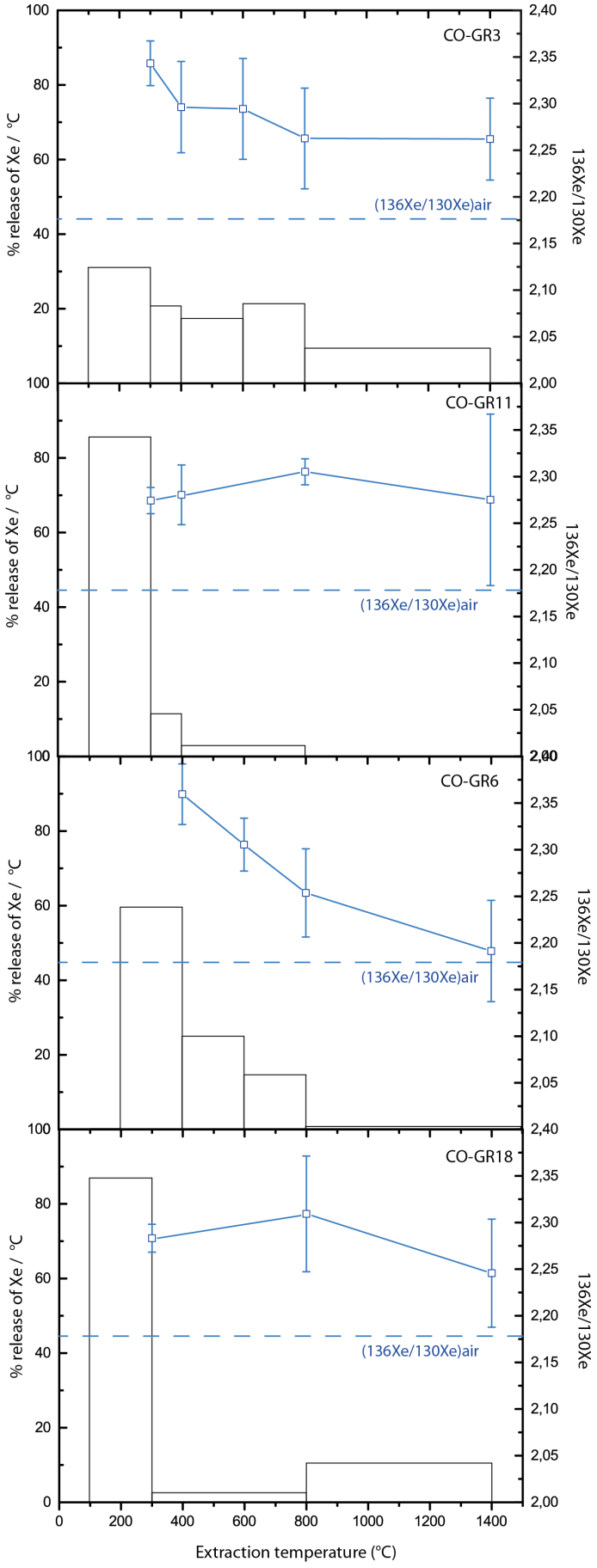

Figure 5.16. Thermal release patterns for ^{130}Xe in four Nebulotron samples, expressed in % of released gas normalized to °C. ^{136}Xe/^{130}Xe ratios and their 1 sigma uncertainties are shown for each step.

5.4 Comparison with previous experiments and with Phase-Q

5.4.1 Xenon concentration and trapping efficiency

The trapped Xe concentrations measured in the Nebulotron samples are compared to that of synthetic carbon solids produced in previous experiments of ion implantation of noble gases into growing (or not) carbon-rich materials (Marrocchi et al., 2011, Frick et al., 1979, Dzizckniec et al., 1981, Fukunaga and Matsuda, 1997, Matsuda et al., 1991, Matsuda et al., 1992) and to Phase Q (Busemann et al., 2000) in Table 5.5.

The Xe concentrations in the Nebulotron samples, as well as the Xe trapping efficiencies, fall in the range displayed by the cited experiments. The ^{132}Xe concentrations in synthetic carbon compounds, as well as trapping efficiencies, range over several orders of magnitude, from 10^{-9} to 10^{-3} ccSTP/g. In the following, concentrations are given in ccSTP/g because trapping efficiency factors are expressed in ccSTP/g/bar. The largest concentrations are not associated systematically with the largest trapping efficiency. For instance, the experiment performed by Marrocchi et al., 2011 yielded the largest ^{132}Xe concentration relative to other studies but was somewhat inefficient in trapping Xe atoms into the solids given the Xe partial pressures. Experiments performed by Matsuda et al., 1991 and Fukunaga and Matsuda, 1997 yielded the largest trapping efficiencies for Xe in carbonaceous synthetic products. This may reflect that their experiments were of the longest durations (50h), enhancing the trapping efficiency (as observed for the Nebulotron samples, see section 4.3.4.2). The ion implantation energies in these experiments may also have been very high, but are not given by their authors. Interestingly, the noble gas implantation into *already* formed carbon phases (Matsuda et al., 1992) resulted in a very low trapping efficiency for Xe. This suggests that **ion implantation into growing materials is a key to efficiently trap the noble gases into carbon-rich materials**. Matsuda et al., 1992 also reported that the concentration of implanted Ar, Kr and Xe atoms into the produced carbonaceous solids increased with the electric potential of the discharge; confirming the observation that the Nebulotron samples produced with a higher power delivered to the discharge had a larger Xe concentration.

The concentration of Xe atoms into chondritic acid residues is about 10^{8} - 10^{7} ccSTP/g of ^{132}Xe (Busemann et al., 2000). Such concentrations are relatively well reproduced by the above experiments, including the Nebulotron one. However, the trapping efficiency for Q gases, assuming that they were trapped from the ambient solar gas (Asplund et al., 2009), is larger by several orders of magnitude relative to the trapping efficiencies yielded in the laboratory experiments (Table 5.5). Moreover, these Xe concentrations are given for the acid residue, but Phase Q itself may account for less than 0.01% of this residue, implying a trapping efficiency from a solar gas of ~ 10^{11} cc/g/bar, surpassing our wildest expectations. This puzzling observation suggests that either the laboratory experiments do not reproduce at all the noble gas trapping mechanism(s) that resulted in the formation of Phase Q, or, that Q gases were trapped in a non-canonical nebular gas which contained much more Xe (and other noble gases) than the present-day Sun's composition.

Table 5.5. Xenon concentrations and trapping efficiencies in synthetic carbon-rich materials in several plasma experiments.

Experiment	experimental conditions	synthetic product	^{132}Xe (ccSTP/g)	H (ccSTP/g/bar)
This study	CO + noble gases (from 1 to 10%) - electric discharge - dynamic mode (1 to 6 h long)	amorphous carbon	5×10^{-8} - 5.4×10^{-5}	0.1 - 71
Marrocchi et al. 2011	'crumbled' anthracite in pure Xe gas - electric discharge - dynamic mode (5 min long)	amorphous carbon	1.1×10^{-4} - 1.2×10^{-3}	0.16 - 1.5
Frick et al. 1979	CH_4+N_2 + noble gases (25:25:50) - electric discharge - static mode (24h long)	amorphous carbon	5.3×10^{-8}	180
Dzizckaniec et al. 1981	CO-N_2-H_2 (84:5:5) + noble gases - electric discharge - dynamic mode (8h long)	amorphous carbon	1.6×10^{-9}	1.2
Fukunaga et al. 1997	CH_4 + noble gases (99:1) - W filament as a electron source - dynamic mode (50h long)	amorphous carbon	4.3×10^{-6} - 1.7×10^{-4}	6.1×10^{3} - 2.4×10^{5}
Matsuda et al. 1991	H_2 + CH_4 + noble gases (98:1:1) - electric discharge - dynamic mode (50h long)	nanodiamonds	1.5×10^{-4} - 6.6×10^{-4}	804 - 1875
Matsuda et al. 1992	noble gases implanted into graphite - electric discharge - dynamic mode (30 min long)	graphite	5.2×10^{-10} - 1.9×10^{-7}	< 0.07
Matsuda et al. 1992	noble gases implanted into diamonds - electric discharge - dynamic mode (30 min long)	nanodiamonds	4×10^{-11} - 6.8×10^{-9}	< 0.002
Phase Q	-	amorphous carbon?	1.6×10^{-8} - 20×10^{-8} *	3×10^{7} - 4×10^{7} **

*concentration in acid residue (Busemann et al. 2000)

** Total pressure in the solar nebula taken at 10^{-5} bar and Xe fraction at 1.6×10^{-10} (Dullemond et al. 2002, Asplund et al. 2009) - if Q represents 0.01% of the acid residue, then H shall be ~ 3×10^{11} cc/g/bar

5.4.2 Elemental fractionation

Elemental fractionation between the noble gases trapped in carbon-rich materials has been determined in the present study and in several other laboratory experiments (Fig. 5.17). The fractionation pattern is essentially the same within errors for all the experiments presented here. This experimental fractionation reproduces well the elemental pattern observed for the Q-gases relative to the solar composition (Fig. 5.17). For comparison, noble gas trapping into water ices, that is, the mechanism suggested for noble gas trapping into comets, does not reproduce the Q-gases pattern. Such a similarity between elemental fractionation produced in plasma experiments and Q-gases strongly suggests that the latters might originate in an ionized environment.

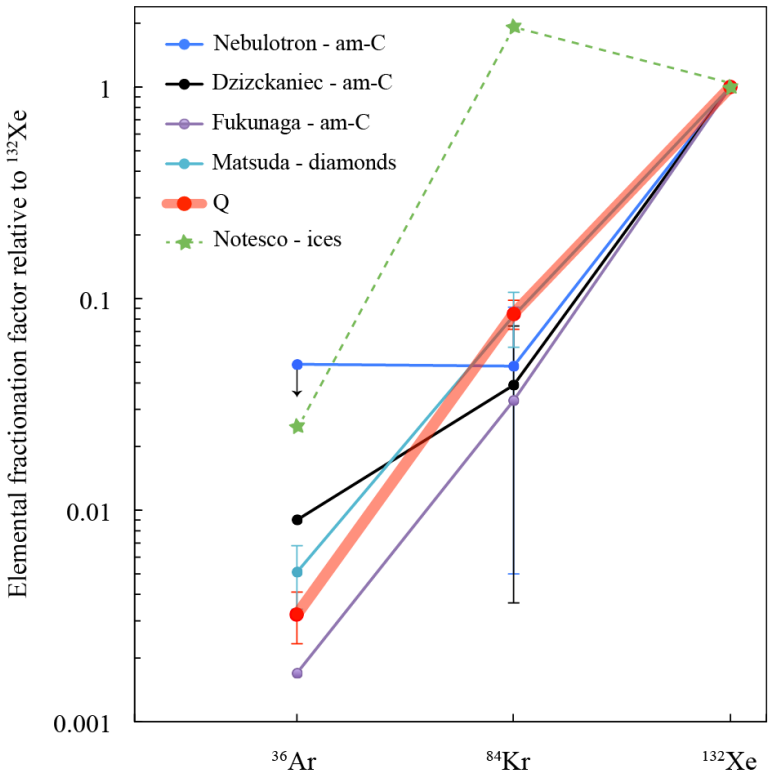

Figure 5.17. Elemental abundances patterns for Xe, Kr and Ar in Q (average of chondrites measured by Busemann et al., 2000) and in ion-implantation experiments (this study, Dzizckniec et al., 1981, Fukunaga and Matsuda, 1997, Matsuda et al., 1991). The fractionation factor is defined in the text. The solar composition is taken as the reference for the Q-gases. The upper limit for ^{36}Ar/^{132}Xe in the Nebulotron samples is shown by the arrow. For comparison, data from noble gas trapping in water ices are shown (Notesco et al., 2003). am-C stands for amorphous carbon.

5.4.3 Isotopic fractionation

Trapped Kr and Xe isotopes were analyzed in several ion implantation experiments (Frick et al., 1979, Dzizckniec et al., 1981, Marrocchi et al., 2011, Bernatowicz and Fahey, 1986, Hohenberg et al., 2002). The results for Xe isotopes in experiments dealing with carbon compounds are shown in Fig. 5.18 along with the composition of Q.

Xenon isotopes in Phase Q do not follow a linear trend with the mass, unlike the experimental data. This has been interpreted as the addition of other isotopic components to Q, such as Xe-HL which is carried by nanodiamonds, and s-process Xe (Meshik et al., 2014, Crowther and Gilmour, 2013). The excess in ^{129}Xe observed in Q is due to radiogenic ^{129}I that was present in the early ages of the solar nebula. Irrespective to these additions, the mass fractionation between Q and the solar wind Xe is ~ 0.8%/amu (Crowther and Gilmour, 2013, Meshik et al., 2014). This is in good agreement with the results from Xe trapping plasma experiments (Fig. 5.18).

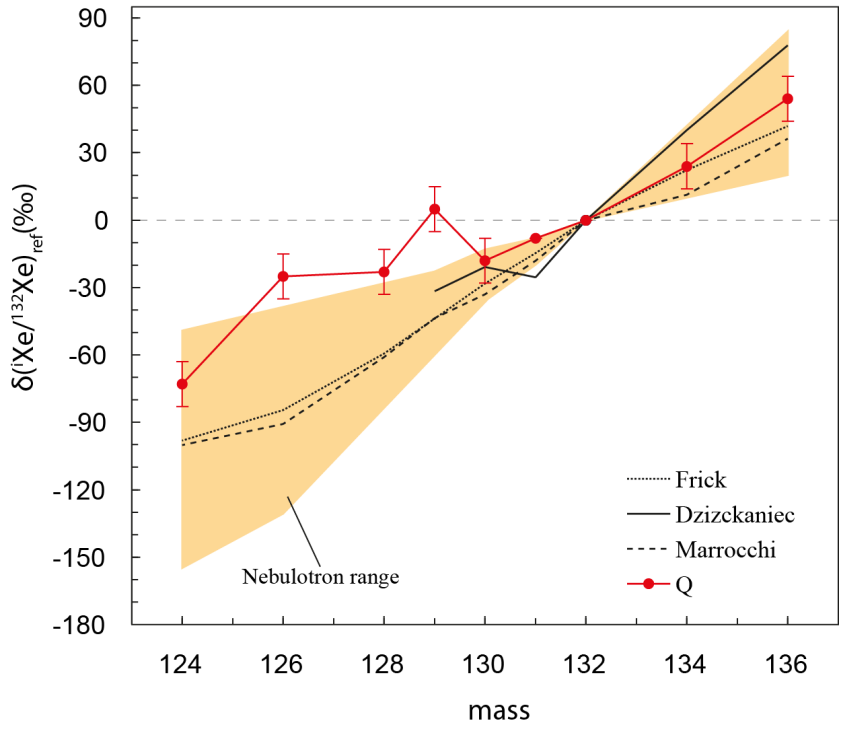

Figure 5.18. Xe isotopic composition in Q (average of all chondrites measured by Busemann et al., 2000) as well as in different plasma experiments: this study, Frick et al., 1979, Dzizckniec et al., 1981 and Marrocchi et al., 2011. The delta notation is used and the ratios are normalized to ^{132}Xe and to the solar wind composition for Q (Meshik et al., 2014) and to air for the plasma experiments. The orange shaded area represents the range of Xe isotopic compositions obtained in the Nebulotron experiment. Typical errors (1σ) on deltas are shown for Q only for visibility.

To summarize, plasma experiments reproduce the elemental and isotopic patterns observed in Q as well as the Xe concentrations. On the other hand, the trapping efficiencies obtained in laboratory experiments are much lower than the trapping efficiency estimated for

Q. The Nebulotron experiment, along with the previous ones, confirm the **essential role played by noble gas ions** in reproducing the Q-gases elemental and isotopic characteristics.

5.5 Noble gas fractionation mechanisms in plasma experiments

5.5.1 Elemental fractionation and ionization energy

Trapped noble gases show a highly fractionated elemental pattern in plasma experiments as well as Phase Q (Ne to Xe, Fig. 5.19). As already observed by several authors, purely mass dependent fractionation processes are not very successful at reproducing the observed elemental fractionation pattern in Q (Ozima et al., 1998, Rai et al., 2003, Ott, 2002, Ott, 2014). If Ar/Xe and Kr/Xe ratios in Q and in experiments follow a linear trend with mass (Fig. 5.19.a), Ne/Xe and He/Xe (not shown here because the uncertainties on experimental ratios are too large) fall off this trend. Hence, while mass might be an important factor, unless Ne and He elements alone suffer additional depletion relative to Ar, Kr and Xe, another mechanism is required to explain this elemental fractionation pattern.

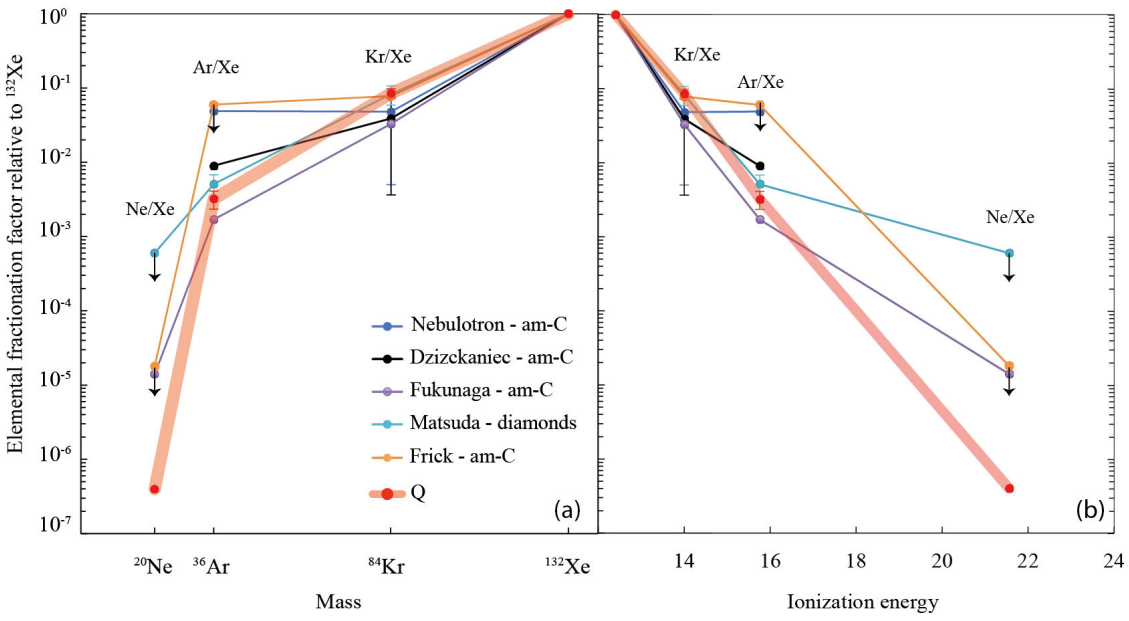

Figure 5.19. Elemental ratios of Q (average from Busemann et al., 2000) and of trapped noble gases in synthetic carbon compounds from plasma experiments (this study and Dzizckniec et al., 1981, Frick et al., 1979, Fukunaga and Matsuda, 1997, Marrocchi et al., 2011, Matsuda et al., 1991). Ratios are normalized to ^{132}Xe and to the solar abundance for Q and to the elemental composition of the starting gases for the experiments. (a) plotted vs. mass and (b) plotted vs. ionization energy. Arrows show the upper limits for some experimental ratios.

The relationship between the 'planetary' elemental fractionation pattern and the ionization energy of the different noble gases was first suggested by Weber et al., 1971 and then by Göbel et al., 1978, Ott, 2002 and Rai et al., 2003. These author observed that the elemental ratios in Q and in ureilites followed a clear trend with ionization energy (Fig. 5.19.b). Göbel et al., 1978 proposed that the depletion factors between noble gases are directly reflecting the ionized fraction of these noble gases in a plasma. One can calculate the ion distribution of an element in a plasma, assuming a Maxwell-Boltzmann distribution of the velocities of the particles (atoms, molecules and electrons too - see EEDF definition in Chapter 2), thanks to the Saha-Langmuir equation (Elwert, 1952). This equation describes the equilibrium between ionization and recombination in a thermal plasma:

$$\frac{N^+ n_e}{N_0} = 2 \times \frac{B_+(T)}{B_0(T)} \times \frac{(2\pi m_e kT)^{\frac{3}{2}}}{h^3} \times exp\left(-\frac{E_i}{kT}\right) \tag{15}$$

Where N^+ and N_0 are the densities of ions and neutrals of the element N, respectively; n_e is the electron density; E_i the ionization energy (eV) of the element N, k the Boltzmann's constant (k=8.617×10^{-5} eV.K^{-1}); T the gas temperature (K); m_e the electron mass; h the Planck's constant, and $B+(T)$ and $B0(T)$ are the partition functions of N^+ and N_0.

The Saha equation can be applied to non-thermal plasmas by taking into account the electron temperature T_e instead of the gas temperature T. The ratio of two ionized elements A and B in a cold plasma is thus given by:

$$\frac{A^+}{B^+} = \frac{A_0}{B_0} \times \frac{B_+^A(T)}{B_0^A(T)} \times \frac{B_0^B(T)}{B_+^B(T)} \times exp\left(-\frac{(E_A - E_B)}{kT_e}\right) \simeq \frac{A_0}{B_0} \times exp\left(-\frac{(E_A - E_B)}{kT_e}\right) \tag{16}$$

The ionization fraction of Ar, Kr and Ne, relative to Xe, were calculated using this equation and are reported in Fig. 5.20. as a function of the electron temperature. One can see that the fractionation between noble gases is greatly enhanced when the energy of electrons is low and that this fractionation tends towards 1 when the electron energy is high. In the latter case, the tail of the EEDF is developed enough to produce equal ionization of all noble gases.

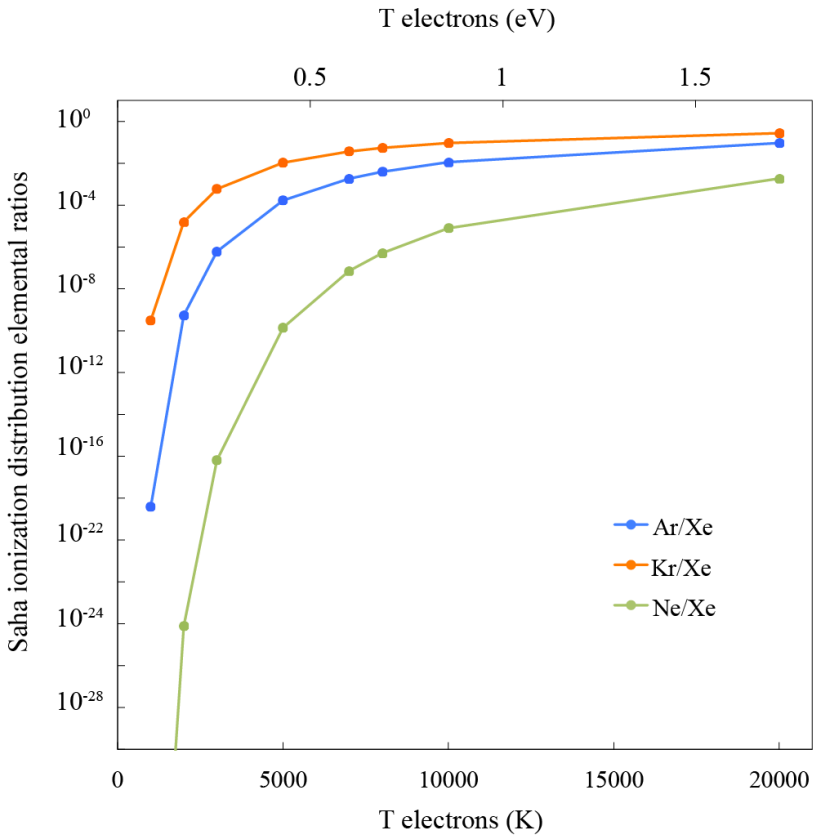

Figure 5.20. Saha-derived elemental ratios of ionized fractions for noble gases in plasmas as a function of the electron temperature.

In Fig. 5.21., the fractionation patterns calculated for different electron temperatures are shown along with the range of fractionation patterns observed in plasma experiments as well as in Q. Good matches are obtained at 8000 K for Q and 10000-15000 K for the experiments, in agreement with an electron temperature of 2 eV in the Nebulotron setup, for instance.

These correlations strongly support that trapped noble gases in synthetic carbon compounds produced in plasma experiments, and in Phase Q, originate from noble gas ions only. This implies that the concentrations of the trapped noble gases should depend on their ionic abundances in the gas phase. Such a behavior was indeed observed in the Nebulotron setup, in which the Xe concentrations in the carbon solids is enhanced at higher discharge powers, e.g. at higher ionization rates. This was also observed by Fukunaga and Matsuda, 1997 in their experiments: the noble gas content increased in their synthetic carbonaceous solids with the voltage of the discharge.

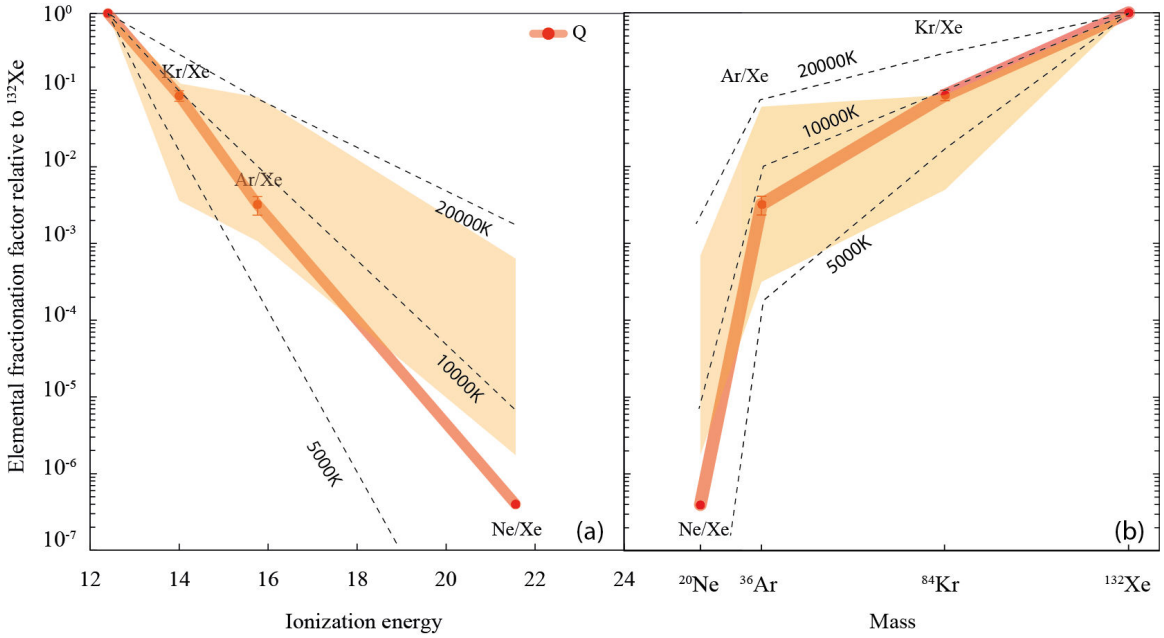

Figure 5.21. Calculated ionic abundance pattern of noble gases at three electron temperatures (5000, 10000 and 20000 K). The red line indicates the average for Q (Busemann et al., 2000) and the shaded orange area indicates the range obtained from plasma experiments (see Fig. 5.18). (a) plotted vs. ionization energy, and (b) plotted vs. mass.

In an ionized environment such as a plasma, one could expect to have similar fractionation for isotopes, since an isotopic fractionation for heavy noble gases is systematically observed in plasma experiments. However, the difference between the ionization energies of isotopes of the same element is much too small to account for the observed isotopic fractionations. For instance, for Xe isotopes, such a mechanism would result is an isotopic fractionation of -0.5 ppm/amu, i.e. four orders of magnitude smaller than the observations (there is a minus sign because $^{124Xe}E_i$ is smaller than $^{136Xe}E_i$, Brandi et al., 2001). Hence, the isotopic fractionation cannot be generated in the gas phase and another mechanism is required to account for the experimental observations on isotopic enrichment of Kr and Xe.

5.5.2 Ambipolar diffusion and noble gas isotopic fractionation in plasmas

Although the isotopic fractionation of noble gases does not originate in the ionization process, it still relates to ions, as only plasma experiments are able to reproduce significant heavy isotope enrichment. As shown in Fig. 5.12, the Xe isotopic fractionation measured in most of the Nebulotron samples seems to depend on a m^1 mass fractionation law. This was also the case for previous experiments (Marrocchi et al., 2011, Dzizckniec et al., 1981, Frick et al., 1979, Bernatowicz and Fahey, 1986). We thus propose that the mechanism causing the fractionation of noble gas isotopes in plasma experiments is ambipolar diffusion.

Ambipolar diffusion is diffusion of charged species with opposite electric charges due to their interaction via an electric field. Electrons move, and thus diffuse, faster than ions (essentially because $m_e << m_i$). Locally, this causes a disequilibrium of charges, which is balanced by the apparition of an electric field, $\vec{E}$. The resulting electric field will tend to slow down the electrons and to accelerate the ions (Fig. 5.22).

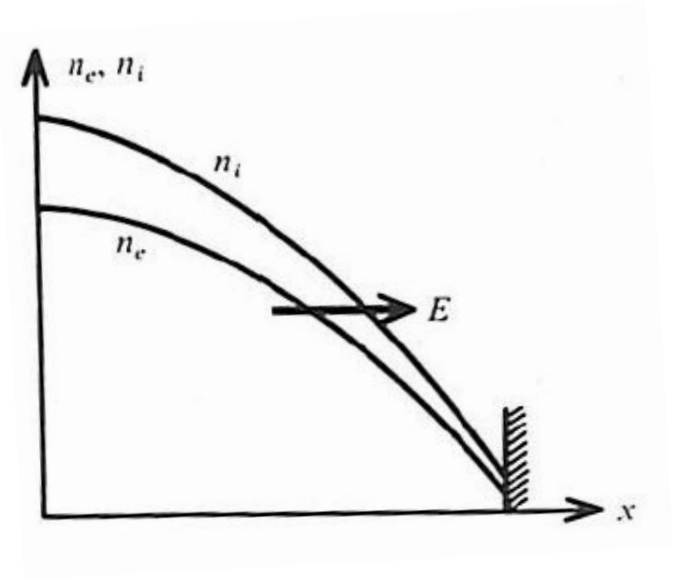

Figure 5.22. Schematic illustration of the ambipolar diffusion mechanism close to a surface (Delcroix, 1966).

Considering a stationary state, in which the active forces are pressure gradients and an electric field E and assuming that T_e and T_i are constant, we have the following equations (Delcroix, 1966):

$$n_e v_e = -n_e \mu_e E - D_e \nabla n_e \tag{17}$$

$$n_i v_i = +n_i \mu_i E - D_i \nabla n_i \tag{18}$$

With n the densities of electrons and ions, v the velocities of electrons and ions, μ the mobility coefficients of charged particles, D the free diffusion coefficients of electrons and ions, and E the electric field.

On an isolating surface (walls of the reactor for instance), the electric current is zero:

$$n_e v_e = n_i v_i \tag{19}$$

When n_e and n_i are high (this is the case for the Nebulotron setup), the coupling between electrons and ions is expected to be total. The local environment is neutral, and we have:

$$n_e = n_i \tag{20}$$

and as a result:

$$v_e = v_i \tag{21}$$

This theoretical calculation stands for one ion species in an electric field. A rigorous modeling would be required to derive the velocities of charged particles in a mixture of different ionic species, which is our case. ***In the following, we will assume that all the ionic species in the plasma have the same velocity v_i.*** Although not checked, this hypothesis is reasonable (G. Cernogora, personal communication). For two particles A and B, it implies that:

$$E_A = \frac{1}{2} m_A v_i^2 \tag{22}$$

$$E_B = \frac{1}{2} m_B v_i^2 \tag{23}$$

Which eventually leads to:

$$\frac{E_A}{E_B} = \frac{m_A}{m_B} \tag{24}$$

The kinetic energy of a particle depends on its mass only and the ratio of kinetic energies for two particles is the ratio of their masses. As a consequence, the particles encountering a surface are in the form of a mono-velocity flow with kinetic energies of the particles depending on their masses. Hence, ^{136}Xe ions have a larger kinetic energy than ^{124}Xe ions in a ratio that depends on m^1. We suggest that the apparent m^1 dependent isotopic fractionation observed in our experiments is due to ambipolar diffusion, which would yield a theoretical isotopic fractionation of 0.76%/amu and 1.19%amu for Xe and Kr, respectively. Within uncertainties (and approximations), these calculated fractionation factors match very well our experimental data, and the previous ones, both for Xe and Kr. In particular, for Xe, all the Nebulotron samples display an isotopic fractionation of ~ 0.7%/amu at least.

5.5.3 A low-energy ion implantation mechanism?

From the above discussion, we suggest that the mechanism responsible for noble gas trapping in the Nebulotron setup, and in plasmas in general, is ion implantation.

5.5.3.1 Trapping low-energy noble gas ions

Kinetic energy of ions in the Nebulotron setup

We have calculated the kinetic energy of ions impinging surfaces in the Nebulotron setup using the approximations given above in the case of ambipolar diffusion. The radial electric field of ambipolar diffusion can be reduced to:

$$E \approx \frac{D_e}{\mu_e} \times \frac{1}{R} = \frac{kT_e}{q_e} \times \frac{1}{R} \tag{25}$$

where D_e is the free diffusion coefficient for electrons, μ_e the electron mobility, T_e the electron temperature, q_e the electron charge, k the Boltzmann's constant and R the characteristic radius of the reactor. Taking R = 4 mm (radius of the Nebulotron reactor), kT_e/q_e = 2 eV for the average electron energy, we find E ≈ 5×10^2 V/m in the Nebulotron plasma. This radial electric field does not depend on the gas composition and governs the charged particles motions everywhere in the plasma.

The ion velocity can be approximated to:

$$v_i \approx D_i \left(1 + \frac{T_e}{T_i}\right) \times \frac{1}{R} \tag{26}$$

Where D_i is the coefficient for free diffusion of the ionic species and T_i the ion temperature. ***Here, we assumed that the main species in the gas was He*** (the He content in the gas flow was 12.5 % and D_i value was not available for CO. D_i values variations are less than one order of magnitude depending on the species).

In weakly ionized plasmas, ion-neutral collisions are dominant and D_i can thus be estimated by the following relation (Delcroix, 1966):

$$D_i \approx \sqrt{\frac{kT_i}{m_i}} \times \frac{1}{n_0 \sigma_{i-0}} \tag{26}$$

Where m_i is the mass of the ion species, n_0 is the neutral density and σ_{i-0} is the ion-neutral collision cross section at a given electron temperature. For He, the latter value is known and taking a neutral density of ~ 7×10^{-15} cm^{-3} (corresponding to a pressure of 1 mbar

with a neutral temperature of 1000 K), T_i = 2000 K and T_e = 2 eV (i.e. 20000 K), we have for He ions:

$$v_i \approx 5.5 \times 10^3 m.s^{-1}$$

Given the above approximations, we can derive the kinetic energies for noble gas ions in the plasma in an ambipolar diffusion regime (Table 5.6).

Table 5.6. Kinetic energies (eV) for noble gas ions calculated from the ambipolar diffusion model in a plasma composed of He, for two electron energies (1.7 eV and 2.6 eV) and with Ti = 2000 K.

		Ec (eV)				
	vi ($m.s^{-1}$)	^{4}He	^{20}Ne	^{36}Ar	^{84}Kr	^{132}Xe
Ti=2000K - Te=1.7 eV	5.5	0.6	0.9	2.8	13.3	20.9
Ti=2000K - Te=2.6eV	9.8	2.0	2.8	8.5	42.2	66.3

The calculated noble gas kinetic energies are in the range 1-70 eV, depending on the electron temperature and on the ion mass. Xenon ions have larger kinetic energies compared to other noble gases. However, these kinetic energies might be underestimated because of the electrostatic sheath present close to the surfaces of the reactor. In this region, the electric field is enhanced and the ions are accelerated, resulting in larger kinetic energies. The energies given in Table 5.6 are thus lower bounds.

Low-energy ion implantation

In order to be implanted into solid materials, ions must have energies above a given threshold. The implantation mechanism also depends on the respective masses of the incident ions and of the target material atoms, as well as density of the latter. Few investigations have been made in the low energy region because of minor technical interest and because of difficulties in measuring the interactions of low-energy ions with solid target material below 1 keV (Bernatowicz and Hagee, 1987, Choi et al., 1993b, Coufal et al., 1991, Ponganis et al., 1997). These studies showed that noble gases in the range 10-500 eV are shallowly implanted in solids, the implantation depth depending, as expected, on the mass of the incident ion and on the energetic features of the target (mass, bonding and lattice energies, surface defects, etc.). At energies below 100 eV, noble gas ions should be implanted in the first 15 Å (Choi et al., 1993a, Ziegler and Biersack, 1985). In detail, other processes like backscattering, spontaneous desorption, thermal diffusion and sputtering - also depending on the ion energies, the target and the temperature of the system - may tend to reduce the fraction of gases implanted. These observations show that low-energy ion implantation is a reliable mechanism for trapping noble gases into carbonaceous solids. The fact that noble gases are

implanted into growing solids may further enhance the trapping efficiency by burying them deeper into the carbon-rich network.

It is worth noting here, although such a process may exist, that "anomalous adsorption" involving chemical bonds between heavy noble gas atoms and surfaces, may be not required (Hohenberg et al., 2002). Physical ion implantation associated with growing solids may account alone for the noble gas trapping into carbon-rich solids and for the isotopic fractionation observed in the plasma experiments.

5.5.3.2 Loss mechanisms: sputtering and diffusion?

Interestingly, the Nebulotron samples display a good correlation between the isotopic fractionation extent and the power delivered to the discharge (Fig. 5.15). For instance, the two samples produced at 60 W present an isotopic enrichment of 2%/amu and 2.6%/amu for Xe and Kr, respectively. This implies that either the fractionation mechanism changes when the discharge power is increased or the light isotopes are preferentially lost by another process, which was not present (or not efficient enough) at lower discharge powers. Ambipolar diffusion is expected to drive essentially the same isotopic fractionation, whatever the electric state of the plasma. As outlined in the previous sections, at higher discharge powers, both the electron and ion densities are enhanced. Both processes tend to increase the temperature of electrons and thus kinetic energies of the ions (Table 5.6). In such a case, sputtering from energetic ions such as He and Ne ions (although they have a lower energy, their low mass allow for a higher sputtering yield) may have depleted the trapped gases from the near-surface region (Choi et al., 1993b, Smentkowski, 2000). Light isotopes are expected to implant at shallower depths than heavy isotopes because of their smaller kinetic energy. Hence light isotopes would be preferentially lost upon sputtering, resulting in an enhanced isotopic fractionation, as observed for these two Nebulotron samples. Enhanced sputtering may also be responsible for the creation of more defects onto the growing surfaces, which may facilitate migration and diffusion of the trapped atoms (Choi et al., 1993b).

A high discharge power also causes the neutral gas temperature to increase. This may induce an enhanced thermal diffusion for the noble gases trapped into the solids, with light elements and isotopes lost preferentially. Thermal diffusion may also be responsible for the larger isotopic fractionation observed for the Nebulotron samples produced at 60 W.

To conclude, in plasma experiments, low-energy ion implantation seems to be a reliable mechanism for trapping large noble gas quantities into growing solids. The elemental fractionation displayed by the trapped noble gases may reflect the ionic fractions in the gas phase. Ion kinetic energies are governed by ambipolar diffusion, resulting in an isotopic fractionation of 0.8 %/amu and 1.2 %/amu for Xe and Kr, respectively. The correlation between Xe isotopic fractionation factor and the power delivered to the discharge observed in the Nebulotron samples suggest that loss mechanisms for light isotopes are required. Such mechanisms may result from sputtering and diffusion.

5.6 Implications for the origin of Phase-Q

As shown in the previous section, the Nebulotron experiments reproduce some of the characteristics of the Q-gases, in particular the elemental and isotopic patterns of the heavy noble gases. Here, we outline the possible implications for the origin of Phase-Q.

5.6.1 A nebular plasma?

As previously proposed by several authors, Q-gases may have been formed by ion-implantation of solar gases in a nebular plasma (Göbel et al., 1978, Matsuda et al., 2010, Rai et al., 2003). Our experiments strongly support such a hypothesis because it might explain both the elemental and isotopic patterns of Q-gases relative to the solar composition.

5.6.1.1 Solar-wind implantation

The second trapped component in meteorites along with Q is implanted solar wind. The so-called 'solar' component was identified in gas-rich meteorites by its solar elemental and isotopic patterns (Black, 1972, Suess et al., 1964). Implanted solar wind was also measured in lunar soils and the isotopic compositions measured in these lunar samples served as the reference for the solar wind composition until the recent analysis of noble gases in Genesis solar wind collectors (Crowther and Gilmour, 2013, Meshik et al., 2014, Pepin et al., 1995). Interestingly, noble gas isotopic ratios were found to be the same within errors in lunar soils and in Genesis collectors. From these observations, one can conclude that solar wind implantation does not result in significant isotopic fractionation (at least for heavy noble gases), or, that the fractionation magnitude was the same in both Genesis targets and lunar soils, preventing any conclusion.

The solar wind consists mostly of electrons and protons with energies in the range 1.5 - 10.5 keV/nucleon. It is composed of two components: the slow solar wind with a velocity of 400 km/s and a temperature of $\sim 10^6$ K and the fast solar wind, with a velocity of 750 km/s and a temperature of 8×10^5 K. For comparison, the particle velocity in the Nebulotron setup is about 5.5 km/s, hence, the energy range of the solar wind is very different from the one produced in laboratory plasma experiments. This may suggest that high energy ion implantation, such as the one resulting from solar wind implantation, does not result in isotopic fractionation, whereas low-energy ion implantation does. The mechanism responsible for this difference is not well understood, especially given that laboratory ion implantation experiments performed in the keV range yielded contradictory results in terms of isotopic fractionation (Hohenberg et al., 2002, Huss et al., 2008, Koscheev et al., 2001).

5.6.1.2 Solar gas implantation

If Q-gases are formed by ion implantation, then the implanted gases are solar. These solar gases must be ionized and have kinetic energies in the range 10-100 eV in order to provide the elemental and isotopic pattern of Phase Q, as suggested by laboratory experiments.

Could plasmas with this energy range have been generated in the solar nebula? Several sources of ionization can be found in the solar nebula. The inner part is hot enough (>1000K) to be thermally ionized. T-Tauri stars are active and emit intense X-rays and FUV radiations, that are sufficient to raise ionization of some gaseous atoms/molecules (see Fig.1.3, Armitage, 2011).

In the MRI (Magnetorotational instability) active zones, in the inner region and in the outer region as well, one expects the ionization fraction to be sufficient enough to drive elemental and isotopic fractionation of noble gases. Dust, in particular carbon-rich dust, must be present in these zones to trap the noble gases. The ionized areas in the disk are characterized by a rich and diverse chemistry, including photochemistry, ion-molecule reactions, neutral-neutral reactions, gas-grain surface interactions, and grain surface reactions (Henning and Semenov, 2013). Depending on the local pressure and temperature, such reactions may occur, or not, but all of them are expected to produce complex organic molecules. Hence, according to the laboratory experimental results and to the understanding of the main chemical processes occurring in protoplanetary disks, Q-gases might have been produced in a variety of environments in the disk where both ionization and complex organic chemistry were present. This possibility is consistent with Phase-Q being ubiquitous in primitive meteorites.

The interstellar medium is also a plasma environment, and although it is diluted, low-energy ion implantation might have occurred there as well, meaning that Phase-Q may have come from the parent cloud, as some presolar dust may have been conserved during the infalling phase (Visser et al., 2011). However, noble gases are highly concentrated in Phase Q (Busemann et al., 2000), requiring a very efficient trapping process, as heavy noble gas partial pressures in the solar nebula (or in the parent cloud) are orders of magnitude lower than in all the laboratory experiments. Yet, if the trapping mechanism is ion implantation at low energy, this suggests that Q gases were trapped in a non-canonical nebular gas, which accounted much more Xe (and other noble gases) than the present-day Sun's composition, or, that the laboratory timescale is limiting the noble gas trapping yield, considering that the trapping of noble gases in a host phase in the parent cloud, the solar nebula or the protoplanetary disk might have taken several years to billions of years.

5.6.2 The host mystery is not resolved

5.6.2.1 A carbon phase?

Phase Q is probably carbonaceous, made of amorphous or porous C (Amari et al., 2013, Amari et al., 2003, Matsuda et al., 2010, Ott et al., 1981). If Q-gases are formed by ion implantation then why are they hosted by a carbon phase only? It may be due to a local process during which solid carbon compounds were dominant over silicate phases, likely in the outer regions of the disk. Nonetheless, the Nebulotron experiment demonstrates that solid carbon phases can be produced in the inner part of the disk, where H_2, CO and N_2 were the main gases and the temperatures ~ 1000 K. In such conditions, noble gases are efficiently trapped in the carbon-rich compounds, although the trapping efficiency in the solar nebula was apparently enhanced compared to the laboratory experiments. Further noble gas

trapping experiments using Si-rich surfaces might help to better understand the nature of Phase Q.

5.6.2.2 A refractory host

Phase Q is a refractory compound as inferred by the stepwise heating studies on chondrites: most noble gases are extracted at temperatures above 1000°C (Huss et al., 1996). Laboratory plasma experiments dealing with amorphous carbon, including the Nebulotron experiment, do not reproduce the high release temperature of noble gases. Hence, the vapor-growth formation of carbon compounds in laboratory plasmas cannot account for the formation of the host of Q-noble gases despite the fact that the elemental and isotopic patterns are well reproduced. Either Phase Q is not amorphous carbon and for instance, Matsuda et al., 1992 have observed that nanodiamonds retained more strongly the implanted noble gases than graphite; or a secondary process is required to make the initial carbon compound more refractory while the large noble gas concentrations and the elemental and isotopic patterns are preserved. These processes might be UV or ion irradiation, soft pyrolysis (to keep the noble gases), pressure or temperature shocks, and have to be investigated in the laboratory.

5.6.3 The solar reference: a chicken and egg question?

As pointed out by Ott, 2014, Q may represent the bulk solar composition rather than have been produced from the solar gases by a fractionation processes such as ion implantation. The solar wind, taken as a reference for all noble gas isotopic compositions, might be fractionated from the bulk solar composition by 0.5-1.1%/amu and 0.5-1.9%/amu for Kr and Xe isotopes, respectively (application of the inefficient Coulomb Drag (ICD) model, Ott, 2014, Heber et al., 2012); well within the range for fractionation between Q-gases and the solar wind. Such a hypothesis would be consistent with the ubiquity of Q-gases. However, reliable knowledge about isotopic fractionation of the solar wind is required before adopting this explaination.

5.7 Conclusions and perspectives

The objective of the work presented in this chapter was to study the trapping, and the associated elemental and isotopic fractionation, of noble gases into organic solids produced in a gaseous atmosphere representative of the solar composition under ionized conditions. The Nebulotron samples, produced from the electronic dissociation of CO ($\pm N_2$, $\pm H_2O$), efficiently trap heavy noble gases, i.e., Ar, Kr and Xe. Kr is depleted by at least one order of magnitude relative to Xe in the carbon-rich solids. The Ar depletion could not be measured accurately because of analytical limitations, but we can infer that it is at least as depleted as Kr. Both Kr and Xe display a strong isotopic fractionation relative to the flowing gas mixture, showing a mass-dependent enrichment in heavy isotopes with an averaged magnitude of 1.3%/amu and 0.9%/amu, respectively. These results are comparable with those obtained in previous noble gas trapping experiments and with the characteristics of the chondritic Q-gases. They strongly suggest the essential role of ionized noble gases to account

for the elemental and isotopic fractionations of heavy noble gases trapped in primitive meteorites, in the case of the solar wind provides an accurate estimate of the solar composition.

The elemental and isotopic fractionations are likely due to two different processes. The elemental fractionation strongly correlates with the ionization energies of the different noble gases. This suggests that the different ionization rates of the noble gases in the gas phase, due to their different ionization energies, is responsible for the depletion of light noble gases relative to Xe, as observed in both the experimental samples and in Phase Q. The present results reinforce this hypothesis that was previously suggested for Q and for trapped noble gases in ureilites (e.g. Ott, 2014, and references therein). In the Nebulotron samples, the magnitude of the isotopic fractionation correlates with the intensity of the power delivered to the discharge. This demonstrates the importance of the kinetic energies of the noble gas ions for fractionating isotopes. We infer that ambipolar diffusion is the process responsible for the mass-dependent isotopic fractionation, by enhancing the kinetic energy of heavy isotopes relative to the light ones, with a m^1 dependence. Further sputtering by light noble gas elements, and thermal diffusion due to heating of the solid in the plasma, are processes that might be responsible for the enhanced isotopic fractionation of Xe observed at high plasma powers in the Nebulotron setup.

Taken together, these results point out low-energy ion implantation as a reliable mechanism for efficient noble gas trapping in carbon-rich solid compounds. Such a physical process can account fort the elemental and isotopic fractionation patterns of the Q-gases. If this is the case, 'anomalous' adsorption, where noble gases (Xe in particular) are chemically bonded to the surface of a material (Hohenberg et al., 2002, Marrocchi et al., 2011), might not be essential for noble gas trapping into solids. In the solar nebula, there are several regions where the ionization degree is high enough to initiate low-energy ion implantation, with ionization sources being UV photons and X-rays from the young Sun or from nearby stars and/or galactic cosmic rays. In order to trap noble gases into carbon-rich solids, these ionized regions must be associated with a rich chemistry allowing the formation of carbonaceous dust. Intermediate disk layers in between the upper one and the mid-plane might offer these conditions. The estimated temperatures of the gas in the Nebulotron setup, e.g., ~ 1,000K, suggest that the initiation of organosynthesis associated with noble gas trapping could occur at low radial distances of the Sun in the accretion disk. The high noble gas trapping efficiency estimated for Phase Q (H = 3×10^7 - 3×10^{11} ccSTP/g/bar), compared to those obtained in the present experiments (H = 0.1 - 71 ccSTP/g/bar) suggest that the composition of the initial gas from which Q was formed was more volatile-rich (that is, higher noble gases/C) than the protosolar composition inferred from the solar one. The refractory character of Phase-Q, not fully reproduced in laboratory experiments, needs further investigations.

The present experimental results may have implications for the noble gas content and isotopic composition of planetary atmospheres. Terrestrial Xe presents an interesting discrepancy, known as the "xenon paradox": it is depleted by one order of magnitude relative to other noble gases and other volatile elements when normalized to the chondritic component, and it is largely enriched in its heavy isotopes by 3-4%/amu relative to chondritic or solar compositions. Furthermore, recent Xe measurements in Archean

sediments (> 3 Ga-old, Pujol et al., 2011) have shown that, at that time, the atmospheric Xe isotope composition was intermediate between those of the present-day atmosphere and of the chondrites or the protosolar nebula. Modeling of atmospheric Archean chemistry suggests efficient incorporation of Xe ionized by solar UV photons into photoproduced organic haze in the upper atmosphere (Hébrard and Marty, 2014). Processes presented in this chapter could have occurred in the early Earth's atmosphere, and efficient Xe trapping into the organic aerosols could have been a major mechanism responsible for the observed Xe depletion together with Xe isotopic fractionation of the present-day atmosphere.

Interestingly, Titan's atmosphere is also largely depleted in heavy noble gases (Niemann et al., 2010), as no Kr or Xe atoms were detected by the Cassini and Huygens instruments. As outlined in the preceding chapter, Titan's atmosphere contains large amounts of organic haze. Similarly to the early Earth's atmosphere, efficient noble gas trapping might occur in Titan's atmosphere by noble gas implantation into the atmospheric organic aerosols. Integrated over more than 4 Gyr, such a process might account for the observed present-day noble gas depletion.

Conclusions and perspectives

The objective of this thesis was to (i) investigate the incorporation of nitrogen and noble gases into growing organic material under ionizing conditions, and (ii) quantify the associated isotopic fractionation of these elements. This work was achieved by performing plasma experiments with two starting gaseous atmospheres, $CO+N_2$ and CH_4+N_2, with the addition of noble gases in order to represent the compositions of the protosolar nebula and of the atmosphere of Titan, respectively.

For that purpose, two cold plasma setups were used in order to produce solid carbon-rich materials: (i) the Nebulotron experiment, dedicated to simulate early solar nebula processes, and (ii) the PAMPRE setup, designed to investigate Titan's ionosphere processes. In a plasma discharge, the ionization energy is supplied by electrons. The electrons possess an energy distribution function that covers energies required to ionize and dissociate CO, N_2, CH_4 and noble gases This allows the initiation of chemical reactions that eventually lead to the formation and growth of organic solid particles, in which nitrogen can be incorporated as a heteroatom, and noble gases can be trapped efficiently.

The organic solids produced in the Nebulotron setup from the dissociation of CO and N_2 were characterized ex-situ by a variety of analytical techniques (Chapter 3). These solid particles display a turbostratic carbon texture, with some heterogeneities at the micron scale. The produced organic compounds are O-, N- and H-rich, pointing to some contamination from a hydrogen source in the plasma setup, likely water. The molecular structure is polyaromatic and highly functionalized, for O and N heteroatoms. Interestingly, the Nebulotron samples share common features with chondritic IOM, such as the elemental ratios H/C, O/C and N/C, the polyaromatic structure, the disorder level of the carbon structure and texture, and some of the O- and N-bearing functional groups. Most of these features have hardly been observed in previous laboratory synthetized materials used as analogues of chondritic organic compounds. These results suggest that the formation of complex organic compounds in a plasma environment might be a reliable mechanism for the formation of IOM (or IOM precursor(s)). Synthetic organic compounds that are formed in a $CO\text{-}N_2$ gas mixture efficiently incorporate nitrogen in the carbonaceous skeleton, resulting in a N/C ratio that is much higher than those observed in chondritic IOMs. Our results suggest that, if the formation of some of the IOM precursors in the solar nebula occurred in such a way, nitrogen was subsequently lost, in order to match the N/C ratio measured in IOMs.

Nitrogen isotopic fractionation during the formation of N-rich organic compounds in plasma was explored (Chapter 4). The nitrogen isotopic composition and speciation of the organic solid particles produced in the Nebulotron ($CO\text{-}N_2$) and in the PAMPRE ($CH_4\text{-}N_2$) setups were measured. Both the Nebulotron and the PAMPRE aerosols showed a comparable

^{15}N-depletion between -15‰ and -25‰ relative to the staring N_2 gas, irrespective of the different speciation of nitrogen in the molecular structure of the two types of aerosols. This ^{15}N-depletion is large compared to those measured in terrestrial natural samples. It is interpreted as resulting from mass-dependent kinetic isotopic fractionation, which could occur at any step in the synthesis of the organic solids, but most likely during polymerization. These results have several implications. First, plasma experiments do not reproduce the large ^{15}N-enrichments measured in cosmomaterials, likely because N_2 dissociation process in a plasma (electron impact and heavy molecule collisions) is not prone to self-shielding or to accidental predissociation (although the latter might occur in plasmas but not often enough to impact the final $^{15}N/^{14}N$ measured in the organic solids). Second, in Titan's atmosphere, a significant part of the aerosols produced in the upper atmosphere are initiated by the electronic dissociation of N_2 and CH_4, especially on the nightside. Therefore, we suggest that kinetic isotopic fractionation might play a non-negligible role in the nitrogen isotope balance in Titan's atmosphere. Third, the Earth's Archaean atmosphere might have contained significant amounts of organic haze, resulting from photochemical reactions between N_2, CO_2 $\pm$ CH_4 $\pm$ H_2. We therefore suggest that the ^{15}N-depletion measured in Archaean sediments might be of abiotic origin, resulting from the formation of ^{15}N-depleted N-rich aerosols in the early Earth's atmosphere.

The elemental and isotopic fractionations, together with the trapping efficiency of heavy noble gases (Ar, Kr and Xe) trapped into the synthetic materials produced in the plasma were quantified (Chapter 5). The elemental and isotopic fractionation patterns measured in the experimental organic solids are comparable to those obtained in previous noble gas trapping experiments and with those of the chondritic Q-gases. They strongly suggest the essential role of ionized noble gases to account for the elemental and isotopic fractionations of heavy noble gases trapped in primitive meteorites. The elemental and isotopic fractionations likely result from two different processes: (i) different ionization rates of the different noble gases due to contrasted ionization energies and (ii) ambipolar diffusion at the surface of solid particles, respectively. The latter process is suggested for the first time to account for the m^1 mass-dependent fractionation of Kr and Xe isotopes, observed both in plasma experiments and in Phase Q. These results point to low-energy ion implantation as a general mechanism for efficient noble gas trapping in carbon-rich solid compounds. Some features of Phase Q are however not fully reproduced in the plasma experiments: the highly refractory behavior of Phase Q and the trapping coefficients for noble gases. The latter are much higher than those obtained in the laboratory, suggesting a possible nebular gas composition richer in volatile elements compared to the present-day solar abundances. The refractory nature of Phase Q has never been reproduced in laboratory experiments and remains an open question.

Taken together, these results have several implications regarding the conditions of the formation of chondritic IOM, of its trapped noble gases and of its nitrogen isotopic composition:

(i) The present results suggest that the isotopic fractionations of nitrogen and of noble gases do not originate from the same processes. Indeed, while the main chondritic noble gas

characteristics are reproduced in plasma experiments, the large ^{15}N enrichments of IOM are not. This contrasting behavior indicates that ionization of noble gases does not depend on the nature of the energy source (electrons/UV photons) whereas N_2 dissociation can lead to large isotopic fractionation only if photons are the energy source. Other processes than electronic dissociation of N_2 are required to account for the ^{15}N-enrichments and anomalies relative to the protosolar composition observed in bulk IOMs and hotspots. Dissociation of N_2 by UV photons and/or ion-molecule reactions remain the best candidates.

(ii) The present experiments reproduce fairly well both the main noble gas characteristics of Phase Q and the molecular structure of chondritic IOM. The elemental and isotopic fractionation patterns of Q-gases can be reproduced in an ionized environment *only*. Because Phase Q and IOM are intimately related in chondrites, this suggests that IOM precursors might have formed in the same region of the solar nebula, which must be ionized, and illuminated with radiations that are energetic enough to ionize the noble gases (i.e., > 25 eV - He ionization energy). Since the ionization energies of noble gases are larger than the dissociation energies of H_2, CO and N_2, the latter were likely (photo)dissociated and/or self-shielded, depending on the density of the gas column and on the radiation field. Dissociation of CO and N_2 can account for the formation of complex organics comparable to IOM, as shown in the present experiments. The synthesis of IOM precursors in these environments is consistent with nitrogen isotopic fractionation processes, e.g., self-shielding, ion-molecule reactions and/or accidental predissociation of N_2.

These experiments, together with natural observation suggest that chondritic IOM, Phase Q and the ^{15}N-enrichments of IOM were formed in an ionized environment by energetic photons. Because Q-gases are presumably derived from the protosolar gas, the formation of these compounds and of their characteristics might have occurred in the solar nebula/protoplanetary disk rather than being inherited from the interstellar medium. Furthermore, the Nebulotron experiments show that noble gases can be trapped efficiently at high temperature (~ 1000K). Hence, the ionized region of the disk where IOM and Phase Q have formed was not necessarily cold, and might have been close to the Sun, or close to the disk surfaces illuminated by the protoSun. If this is the case, ion-molecule reactions might not have been the main mechanism responsible for the ^{15}N-enrichments and anomalies measured in IOM. Alternatively, ^{15}N-enrichments and anomalies may have been acquired later than the formation of the organic compounds, requiring transport in the disk. This possibility would be compatible with the late deuteration of IOM as suggested by the relation between the D/H ratio and the bonding energy of C-H in Orgueil IOM (Remusat et al., 2006, Robert et al., 2011).

Short-term perspectives

The Nebulotron setup made use of CO and N_2 as the two main gases. To be fully comparable to the solar nebula gas composition, further experiments should be performed with H_2, CO and N_2 in solar abundances.

Some of the Q-gases characteristics were not reproduced in the Nebulotron experiments, especially the high release temperature. This point requires further experiments. For instance, soft heating, flash heating, and pressure shocks experiments onto the organic solids produced in the Nebulotron setup could be performed to study the resulting refractory nature of the organics, the concentration and the release temperature of the trapped noble gases.

Long-term perspectives

Photons are clearly required to account for the isotopic fractionation of nitrogen, either by self-shielding or by accidental predissociation. Designing an experiment comparable to the Nebulotron one, but with UV photons as the energy source for ionization and dissociation of atoms/molecules would help to study the formation of organic compounds, and the trapping/isotopic fractionation of noble gases and of nitrogen. Such an experiment would require a window-less setup for nitrogen and noble gases to be dissociated/ionized and far UV photons, which can be delivered either by synchrotron radiation or by UV lamps (only He^+ provides radiation wavelength below 100 nm).

Finally, the relationships between organic compounds and mineral phases in chondrites at the submicron scale are not well known. *In-situ* studies of matrix from different types of chondrites, with TEM analyses on FIB sections first, then with synchrotron-based STXM and/or NanoSIMS analyses, would help to understand these relations. As organic compounds may be sensible to both aqueous alteration and thermal metamorphism, type 1 to type 4 (higher grades lack of organics and Q-gases) chondrites should be studied. This would help to give constraints on the environment of accretion of the chondrite parent bodies and on the modifications of the organic matter-minerals relation resulting from secondary processes. Complementary experiments on the thermal metamorphism and aqueous alteration effects onto minerals-organics mixtures, representative of the ones observed in chondrite matrix, would shed light on the *in-situ* observations.

References

Alcouffe G., Cavarroc M., Cernogora G., Ouni F., Joli A., Boufendi L., and C. S. (2010) Capacitively coupled plasma used to simulate Titan's atmospheric chemistry. Plasma Sources Science and Technology 19, 015008.

Aléon J. (2010) Multiple Origins of Nitrogen Isotopic Anomalies in Meteorites and Comets. The Astrophysical Journal 722, 1342.

Aléon J., Robert F., Chaussidon M., and Marty B. (2003) Nitrogen isotopic composition of macromolecular organic matter in interplanetary dust particles. Geochimica et Cosmochimica Acta 67, 3773-3783.

Alexander C. M. O. D., Bowden R., Fogel M. L., Howard K. T., Herd C. D. K., and Nittler L. R. (2012) The Provenances of Asteroids, and Their Contributions to the Volatile Inventories of the Terrestrial Planets. Science 337, 721-723.

Alexander C. M. O. D., Fogel M., Yabuta H., and Cody G. D. (2007) The origin and evolution of chondrites recorded in the elemental and isotopic compositions of their macromolecular organic matter. Geochimica et Cosmochimica Acta 71, 4380-4403.

Alexander C. M. O. D., Newsome S. D., Fogel M. L., Nittler L. R., Busemann H., and Cody G. D. (2010) Deuterium enrichments in chondritic macromolecular material--Implications for the origin and evolution of organics, water and asteroids. Geochimica et Cosmochimica Acta 74, 4417-4437.

Alexander R. (2008) From discs to planetesimals: Evolution of gas and dust discs. New Astronomy Reviews 52, 60-77.

Alves L. L., Marques L., Pintassilgo C. D., Wattieaux G., Es-sebbar E., Berndt J., Kovacevic E., Carrasco N., Boufendi L., and Cernogora G. (2012) Capacitively coupled radio-frequency discharges in nitrogen at low pressures. Plasma Sources Science and Technology 21, 045008.

Amari S., Matsuda J.-i., Stroud R. M., and Chisholm M. F. (2013) Highly Concentrated Nebular Noble Gases in Porous Nanocarbon Separates from the Saratov (L4) Meteorite. The Astrophysical Journal 778, 37.

Amari S., Zaizen S., and Matsuda J. I. (2003) An attempt to separate Q from the Allende meteorite by physical methods. Geochimica Et Cosmochimica Acta 67, 4665-4677.

Amelin Y., Krot A. N., Hutcheon I. D., and Ulyanov A. A. (2002) Lead Isotopic Ages of Chondrules and Calcium-Aluminum-Rich Inclusions. Science 297, 1678-1683.

Armitage P. J. (2011) Dynamics of Protoplanetary Disks. Annual Review of Astronomy and Astrophysics 49, 195-236.

Asplund M., Grevesse N., Sauval A. J., and Scott P. (2009) The Chemical Composition of the Sun. Annual Review of Astronomy and Astrophysics 47, 481-522.

Avice G. and Marty B. (2014) The iodine–plutonium–xenon age of the Moon–Earth system revisited. Philosophical Transactions of the Royal Society A: Mathematical, Physical and Engineering Sciences 372.

Baratta G. A., Mennella V., Brucato J. R., Colangeli L., Leto G., Palumbo M. E., and Strazzulla G. (2004) Raman spectroscopy of ion-irradiated interplanetary carbon dust analogues. Journal of Raman Spectroscopy 35, 487-496.

Beck P., Pommerol A., Thomas N., Schmitt B., Moynier F., and Barrat J. A. (2012) Photometry of meteorites. Icarus 218, 364-377.

Bernard J.-M. (2004) Simulation expérimentale de la chimie atmosphérique de Titan: Suivi des espèces produites et comparaison à un modèle cinétique. Paris 7.

Bernatowicz T. J. and Fahey A. J. (1986) Xe Isotopic Fractionation in a Cathodeless Glow-Discharge. Geochimica Et Cosmochimica Acta 50, 445-452.

Bernatowicz T. J. and Hagee B. E. (1987) Isotopic fractionation of Kr and Xe implanted in solids at very low energies. Geochimica et Cosmochimica Acta 51, 1599-1611.

Beyssac O., Goffé B., Petitet J.-P., Froigneux E., Moreau M., and Rouzaud J.-N. (2003) On the characterization of disordered and heterogeneous carbonaceous materials by Raman spectroscopy. Spectrochimica Acta Part A: Molecular and Biomolecular Spectroscopy 59, 2267-2276.

Beyssac O. and Lazzeri M. (2012) Application of Raman spectroscopy to the study of graphitic carbons in the Earth Sciences. In *Applications of Raman spectroscopy to Earth sciences and cultural heritage.* (eds. J. Dubessy, M.-C. Caumon, and F. Rull). European Mineralogical Union Notes in Mineralogy, London. pp. 413-452.

Bigeleisen J. and Mayer M. G. (1947) Calculation of Equilibrium Constants for Isotopic Exchange Reactions. The Journal of Chemical Physics 15, 261-267.

Binet L., Gourier D., Derenne S., Robert F., and Ciofini I. (2004) Occurence of abundant diradicaloid moieties in the insoluble organic matter from the Orgueil and Murchison meteorites: a fingerprint of its extraterrestrial origin? Geochimica et Cosmochimica Acta 68, 881-891.

Birnstiel T., Dullemond C. P., and Brauer F. (2010) Gas- and dust evolution in protoplanetary disks. A&A 513, A79.

Black D. C. (1972) On the origins of trapped helium, neon and argon isotopic variations in meteorites—I. Gas-rich meteorites, lunar soil and breccia. Geochimica et Cosmochimica Acta 36, 347-375.

Bockelée-Morvan D., Biver N., Jehin E., Cochran A. L., Wiesemeyer H., Manfroid J., Hutsemékers D., Arpigny C., Boissier J., Cochran W., Colom P., Crovisier J., Milutinovic N., Moreno R., Prochaska J. X., Ramirez I., Schulz R., and Zucconi J.-M. (2008) Large Excess of Heavy Nitrogen in Both Hydrogen Cyanide and Cyanogen from Comet 17P/Holmes. The Astrophysical Journal Letters 679, L49.

Bockelée-Morvan D., Gautier D., Lis D. C., Young K., Keene J., Phillips T., Owen T., Crovisier J., Goldsmith P. F., Bergin E. A., Despois D., and Wootten A. (1998) Deuterated Water in Comet C/1996 B2 (Hyakutake) and Its Implications for the Origin of Comets. Icarus 133, 147-162.

Bonal L. (2006) Matière organique et métamorphisme thermique dans les chondrites primitives. Grenoble 1.

Bonal L., Alexander C. M. O. D., Huss G. R., Nagashima K., Quirico E., and Beck P. (2013) Hydrogen isotopic composition of the water in CR chondrites. Geochimica et Cosmochimica Acta 106, 111-133.

Bonal L., Bourot-Denise M., Quirico E., Montagnac G., and Lewin E. (2007) Organic matter and metamorphic history of CO chondrites. Geochimica et Cosmochimica Acta 71, 1605-1623.

Bonal L., Huss G. R., Krot A. N., Nagashima K., Ishii H. A., and Bradley J. P. (2010) Highly 15N-enriched chondritic clasts in the CB/CH-like meteorite Isheyevo. Geochimica et Cosmochimica Acta 74, 6590-6609.

Bonal L., Quirico E., Bourot-Denise M., and Montagnac G. (2006) Determination of the petrologic type of CV3 chondrites by Raman spectroscopy of included organic matter. Geochimica et Cosmochimica Acta 70, 1849-1863.

Bonnet J.-Y. (2012) L'azote comme élément mineur dans les macromolécules organiques chondritiques et cométaires: simulations expérimentales contraintes par les cosmomatériaux. Université de Grenoble.

Bordage M. C., Biagi S. F., Alves L. L., Bartschat K., Chowdhury S., Pitchford L. C., Hagelaar G. J. M., Morgan W. L., Puech V., and Zatsarinny O. (2013) Comparisons of sets of electron–neutral scattering cross sections and swarm parameters in noble gases: III. Krypton and xenon. Journal of Physics D: Applied Physics 46, 334003.

Boss A. P. and Ciesla F. J. (2014) The Solar Nebula. In *Treatise on Geochemistry (Second Edition)* (eds. H. D. Holland and K. K. Turekian). Elsevier, Oxford. pp. 37-53.

Botta O. and Bada J. (2002) Extraterrestrial Organic Compounds in Meteorites. Surveys in Geophysics 23, 411-467.

Bouvier A. and Wadhwa M. (2010) The age of the Solar System redefined by the oldest Pb-Pb age of a meteoritic inclusion. Nature Geosci 3, 637-641.

Brandi F., Velchev I., Hogervorst W., and Ubachs W. (2001) Vacuum-ultraviolet spectroscopy of Xe: Hyperfine splittings, isotope shifts, and isotope-dependent ionization energies. Physical Review A 64, 032505.

Briani G., Gounelle M., Marrocchi Y., Mostefaoui S., Leroux H., Quirico E., and Meibom A. (2009) Pristine extraterrestrial material with unprecedented nitrogen isotopic variation. Proceedings of the National Academy of Sciences 106, 10522-10527.

Briani G., Morbidelli A., Gounelle M., and Nesvorny D. (2011) Evidence for an asteroid–comet continuum from simulations of carbonaceous microxenolith dynamical evolution. Meteoritics & Planetary Science 46, 1863-1877.

Brownlee D.Tsou P.Aléon J.Alexander C. M. O. D.Araki T.Bajt S.Baratta G. A.Bastien R.Bland P.Bleuet P.Borg J.Bradley J. P.Brearley A.Brenker F.Brennan S.Bridges J. C.Browning N. D.Brucato J. R.Bullock E.Burchell M. J.Busemann H.Butterworth A.Chaussidon M.Cheuvront A.Chi M.Cintala M. J.Clark B. C.Clemett S. J.Cody G.Colangeli L.Cooper G.Cordier P.Daghlian C.Dai Z.D'Hendecourt L.Djouadi Z.Dominguez G.Duxbury T.Dworkin J. P.Ebel D. S.Economou T. E.Fakra S.Fairey S. A. J.Fallon S.Ferrini G.Ferroir T.Fleckenstein H.Floss C.Flynn G.Franchi I. A.Fries M.Gainsforth Z.Gallien J.-P.Genge M.Gilles M. K.Gillet P.Gilmour J.Glavin D. P.Gounelle M.Grady M. M.Graham G. A.Grant P. G.Green S. F.Grossemy F.Grossman L.Grossman J. N.Guan Y.Hagiya K.Harvey R.Heck P.Herzog G. F.Hoppe P.Hörz F.Huth J.Hutcheon I. D.Ignatyev K.Ishii H.Ito M.Jacob D.Jacobsen C.Jacobsen S.Jones S.Joswiak D.Jurewicz A.Kearsley A. T.Keller L. P.Khodja H.Kilcoyne A. L. D.Kissel J.Krot A.Langenhorst F.Lanzirotti A.Le L.Leshin L. A.Leitner J.Lemelle L.Leroux H.Liu M.-C.Luening K.Lyon I., et al. (2006) Comet 81P/Wild 2 Under a Microscope. Science 314, 1711-1716.

Brunetto R., Borg J., Dartois E., Rietmeijer F. J. M., Grossemy F., Sandt C., Le Sergeant d'Hendecourt L., Rotundi A., Dumas P., Djouadi Z., and Jamme F. (2011) Mid-IR, Far-IR, Raman micro-spectroscopy, and FESEM–EDX study of IDP L2021C5: Clues to its origin. Icarus 212, 896-910.

Brunetto R., Pino T., Dartois E., Cao A. T., d'Hendecourt L., Strazzulla G., and Brèchignac P. (2009) Comparison of the Raman spectra of ion irradiated soot and collected extraterrestrial carbon. Icarus 200, 323-337.

Burkhardt C., Kleine T., Bourdon B., Palme H., Zipfel J., Friedrich J. M., and Ebel D. S. (2008) Hf–W mineral isochron for Ca,Al-rich inclusions: Age of the solar system and the timing of core formation in planetesimals. Geochimica et Cosmochimica Acta 72, 6177-6197.

Busemann H., Alexander M. O. D., and Nittler L. R. (2007) Characterization of insoluble organic matter in primitive meteorites by microRaman spectroscopy. Meteoritics & Planetary Science 42, 1387-1416.

Busemann H., Baur H., and Wieler R. (2000) Primordial noble gases in "phase Q" in carbonaceous and ordinary chondrites studied by closed-system stepped etching. Meteoritics & Planetary Science 35, 949-973.

Busemann H., Nguyen A. N., Cody G. D., Hoppe P., Kilcoyne A. L. D., Stroud R. M., Zega T. J., and Nittler L. R. (2009) Ultra-primitive interplanetary dust particles from the comet 26P/Grigg–Skjellerup dust stream collection. Earth and Planetary Science Letters 288, 44-57.

Busemann H., Young A. F., Alexander C. M. O. D., Hoppe P., Mukhopadhyay S., and Nittler L. R. (2006) Interstellar Chemistry Recorded in Organic Matter from Primitive Meteorites. Science 312, 727-730.

Canup R. M. (2012) Forming a Moon with an Earth-like Composition via a Giant Impact. Science 338, 1052-1055.

Carpentier Y., Féraud G., Dartois E., Brunetto R., Charon E., Cao A.-T., d'Hendecourt L., Bréchignac P., Rouzaud J.-N., and Pino T. (2012) Nanostructuration of carbonaceous dust as seen through the positions of the 6.2 and 7.7 μm AIBs. Astronomy & Astrophysics 548, A40.

Carrasco N., Gautier T., Es-sebbar E.-t., Pernot P., and Cernogora G. (2012) Volatile products controlling Titan's tholins production. Icarus 219, 230-240.

Caselli P. and Ceccarelli C. (2012) Our astrochemical heritage. The Astronomy and Astrophysics Review 20, 1-68.

Cavarroc M. (2007) Nucléation, croissance et comportement de poussières dans les plasmas réactifs radiofréquence basse pression: Des nanocristaux aux grains submicroniques polycristallins. Université d'Orléans.

Chakraborty S., Jackson T. L., Muskatel B. H., Ahmed M., Levine R. D., and Thiemens M. H. (2012) Nitrogen Isotopic Fractionation in VUV Photodissociation of N2: Implications for the Early Solar System. 43rd Lunar and Planetary Science Conference.

Chakraborty S., Jackson T. L., Muskatel B. H., Ahmed M., Thiemens M. H., and Levine R. D. (2013) Huge Isotope Effect in VUV Photodissociation of N2: Implications for Meteorite Data. 44th Lunar and Planetary Science Conference.

Chambers J. E. and Wetherill G. W. (1998) Making the Terrestrial Planets: N-Body Integrations of Planetary Embryos in Three Dimensions. Icarus 136, 304-327.

Chapman C. R. and Salisbury J. W. (1973) Comparisons of meteorite and asteroid spectral reflectivities. Icarus 19, 507-522.

Chiar J. E., Tielens A. G. G. M., Adamson A. J., and Ricca A. (2013) The Structure, Origin, and Evolution of Interstellar Hydrocarbon Grains. The Astrophysical Journal 770, 78.

Choi W., Kim C., and Kang H. (1993) Interactions of low energy (10–600 eV) noble gas ions with a graphite surface: surface penetration, trapping and self-sputtering behaviors. Surface Science 281, 323-335.

Ciesla F. J. (2006) Chondrule collisions in shock waves. Meteoritics & Planetary Science 41, 1347-1359.

Ciesla F. J. (2007) Outward Transport of High-Temperature Materials Around the Midplane of the Solar Nebula. Science 318, 613-615.

Clayton R. N. (2002) Solar System: Self-shielding in the solar nebula. Nature 415, 860-861.

Cloutis E. A., Gaffey M. J., and Moslow T. F. (1994) Spectral Reflectance Properties of Carbon-Bearing Materials. Icarus 107, 276-287.

Cody G. D. and Alexander C. M. O. D. (2005) NMR studies of chemical structural variation of insoluble organic matter from different carbonaceous chondrite groups. Geochimica et Cosmochimica Acta 69, 1085-1097.

Connelly J. N., Bizzarro M., Krot A. N., Nordlund Å., Wielandt D., and Ivanova M. A. (2012) The Absolute Chronology and Thermal Processing of Solids in the Solar Protoplanetary Disk. Science 338, 651-655.

Coufal H., Winters H. F., Bay H. L., and Eckstein W. (1991) Energy transfer from noble-gas ions to surfaces: Collisions with carbon, silicon, copper, silver, and gold in the range 100–4000 eV. Physical Review B 44, 4747-4758.

Croteau P., Randazzo J. B., Kostko O., Ahmed M., Liang M.-C., Yung Y. L., and Boering K. A. (2011) Measurements of Isotope Effects in the Photoionization of N2 and Implications for Titan's Atmosphere. Astrophysical Journal Letters 728.

Crowther S. A. and Gilmour J. D. (2013) Solar System Xenon Signatures: Solar, Fractionated Solar and an S-Process Deficit. 44th Lunar and Planetary Science Conference.

Cuzzi J. N., Hogan R. C., and Shariff K. (2008) Toward Planetesimals: Dense Chondrule Clumps in the Protoplanetary Nebula. The Astrophysical Journal 687, 1432.

D'Alessio P., Cantö J., Calvet N., and Lizano S. (1998) Accretion Disks around Young Objects. I. The Detailed Vertical Structure. The Astrophysical Journal 500, 411.

Dartois E., Caro G. M. M., Deboffle D., and d'Hendecourt L. (2004) Diffuse interstellar medium organic polymers. Astronomy & Astrophysics 423, L33-L36.

Dartois E., Caro G. M. M., Deboffle D., Montagnac G., and d'Hendecourt L. (2005) Ultraviolet photoproduction of ISM dust. Astronomy & Astrophysics 432, 895-908.

Dartois E., Engrand C., Brunetto R., Duprat J., Pino T., Quirico E., Remusat L., Bardin N., Briani G., Mostefaoui S., Morinaud G., Crane B., Szwec N., Delauche L., Jamme F., Sandt C., and Dumas P. (2013) UltraCarbonaceous Antarctic micrometeorites, probing the Solar System beyond the nitrogen snow-line. Icarus 224, 243-252.

Dauphas N. (2003) The dual origin of the terrestrial atmosphere. Icarus 165, 326-339.

Dauphas N. and Chaussidon M. (2011) A Perspective from Extinct Radionuclides on a Young Stellar Object: The Sun and Its Accretion Disk. Annual Review of Earth and Planetary Sciences 39, 351-386.

Dauphas N. and Pourmand A. (2011) Hf-W-Th evidence for rapid growth of Mars and its status as a planetary embryo. Nature 473, 489-492.

De Gregorio B. T., Stroud R. M., Nittler L. R., Alexander C. M. O. D., Bassim N. D., Cody G. D., Kilcoyne A. L. D., Sandford S. A., Milam S. N., Nuevo M., and Zega T. J. (2013) Isotopic and chemical variation of organic nanoglobules in primitive meteorites. Meteoritics & Planetary Science 48, 904-928.

Delcroix J.-L. (1966) *Physique des plasmas-Tome 2*. Dunod.

Demarais N. J., Yang Z., Snow T. P., and Bierbaum V. M. (2014) Gas-phase Reactions of Polycyclic Aromatic Hydrocarbon Cations and their Nitrogen-containing Analogs with H Atoms. The Astrophysical Journal 784, 25.

Derenne S., Coelho C., Anquetil C., Szopa C., Rahman A. S., McMillan P. F., Corà F., Pickard C. J., Quirico E., and Bonhomme C. (2012) New insights into the structure and chemistry of Titan's tholins via 13C and 15N solid state nuclear magnetic resonance spectroscopy. Icarus 221, 844-853.

Derenne S. and Robert F. (2010) Model of molecular structure of the insoluble organic matter isolated from Murchison meteorite. Meteoritics & Planetary Science 45, 1461-1475.

Derenne S., Rouzaud J.-N., Clinard C., and Robert F. (2005) Size discontinuity between interstellar and chondritic aromatic structures: A high-resolution transmission electron microscopy study. Geochimica et Cosmochimica Acta 69, 3911-3917.

Desch S. J., Morris M. A., Connolly H. C., and Boss A. P. (2012) The importance of experiments: Constraints on chondrule formation models. Meteoritics & Planetary Science 47, 1139-1156.

Dobrică E., Engrand C., Quirico E., Montagnac G., and Duprat J. (2011) Raman characterization of carbonaceous matter in CONCORDIA Antarctic micrometeorites. Meteoritics & Planetary Science 46, 1363-1375.

Dullemond C. P., Zadelhoff G. J. v., and Natta A. (2002) Vertical structure models of T Tauri and Herbig Ae/Be disks. A&A 389, 464-474.

Dutrey A., Semenov D., Chapillon E., Gorti U., Guilloteau S., Hersant F., Hogerheijde M., Hughes M., Meeus G., and Nomura H. (2014) Physical and chemical structure of planet-forming disks probed by millimeter observations and modeling. arXiv preprint arXiv:1402.3503.

Dzizckniec M., Lumkin G. R., Donohoe K., and Chang S. (1981) Plasma synthesis of carbonaceous material with noble gas tracers. 12th Lunar and Planetary Science Conference.

Ebel D. S. (2006) Condensation of rocky material in astrophysical environments. In *Meteorites and the early solar system II* (eds. D. Lauretta and H. J. McSween). University of Arizona Press. pp. 253-277.

Ehrenfreund P. and Charnley S. B. (2000) Organic Molecules In The Interstellar Medium, Comets, And Meteorites: A Voyage from Dark Clouds to the Early Earth. Annual Review of Astronomy and Astrophysics 38, 427-483.

Elwert G. (1952) Über die Ionisations und Rekombinationsprozesse in einem plasma und die Ionisationsformel der Sonnenkorona. Z Naturforsch. 7a 432.

Feigelson E. D. and Montmerle T. (1999) High-Energy Processes In Young Stellar Objects. Annual Review of Astronomy and Astrophysics 37, 363-408.

Ferrari A. C. and Robertson J. (2000) Interpretation of Raman spectra of disordered and amorphous carbon. Physical Review B 61, 14095-14107.

Ferrari A. C. and Robertson J. (2001) Resonant Raman spectroscopy of disordered, amorphous, and diamondlike carbon. Physical Review B 64, 075414.

Ferrari A. C., Rodil S. E., and Robertson J. (2003) Interpretation of infrared and Raman spectra of amorphous carbon nitrides. Physical Review B 67, 155306.

Fierro A., Laity G., and Neuber A. (2012) Optical emission spectroscopy study in the VUV–VIS regimes of a developing low-temperature plasma in nitrogen gas. Journal of Physics D: Applied Physics 45, 495202.

Floss C., Stadermann F. J., Mertz A. F., and Bernatowicz T. J. (2010) A NanoSIMS and Auger Nanoprobe investigation of an isotopically primitive interplanetary dust particle from the 55P/Tempel-Tuttle targeted stratospheric dust collector. Meteoritics & Planetary Science 45, 1889-1905.

Fogel J. K. J., Bethell T. J., Bergin E. A., Calvet N., and Semenov D. (2011) Chemistry of a Protoplanetary Disk with Grain Settling and Lyα Radiation. The Astrophysical Journal 726, 29.

Frick U., Mack R., and Chang S. (1979) Noble Gas Fractionation during Synthesis of Carbonaceous Matter. 10th LPSC, Abstract #1146.

Fridman A. (2008) *Plasma chemistry*. Cambridge University Press.

Fukunaga K. and Matsuda J.-i. (1997) Vapor-growth carbon and the origin of carbonaceous material in ureilites. Geochemical Journal-Japan 31, 263-274.

Gaffey M. J., Burbine T. H., and Binzel R. P. (1993) Asteroid spectroscopy: Progress and perspectives. Meteoritics 28, 161-187.

Gardinier A., Derenne S., Robert F., Behar F., Largeau C., and Maquet J. (2000) Solid state CP/MAS 13C NMR of the insoluble organic matter of the Orgueil and Murchison meteorites: quantitative study. Earth and Planetary Science Letters 184, 9-21.

Gautier T. (2013) Experimental simulation of Titan's aerosols formation. Université de Versailles-Saint Quentin en Yvelines.

Gautier T., Carrasco N., Buch A., Szopa C., Sciamma-O'Brien E., and Cernogora G. (2011) Nitrile gas chemistry in Titan's atmosphere. Icarus 213, 625-635.

Gautier T., Carrasco N., Mahjoub A., Vinatier S., Giuliani A., Szopa C., Anderson C. M., Correia J.-J., Dumas P., and Cernogora G. (2012) Mid- and far-infrared absorption spectroscopy of Titan's aerosols analogues. Icarus 221, 320-327.

Geiss J. and Bochsler P. (1982) Nitrogen isotopes in the solar system. Geochimica et Cosmochimica Acta 46, 529-548.

Göbel R., Ott U., and Begemann F. (1978) On trapped noble gases in ureilites. Journal of Geophysical Research: Solid Earth 83, 855-867.

Gomes R., Levison H. F., Tsiganis K., and Morbidelli A. (2005) Origin of the cataclysmic Late Heavy Bombardment period of the terrestrial planets. Nature 435, 466-469.

Gounelle M. (2011) The Asteroid–Comet Continuum: In Search of Lost Primitivity. Elements 7, 29-34.

Gourier D., Robert F., Delpoux O., Binet L., Vezin H., Moissette A., and Derenne S. (2008) Extreme deuterium enrichment of organic radicals in the Orgueil meteorite: Revisiting the interstellar interpretation? Geochimica et Cosmochimica Acta 72, 1914-1923.

Greenberg J. M. (1998) Making a comet nucleus. Astronomy and Astrophysics 330, 375-380.

Greenberg R., Wacker J. F., Hartmann W. K., and Chapman C. R. (1978) Planetesimals to planets: Numerical simulation of collisional evolution. Icarus 35, 1-26.

Grossman L. (1972) Condensation in the primitive solar nebula. Geochimica et Cosmochimica Acta 36, 597-619.

Guo X. J., Sung S. L., Lin J. C., Chen F. R., and Shih H. C. (2000) Heteroepitaxial diamond nucleation and growth on silicon by microwave plasma-enhanced chemical vapor deposition synthesis. Diamond and Related Materials 9, 1840-1849.

Hadamcik E. and Levasseur-Regourd A. C. (2003) Imaging polarimetry of cometary dust: different comets and phase angles. Journal of Quantitative Spectroscopy and Radiative Transfer 79–80, 661-678.

Hadamcik E., Renard J. B., Alcouffe G., Cernogora G., Levasseur-Regourd A. C., and Szopa C. (2009) Laboratory light-scattering measurements with Titan's aerosols analogues produced by a dusty plasma. Planetary and Space Science 57, 1631-1641.

Hadamcik E., Renard J. B., Rietmeijer F. J. M., Levasseur-Regourd A. C., Hill H. G. M., Karner J. M., and Nuth J. A. (2007) Light scattering by fluffy Mg–Fe–SiO and C mixtures as cometary analogs (PROGRA2 experiment). Icarus 190, 660-671.

Hadamcik E., Sen A. K., Levasseur-Regourd A. C., Gupta R., Lasue J., and Botet R. (2013) Dust in Comet 103P/Hartley 2 coma during EPOXI mission. Icarus 222, 774-785.

Haisch K. J., Lada E. A., and J L. C. (2001) Disk Frequencies and Lifetimes in Young Clusters. The Astrophysical Journal Letters 553, L153.

Hartmann L., Kenyon S., and Hartigan P. (1993) Young stars-Episodic phenomena, activity and variability. In *Protostars and Planets III* (eds. E. Levy and J. Lunine). University of Arizona Press. pp. 497-518.

Hayashi C., Nakazawa K., and Nakagawa Y. (1985) Formation of the solar system. In *Protostars and planets II*. pp. 1100-1153.

Hayatsu R., Matsuoka S., Scott R. G., Studier M. H., and Anders E. (1977) Origin of organic matter in the early solar system—VII. The organic polymer in carbonaceous chondrites. Geochimica et Cosmochimica Acta 41, 1325-1339.

Heber V. S., Baur H., Bochsler P., McKeegan K. D., Neugebauer M., Reisenfeld D. B., Wieler R., and Wiens R. C. (2012) Isotopic Mass Fractionation of Solar Wind: Evidence from Fast and Slow Solar Wind Collected by the Genesis mission. The Astrophysical Journal 759, 121.

Heber V. S., Wieler R., Baur H., Olinger C., Friedmann T. A., and Burnett D. S. (2009) Noble gas composition of the solar wind as collected by the Genesis mission. Geochimica et Cosmochimica Acta 73, 7414-7432.

Hébrard E. and Marty B. (2014) Coupled noble gas–hydrocarbon evolution of the early Earth atmosphere upon solar UV irradiation. Earth and Planetary Science Letters 385, 40-48.

Henning T. (2010) Cosmic Silicates. Annual Review of Astronomy and Astrophysics 48, 21-46.

Henning T. and Semenov D. (2013) Chemistry in Protoplanetary Disks. Chemical Reviews 113, 9016-9042.

Herbst E. (2014) Three milieux for interstellar chemistry: gas, dust, and ice. Physical Chemistry Chemical Physics 16, 3344-3359.

Hewins R. H. (1997) Chondrules. Annual Review of Earth and Planetary Sciences 25, 61-83.

Hily-Blant P., Bonal L., Faure A., and Quirico E. (2013) The 15N-enrichment in dark clouds and Solar System objects. Icarus 223, 582-590.

Hohenberg C. M., Thonnard N., and Meshik A. (2002) Active capture and anomalous adsorption: New mechanisms for the incorporation of heavy noble gases. Meteoritics & Planetary Science 37, 257-267.

Huang Y., Alexandre M. R., and Wang Y. (2007) Structure and isotopic ratios of aliphatic side chains in the insoluble organic matter of the Murchison carbonaceous chondrite. Earth and Planetary Science Letters 259, 517-525.

Huss G. R. and Lewis R. S. (1995) Presolar diamond, SiC, and graphite in primitive chondrites: Abundances as a function of meteorite class and petrologic type. Geochimica et Cosmochimica Acta 59, 115-160.

Huss G. R., Lewis R. S., and Hemkin S. (1996) The "normal planetary" noble gas component in primitive chondrites: Compositions, carrier, and metamorphic history. Geochimica et Cosmochimica Acta 60, 3311-3340.

Huss G. R., Meshik A. P., Smith J. B., and Hohenberg C. M. (2003) Presolar diamond, silicon carbide, and graphite in carbonaceous chondrites: implications for thermal processing in the solar nebula. Geochimica et Cosmochimica Acta 67, 4823-4848.

Huss G. R., Ott U., and Koscheev A. P. (2008) Noble gases in presolar diamonds III: Implications of ion implantation experiments with synthetic nanodiamonds. Meteoritics & Planetary Science 43, 1811-1826.

Ida S. and Makino J. (1993) Scattering of Planetesimals by a Protoplanet: Slowing Down of Runaway Growth. Icarus 106, 210-227.

Irvine W. M., Schloerb F. P., Crovisier J., Fegley Jr B., and Mumma M. J. (2000) Comets: A link between interstellar and nebular chemistry. In *Protostars and planets IV* (eds. V. Mannings, A. P. Boss, and S. Russell). University of Arizona Press.

Israël G., Szopa C., Raulin F., Cabane M., Niemann H., Atreya S., Bauer S., Brun J.-F., Chassefière E., and Coll P. (2005) Complex organic matter in Titan's atmospheric aerosols from in situ pyrolysis and analysis. Nature 438, 796-799.

Jehin E., Manfroid J., Hutsemékers D., Arpigny C., and Zucconi J. M. (2009) Isotopic Ratios in Comets: Status and Perspectives. Earth, Moon, and Planets 105, 167-180.

Johansen A., Oishi J. S., Low M.-M. M., Klahr H., Henning T., and Youdin A. (2007) Rapid planetesimal formation in turbulent circumstellar disks. Nature 448, 1022-1025.

Johansen A. and Youdin A. (2007) Protoplanetary Disk Turbulence Driven by the Streaming Instability: Nonlinear Saturation and Particle Concentration. The Astrophysical Journal 662, 627.

Kamo M., Sato Y., Matsumoto S., and Setaka N. (1983) Diamond synthesis from gas phase in microwave plasma. Journal of Crystal Growth 62, 642-644.

Kamp I. and Kamp I. (2011) Evolution of PAHs in Protoplanetary Disks. European Astronomical Society Publications Series 46, 271-283.

Kebukawa Y., Kilcoyne A. L. D., and Cody G. D. (2013) Exploring the Potential Formation of Organic Solids in Chondrites and Comets through Polymerization of Interstellar Formaldehyde. The Astrophysical Journal 771, 19.

Kissel J. and Krueger F. R. (1987) The organic component in dust from comet Halley as measured by the PUMA mass spectrometer on board Vega 1. Nature 326, 755-760.

Kleine T., Touboul M., Bourdon B., Nimmo F., Mezger K., Palme H., Jacobsen S. B., Yin Q.-Z., and Halliday A. N. (2009) Hf–W chronology of the accretion and early evolution of asteroids and terrestrial planets. Geochimica et Cosmochimica Acta 73, 5150-5188.

Kokubo E. and Ida S. (1998) Oligarchic Growth of Protoplanets. Icarus 131, 171-178.

Kokubo E. and Ida S. (2000) Formation of Protoplanets from Planetesimals in the Solar Nebula. Icarus 143, 15-27.

Koscheev A. P., Gromov M. D., Mohapatra R. K., and Ott U. (2001) History of trace gases in presolar diamonds inferred from ion-implantation experiments. Nature 412, 615-617.

Krot A. N., Hutcheon I. D., Brearley A. J., Pravdivtseva O. V., Petaev M. I., and Hohenberg C. M. (2006) Timescales and settings for alteration of chondritic meteorites. In *Meteorites and the early solar system II* (eds. S. L. Dante and Y. M. Harry). The University of Arizona Press. pp. 525-553.

Kuga M., Carrasco N., Marty B., Marrocchi Y., Bernard S., Rigaudier T., Fleury B., and Tissandier L. (2014) Nitrogen isotopic fractionation during abiotic synthesis of organic solid particles. Earth and Planetary Science Letters 393, 2-13.

Lahfid A., Beyssac O., Deville E., Negro F., Chopin C., and Goffé B. (2010) Evolution of the Raman spectrum of carbonaceous material in low-grade metasediments of the Glarus Alps (Switzerland). Terra Nova 22, 354-360.

Lauretta D. S. (2011) A Cosmochemical View of the Solar System. Elements 7, 11-16.

Lavvas P., Galand M., Yelle R., Heays A., Lewis B., Lewis G., and Coates A. (2011) Energy deposition and primary chemical products in Titan's upper atmosphere. Icarus 213, 233-251.

Le Guillou C., Bernard S., Brearley A. J., and Remusat L. (2014) Evolution of organic matter in Orgueil, Murchison and Renazzo during parent body aqueous alteration: In situ investigations. Geochimica et Cosmochimica Acta 131, 368-392.

Le Guillou C., Rouzaud J.-N., Bonal L., Quirico E., Derenne S., and Remusat L. (2012) High resolution TEM of chondritic carbonaceous matter: Metamorphic evolution and heterogeneity. Meteoritics & Planetary Science 47, 345-362.

Lefebvre-Brion H. and Field R. W. (2004) Chapter 7 - Photodissociation Dynamics. In *The Spectra and Dynamics of Diatomic Molecules*. Academic Press, San Diego. pp. 469-549.

Levine J. (1985) *The photochemistry of atmospheres*. Elsevier.

Lewis R. S., Srinivasan B., and Anders E. (1975) Host phase of a strange xenon component in Allende. Science 190, 1251-1262.

Liang M.-C., Heays A. N., Lewis B. R., Gibson S. T., and Yung Y. L. (2007) Source of Nitrogen Isotope Anomaly in HCN in the Atmosphere of Titan. The Astrophysical Journal Letters 664, L115.

Lodders K. (2003) Solar System Abundances and Condensation Temperatures of the Elements. The Astrophysical Journal 591, 1220.

Lorquet A. J. and Lorquet J. C. (1974) Isotopic effects in accidental predissociation. The case of the C2Σ+u state of N+2. Chemical Physics Letters 26, 138-143.

Lyons J. R., Bergin E. A., Ciesla F. J., Davis A. M., Desch S. J., Hashizume K., and Lee J. E. (2009) Timescales for the evolution of oxygen isotope compositions in the solar nebula. Geochimica et Cosmochimica Acta 73, 4998-5017.

Marrocchi Y. (2005) Incorporation des gaz rares dans la matière organique primitive du système solaire. Institut National Polytechnique de Lorraine.

Marrocchi Y., Derenne S., Marty B., and Robert F. (2005a) Interlayer trapping of noble gases in insoluble organic matter of primitive meteorites. Earth and Planetary Science Letters 236, 569-578.

Marrocchi Y. and Marty B. (2013) Experimental determination of the xenon isotopic fractionation during adsorption. Geophysical Research Letters 40, 4165-4170.

Marrocchi Y., Marty B., Reinhardt P., and Robert F. (2011) Adsorption of xenon ions onto defects in organic surfaces: Implications for the origin and the nature of organics in primitive meteorites. Geochimica Et Cosmochimica Acta 75, 6255-6266.

Marrocchi Y., Razafitianamaharavo A., Michot L. J., and Marty B. (2005b) Low-pressure adsorption of Ar, Kr, and Xe on carbonaceous materials (kerogen and carbon blacks), ferrihydrite, and montmorillonite: Implications for the trapping of noble gases onto meteoritic matter. Geochimica et Cosmochimica Acta 69, 2419-2430.

Marty B. (2012) The origins and concentrations of water, carbon, nitrogen and noble gases on Earth. Earth and Planetary Science Letters 313–314, 56-66.

Marty B., Chaussidon M., Wiens R., Jurewicz A., and Burnett D. (2011) A 15N-poor isotopic composition for the solar system as shown by Genesis solar wind samples. Science 332, 1533-1536.

Marty B., Zimmermann L., Burnard P. G., Wieler R., Heber V. S., Burnett D. L., Wiens R. C., and Bochsler P. (2010) Nitrogen isotopes in the recent solar wind from the analysis of Genesis targets: Evidence for large scale isotope heterogeneity in the early solar system. Geochimica et Cosmochimica Acta 74, 340-355.

Matsuda J.-i., Fukunaga K., and Ito K. (1991) Noble gas studies in vapor-growth diamonds: Comparison with shock-produced diamonds and the origin of diamonds in ureilites. Geochimica et Cosmochimica Acta 55, 2011-2023.

Matsuda J.-i., Maekawa T., Togashi S., Tanaka T., Yoshida T., Ishikawa K., Fujinawa A., Kurasawa H., Sekine T., and Aramaki S. (1992) Noble gas implantation in glow discharge: Comparison between diamond and graphite. Geochem. J 26, 251-260.

Matsuda J.-i., Morishita K., Tsukamoto H., Miyakawa C., Nara M., Amari S., Uchiyama T., and Takeda S. (2010) An attempt to characterize phase Q: Noble gas, Raman spectroscopy and transmission electron microscopy in residues prepared from the Allende meteorite. Geochimica et Cosmochimica Acta 74, 5398-5409.

Mazor E., Heymann D., and Anders E. (1970) Noble gases in carbonaceous chondrites. Geochimica et Cosmochimica Acta 34, 781-824.

McCarroll B. (1970) An Improved Microwave Discharge Cavity for 2450 MHz. Review of Scientific Instruments 41, 279-280.

McKeegan K. D., Aléon J., Bradley J., Brownlee D., Busemann H., Butterworth A., Chaussidon M., Fallon S., Floss C., Gilmour J., Gounelle M., Graham G., Guan Y., Heck P. R., Hoppe P., Hutcheon I. D., Huth J., Ishii H., Ito M., Jacobsen S. B., Kearsley A., Leshin L. A., Liu M.-C., Lyon I., Marhas K., Marty B., Matrajt G., Meibom A., Messenger S., Mostefaoui S., Mukhopadhyay S., Nakamura-Messenger K., Nittler L., Palma R., Pepin R. O., Papanastassiou D. A., Robert F., Schlutter D., Snead C. J., Stadermann F. J., Stroud R., Tsou P., Westphal A., Young E. D., Ziegler K., Zimmermann L., and Zinner E. (2006) Isotopic Compositions of Cometary Matter Returned by Stardust. Science 314, 1724-1728.

Meibom A., Krot A. N., Robert F., Mostefaoui S., Russell S. S., Petaev M. I., and Gounelle M. (2007) Nitrogen and Carbon Isotopic Composition of the Sun Inferred from a High-Temperature Solar Nebular Condensate. The Astrophysical Journal Letters 656, L33.

Meshik A., Hohenberg C., Pravdivtseva O., and Burnett D. (2014) Heavy noble gases in solar wind delivered by Genesis mission. Geochimica et Cosmochimica Acta 127, 326-347.

Millar T., Bennett A., and Herbst E. (1989) Deuterium fractionation in dense interstellar clouds. The Astrophysical Journal 340, 906-920.

Miller S. L. (1953) A Production of Amino Acids Under Possible Primitive Earth Conditions. Science 117, 528-529.

Mishra R. K. and Chaussidon M. (2014) Timing and extent of Mg and Al isotopic homogenization in the early inner Solar System. Earth and Planetary Science Letters 390, 318-326.

Mishra R. K., Goswami J. N., Tachibana S., Huss G. R., and Rudraswami N. G. (2010) 60Fe and 26Al in Chondrules from Unequilibrated Chondrites: Implications for Early Solar System Processes. The Astrophysical Journal Letters 714, L217.

Montmerle T., Augereau J.-C., Chaussidon M., Gounelle M., Marty B., and Morbidelli A. (2006) Solar System Formation and Early Evolution: the First 100 Million Years. In *From Suns to Life: A Chronological Approach to the History of Life on Earth* (eds. M. Gargaud, P. Claeys, P. López-García, H. Martin, T. Montmerle, R. Pascal, and J. Reisse). Springer New York. pp. 39-95.

Morbidelli A., Bottke W. F., Nesvorný D., and Levison H. F. (2009) Asteroids were born big. Icarus 204, 558-573.

Morbidelli A., Crida A., Masset F., and Nelson R. P. (2008) Building giant-planet cores at a planet trap. A&A 478, 929-937.

Morbidelli A., Lunine J. I., O'Brien D. P., Raymond S. N., and Walsh K. J. (2012) Building Terrestrial Planets. Annual Review of Earth and Planetary Sciences 40, 251-275.

Moreno M. (2006) Synthèse en phase gazeuse de nanoparticules de carbone par plasma hors équilibre. École Nationale Supérieure des Mines de Paris.

Mostefaoui S., Lugmair G. W., and Hoppe P. (2005) 60Fe: A Heat Source for Planetary Differentiation from a Nearby Supernova Explosion. The Astrophysical Journal 625, 271.

Mumma M. J. and Charnley S. B. (2011) The Chemical Composition of Comets—Emerging Taxonomies and Natal Heritage. Annual Review of Astronomy and Astrophysics 49, 471-524.

Muñoz Caro G. M. and Schutte W. A. (2003) UV-photoprocessing of interstellar ice analogs: New infrared spectroscopic results. Astronomy & Astrophysics 412, 121-132.

Muskatel B. H., Remacle F., Thiemens M. H., and Levine R. D. (2011) On the strong and selective isotope effect in the UV excitation of N2 with implications toward the nebula and Martian atmosphere. Proceedings of the National Academy of Sciences 108, 6020-6025.

Nichols R. H., Nuth J. A., Hohenberg C. M., Olinger C. T., and Moore M. H. (1992) Trapping of Noble-Gases in Proton-Irradiated Silicate Smokes. Meteoritics 27, 555-559.

Niemann H., Atreya S., Bauer S., Carignan G., Demick J., Frost R., Gautier D., Haberman J., Harpold D., and Hunten D. (2005) The abundances of constituents of Titan's atmosphere from the GCMS instrument on the Huygens probe. Nature 438, 779-784.

Niemann H., Atreya S., Demick J., Gautier D., Haberman J., Harpold D., Kasprzak W., Lunine J., Owen T., and Raulin F. (2010) Composition of Titan's lower atmosphere and simple surface volatiles as measured by the Cassini-Huygens probe gas chromatograph mass spectrometer experiment. Journal of Geophysical Research 115, E12006.

Nishijima D., Ye M. Y., Ohno N., and Takamura S. (2004) Formation mechanism of bubbles and holes on tungsten surface with low-energy and high-flux helium plasma irradiation in NAGDIS-II. Journal of Nuclear Materials 329–333, Part B, 1029-1033.

Notesco G., Bar-Nun A., and Owen T. (2003) Gas trapping in water ice at very low deposition rates and implications for comets. Icarus 162, 183-189.

Nuevo M., Milam S., Sandford S., De Gregorio B., Cody G., and Kilcoyne A. (2011) XANES analysis of organic residues produced from the UV irradiation of astrophysical ice analogs. Advances in Space Research 48, 1126-1135.

Nuth J. (2008) What was the Volatile Composition of the Planetesimals that Formed the Earth? Earth, Moon, and Planets 102, 435-445.

Oberlin A., Goma J., and Rouzaud J. (1984) Techniques d'étude des structures et textures (microtextures) des matériaux carbonés. J Chim Phys 81, 701-710.

Orthous-daunay F.-R. (2011) Empreinte moléculaire des processus post-accrétionnels dans la matière organique des chondrites carbonées. Université Joseph Fourier, Grenoble.

Orthous-Daunay F.-R., Quirico E., Beck P., Brissaud O., and Schmitt B. (2010a) Structural and functional micro-infrared survey of pristine carbonaceous chondrites insoluble organic matter. In *Lunar and Planetary Institute Science Conference Abstracts*. pp. 1803.

Orthous-Daunay F. R., Quirico E., Beck P., Brissaud O., Dartois E., Pino T., and Schmitt B. (2013) Mid-infrared study of the molecular structure variability of insoluble organic matter from primitive chondrites. Icarus 223, 534-543.

Orthous-Daunay F. R., Quirico E., Lemelle L., Beck P., deAndrade V., Simionovici A., and Derenne S. (2010b) Speciation of sulfur in the insoluble organic matter from carbonaceous chondrites by XANES spectroscopy. Earth and Planetary Science Letters 300, 321-328.

Ott U. (2002) Noble Gases in Meteorites - Trapped Components. In *Reviews in Mineralogy and Geochemistry* (eds. D. Porcelli, C. J. Ballentine, and R. Wieler). The Mineralogical Society of America. pp. 71-100.

Ott U. (2014) Planetary and pre-solar noble gases in meteorites. Chemie der Erde - Geochemistry.

Ott U., Mack R., and Sherwood C. (1981) Noble-gas-rich separates from the Allende meteorite. Geochimica et Cosmochimica Acta 45, 1751-1788.

Owen T., Mahaffy P. R., Niemann H. B., Atreya S., and Wong M. (2001) Protosolar Nitrogen. The Astrophysical Journal Letters 553, L77.

Ozima M., Wieler R., Marty B., and Podosek F. A. (1998) Comparative studies of solar, Q-gases and terrestrial noble gases, and implications on the evolution of the solar nebula. Geochimica Et Cosmochimica Acta 62, 301-314.

Painter P. C., Snyder R. W., Starsinic M., Coleman M. M., Kuehn D. W., and Davis A. (1981) Concerning the Application of FT-IR to the Study of Coal: A Critical Assessment of Band Assignments and the Application of Spectral Analysis Programs. Applied Spectroscopy 35, 475-485.

Pendleton Y. J. and Allamandola L. J. (2002) The Organic Refractory Material in the Diffuse Interstellar Medium: Mid-Infrared Spectroscopic Constraints. The Astrophysical Journal Supplement Series 138, 75.

Peng Z. (2013) Experimental and theoretical simulations of Titan's VUV photochemistry. Université Paris Sud-Paris XI.

Peng Z., Gautier T., Carrasco N., Pernot P., Giuliani A., Mahjoub A., Correia J. J., Buch A., Bénilan Y., Szopa C., and Cernogora G. (2013) Titan's atmosphere simulation experiment using continuum UV-VUV synchrotron radiation. Journal of Geophysical Research: Planets 118, 778-788.

Pepin R. O. (1991) On the origin and early evolution of terrestrial planet atmospheres and meteoritic volatiles. Icarus 92, 2-79.

Pepin R. O., Becker R. H., and Rider P. E. (1995) Xenon and krypton isotopes in extraterrestrial regolith soils and in the solar wind. Geochimica et Cosmochimica Acta 59, 4997-5022.

Pernot P., Carrasco N., Thissen R., and Schmitz-Afonso I. (2010) Tholinomics—Chemical analysis of nitrogen-rich polymers. Analytical chemistry 82, 1371-1380.

Pizzarello S., Cooper G., and Flynn G. (2006) The nature and distribution of the organic material in carbonaceous chondrites and interplanetary dust particles. In *Meteorites and the early solar system II* (eds. D. S. Lauretta and H. J. McSween). University of Arizon Press. pp. 625-651.

Ponganis K. V., Graf T., and Marti K. (1997) Isotopic fractionation in low-energy ion implantation. J. Geophys. Res. 102, 19335-19343.

Pujol M., Marty B., and Burgess R. (2011) Chondritic-like xenon trapped in Archean rocks: A possible signature of the ancient atmosphere. Earth and Planetary Science Letters 308, 298-306.

Qin L., Dauphas N., Wadhwa M., Masarik J., and Janney P. E. (2008) Rapid accretion and differentiation of iron meteorite parent bodies inferred from 182Hf–182W chronometry and thermal modeling. Earth and Planetary Science Letters 273, 94-104.

Quirico E., Borg J., Raynal P.-I., Montagnac G., and d'Hendecourt L. (2005) A micro-Raman survey of 10 IDPs and 6 carbonaceous chondrites. Planetary and Space Science 53, 1443-1448.

Quirico E., Montagnac G., Lees V., McMillan P. F., Szopa C., Cernogora G., Rouzaud J.-N., Simon P., Bernard J.-M., Coll P., Fray N., Minard R. D., Raulin F., Reynard B., and Schmitt B. (2008) New experimental constraints on the composition and structure of tholins. Icarus 198, 218-231.

Quirico E., Montagnac G., Rouzaud J. N., Bonal L., Bourot-Denise M., Duber S., and Reynard B. (2009) Precursor and metamorphic condition effects on Raman spectra of poorly ordered carbonaceous matter in chondrites and coals. Earth and Planetary Science Letters 287, 185-193.

Quirico E., Orthous-Daunay F.-R., Beck P., Bonal L., Brunetto R., Dartois E., Pino T., Montagnac G., Rouzaud J.-N., Engrand C., and Duprat J. (2014) Origin of insoluble organic matter in type 1 and 2 chondrites: new clues, new questions. Geochimica et Cosmochimica Acta.

Quirico E., Raynal P.-I., and Bourot-Denise M. (2003) Metamorphic grade of organic matter in six unequilibrated ordinary chondrites. Meteoritics & Planetary Science 38, 795-811.

Rai V. K., Murty S. V. S., and Ott U. (2003) Noble gases in ureilites: Cosmogenic, radiogenic, and trapped components. Geochimica Et Cosmochimica Acta 67, 4435-4456.

Raymond S. N., Kokubo E., Morbidelli A., Morishima R., and Walsh K. J. (2013) Terrestrial Planet Formation at Home and Abroad. arXiv preprint arXiv:1312.1689.

Raymond S. N., Quinn T., and Lunine J. I. (2006) High-resolution simulations of the final assembly of Earth-like planets I. Terrestrial accretion and dynamics. Icarus 183, 265-282.

Remusat L., Derenne S., Robert F., and Knicker H. (2005) New pyrolytic and spectroscopic data on Orgueil and Murchison insoluble organic matter: A different origin than soluble? Geochimica et Cosmochimica Acta 69, 3919-3932.

Remusat L. and et al. (2009) Proto-Planetary Disk Chemistry Recorded by D-Rich Organic Radicals in Carbonaceous Chondrites. The Astrophysical Journal 698, 2087.

Remusat L., Guan Y. Y., Wang Y., and Eiler J. M. (2010) Accretion and Preservation of D-rich Organic Particles in Carbonaceous Chondrites: Evidence for Important Transport in the Early Solar System Nebula. The Astrophysical Journal 713, 1048.

Remusat L., Palhol F., Robert F., Derenne S., and France-Lanord C. (2006) Enrichment of deuterium in insoluble organic matter from primitive meteorites: A solar system origin? Earth and Planetary Science Letters 243, 15-25.

Reynolds J. H. (1956) High Sensitivity Mass Spectrometer for Noble Gas Analysis. Review of Scientific Instruments 27, 928-934.

Ristein J., Stief R. T., Ley L., and Beyer W. (1998) A comparative analysis of a-C:H by infrared spectroscopy and mass selected thermal effusion. Journal of Applied Physics 84, 3836-3847.

Robert F., Derenne S., Thomen A., Anquetil C., and Hassouni K. (2011) Deuterium exchange rate between and organic CH bonds: Implication for D enrichment in meteoritic IOM. Geochimica et Cosmochimica Acta 75, 7522-7532.

Robert F. and Epstein S. (1982) The concentration and isotopic composition of hydrogen, carbon and nitrogen in carbonaceous meteorites. Geochimica et Cosmochimica Acta 46, 81-95.

Rodgers S. D. and Charnley S. B. (2008a) Nitrogen Isotopic Fractionation of Interstellar Nitriles. The Astrophysical Journal 689, 1448.

Rodgers S. D. and Charnley S. B. (2008b) Nitrogen superfractionation in dense cloud cores. Monthly Notices of the Royal Astronomical Society: Letters 385, L48-L52.

Rotundi A., Baratta G. A., Borg J., Brucato J. R., Busemann H., Colangeli L., D'Hendecourt L., Djouadi Z., Ferrini G., Franchi I. A., Fries M., Grossemy F., Keller L. P., Mennella V., Nakamura K., Nittler L. R., Palumbo M. E., Sandford S. A., Steele A., and Wopenka B. (2008) Combined micro-Raman, micro-infrared, and field emission scanning electron microscope analyses of comet 81P/Wild 2 particles collected by Stardust. Meteoritics & Planetary Science 43, 367-397.

Rousselot P., Pirali O., Jehin E., Vervloet M., Hutsemékers D., Manfroid J., Cordier D., Martin-Drumel M.-A., Gruet S., Arpigny C., Decock A., and Mousis O. (2014) Toward a Unique Nitrogen Isotopic Ratio in Cometary Ices. The Astrophysical Journal Letters 780, L17.

Rouzaud J.-N. and Clinard C. (2002) Quantitative high-resolution transmission electron microscopy: a promising tool for carbon materials characterization. Fuel Processing Technology 77-78, 229-235.

Sadezky A., Muckenhuber H., Grothe H., Niessner R., and Pöschl U. (2005) Raman microspectroscopy of soot and related carbonaceous materials: Spectral analysis and structural information. Carbon 43, 1731-1742.

Samson S. D. and Alexander Jr E. C. (1987) Calibration of the interlaboratory 40Ar-39Ar dating standard, MMhb-1. Chemical Geology: Isotope Geoscience section 66, 27-34.

Sandford S. A., Aléon J., Alexander C. M. O. D., Araki T., Bajt S. a., Baratta G. A., Borg J., Bradley J. P., Brownlee D. E., Brucato J. R., Burchell M. J., Busemann H., Butterworth A., Clemett S. J., Cody G., Colangeli L., Cooper G., D'Hendecourt L., Djouadi Z., Dworkin J. P., Ferrini G., Fleckenstein H., Flynn G. J., Franchi I. A., Fries M., Gilles M. K., Glavin D. P., Gounelle M., Grossemy F., Jacobsen C., Keller L. P., Kilcoyne A. L. D., Leitner J., Matrajt G., Meibom A., Mennella V., Mostefaoui S., Nittler L. R., Palumbo M. E., Papanastassiou D. A., Robert F., Rotundi A., Snead C. J., Spencer M. K., Stadermann F. J., Steele A., Stephan T., Tsou P., Tyliszczak T., Westphal A. J., Wirick S., Wopenka B., Yabuta H., Zare R. N., and Zolensky M. E. (2006) Organics Captured from Comet 81P/Wild 2 by the Stardust Spacecraft. Science 314, 1720-1724.

Sanloup C., Schmidt B. C., Gudfinnsson G., Dewaele A., and Mezouar M. (2011) Xenon and Argon: A contrasting behavior in olivine at depth. Geochimica et Cosmochimica Acta 75, 6271-6284.

Sciamma-O'Brien E., Carrasco N., Szopa C., Buch A., and Cernogora G. (2010) Titan's atmosphere: An optimal gas mixture for aerosol production? Icarus 209, 704-714.

Sciamma-O'Brien E., Dahoo P. R., Hadamcik E., Carrasco N., Quirico E., Szopa C., and Cernogora G. (2012) Optical constants from 370 nm to 900 nm of Titan tholins produced in a low pressure RF plasma discharge. Icarus 218, 356-363.

Selwyn G. S., McKillop J. S., and Haller K. L. (1990) In-situ Particulate Contamination Studies In Process Plasmas. pp. 86-97.

Sephton M. A. (2013) Aromatic units from the macromolecular material in meteorites: Molecular probes of cosmic environments. Geochimica et Cosmochimica Acta 107, 231-241.

Sforna M. C., van Zuilen M. A., and Philippot P. (2014) Structural characterization by Raman hyperspectral mapping of organic carbon in the 3.46 billion-year-old Apex chert, Western Australia. Geochimica et Cosmochimica Acta 124, 18-33.

Shcheka S. S. and Keppler H. (2012) The origin of the terrestrial noble-gas signature. Nature 490, 531-534.

Sloots B. (2008) Measuring the low OH content in quartz glass. Vibrational Spectroscopy 48, 158-161.

Smentkowski V. S. (2000) Trends in sputtering. Progress in Surface Science 64, 1-58.

Stewart S. T. and Leinhardt Z. M. (2012) Collisions between Gravity-dominated Bodies. II. The Diversity of Impact Outcomes during the End Stage of Planet Formation. The Astrophysical Journal 751, 32.

Strobel D., Atreya S., Bézard B., Ferri F., Flasar F. M., Fulchignoni M., Lellouch E., and Müller-Wodarg I. (2010) Atmospheric Structure and Composition. In *Titan from Cassini-Huygens* (eds. R. Brown, J.-P. Lebreton, and J. H. Waite). Springer Netherlands. pp. 235-257.

Stuart R. V. and Wehner G. K. (1962) Sputtering Yields at Very Low Bombarding Ion Energies. Journal of Applied Physics 33, 2345-2352.

Suess H. E., Wänke H., and Wlotzka F. (1964) On the origin of gas-rich meteorites. Geochimica et Cosmochimica Acta 28, 595-607.

Szopa C., Cernogora G., Boufendi L., Correia J. J., and Coll P. (2006) PAMPRE: A dusty plasma experiment for Titan's tholins production and study. Planetary and Space Science 54, 394-404.

Tachibana S. and Huss G. R. (2003) The Initial Abundance of 60Fe in the Solar System. The Astrophysical Journal Letters 588, L41.

Terzieva R. and Herbst E. (2000) The possibility of nitrogen isotopic fractionation in interstellar clouds. Monthly Notices of the Royal Astronomical Society 317, 563-568.

Thi W. F., Woitke P., and Kamp I. (2010) Warm non-equilibrium gas phase chemistry as a possible origin of high HDO/H2O ratios in hot and dense gases: application to inner protoplanetary discs. Monthly Notices of the Royal Astronomical Society 407, 232-246.

Thomsen C. and Reich S. (2000) Double Resonant Raman Scattering in Graphite. Physical Review Letters 85, 5214-5217.

Tielens A. G. (2005) *The physics and chemistry of the interstellar medium.* Cambridge University Press.

Tielens A. G. G. M. (2008) Interstellar Polycyclic Aromatic Hydrocarbon Molecules. Annual Review of Astronomy and Astrophysics 46, 289-337.

Tolstikhin I. N. and Marty B. (1998) The evolution of terrestrial volatiles: a view from helium, neon, argon and nitrogen isotope modelling. Chemical Geology 147, 27-52.

Tomasko M. G. and Smith P. H. (1982) Photometry and polarimetry of Titan: Pioneer 11 observations and their implications for aerosol properties. Icarus 51, 65-95.

Tuinstra F. and Koenig J. L. (1970) Characterization of Graphite Fiber Surfaces with Raman Spectroscopy. Journal of Composite Materials 4, 492-499.

Urey H. C. (1947) The thermodynamic properties of isotopic substances. Journal of the Chemical Society (Resumed), 562-581.

Uzun B. B., Pütün A. E., and Pütün E. (2007) Composition of products obtained via fast pyrolysis of olive-oil residue: Effect of pyrolysis temperature. Journal of Analytical and Applied Pyrolysis 79, 147-153.

van de Runstraat C. A., de Heer F. J., and Govers T. R. (1974) Excitation and decay of the C2Σ+u state of N+u in the case of electron impact on N2. Chemical Physics 3, 431-450.

Van Schmus W. R. and Wood J. A. (1967) A chemical-petrologic classification for the chondritic meteorites. Geochimica et Cosmochimica Acta 31, 747-765.

Vidano R. P., Fischbach D. B., Willis L. J., and Loehr T. M. (1981) Observation of Raman band shifting with excitation wavelength for carbons and graphites. Solid State Communications 39, 341-344.

Villeneuve J., Chaussidon M., and Libourel G. (2009) Homogeneous Distribution of 26Al in the Solar System from the Mg Isotopic Composition of Chondrules. Science 325, 985-988.

Vinatier S., Bézard B., and Nixon C. A. (2007) The Titan 14N/15N and 12C/13C isotopic ratios in HCN from Cassini/CIRS. Icarus 191, 712-721.

Vis R. D., Mrowiec A., Kooyman P. J., Matsubara K., and Heymann D. (2002) Microscopic search for the carrier phase Q of the trapped planetary noble gases in Allende, Leoville and Vigarano. Meteoritics & Planetary Science 37, 1391-1399.

Visser R., Doty S. D., and van Dishoeck E. F. (2011) The chemical history of molecules in circumstellar disks II. Gas-phase species. Astronomy & Astrophysics 534.

Vuitton V., Bonnet J.-Y., Frisari M., Thissen R., Quirico E., Dutuit O., Schmitt B., Le Roy L., Fray N., Cottin H., Sciamma-O'Brien E., Carrasco N., and Szopa C. (2010) Very high resolution mass spectrometry of HCN polymers and tholins. Faraday Discussions 147, 495-508.

Wacker J. F. and Anders E. (1984) Trapping of xenon in ice: implications for the origin of the Earth's noble gases. Geochimica et Cosmochimica Acta 48, 2373-2380.

Wacker J. F., Zadnik M. G., and Anders E. (1985) Laboratory simulation of meteoritic noble gases. I. Sorption of xenon on carbon: Trapping experiments. Geochimica et Cosmochimica Acta 49, 1035-1048.

Walsh C., Nomura H., Millar T. J., and Aikawa Y. (2012a) Chemical Processes in Protoplanetary Disks. II. On the Importance of Photochemistry and X-Ray Ionization. The Astrophysical Journal 747, 114.

Walsh K. J., Morbidelli A., Raymond S. N., O'Brien D. P., and Mandell A. M. (2011) A low mass for Mars from Jupiter/'s early gas-driven migration. Nature 475, 206-209.

Walsh K. J., Morbidelli A., Raymond S. N., O'Brien D. P., and Mandell A. M. (2012b) Populating the asteroid belt from two parent source regions due to the migration of giant planets—"The Grand Tack". Meteoritics & Planetary Science 47, 1941-1947.

Watson W. D. (1974) Ion-molecule reactions, molecule formation, and hydrogen-isotope exchange in dense interstellar clouds. The Astrophysical Journal 188, 35-42.

Weber H. W., Hintenberger H., and Begemann F. (1971) Noble gases in the Haveröureilite. Earth and Planetary Science Letters 13, 205-209.

Weidenschilling S. (2000) Formation of Planetesimals and Accretion of the Terrestrial Planets. Space Science Reviews 92, 295-310.

Williams J. P. and Cieza L. A. (2011) Protoplanetary Disks and Their Evolution. Annual Review of Astronomy and Astrophysics 49, 67-117.

Wirström E. S., Charnley S. B., Cordiner M. A., and Milam S. N. (2012) Isotopic Anomalies in Primitive Solar System Matter: Spin-state-dependent Fractionation of Nitrogen and Deuterium in Interstellar Clouds. The Astrophysical Journal Letters 757, L11.

Woolfson M. (1993) The solar-origin and evolution. Quarterly Journal of the Royal Astronomical Society 34, 1-20.

Wopenka B. and Pasteris J. D. (1993) *Structural characterization of kerogens to granulite-facies graphite : applicability of Raman microprobe spectroscopy.* Mineralogical Society of America, Washington, DC, ETATS-UNIS.

Yokochi R. (2005) L' azote, le néon et le xénon dans le manteau : sources, processus et hétérogénéités. INPL, Nancy.

Young E. D., Galy A., and Nagahara H. (2002) Kinetic and equilibrium mass-dependent isotope fractionation laws in nature and their geochemical and cosmochemical significance. Geochimica et Cosmochimica Acta 66, 1095-1104.

Ziegler J. and Biersack J. (1985) The Stopping and Range of Ions in Matter. In *Treatise on Heavy-Ion Science* (ed. D. A. Bromley). Springer US. pp. 93-129.

Zipf E. C. and McLaughlin R. W. (1978) On the dissociation of nitrogen by electron impact and by E.U.V. photo-absorption. Planetary and Space Science 26, 449-462.

Zolensky M. E., Zega T. J., Yano H., Wirick S., Westphal A. J., Weisberg M. K., Weber I., Warren J. L., Velbel M. A., Tsuchiyama A., Tsou P., Toppani A., Tomioka N., Tomeoka K., Teslich N., Taheri M., Susini J., Stroud R., Stephan T., Stadermann F. J., Snead C. J., Simon S. B., Simionovici A., See T. H., Robert F., Rietmeijer F. J. M., Rao W., Perronnet M. C., Papanastassiou D. A., Okudaira K., Ohsumi K., Ohnishi I., Nakamura-Messenger K., Nakamura T., Mostefaoui S., Mikouchi T., Meibom A., Matrajt G., Marcus M. A., Leroux H., Lemelle L., Le L., Lanzirotti A., Langenhorst F., Krot A. N., Keller L. P., Kearsley A. T., Joswiak D., Jacob D., Ishii H., Harvey R., Hagiya K., Grossman L., Grossman J. N., Graham G. A., Gounelle M., Gillet P., Genge M. J., Flynn G., Ferroir T., Fallon S., Ebel D. S., Dai Z.

R., Cordier P., Clark B., Chi M., Butterworth A. L., Brownlee D. E., Bridges J. C., Brennan S., Brearley A., Bradley J. P., Bleuet P., Bland P. A., and Bastien R. (2006) Mineralogy and Petrology of Comet 81P/Wild 2 Nucleus Samples. Science 314, 1735-1739.

Zubko V., Dwek E., and Arendt R. G. (2004) Interstellar Dust Models Consistent with Extinction, Emission, and Abundance Constraints. The Astrophysical Journal Supplement Series 152, 211.

List of figures

List of Tables

Appendix A

Experimental conditions for the samples produced in the Nebulotron setup

Analytical techniques performed on each of them

Samples' name: CO-i stands for a starting gas mixture composed of CO only
CO-GR-i stands for a CO-Noble Gas mixture
CO-N2 stands for a CO-N2 gas mixture
CO-N2-GR-i stands for a CO-N2-Noble Gas mixture

i = order of production in time
N stands for black powders (center of the discharge)
R stands for red films (edges of the discharge)

As a function of the production date

date	sample	gas	duration (min)	flowrate CO (sccm)	flowrate N2/GR (sccm)	pressure (mbar)	input power (W)	net power (W)	mass recovered (mg)	production rate (mg/h)	elem. analysis	FTIR	Raman (514 nm)	Raman (UV)	Xe analysis	Kr analysis	Ar analysis
01/06/11	CO-3	CO	60	5		0.75	70	60	3.5	3.50	x			x			
01/06/11	CO-4	CO	30	5		0.75	70	55	2.7	5.40							
07/06/11	CO-6	CO	5	5		0.77	80	60									
	CO-7	CO	15	5		0.75	75	60									
08/06/11	CO-8	CO	240	5		0.75	80	60	0.3	0.08							
	CO-9	CO	240	5		0.75	80	60	12.8	3.20	x	x	x	x			
09/06/11	CO-10	CO	240	5		0.75	50	40	0.8	0.20				x			
	CO-11	CO	240	5		0.75	50	40	12.6	3.15	x	x	x	x			
10/06/11	CO-Ar-1	CO-Ar	120	5	1	0.6	60	48	?								
	CO-Ar-2	CO-Ar	120	5	1			40									
	CO-Ar-3	CO-Ar	240	5	1			40									
	CO-Ar-4	CO-Ar		5	1			40									
29/06/11	CO-12	CO	120	5		0.688	50	40			x	x	x				
27/07/11	CO-GR1	CO-GR	60	5	1	0.753	60	45	0.2	0.20					x	x	x
28/07/11	CO-GR2	CO-GR	60	5	1	0.723	60	45	0.4	0.40					x	x	x
03/08/11	CO-GR3	CO-GR	120	8	1	0.969	60	40	6.1	3.05	x	x	x	x	x	x	x
	CO-GR4	CO-GR	120	5	1	0.774	60	40	0.2	0.10					x	x	x
	CO-GR5	CO-GR	120	5	3	0.98	60	40	1.4	0.70	x			x	x	x	x
	CO-GR6R	CO-GR	210	5	1	0.794	60	40	0.5	0.14		x		x			
	CO-GR6N	CO-GR	210	5	1	0.794	60	40	7.5	2.14	x	x	x	x	x	x	x
24/10/11	CO-GR7R	CO-GR	120	5	1	0.825	75	50	0.7	0.35							
	CO-GR7N	CO-GR	120	5	*1*				3	1.50					x		
25/10/11	CO-GR8R	CO-GR	120	5	1	0.805	40	30	1	0.50				x			
	CO-GR8N	CO-GR	120	5	1				5	2.50	x			x	x		
25/10/11	CO-GR9	CO-GR	120	5	1	0.8	90	65	7.5	3.75	x	x		x	x		
26/10/11	CO-GR10R	CO-GR	120	5	4	1.11	60	40	0.3	0.15				x			
	CO-GR10N	CO-GR	120	5	4			40	2.5	1.25	x			x	x		
27/10/11	CO-GR11R	CO-GR	120	5	5	1.19	60	40	0.7	0.35				x			
	CO-GR11N	CO-GR	120	5	5			40	4	2.00	x			x	x	x	

date	sample	gas	duration (min)	flowrate CO (sccm)	flowrate N2/GR (sccm)	pressure (mbar)	input power (W)	net power (W)	mass recovered (mg)	production rate (mg/h)	elem. analysis	FTIR	Raman (514 nm)	Raman (UV)	Xe analysis	Kr analysis	Ar analysis
28/10/11	CO-GR12R	CO-GR	120	8	1	1.02	60	40	0.8	0.40							
	CO-GR12N	CO-GR	120	8	1			40	10.4	5.20					x		
31/10/11	CO-GR13	CO-GR	120	5	1	0.878-0.806	60	40	3.2	1.60	x						
03/11/11	CO-GR14R	CO-GR	120	5	4	1.11	60	40	0.5	0.25		x		x			
	CO-GR14N	CO-GR	120	5	4			40	2.6	1.30		x		x			
04/11/11	CO-GR15	CO-GR	120	8	1	0.99	60	40	9.5	4.75							
18/11/11	CO-GR16R	CO-GR	120	5	1	0.601	60	40	0.8	0.40				x			
	CO-GR16N	CO-GR	120	5	1			40	2.5	1.25	x			x			
21/11/11	CO-GR17R	CO-GR	120	5	5	0.84	60	40	0.3	0.15							
	CO-GR17N	CO-GR	120	5	5			40	2.9	1.45					x		
22/11/11	CO-N2-2	CO-N2	120	5	1	0.58	60	40	1.2	0.60		x		x			
14/02/12	CO-GR18R	CO-GR	360	5	1	0.833	60	40	1.1	0.18				x			
	CO-GR18N	CO-GR	360	5	1			40	47.7	7.95	x	x		x	x	x	
19/04/12	CO-GR19R	CO-GR	360	5	1		60	40	1.4	0.23							
	CO-GR19N	CO-GR	360	5	1			40	38.3	6.38	x	x			x		
02/05/12	CO-N2 20N	CO-N2	360	5	1		60	40	22.7	3.78	x	x					
	CO-N2 20R	CO-N2	360	5	1			40	5.5	0.92	x						
	CO-N2 20B	CO-N2	360	5	1			40	8	1.33	x	x					
03/05/12	CO-N-GR21N	CO-N2-GR	360	5	1		60	40	56.15	9.36	x				x		
	CO-N-GR21R	CO-N2-GR	360	5	1			40	4.6	0.77	x						
30/07/12	CO-GR-22	CO-GR	300	5	1	0.6	60	35	1	0.20							
31/07/12	CO-GR-23N	CO-GR	120	5	1	1	70	40	2.8	1.40		x			x		
	CO-GR23R	CO-GR	120	5	1			40	0.3	0.15							
	CO25	CO		5								x			x		
29/08/12	CO26	CO	915	5		0.8	60	40	64.2	4.21		x					
18/09/12	CO-GR27	CO-GR	120	5	1	1	60	40	5.7	2.85		x					
10/06/13	CO28	CO	120	10		2.28	31	30			x	x			x		
05/08/13	CON2-3	CO-N2	240	5/1	1	0.9	31	30	39.8	9.95							
08/08/13	CO-GR29	CO-GR	360	5	1	0.7	31	30	25.2	4.20	x	x			x		
13/08/13	CO-GR30	CO-GR	360	5	1	0.6	60	60	25.4	4.23	x	x			x		
03/09/13	CO-GR31	CO-GR	360	5	1	0.5	30	30	30.6	5.10	x	x			x		
05/09/13	CO-GR32	CO-GR	360	5	1	0.6	30	30	23.6	3.93	x	x					
09/09/13	CO-N-GR34	CO-N2-GR	360	5	1	0.6	30	30	72.1	12.02	x	x			x		
12/09/13	CO-N-GR35	CO-N2-GR	360	5	1	0.6	30	30	65.6	10.93	x	x					
16/09/13	CO-N-GR36	CO-N2-GR	360	5	1	0.6	30	30	58.2	9.70	x	x					
21/11/13	CO-N-GR37	CO-N2-GR	420	5	1	0.6	30	30	122.2	17.46	x						

As a function of the gas mixtures used

date	sample	gas	duration (min)	flowrate CO (sccm)	flowrate N2/GR (sccm)	pressure (mbar)	input power (W)	net power (W)	mass recovered (mg)	production rate (mg/h)	elem. analysis	FTIR	Raman (514 nm)	Raman (UV)	Xe analysis	Kr analysis	Ar analysis
Experiments with CO only																	
01/06/11	CO-3	CO	60	5		0.75	70	60	3.5	3.50	x			x			
01/06/11	CO-4	CO	30	5		0.75	70	55	2.7	5.40							
07/06/11	CO-6	CO	5	5		0.77	80	60									
	CO-7	CO	15	5		0.75	75	60									
08/06/11	CO-8	CO	240	5		0.75	80	60	0.3	0.08							
	CO-9	CO	240	5		0.75	80	60	12.8	3.20	x	x	x	x			
09/06/11	CO-10	CO	240	5		0.75	50	40	0.8	0.20				x			
	CO-11	CO	240	5		0.75	50	40	12.6	3.15	x	x	x	x			
29/06/11	CO-12	CO	120	5		0.688	50	40			x	x	x				
	CO25	CO		5								x			x		
29/08/12	CO26	CO	915	5		0.8	60	40	64.2	4.21		x					
10/06/13	CO28	CO	120	10		2.28	31	30			x	x			x		
Experiments with CO + Noble gases																	
10/06/11	CO-Ar-1	CO-Ar	120	5	1	0.6	60	48	?								
	CO-Ar-2	CO-Ar	120	5	1			40									
	CO-Ar-3	CO-Ar	240	5	1			40									
	CO-Ar-4	CO-Ar		5	1			40									
27/07/11	CO-GR1	CO-GR	60	5	1	0.753	60	45	0.2	0.20					x	x	x
28/07/11	CO-GR2	CO-GR	60	5	1	0.723	60	45	0.4	0.40					x	x	x
03/08/11	CO-GR3	CO-GR	120	8	1	0.969	60	40	6.1	3.05	x	x	x	x	x	x	x
	CO-GR4	CO-GR	120	5	1	0.774	60	40	0.2	0.10					x	x	x
	CO-GR5	CO-GR	120	5	3	0.98	60	40	1.4	0.70	x			x	x	x	x
	CO-GR6R	CO-GR	210	5	1	0.794	60	40	0.5	0.14		x		x			
	CO-GR6N	CO-GR	210	5	1	0.794	60	40	7.5	2.14	x	x	x	x	x	x	x
24/10/11	CO-GR7R	CO-GR	120	5	1	0.825	75	50	0.7	0.35							
	CO-GR7N	CO-GR	120	5	*1*				3	1.50					x		
25/10/11	CO-GR8R	CO-GR	120	5	1	0.805	40	30	1	0.50				x			
	CO-GR8N	CO-GR	120	5	1				5	2.50	x			x	x		
25/10/11	CO-GR9	CO-GR	120	5	1	0.8	90	65	7.5	3.75	x	x		x	x		
26/10/11	CO-GR10R	CO-GR	120	5	4	1.11	60	40	0.3	0.15				x			
	CO-GR10N	CO-GR	120	5	4			40	2.5	1.25	x			x	x		
27/10/11	CO-GR11R	CO-GR	120	5	5	1.19	60	40	0.7	0.35				x			
	CO-GR11N	CO-GR	120	5	5			40	4	2.00	x			x	x	x	

date	sample	gas	duration (min)	flowrate CO (sccm)	flowrate N2/GR (sccm)	pressure (mbar)	input power (W)	net power (W)	mass recovered (mg)	production rate (mg/h)	elem. analysis	FTIR	Raman (514 nm)	Raman (UV)	Xe analysis	Kr analysis	Ar analysis
28/10/11	CO-GR12R	CO-GR	120	8	1	1.02	60	40	0.8	0.40							
	CO-GR12N	CO-GR	120	8	1			40	10.4	5.20					x		
31/10/11	CO-GR13	CO-GR	120	5	1	0.878-0.806	60	40	3.2	1.60	x						
03/11/11	CO-GR14R	CO-GR	120	5	4	1.11	60	40	0.5	0.25		x		x			
	CO-GR14N	CO-GR	120	5	4			40	2.6	1.30		x		x			
04/11/11	CO-GR15	CO-GR	120	8	1	0.99	60	40	9.5	4.75							
18/11/11	CO-GR16R	CO-GR	120	5	1	0.601	60	40	0.8	0.40				x			
	CO-GR16N	CO-GR	120	5	1			40	2.5	1.25	x			x			
21/11/11	CO-GR17R	CO-GR	120	5	5	0.84	60	40	0.3	0.15							
	CO-GR17N	CO-GR	120	5	5			40	2.9	1.45					x		
14/02/12	CO-GR18R	CO-GR	360	5	1	0.833	60	40	1.1	0.18				x			
	CO-GR18N	CO-GR	360	5	1			40	47.7	7.95	x	x		x	x	x	
19/04/12	CO-GR19R	CO-GR	360	5	1		60	40	1.4	0.23							
	CO-GR19N	CO-GR	360	5	1			40	38.3	6.38	x	x			x		
30/07/12	CO-GR-22	CO-GR	300	5	1	0.6	60	35	1	0.20							
31/07/12	CO-GR-23N	CO-GR	120	5	1	1	70	40	2.8	1.40		x			x		
	CO-GR23R	CO-GR	120	5	1			40	0.3	0.15							
18/09/12	CO-GR27	CO-GR	120	5	1	1	60	40	5.7	2.85		x					
08/08/13	CO-GR29	CO-GR	360	5	1	0.7	31	30	25.2	4.20	x	x			x		
13/08/13	CO-GR30	CO-GR	360	5	1	0.6	60	60	25.4	4.23	x	x			x		
03/09/13	CO-GR31	CO-GR	360	5	1	0.5	30	30	30.6	5.10	x	x			x		
05/09/13	CO-GR32	CO-GR	360	5	1	0.6	30	30	23.6	3.93	x	x					
Experiments with CO + N2 + Noble gases																	
03/05/12	CO-N-GR21N	CO-N2-GR	360	5	1		60	40	56.15	9.36	x				x		
	CO-N-GR21R	CO-N2-GR	360	5	1			40	4.6	0.77	x						
09/09/13	CO-N-GR34	CO-N2-GR	360	5	1	0.6	30	30	72.1	12.02	x	x			x		
12/09/13	CO-N-GR35	CO-N2-GR	360	5	1	0.6	30	30	65.6	10.93	x	x					
16/09/13	CO-N-GR36	CO-N2-GR	360	5	1	0.6	30	30	58.2	9.70	x	x					
21/11/13	CO-N-GR37	CO-N2-GR	420	5	1	0.6	30	30	122.2	17.46	x						
Experiments with CO + N2																	
22/11/11	CO-N2-2	CO-N2	120	5	1	0.58	60	40	1.2	0.60		x		x			
02/05/12	CO-N2 20N	CO-N2	360	5	1		60	40	22.7	3.78	x	x					
	CO-N2 20R	CO-N2	360	5	1			40	5.5	0.92	x						
	CO-N2 20B	CO-N2	360	5	1			40	8	1.33	x	x					
05/08/13	CON2-3	CO-N2	240	5/1	1	0.9	31	30	39.8	9.95							

Appendix B

Xe and Kr isotopic ratios measured in the Nebulotron samples

sample name	124Xe/132Xe	±1σ	126Xe/132Xe	±1σ	128Xe/132Xe	±1σ	129Xe/132Xe	±1σ	130Xe/132Xe	±1σ	131Xe/132Xe	±1σ	134Xe/132Xe	±1σ	136Xe/132Xe	±1σ
Argus																
COGR18N-A	-	-	-	-	0.0690	0.0056	0.9619	0.0043	0.1483	0.0033	0.7833	0.0042	0.3926	0.0040	0.3382	0.0045
COGR18N-B	-	-	-	-	0.0681	0.0036	0.9534	0.0021	0.1474	0.0041	0.7790	0.0041	0.3925	0.0027	0.3396	0.0027
COGR18N-C	-	-	-	-	0.0685	0.0040	0.9583	0.0024	0.1479	0.0048	0.7796	0.0045	0.3939	0.0034	0.3389	0.0033
COGR19N-B	-	-	-	-	0.0690	0.0033	0.9622	0.0024	0.1486	0.0046	0.7847	0.0043	0.3934	0.0027	0.3396	0.0030
COGR12	-	-	-	-	0.0690	0.0042	0.9615	0.0034	0.1488	0.0049	0.7836	0.0051	0.3932	0.0038	0.3393	0.0043
COGR10	-	-	-	-	0.0686	0.0060	0.9617	0.0060	0.1492	0.0057	0.7810	0.0060	0.3937	0.0038	0.3376	0.0054
COGR23N	-	-	-	-	0.0677	0.0046	0.9456	0.0033	0.1474	0.0052	0.7819	0.0052	0.3968	0.0033	0.3451	0.0041
COGR11N	-	-	-	-	0.0687	0.0039	0.9509	0.0035	0.1497	0.0048	0.7769	0.0043	0.3957	0.0027	0.3401	0.0033
COGR17N	-	-	-	-	0.0685	0.0033	0.9576	0.0023	0.1480	0.0046	0.7820	0.0045	0.3936	0.0030	0.3385	0.0032
COGR9N	-	-	-	-	0.0656	0.0065	0.9253	0.0052	0.1447	0.0045	0.7698	0.0050	0.3994	0.0051	0.3533	0.0053
COGR8	-	-	-	-	0.0693	0.0067	0.9695	0.0054	0.1483	0.0045	0.7870	0.0050	0.3941	0.0043	0.3398	0.0054
COGR7N	-	-	-	-	0.0687	0.0041	0.9556	0.0036	0.1490	0.0052	0.7825	0.0050	0.3961	0.0034	0.3420	0.0032
COGR21N	-	-	-	-	0.0692	0.0061	0.9496	0.0061	0.1503	0.0060	0.7796	0.0065	0.4004	0.0048	0.3464	0.0057
Helix MC																
GR18-800	0.00324	0.00005	0.00304	0.00005	0.0679	0.0008	0.9530	0.0022	0.1477	0.0007	0.7797	0.0018	0.3972	0.0014	0.3429	0.0017
GR29-1100	0.00327	0.00004	0.00309	0.00005	0.0684	0.0008	0.9598	0.0024	0.1486	0.0008	0.7828	0.0018	0.3975	0.0016	0.3431	0.0017
GR30-1100	0.00299	0.00004	0.00287	0.00004	0.0654	0.0007	0.9249	0.0020	0.1460	0.0007	0.7734	0.0020	0.4037	0.0014	0.3571	0.0016
GR31-1100	0.00330	0.00004	0.00313	0.00005	0.0690	0.0007	0.9555	0.0020	0.1490	0.0007	0.7812	0.0017	0.3945	0.0014	0.3430	0.0016
GR29-choc-1100	0.00329	0.00006	0.00313	0.00006	0.0675	0.0008	0.9621	0.0030	0.1490	0.0008	0.7841	0.0028	0.3972	0.0017	0.3422	0.0019
GR34-choc-1100	0.00330	0.00007	0.00322	0.00006	0.0684	0.0007	0.9683	0.0028	0.1498	0.0008	0.7855	0.0022	0.3915	0.0015	0.3384	0.0018
GR34-1100	0.00332	0.00007	0.00314	0.00005	0.0690	0.0010	0.9654	0.0031	0.1487	0.0009	0.7839	0.0027	0.3931	0.0019	0.3405	0.0020

	124Xe/130Xe	±1σ	126Xe/130Xe	±1σ	128Xe/130Xe	±1σ	129Xe/130Xe	±1σ	131Xe/130Xe	±1σ	132Xe/130Xe	±1σ	134Xe/130Xe	±1σ	136Xe/130Xe	±1σ
VG 5400																
COGR6N	0.0200	0.0011	0.0209	0.0008	0.4582	0.0108	6.3917	0.0530	5.2944	0.0422	6.8216	0.0603	0.0650	0.0017	2.3813	0.0236
COGR3	0.0200	0.0006	0.0211	0.0006	0.4644	0.0041	6.4362	0.0380	5.2484	0.0366	6.7326	0.0417	2.6715	0.0201	2.3001	0.0185
COGR11N	0.0219	0.0003	0.0205	0.0002	0.4497	0.0022	6.5590	0.0408	5.3428	0.0307	6.8592	0.0380	2.6600	0.0172	2.2758	0.0127
COGR18	0.0212	0.0005	0.0212	0.0005	0.4603	0.0044	6.4411	0.0322	5.2695	0.0343	6.7407	0.0455	2.6525	0.0211	2.2771	0.0160
COGR5	0.0225	0.0006	0.0213	0.0005	0.4641	0.0045	6.4296	0.0239	5.2381	0.0320	6.6923	0.0395	2.6244	0.0219	2.2486	0.0150
COGR1	0.0215	0.0021	0.0234	0.0019	0.4735	0.0238	6.5578	0.1998	5.2867	0.1643	6.6762	0.1700	2.6495	0.0821	2.2621	0.0845

	80Kr/84Kr	±1σ	82Kr/84Kr	±1σ	83Kr/84Kr	±1σ	86Kr/84Kr	±1σ
VG5400								
COGR6			0.2179	0.0248	0.1984	0.0222	0.3144	0.0313
COGR3			0.2154	0.0139	0.2025	0.0155	0.3116	0.0149
COGR11			0.2005	0.0040	0.2028	0.0052	0.3157	0.0066
COGR18			0.2028	0.0094	0.2052	0.0099	0.3087	0.0110
Helix MC								
GR18-800	0.0366	0.0056	0.1899	0.0048	0.1965	0.0052	0.3128	0.0064
GR29-1100	0.0299	0.0035	0.1986	0.0037	0.2017	0.0040	0.3161	0.0038
GR30-1100	0.0235	0.0028	0.1937	0.0032	0.1994	0.0032	0.3238	0.0036
GR31-1100	0.0356	0.0026	0.2017	0.0020	0.1989	0.0018	0.3113	0.0031
GR34-1100	0.0442	0.0066	0.2064	0.0073	0.2027	0.0077	0.2992	0.0092

Origine des fractionnements isotopiques de l'azote et des gaz rares dans les météorites et les atmosphères planétaires

L'azote et les gaz rares présents dans les astéroïdes, les comètes et les atmosphères planétaires sont piégés dans de la matière organique et ont des compositions chimiques qui sont différentes de celle du Soleil, représentatif du gaz primordial à partir duquel les différents objets du système solaire se sont formés il y a 4,5 milliards d'années. Au cours de cette thèse, des synthèses de matière carbonée à partir d'un mélange de gaz ont été réalisées dans un plasma appelé le *Nébulotron*, afin de mieux comprendre les processus à l'origine des compositions de l'azote et des gaz rares présents dans les météorites. Les caractéristiques de la matière organique ainsi que la composition des gaz rares piégés dans les météorites sont relativement bien reproduites dans les expériences, mais pas celle de l'azote. Ces résultats expérimentaux permettent de proposer des mécanismes clé à l'origine des compositions des éléments volatils présents dans les objets du système solaire.

Mots-clés : système solaire, fractionnement isotopique, azote, gaz rares, matière organique, étude expérimentale

Origin of isotopic fractionations of nitrogen and noble gases in meteorites and planetary atmospheres

Nitrogen and noble gases present in asteroids, comets or planetary atmospheres are trapped in organic matter and bear a composition that is different from the composition of the Sun, which is representative of the primordial gas from which the different objects in the solar system were formed 4.5 billion years ago. During this thesis, experimental syntheses of organic matter from gas mixtures in a plasma setup called the *Nebulotron* were performed in order to better understand the processes responsible for this chemical difference between the meteorites and the Sun for nitrogen and noble gases. The characteristics of the organic matter and the signature of the noble gases trapped in meteorites are relatively well reproduced in the experiments, whereas the composition of nitrogen is not. These experimental results give hints about the key mechanisms that are responsible for the variations of the volatile elements composition in the solar system objects.

Keywords : Solar System, isotopic fractionation, nitrogen, noble gases, organic matter, experimental study